The Pennsylvania State University

The Graduate School

Department of Materials Science and Engineering

DIELECTRIC NONLINEARITY OF FERROELECTRICS

A Dissertation in

Materials Science and Engineering

by

Ichiro Fujii

Submitted in Partial Fulfillment
of the Requirements
for the Degree of

Doctor of Philosophy

May 2010

The Dissertation of Ichiro Fujii was reviewed and approved* by the following:

Susan Trolier-McKinstry
Professor of Ceramic Science and Engineering
Dissertation Advisor
Chair of Committee

Clive A. Randall
Professor of Materials Science of Engineering

Wenwu Cao
Professor of Mathematics

Eric Cross
Evan Pugh Professor Emeritus of Electrical Engineering

Gary L. Messing
Distinguished Professor of Ceramics Science and Engineering
Head of the Department of Materials Science and Engineering

*Signatures are on file in the Graduate School

ABSTRACT

The ac field dependence of the dielectric constant and first order reversal curves (FORC) distribution were employed to quantify the effect of dielectric thickness, grain size, oxygen vacancy concentration, and microstructural heterogeneity on the dielectric nonlinearity of $PbZr_{0.52}Ti_{0.48}O_3$ thin films and $BaTiO_3$ – based ceramics on a wide electric field range. With the FORC distribution, the dielectric properties were calculated using Preisach model.

The FORC distribution of $PbZr_{0.52}Ti_{0.48}O_3$ thin films was characterized as a function of film thickness. It was found that the thickness dependence of the small field dielectric constant is due primarily to differences in the domain wall contributions to the properties. The irreversible FORC distribution decreased and the switching fields increased as the thickness decreased. Prediction of the polarization-electric field curves and the ac field dependence of the dielectric constant were found to give a good fit to the experimental results. Some discrepancies remain in the high field dielectric constant, probably caused by its definition.

The dielectric nonlinearity of $BaTiO_3$ ceramics with grain sizes from 1.2 to 76 μm was investigated. Defect dipoles in samples with large grains led to pinching of minor polarization – electric field loops as well as a threshold field in the ac field dependence of the dielectric constant and loss. For samples with small grains, a sublinear ac field dependence was observed. The irreversible FORC distributions characterizing the responses showed two strong and narrow peaks for large-grained samples and a weak, broad peak centered near the origin for samples with small grains. As the grain size decreased, the reversible FORC distribution at zero-bias field increased. No grain size dependence of the reversible FORC distributions was observed at high dc electric fields. These results indicate that the grain size dependence of the small field dielectric constant is attributable to a domain wall contribution and long-range domain wall motion suppressed while short-range domain wall motion enhanced as the grain size decreased.

The effect of the oxygen vacancies on the dielectric nonlinearity of formulated and undoped $BaTiO_3$ ceramics was investigated by changing oxygen partial pressure during firing. For the formulated ceramics, the dielectric constant of both oxygen and air fired samples increased almost linearly with the amplitude of the ac driving field. Formulated $BaTiO_3$ samples sintered in a reducing atmosphere produced a sub-linear increase in the permittivity with the ac field amplitude. For undoped $BaTiO_3$ ceramics, the dielectric constant increased sub-linearly over a wide range of oxygen partial pressures during firing. It is proposed for the formulated ceramics that the dopant – oxygen vacancy defect dipoles in the shell region accounted for the curvature in the field dependence of the permittivity. These defects appear to add a concentration of weak pinning centers to the potential energy profile through which domain walls move.

FORC distributions as well as the ac field dependence of the dielectric constant were investigated for model $BaTiO_3$ – based multilayer ceramic capacitors with dielectric layer thicknesses from 2.2 μm to 8.6 μm and those in which the grain size of the dielectrics varied from 0.28 μm to 0.39 μm while the layer thickness was held constant. In both cases, core-shell microstructures were observed. It was found that as the dielectric thickness decreased, the small and high electric field dielectric constants decreased, as did the peaks near the origin in the irreversible and reversible parts of the FORC distribution. The reversible FORC distributions of all the parts did not converge at high bias. These results indicate that the thickness dependence is attributable to a low dielectric constant interfacial layer and/or Schottky depletion layer at dielectric – electrode interfaces.

It was also found that the high field dielectric constant, the peak in the irreversible FORC distribution at the origin, and the reversible FORC distribution at zero bias decreased as grain size decreased, as was observed for the undoped ceramics. The reversible FORC distribution of all the parts converged at high biases, indicating the grain size dependence was influenced by domain

wall contributions. Dielectric contributions from the core and shell were estimated based on the temperature dependence of the permittivity. Not unexpectedly, the relative response of the core decreased while that of the shell increased as the grain size decreased. A Preisach model using the measured FORC distribution gave a good fit to the experimental polarization-electric field loops as a function of grain size and dielectric layer thickness.

TABLE OF CONTENTS

LIST OF FIGURES

LIST OF TABLES

ACKNOWLEDGEMENTS

I would like to express my sincere gratitude to my adviser: Prof. Susan Trolier-McKinstry for her guidance and support during the course of my studies. It has been an exciting opportunity to learn a subject with a long history under her supervision. I would also like to thank the other members of my committee: Prof. Clive Randall, Prof. Wenwu Cao and Prof. Eric Cross for their helpful suggestions.

I would like to acknowledge the Center for Dielectric Studies at Penn State and a National Security Science and Engineering Faculty Fellowship for financial support.

I would like to thank Youichi Mizuno of Taiyo Yuden Co. Ltd and Craig Nies of AVX Corp. for providing the model multilayer ceramic capacitors. Mike Chu of Ferro provided the X7R powder, Eunki Hong made the PZT films, and Michael Ugorek prepared the tape-cast green $BaTiO_3$ compacts; their help is greatly appreciated. I would like to thank Yisong Han of University of Sheffield and Joe Kulik and Josh Maier of Penn State for sample preparation and TEM observation .

I would like to thank Paul Moses and Jeff Long for helping with the dielectric measurements. Paul Moses, Jeff Long, and Chris Jabco built the HALT system. I would like to thank Anton Polotai for allowing me to use his reducing furnace. John Cantolina and Flavio Griggio should be acknowledged for helping with the FE-SEM observations. I would like to thank Maria DiCola for aid in polishing my samples and Maria Klimkiewicz for her help with SEM observations. I would like to thank Nichole Wondering for assistance for XRD. I would like to thank Amy, Sharon, and Susie for paper works for purchasing stuffs.

Thank you to STM group members for daily discussion: Aaron, Adarsh, Azo, Barb, Charley, Cheng, Dan, Derek, David, Eunki, Flavio, Hajime, Han, Heidi, Hideki, Ioanna, Mike, Mustafa, Nazanin, Pum, Raegan, Raffi, Raja, Ravi, Song Won, Susie, Tana, and Wanlin.

Chapter 1

Introduction

1.1 Introduction

Ferroelectric materials such as lead zirconate titanate (PZT) and barium titanate are used for electric devices due to their large dielectric and piezoelectric properties. However, when the materials are used at high ac electric fields, the polarization-electric field, strain-electric field, and polarization-stress responses become nonlinear and hysteretic, which is often a disadvantage for controlling device response. This matters for thin film applications since a high field is easily applied. For capacitors, high electric fields are also present due to recent progressive thinning of the dielectric layer thickness.

The origin of the large nonlinear and hysteretic dielectric responses in ferroelectrics is extrinsic contributions, that is, the motion of interfaces such as domain walls and phase boundaries.[1-3] The mobility and density of the interfaces may be influenced by many factors, as a result, the dielectric responses change accordingly.[4] For $BaTiO_3$ dielectrics, grain boundaries, core/shell microstructures, and dielectric/electrode interfaces can all act as pinning sources for domain wall motion (See Fig. 1-1). Moreover, these dielectrics are sintered in a reducing atmosphere. Consequently, the concentration of oxygen vacancy point defects can be high. The local electric or elastic fields associated with these defects could influence domain wall motion. In addition, an oxygen vacancy coupled with a metal vacancy or metal ion results in defect dipole, these are also reported to affect domain wall motion. These pinning sources result in dielectric nonlinearity; this thesis is directed towards quantifying their relative influence.

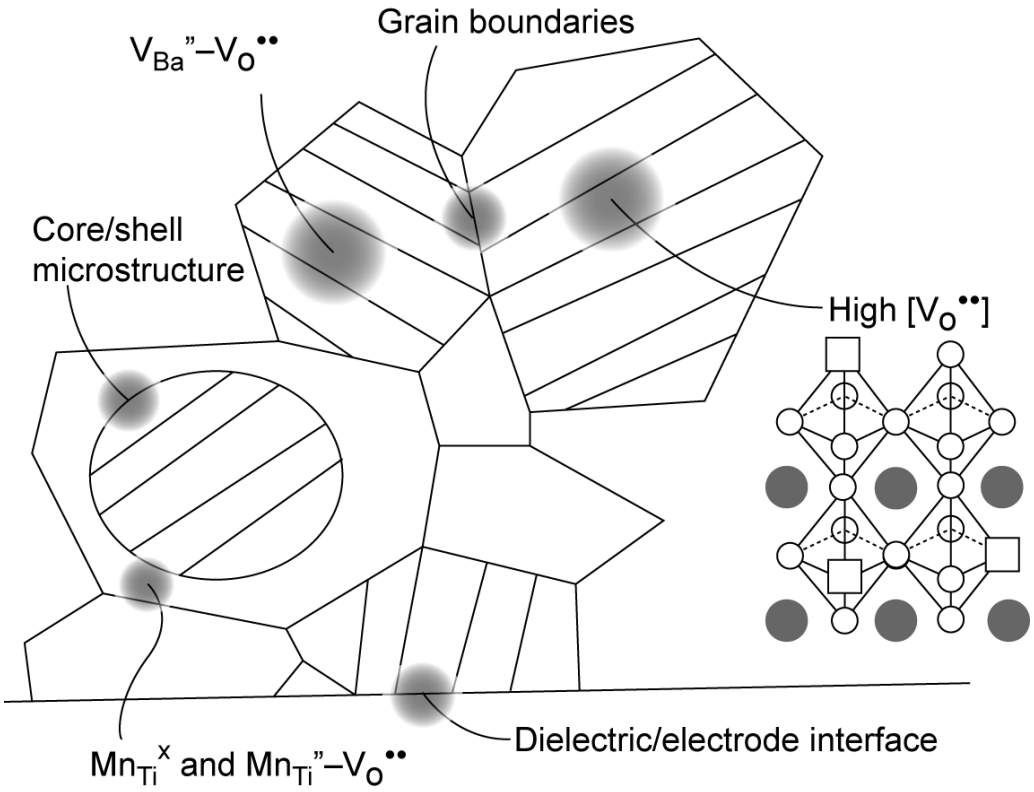

Figure **1-1**: Possible pinning sources in $BaTiO_3$ dielectrics.

Of several available means of describing and quantifying hysteretic phenomena, the Rayleigh Law[5, 6] is one of the simplest. The Rayleigh Law states that there should be a linear increase in the dielectric and piezoelectric properties as a function of the ac field amplitude (at subcoercive fields) that correlates directly with the observed hysteresis in the polarization or strain response, respectively. For the dielectric case, this is expressed by [6]

$$\varepsilon' = \varepsilon_{init}' + \alpha' E_{ac} \qquad \text{Eq. 1-1}$$

$$P = \varepsilon_0(\varepsilon_{init}' + \alpha' E_{ac})E \pm \varepsilon_0 \frac{\alpha'}{2}(E_{ac}^2 - E^2) \qquad \text{Eq. 1-2}$$

where ε' is the dielectric constant, the applied field is $E=E_{ac}\sin(\omega t)$, ε_{init}' is the reversible Rayleigh coefficient, α' is the irreversible Rayleigh coefficient, P is the polarization, and ε_0 is the permittivity of free space. ε_{init}' is thus a measure of the intrinsic contributions and contributions from reversible motion of the interfaces, while α' is a measures of a contribution of irreversible motions of the interfaces. Here, the intrinsic contributions are attributed to the field-induced response of an ensemble of single domains.

The dielectric response for some ferroelectric materials including lead zirconate titanate is well-described with Rayleigh Law.[4] However, it has been also reported that the dielectric response of $BaTiO_3$ dielectrics did not follow the Rayleigh Law.[7] When the Rayleigh approach is not applicable, the nonlinear response can be described and quantified by the Preisach model with appropriate distributions of the switching elements.[8]

The Preisach model describes hysteretic responses over a wider field range, and does not carry any implicit assumption about the distribution of the potential energy barriers through which domain walls move.[8-10] It assumes that the ferroelectric response consists of a set of rectangular hysteresis loops, called hysterons, with different up and down switching fields α and β ($\alpha \geq \beta$), so that the summation gives[9]

$$P = \iint_{\alpha>\beta} q(\alpha,\beta)\cdot\, p(\alpha,\beta)d\alpha d\beta + \int k(\alpha)\cdot\, p_{rev}(\alpha)d\alpha \qquad \text{Eq. 1-3}$$

where $q(\alpha,\beta)$ and $k(\alpha)$ are the irreversible and reversible Preisach operators; they are either +1 or -1, depending on the field history. $p(\alpha,\beta)$ and $p_{rev}(\alpha)$ are the irreversible and reversible Preisach distributions. The Preisach distribution can be experimentally obtained by the first order reversal curves (FORC) method[9] if the hysterons follows congruency and deletion properties; otherwise the Preisach-like distribution is called a FORC distribution[11]. In this case, the reversible FORC distribution describes the reversible dielectric contributions, while the irreversible FORC distribution describes the hysteresis in the polarization response.

1.2 Thesis Organization and Statement of Goals

In this study, the ac field dependence of the dielectric properties, FORC distribution, and Preisach model were used to quantify the dielectric nonlinearity of PZT thin films, $BaTiO_3$ dielectrics, and $BaTiO_3$ – based multilayer ceramic capacitors (MLCC). The backgrounds of the samples and the dielectric nonlinearity are described in Chapter 2. High field dielectric measurements are introduced in Chapter 3.

PZT thin films are used for applications such as non-volatile memories, accelerometers, micropumps, RF microelectromechanical systems switches, and power generators[12, 13]. In those applications, a wide range of the film thickness is utilized. It is known that the dielectric properties decrease with the thickness[14]. To date, the subcoercive dielectric nonlinearity was reported to be quantified by Rayleigh Law[4]. In this study, the FORC distribution was utilized to extend the field range over which the dielectric response of PZT films can be described for PZT films with thicknesses from 0.26 μm to 6 μm. The Preisach model was used to calculate the high field dielectric response using the FORC distributions. This is discussed in Chapter 4.

$BaTiO_3$ based dielectric are used for MLCCs due to the large and temperature-stable dielectric constant. Progressive miniaturization reduced the dielectric layer thickness. As a result,

the grain size of the dielectrics needs to decrease. The ac field dependence of the dielectric constant of $BaTiO_3$ based ceramics depends on grain size; the ac field dependence of the dielectric constant of large grains (>10 μm) is superlinear[7], while that of small grains (<1~3 μm) is sublinear[15]. To understand this, the ac field dependence of the dielectric properties and FORC distribution were studied for $BaTiO_3$ ceramics with grain sizes from 1.2 μm to 76 μm and the results are discussed in Chapter 5.

The miniaturization of MLCCs led to use of Ni for internal electrodes. This required MLCCs to be fired in a reducing atmosphere to prevent oxidation of Ni. This induces a high concentration of oxygen vacancies in the $BaTiO_3$ dielectric, even after a reoxidation process. The resulting local electric or elastic fields could influence domain wall motion. In addition, defect dipoles associated with oxygen vacancies may affect the nonlinearity. Therefore, formulated as well as undoped $BaTiO_3$ ceramics were fired in various atmospheres to study the effect of the oxygen vacancy concentration on the domain wall contributions. This is covered in Chapter 6.

As MLCCs are miniaturized, the dielectric layer thickness has been reduced to the point that $BaTiO_3$ – based MLCC are anticipated to show a thickness dependence. Here, MLCCs with the thickness varied from 2.2 μm to 8.6 μm were prepared and the nonlinearity was quantified.

Prior to this research, the effect of grain size of the nonlinearity of undoped $BaTiO_3$ ceramics was studied between 60 μm to 0.6 μm. Recent MLCCs utilize dielectrics with grain sizes smaller than 0.6 μm. In addition, the microstructure of dielectrics used for MLCCs is heterogeneous, or core/shell, which may affect the dielectric nonlinearity. Thus, the grain size effect on the dielectric nonlinearity was studied for MLCC with grain sizes from 0.28 μm to 0.39 μm. The dielectric nonlinearity of $BaTiO_3$ based MLCCs is discussed in Chapter 7.

Finally, conclusions and suggested future work are given in Chapter 8.

Chapter 2

Background

2.1 Ferroelectric Materials

2.1.1 $BaTiO_3$, Ferroelectric Properties, and $BaTiO_3$ – Based Dielectrics for Ceramic Capacitors

The prototype crystal structure for the ferroelectrics examine in this thesis is the perovskite structure; a unit cell for $BaTiO_3$ is shown in Fig. 2-1.[16] Barium ions sit at the corners, oxygen ions sit at the face centers, and a titanium ion sits near the body center. The oxygen ions form an octahedron around the Ti. $BaTiO_3$ experiences polymorphic phase transitions (See Fig. 2-2).[17] Above 130˚C, the phase is cubic. With decreasing temperature, it distorts to tetragonal at 130˚C, orthorhombic at 0˚C, and rhombohedral at -90˚C. At these temperatures, the cubic prototype structure extends along one of <100>, <110>, and <111> orientations, respectively. For the non cubic phases, ferroelectricity is developed. That is, a net electric dipole is created by displacements of the atoms (See Fig. 2-3)[16] and the dipole is reorientable between different orientations by an applied electric field. The dipole is called the spontaneous polarization. In some perovskites, the development of aligned dipoles can be explained by a soft mode, where the frequency of an optical mode lattice vibration decreases to zero at the cubic-tetragonal phase transition and the displacement remains.[18] For a grain, all the dipoles do not align the same direction. Rather, they are divided to regions where the dipoles are aligned (See Fig. 2-4).[16, 19]

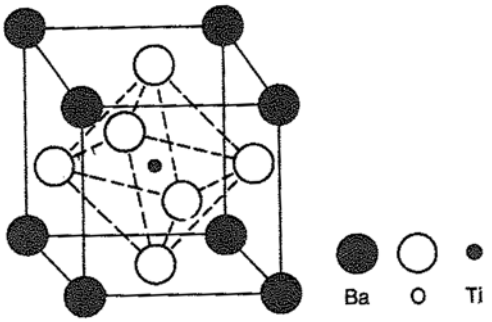

Figure **2-1**: An unit cell of the perovskite structure of $BaTiO_3$. The dotted lines illustrate the octahedron of the oxygen ions.[16]

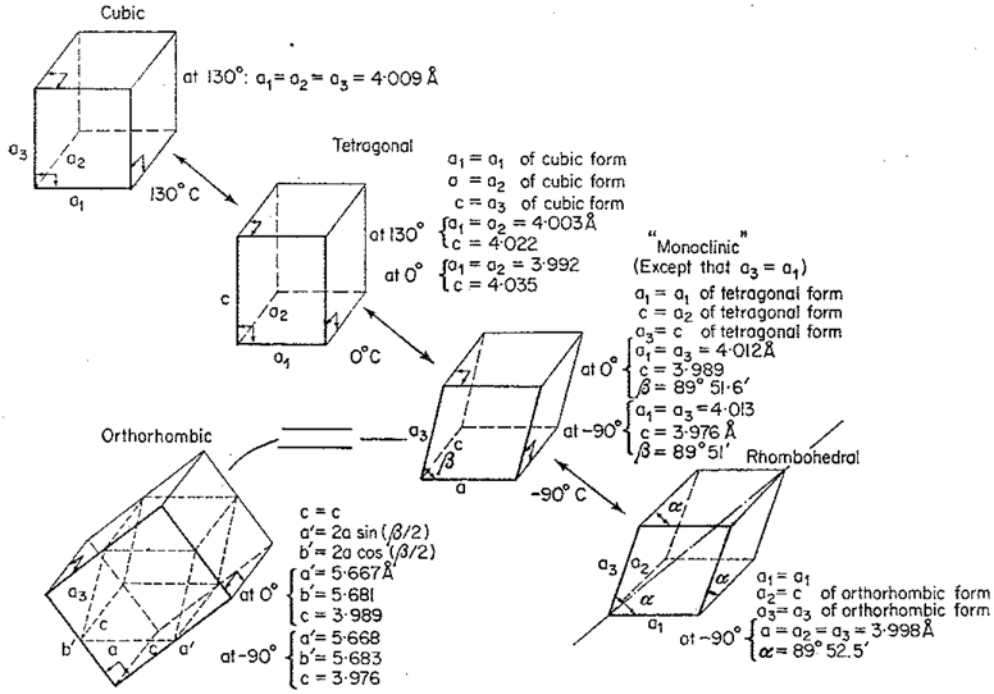

Figure **2-2**: Unit-cell distortions of the polymorphs of $BaTiO_3$.[17]

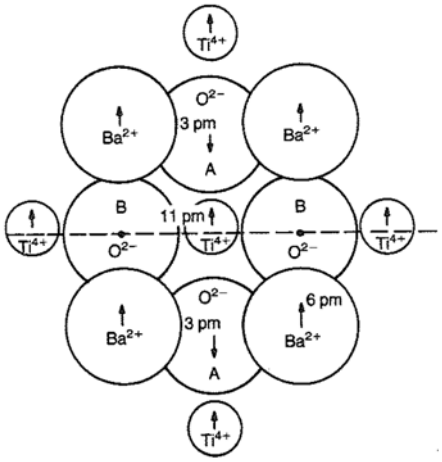

Figure **2-3**: Approximate ion displacements at the cubic-tetragonal phase transition.[16]

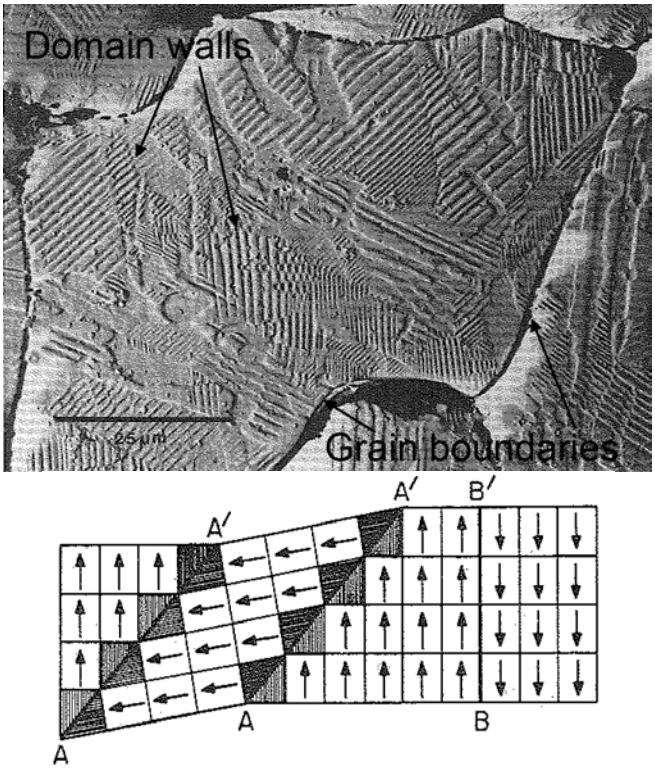

Figure **2-4**: Domains and domain walls of $BaTiO_3$ ceramics.[16, 19]

A volume in which the polarization direction is uniform (or nearly so) is called a domain, any boundary between domains is called a domain wall. Formation of domains is explained by the following factors: When $BaTiO_3$ experiences the cubic-tetragonal phase transition, each grain is strained and an electric dipole is created. The dipoles result in surface charges. If the charges are not compensated by the surroundings, a depolarization field is created which makes the dipoles unstable. To circumvent this, domains with other orientations are created to reduce the depolarization fields (that is proportional to the volume) as shown in Figs. 2-5 (a) to (b).[20] The domain walls shown in Fig. 2-5 (b) are called 180˚ domain walls, since this is the angle between the polarization directions. The domains have an optimum average size because the dipoles do not align across a domain wall, which costs a surface energy.[20] When the grain is clamped by the surroundings, i.e. adjacent grains, a stress field can develop at the phase transition temperatures. Suppose that a cubic grain possesses a spontaneous polarization with an orientation diagonal to a face (See Fig. 2-5 (c)).[21] The stress in the grain can be significantly reduced by twinning as shown in Fig. 2-5 (d)[21] Shown is a series of 90˚ domain walls. This also decreases the depolarization field. For $BaTiO_3$, in addition to 180° domain walls, 90˚ domain walls are present for the orthorhombic phase, while 109˚ and 71˚ domain walls are observed in the rhombohedral phase.[22] The 90˚, 109˚, and 71˚ domain walls are collectively referred to as non-180˚ domain walls.

At small ac electric fields, the polarization – electric field (P-E) response of ferroelectrics is almost linear (See Fig. 2-6), that is,

$$P = \varepsilon_r \varepsilon_0 E \qquad \text{Eq. 2-1}$$

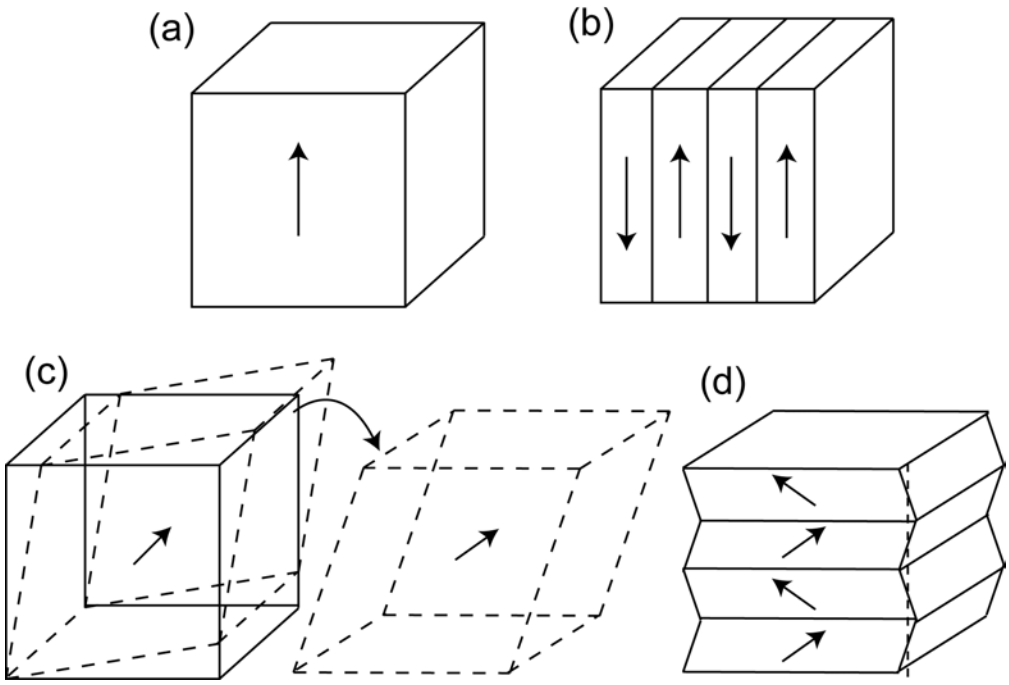

Figure **2-5**: Formation of domains and domain walls for a cubic grain of a tetragonal perovskite ferroelectric. The arrow indicates the orientation of the spontaneous polarization (a) a cubic grain with single domain (b) a cubic grain with 180˚ domain walls (c) a sheared cubic grain with single domain (d) a twinned grain with 90˚ domain walls.[20, 21]

where ε_r is the relative permittivity or dielectric constant. This linear response is, in part, attributed to deformation of the lattice. However, with increasing ac field amplitude, the response becomes hysteretic and nonlinear, which can be expressed with polynomials: [22]

$$P = P_0 + a_1 E + a_2 E^2 + a_3 E^3 + a_4 E^4 + \cdots \qquad \text{Eq. 2-2}$$

which suggests generation of higher harmonics when the response is Fourier transformed.

The hysteretic and nonlinear response is explained by domain wall motion.[23] A spontaneous dipole inside a domain is stabilized by the surrounding polarization. In contrast, dipoles near domain walls are more subject to reorientation by the electric field. In principle, if a ferroelectric were defect-free, the energy needed to translate a domain wall would be the energy required to reorient the dipole, and the domain would move smoothly once the energy barrier was passed. However, in reality, there are lots of defects inside real ferroelectrics and domain walls travel through a distribution of pinning centers. This is schematically depicted in Fig. 2-7, [23] where the domain wall is assumed to traverse a potential landscape with some potential wells. When the electric field is small, the domain wall is displaced somewhat, but cannot exceed an energy barrier and so returns to its original position once the electric field is removed. This could result, for example, from bending of domain walls.[24] This corresponds to a linear dielectric or strain response. When the field is large, the domain wall can exceed the energy barrier and jump to another well. Then, the response becomes hysteretic and nonlinear. The former is called reversible domain motion and the latter is called irreversible domain wall motion.

A schematic showing the relation between possible domain configurations and a polarization – electric field (P-E) loop for a ferroelectric is shown in Fig. 2-8.[22] Initially, the ferroelectric is depolarized (point O). A large applied field could produce a single domain state for an appropriately oriented single crystal (point A). When the field decreases to zero, some domains with the opposite direction nucleate (point B). The polarization is called the remanent

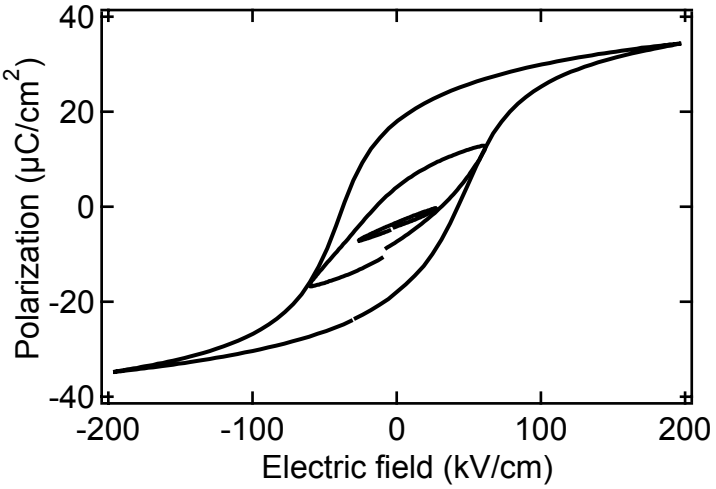

Figure **2-6**: Polarization – electric field loops of a lead zirconate titanate film as a function of the ac field amplitude.

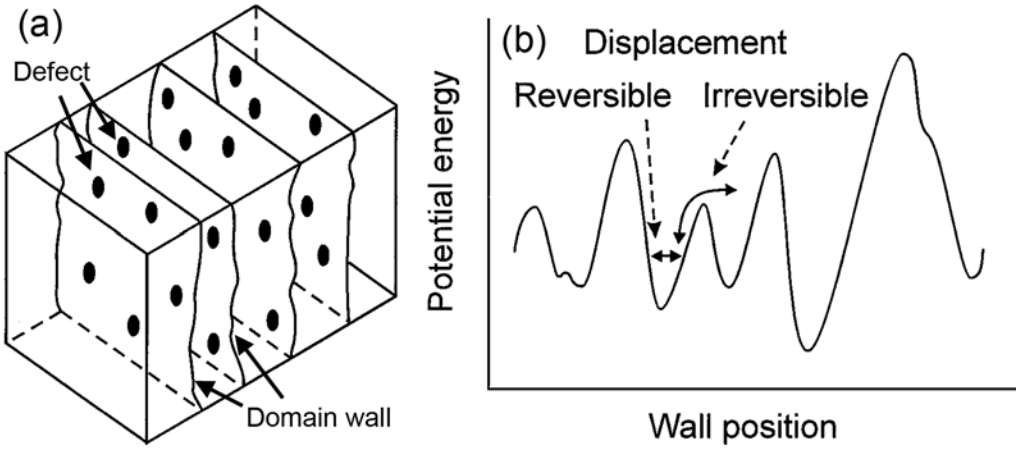

Figure **2-7**: Schematic illustration of interaction of (a) domain walls with randomly distributed pinning centers and (b) the corresponding energy profile associated with the domain wall position.[23]

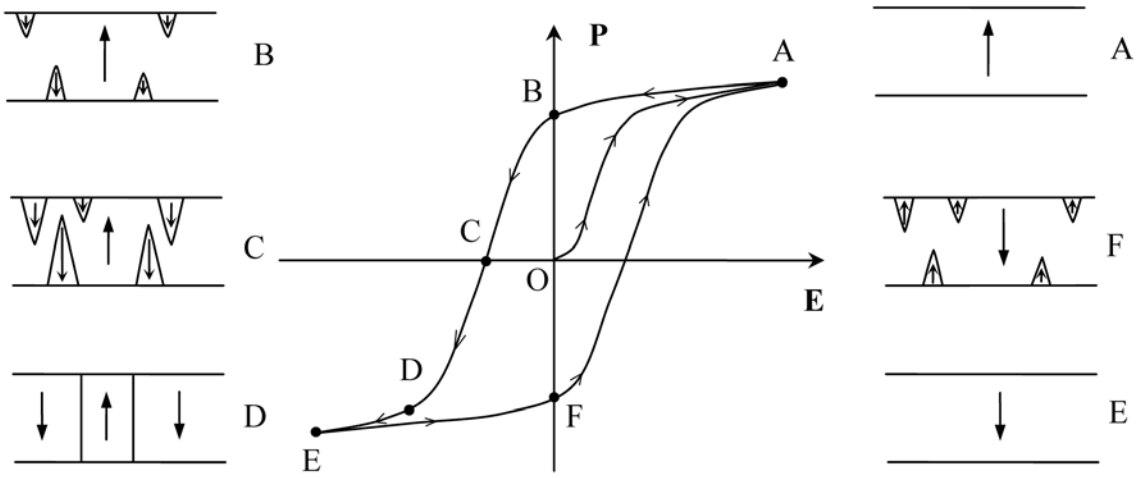

Figure **2-8**: Schematic for the relation between a P-E loop and domain configurations at some point in a uniaxial ferroelectric single crystal.[22]

polarization, P_r. With decreasing field, domains with the opposite direction nucleate and grow until the domains merge and a single domain state with the opposite direction is achieved (point B to E). The electric field with net zero polarization at point C is called the coercive field, E_c. When the field increases, some domain with the original direction nucleate (point F) and finally the material returns to the original single crystal state (point A).

Figure 2-9 (a) shows the temperature dependence of the dielectric constant of a $BaTiO_3$ ceramic. The large dielectric constant is attributed to the large dipolar polarizability (which is intrinsic) as well as domain wall contributions (which are extrinsic). This is a reason why $BaTiO_3$ is used for capacitors. At phase transitions, the dielectric constant is increased. This large variation of the dielectric constant over temperature is not desirable in capacitor applications as specifications such as X7R (the capacitance change no more than 15% of that at 25˚C at temperatures between -55˚C and 125˚C) must be achieved for particular applications. For this purpose, small grains and core/shell microstructure are applied to $BaTiO_3$ – based dielectrics. As shown in Fig. 2-9 (b)[25], the dielectric constant of $BaTiO_3$ ceramics is suppressed with grain size, so that the temperature variation is minimized. This is explained by dilution of the dielectric properties from an increased density of grain boundaries and reduced domain wall contributions. The core/shell microstructure indicates grains with a core of almost pure $BaTiO_3$ surrounded by a shell of $BaTiO_3$ doped with additives such as Mg, Mn, Ca, or a rare earth element (Fig. 2-10).[26] Note that $BaTiO_3$ can be doped with elements with similar ionic sizes and the doping suppresses the permittivity peaks and changes the phase transition temperatures, along with improving the reliability of capacitors. The shell possesses a diffused phase transition with a lower phase transition temperature. The temperature dependence of the dielectric constant of core/shell dielectrics is a mixture of the dependences of the core the shell. Therefore, it is possible to flatten the response considerably (Fig. 2-11).[27]

Such $BaTiO_3$ – based dielectrics are used in multilayer ceramic capacitors (MLCCs).

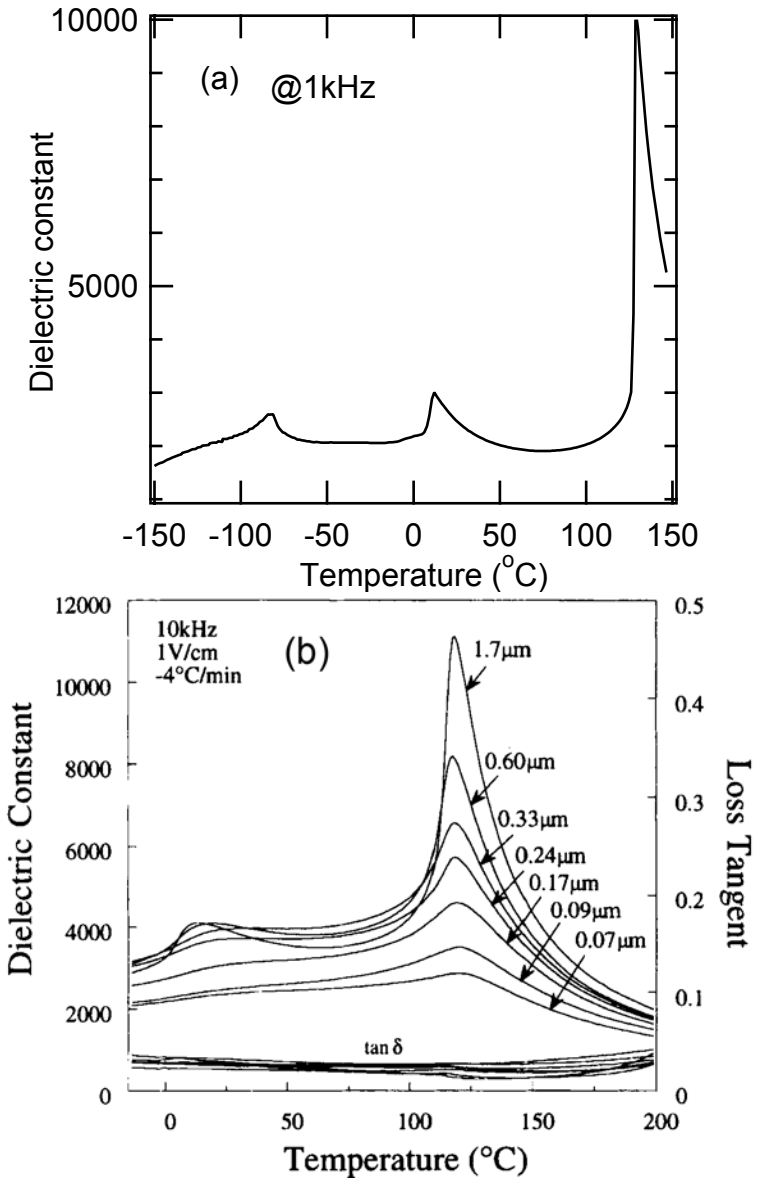

Figure **2-9**: Temperature dependence of the dielectric constant of $BaTiO_3$ ceramics with (a) large grain (grain size : 76 μm) and (b) small grains[25].

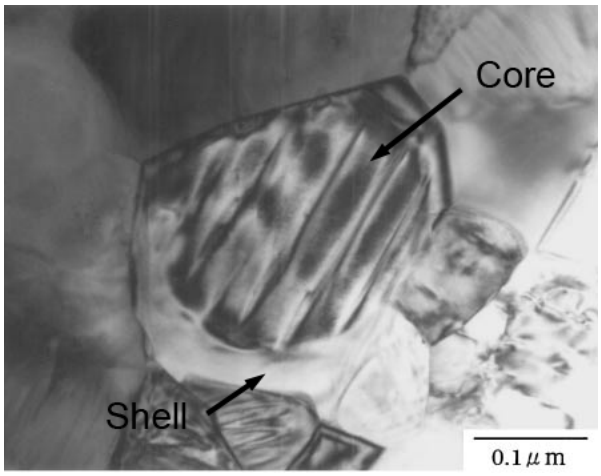

Figure **2-10**: TEM image of a core/shell microstructure.[26]

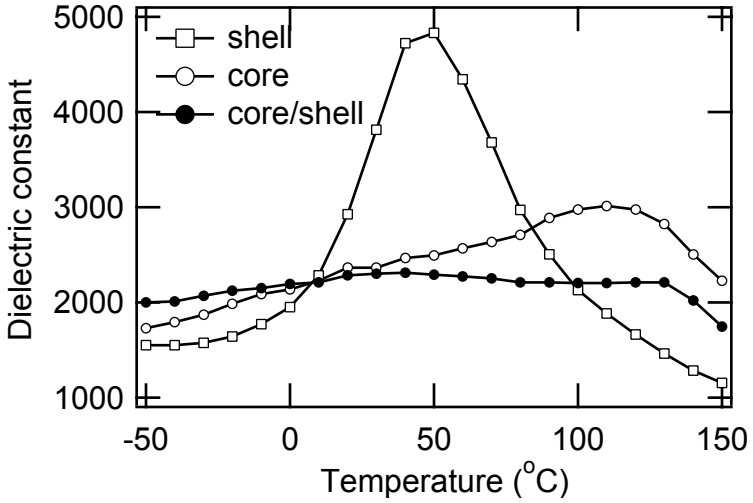

Figure **2-11**: Temperature dependence of the dielectric properties of core/shell, core and shell grains. Data were extracted from Ref[27].

Figure 2-12 shows a schematic configuration of a MLCC.[26] It consists of dielectric layers, internal electrodes, and external electrodes. When the dielectric layer thickness is t, the overlap area of the internal electrodes is A, and the number of the dielectric layer is n, the capacitance of the MLCC, C, is expressed as

$$C = \varepsilon_r \varepsilon_0 \frac{nA}{t} \qquad \text{Eq. 2-3}$$

where ε_r is the relative permittivity of the dielectrics and ε_0 is the permittivity of free space.

The MLCC industry is continuously asked to reduce the size of MLCC without sacrificing capacitance. This can be done by reducing the dielectric thickness and increasing n. Previously, noble metals such as Pd and Pd/Ag were used for internal electrodes because they do not oxidize during co-firing of the dielectrics and electrodes in air. Note that most metal oxides have lower dielectric constants than $BaTiO_3$, and a series connection of the dielectrics and metal oxides results in reduction in the capacitance. A rise in the price of Pd during the 1990s led to use of inexpensive base metals such as Ni. When Ni is annealed in air at the sintering temperatures needed for the $BaTiO_3$ dielectric, 1200~1300˚C, the Ni is oxidized as shown in Fig. 2-13.[28] To prevent this, the $BaTiO_3$ dielectric and Ni are co-fired at a low oxygen partial pressure: ~10^{-9} atm pO_2. However, such capacitors are known to have reduced reliability and fail in a short time if the dielectric formulation is not changed. This occurs because when $BaTiO_3$ is sintered in the reducing atmosphere, a large amount of oxygen vacancies are created. They migrate toward the cathode and pile up at the cathode.[29] Since the oxygen vacancies are positively charged, electrons are injected from the cathode to compensate, which results in lowering the resistance. Early failure was overcome by a combination of reoxidation treatments and use of amphoteric dopants.[26] Reoxidation is done by annealing the capacitors at a lower temperature ~1000˚C with a weakly oxidizing atmosphere, so that the oxygen vacancies of $BaTiO_3$ are annihilated without strong oxidation of Ni electrodes. Amphoteric dopants are dopants for which the ionic size is in

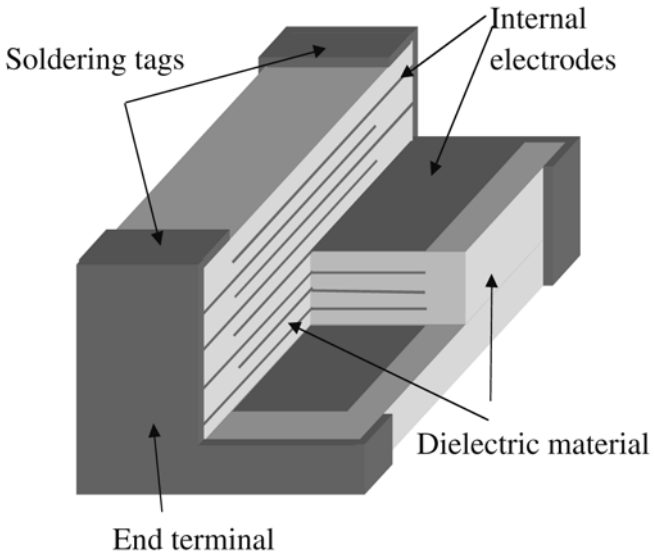

Figure **2-12**: A typical configuration for an MLCC.[26]

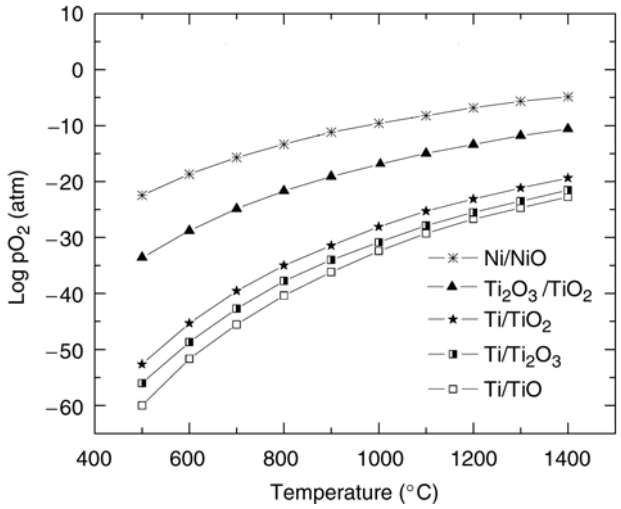

Figure **2-13**: Oxidation of metals as a function of partial oxygen pressure, pO_2, and temperature.[28]

between Ba and Ti. They are believed to substitute on both sites and reduce the oxygen vacancy concentration. Amphoteric dopants includes Ca, Y, and rare earth metals such as Ho and Dy.[26, 30]

2.1.2 Lead Zirconate Titanate

Lead zirconate titanate (PZT) films are used for actuators, sensors, energy harvesters, and non-volatile memories due to their large piezoelectric coefficients and switchable polarization.[12, 13] Figure 2-14 shows the $PbZrO_3$-$PbTiO_3$ phase diagram.[31] The prototype crystal structure of both the $PbZrO_3$ and $PbTiO_3$ end members is the perovskite structure. $PbZrO_3$ is cubic above 230˚C. Below the temperature, it distorts to an orthorhombic antiferroelectric phase. On the other hand, $PbTiO_3$ is cubic above 490˚C. Below the temperature, it distorts to a tetragonal ferroelectric phase. The high Curie temperature is attributable to a large displacement of Ti ions and the lone pair electrons for the Pb^{2+} ion. Above the curve connecting the Néel temperature of $PbZrO_3$ and the Curie temperature of $PbTiO_3$, the solid solution is cubic and paraelectric. Below the temperatures, solid solutions of $PbZrO_3$ with a few mol% of $PbTiO_3$ possess an antiferroelectric orthorhombic phase. The solid solutions with a few to ~ 48 mol% $PbZrO_3$ are ferroelectric and rhombohedral. Over much of the rhombohedral part of the phase diagram there are high temperature phases with untilted oxygen octahedra and low temperature phases with tilted oxygen octahedra. The tilt occurs due to reduction in the volume of the unit cell with temperature. For Ti-rich compositions, the phase is ferroelectric tetragonal. Between the tetragonal and rhombohedral phases, there are ferroelectric monoclinic phases.

Figures 2-15 show the composition dependence of the reported dielectric and piezoelectric properties of PZT films[32, 33]. Here, the effective d_{33}, or $d_{33,f}$ is $\propto x_3/E_3$ and $-e_{31,f} = p_1/x_3$ where E is applied electric field, x is strain, p is polarization, "1" and "3" indicate the directions parallel and perpendicular to the film, respectively[12]. The dielectric constant, effective

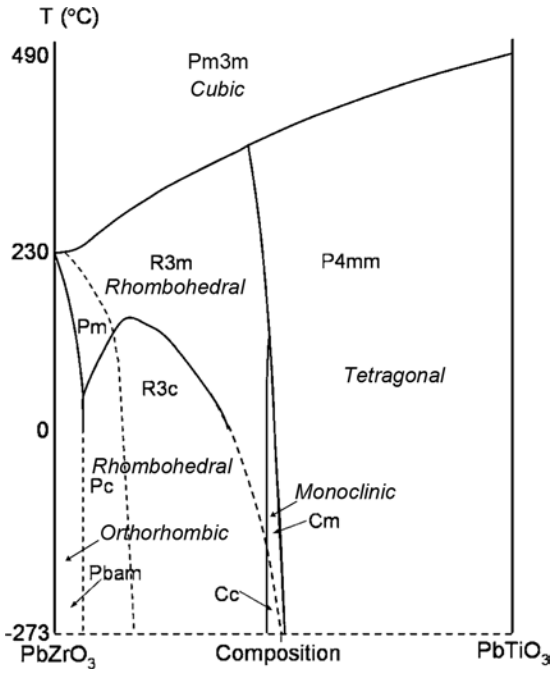

Figure **2-14**: $PbZrO_3$-$PbTiO_3$ phase diagram. Noted in the different phase fields are the observed space groups.[31]

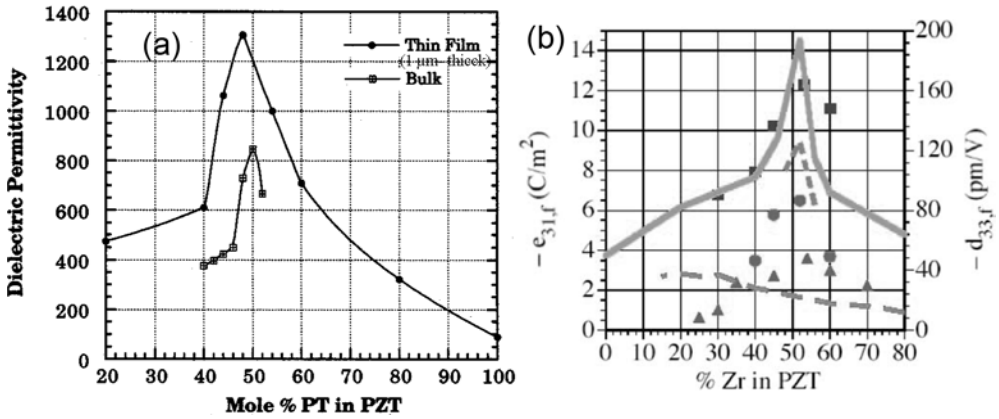

Figure **2-15**: Composition dependence of (a) the dielectric constant of PZT and (b) effective piezoelectric properties of PZT film (symbols are for $e_{31,f}$ data, lines are for $d_{33,f}$ data; the composition dependence is expected to be correct, although there may be systematic errors in some of the reported $d_{33,f}$ measurements).[12, 32]

d_{33}, and $-e_{31,f}$ increase near 48mol%$PbTiO_3$ content. The composition corresponds to the morphotropic phase boundary (MPB). Large domain wall contributions are reported near the MPB.[34] Therefore, the large dielectric and piezoelectric properties are, in part, attributed to the domain wall motions, at least for bulk ceramics.

2.2 Dielectric Nonlinearity

2.2.1 Rayleigh Law

Lord Rayleigh empirically found a quadratic relation between the magnetization M and the applied magnetic field H for ferromagnetic materials when H is cycled between $-H_o$ and $+H_o$, with H_o being smaller than the coercive force:[5]

$$M = (A + BH_0)H \pm \frac{B}{2}(H^2 - H_0^2) \qquad \text{Eq. 2-4}$$

where A and B are constants and the '+' in the '±' is for the ascending field branch while the '–' is for the descending branch. A linear expression for the permeability χ at $H=H_0$ was then derived:

$$\chi = \frac{M_0}{H_0} = A + BH_0 \qquad \text{Eq. 2-5}$$

where $M_0=M(H_0)$. Eqs. 2-4 and 2-5 are called the Rayleigh Law. Initially, there were discussions as to whether the expression constituted a physical law or merely the first terms of a power series in H.[35] Later, the Rayleigh Law was theoretically derived via a magnetic domain wall model where a magnetic domain wall travels a uniformly rough potential landscape created by a randomly distributed pinning centers, this provided underlying support for the Rayleigh Law.

A comparable derivation of the Rayleigh Law is also valid for ferroelectric materials.[36] Experimental evidence of dielectric and piezoelectric Rayleigh responses has been reported for PZT ceramics and thin films, as well as some other ferroelectrics [4, 6, 37].

Using the Rayleigh Law, it is possible to quantify the reversible and irreversible dielectric responses at subcoercive fields. That is, the hysteretic and nonlinear response of a P-E loop is attributed to irreversible domain wall motion, as is explained with Fig. 2-7. Eqs. 1-1 and 1-2 shows that ε_{init}' describes the linear response while α' describes the hysteretic and nonlinear response. Thus, ε_{init}' quantifies the dielectric contributions from the deformation of the lattice and the reversible domain wall motion, while α' quantifies the irreversible domain wall contributions. Quantification of the domain wall contributions is summarized for some ferroelectrics elsewhere.[4]

2.2.2 Preisach Model

In some cases, the assumptions inherent in deriving the Rayleigh Law are too simplistic to completely describe the response of a material and the applicability is limited below the coercive field. Thus, a more general approach is required. It has been shown that the Preisach model[8] could give reasonable descriptions of hysteretic phenomena for magnetic[9, 10], piezoelectric[38, 39], and dielectric materials[40]. Recently, successful descriptions of the ac field dependence of the piezoelectric coefficient of the ferroelectric ceramics have been reported.[39, 41]

The Preisach model is a mathematical model that assumes that a P-E loop of a ferroelectric consists of a set of rectangular hysteresis loops, referred as to hysterons, with different up and down switching fields α and β ($\alpha \geq \beta$). A hysteron with $\alpha > \beta$ is called an irreversible hysteron, while one with $\alpha = \beta$ is called a reversible hysteron (See Fig. 2-16). The hysterons have a distribution with respect to the switching fields, called the Preisach distribution,

which determines the switching characteristics. Figure 2-17 shows an example of a Preisach distribution with representative hysterons that show the relation between the α and β coordinates and the corresponding hysteron. The distribution on the $\alpha=\beta$ line corresponds to the reversible Preisach distribution, $p_{rev}(\alpha,\beta)$, while the distribution at $\alpha>\beta$ is the irreversible Preisach distribution, $p(\alpha,\beta)$. For the Preisach distribution shown, the density of hysteron with switching fields corresponding to hysteron 1 is higher than that of the hysterons 3 and 4.

The total polarization of the ferroelectric is calculated as the summation of the polarizations of each hysteron, as expressed in Eq. 1-3. The Preisach plane facilitates an understanding of the calculation. The Preisach plane is a diagram with coordinates of α and β, which describes the state of the Preisach operators $q(\alpha,\beta)$ and $k(\alpha)$, that is, either +1 or -1, for a given field excursion. The evolution of a Preisach plane for a P-E response is shown in Fig. 2-18. For the Preisach plane, blue hysterons are the negatively polarized, while yellow hysterons are positively polarized. Initially, a negative field switches all the hysterons to a negatively polarized state (a). With increasing applied field, hysterons with α smaller than the applied field switch up. For large enough applied fields, all the hysterons become positively polarized (c). With decreasing applied field, those up-switched hysterons with β larger than the field switch to the down state (d). The 2^{nd} and 3^{rd} order reversal polarization curves were drawn for the applied field (e,f).

The ac field dependence of the dielectric constant is calculated as follows. For an alternating field with amplitude E_0, the Preisach plane is divided into four parts: R_1, R_2, R_3, and R_4 (see Fig. 2-19 (a)). R_1 is switched when the field is cycled. R_2 is always in the down-state, and R_3 is always in the up-state. R_4 is not switched in the process. Therefore, only R_1 contributes to the change in the polarization. As the amplitude increases, R_1 expands triangularly (see Fig. 2-19

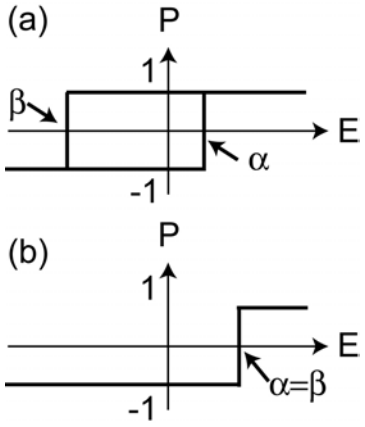

Figure **2-16**: Schematics showing (a) an irreversible hysteron and (b) a reversible hysteron.

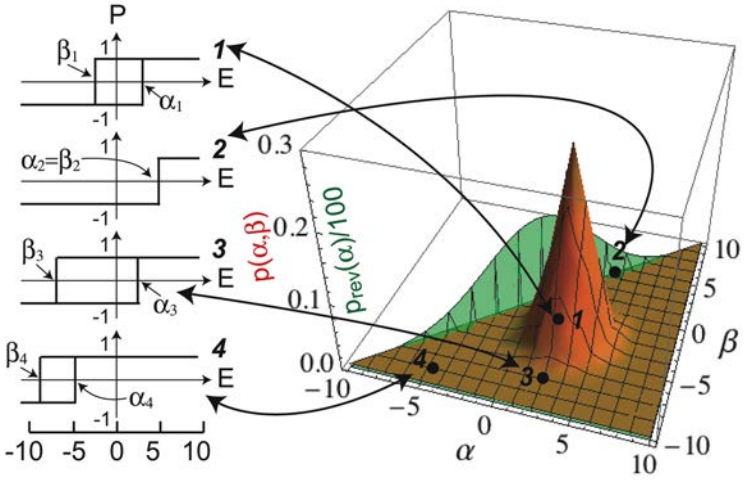

Figure **2-17**: A Preisach distribution with representative hysterons that show the relation between the α and β coordinates and the corresponding hysteron. The distribution on the α=β line corresponds to the reversible Preisach distribution, while the distribution at α>β is the irreversible Preisach distribution. For the Preisach distribution, the density of hysterons with switching fields given at point 1 is higher than that of the hysterons at points 3 and 4.

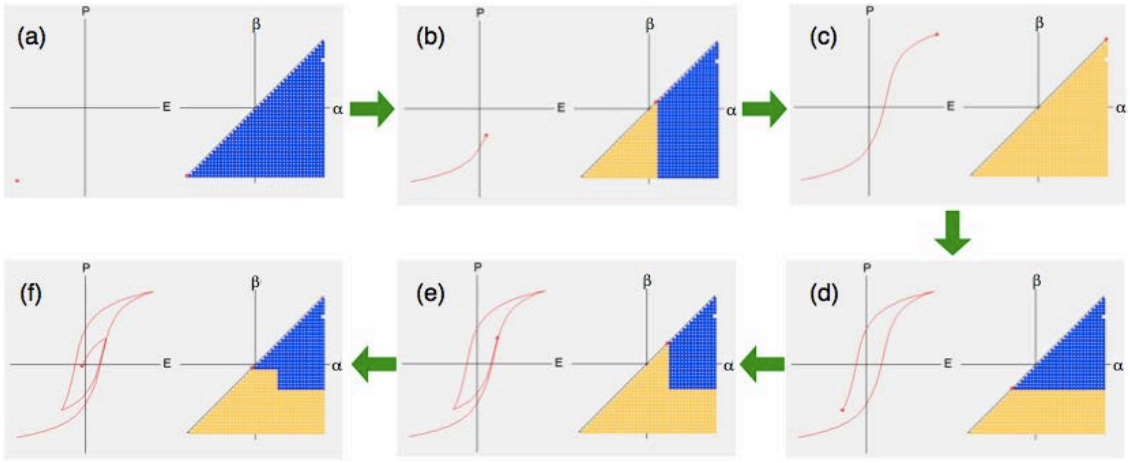

Figure **2-18**: Preisach modeling of the evolution of a P-E loop and the Preisach plane for a ferroelectric with a known Preisach distribution. For the Preisach plane, the blue hysterons are negatively polarized, while the yellow hysterons are positively polarized. (a) A negative field switches all the hysterons to a negatively polarized state. (b) With increasing applied field, hysterons with α smaller than the applied field switch up. (c) All the hysterons are positively polarized. (d) With decreasing applied field, hysterons with β larger than the applied field switched down. (e, f) The 2nd and 3rd order reversal polarization curves as a function of applied field.

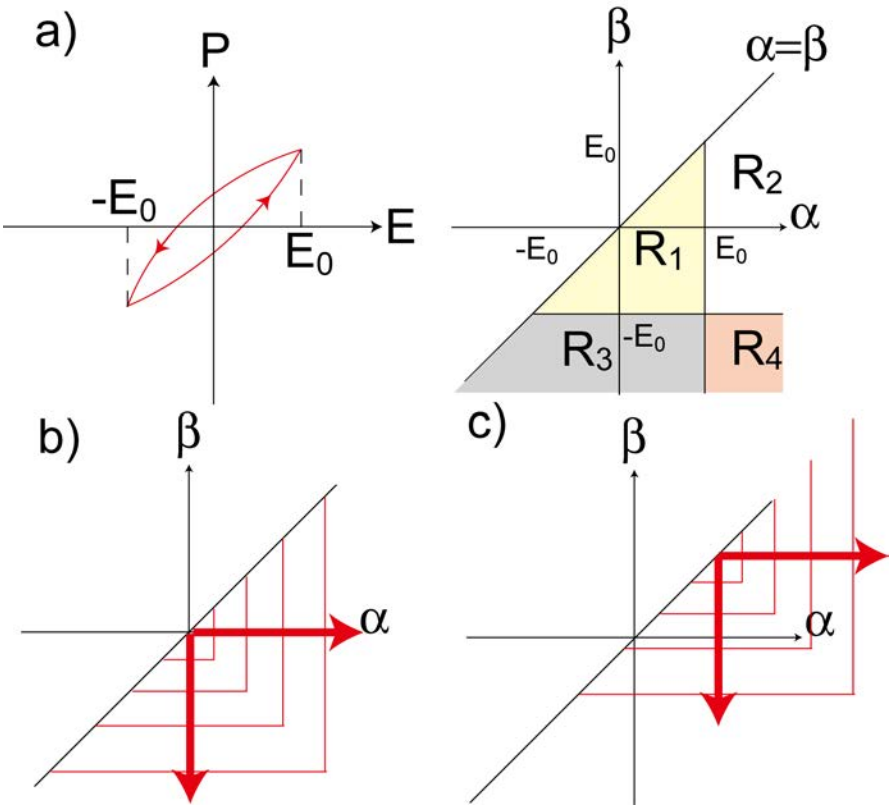

Figure **2-19**: (a) The partitioning of the Preisach plane by the ac field.[10] (b) The triangular expansion of the switching area with increasing ac field. (c) The shift of the switching center by a positive dc bias.

(b)) and more hysterons become involved in the switching process. If a dc bias, E_{dc}, is superimposed on the ac field, the field is cycled between E_{dc}-E_o and E_{dc}+E_o. This is illustrated in Fig. 2-19 (c). When the dielectric constant is defined as a slope of the cycled polarization-electric field loop, it can be expressed as[39]

$$\varepsilon = \frac{1}{\varepsilon_0 E_0}\left(\iint_{R_1} p(\alpha,\beta)d\alpha d\beta + \int_{-E_0+E_{dc}}^{E_0+E_{dc}} p_{rev}(\alpha)d\alpha\right) \qquad \text{Eq. 2-6}$$

There is a link between the mathematical Preisach model and the Rayleigh Law. At small switching fields, i.e. near the origin, the Preisach distribution can be nearly flat[8], that is, $p(\alpha,\beta)=c_1$ and $p_{rev}(\alpha,\beta)=c_2$ where c_1 and c_2 are constants. Suppose, in such a case that the ferroelectric is cycled between $-E_0$ and $+E_0$, as shown in Fig. 2-19 (a). At $E=-E_0$, all the hysterons are negatively polarized, so that $q(\alpha,\beta)=-1$ and $k(\alpha)=-1$. Using Eq. 1-3, the polarization is:

$$\begin{aligned} P(-E_0) &= -\int_{-E_0}^{E_0}\int_{-E_0}^{\alpha} c_1 d\alpha d\beta - \int_{-E_0}^{E_0} c_2 d\alpha \\ &= -2c_1E_0^2 - 2c_2E_0 \end{aligned} \qquad \text{Eq. 2-7}$$

When the field increases from $-E_0$ to E ($\leq E_0$), the polarization for the ascending curve is

$$\begin{aligned} P(E) &= P(-E_0) + 2\int_{-E_0}^{E}\int_{-E_0}^{\alpha} c_1 d\alpha d\beta + 2\int_{-E_0}^{E} c_2 d\alpha \\ &= (2c_2 + 2c_1E_0)E + c_1(E^2 - E_0^2) \end{aligned} \qquad \text{Eq. 2-8}$$

Here, the "2" that appears on the integration in Eq. 2-8 is attributed to the change of the state of the hysterons from -1 to +1. Replacing $2c_2 = \varepsilon_{init}$' and $2c_1 = \alpha$' in Eq. 2-8 yield the Rayleigh Law, Eq. 1-2. Néel used this relation to derive the Rayleigh Law by regarding the hysterons in the Preisach model as the irreversible and reversible hysteretic responses of a single domain wall traveling through a potential landscape with randomly distributed pinning centers.[42, 43]

Using Eqs. 1-3 and 2-6, it is possible to calculate the dielectric properties, once the Preisach distribution is known. There are two ways to determine the Preisach distribution. One method is to assume an analytical function for the Preisach distribution. For example,

polynomial, Gaussian, and hyperbolic functions have been reported[10, 39, 40]. In this case, the assigned function with unknown coefficients is inserted into Eq. 1-3 to generate a mathematical expression for a P-E curve for a given field sequence. Then, the coefficients are determined by comparison between the calculated P-E curve and an experimental P-E curve for the same field sequence. This method has the advantage that the Preisach distribution is a continuous function, so that a P-E curve can be calculated for *any* field sequence. Furthermore, there is a possibility to extend the Preisach model to more sophisticated one, i.e. a moving Preisach model, to improve an accuracy of the modeling, if the analytical function is Gaussian. In contrast, the disadvantages are to find an appropriate analytical function for a ferroelectric and to solve the complicated simultaneous equations to determine the coefficients.

A second method is to measure a series of first order reversal curves (FORC)[9]. The FORC method is explained in the following. Suppose a ferroelectric is exposed to a field which increases from a negative saturation field $-E_{max}$ to α_i and then decreases to β_i. (See Fig. 2-20) Let the polarizations at $E=\alpha_i$ and $E=\beta_i$ be $P(\alpha_i, \alpha_i)$ and $P(\alpha_i, \beta_i)$, respectively. Using the Preisach model, the difference between the polarizations can be expressed as:[9]

$$P(\alpha_i,\beta_i) - P(\alpha_i,\alpha_i) = -2\int_{\beta_i}^{\alpha}\left(\int_{\beta_i}^{\alpha_i} p(\alpha,\beta)d\alpha\right)d\beta - 2\int_{\beta_i}^{\alpha_i} p_{rev}(\alpha)d\alpha \qquad \text{Eq. 2-9}$$

where the "-2" in Eq. 2-9 is attributed to the change of the state of hysterons from +1 to -1. Differentiation of Eq. 2-9 with respect to β_i gives

$$\frac{\partial P(\alpha_i,\beta_i)}{\partial \beta_i} = 2\int_{\beta_i}^{\alpha_i} p(\alpha,\beta_i)d\alpha + 2p_{rev}(\beta_i) \qquad \text{Eq. 2-10}$$

where $\frac{d}{dx}\left(\int_x^c f(t)dt\right) = -\frac{d}{dx}\left(\int_c^x f(t)dt\right) = -f(x)$ and c is constant.

Differentiation of Eq. 2-10 with respect to α_i gives

$$\frac{\partial^2 P(\alpha_i,\beta_i)}{\partial \alpha_i \partial \beta_i} = 2p(\alpha_i,\beta_i) \qquad \text{Eq. 2-11}$$

Eq. 2-11 indicates that the differentiations of the polarization $P(\alpha_i, \beta_i)$ with respect to the returning field α_i and instantaneous field β_i yields twice the irreversible Preisach distribution for hysterons with up-switching field α_i and down-switching field β_i. Thus, the returning field and the up-switching field, and instantaneous field and down-switching field are linked.

The reversible Preisach distribution can be calculated when β_i approaches α_i in Eq. 2-10:

$$\lim_{\beta_i \to \alpha_i -} \frac{\partial P(\alpha_i,\beta_i)}{\partial \beta_i} = 2 p_{rev}(\alpha_i) \qquad \text{Eq. 2-12}$$

Thus, the Preisach distributions can be mapped out through a family of descending curves of P-E loops measured using an electric field which increases from $-E_{max}$ to α_i and decreases to $-E_{max}$, where α_i increases from $-E_{max}$ to $+E_{max}$, as is shown in Fig. 2-21. The irreversible and reversible FORC distributions are then re-defined for $\alpha_i \in \alpha$ and $\beta_i \in \beta$ as:[9, 44, 45]

$$p(\alpha,\beta) = \frac{1}{2}\frac{\partial^2 P(\alpha,\beta)}{\partial \alpha \partial \beta} \qquad \text{Eq. 2-13}$$

$$p_{rev}(\alpha) = \lim_{\beta \to \alpha -} \frac{1}{2}\frac{\partial P(\alpha,\beta)}{\partial \beta} \qquad \text{Eq. 2-14}$$

The advantage of the FORC method is that the method does not need an assumption on the analytical function and the Preisach distribution can be experimentally obtained. The disadvantage is that there can be *a field-path dependence* in the obtained Preisach distribution. The Preisach model is developed with a symmetry condition: $M(H)=-M(-H)$.[9, 11] This corresponds to the presumption that the Preisach distribution is mirrored along the $\alpha=-\beta$ line. However, this is often not true for the Preisach distribution function obtained by the FORC method. Nevertheless, the Preisach distribution estimated in this way is reported to give an acceptable prediction for a hysteretic response.[38, 46]

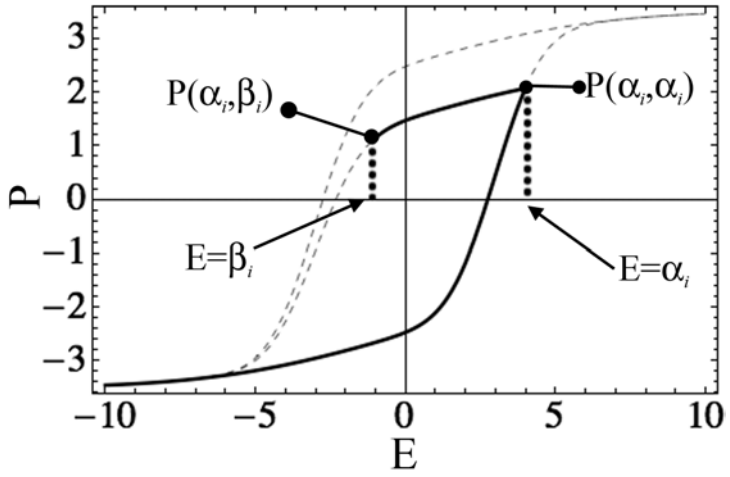

Figure **2-20**: A first order reversal curve for a ferroelectric with the Preisach distribution shown in Fig. 2-17. The polarization $P(\alpha_i,\beta_i)$ stands for the polarization of a ferroelectric exposed to an electric field that increased from $-E_{max}$ (=-10) to α_i and then decreased to β_i. $P(\alpha_i, \alpha_i)$ stands for the polarization at the reversal field α_i.

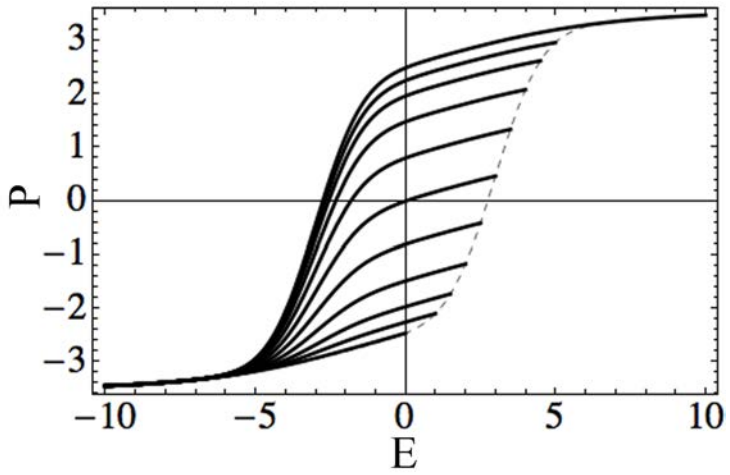

Figure **2-21**: First order reversal curves (FORC) showing the polarization response on decreasing field for a ferroelectric with the Preisach distribution shown in Fig. 2-17.

2.2.3 FORC Distribution

Since the Preisach distribution measured by the FORC method can be experimentally obtained without any assumptions and it expresses the switching characteristic of hysteretic responses, it has been used to quantify the magnetic nonlinear responses. Due to the deviation of the FORC-derived Preisach distribution from the analytically-derived one, the former is called the FORC distribution.[11, 47] Dielectric FORC distributions have recently been applied to ferroelectric materials to quantify the dielectric nonlinearity.[44, 48 46, 49]

The FORC distribution is calculated from Eqs. 2-13 and 2-14. Since $P(\alpha,\beta)$ is not continuous, but discrete, the calculation involves discrete differentiations. There are two methods for the calculation reported. One is the first order approximation of the differentiations. That is,[10]

$$p(\alpha,\beta) \approx \frac{1}{2}\frac{P(\alpha,\beta+\Delta\beta) - P(\alpha,\beta) - P(\alpha-\Delta\alpha,\beta+\Delta\beta) + P(\alpha-\Delta\alpha,\beta)}{\Delta\alpha\Delta\beta} \qquad \text{Eq. 2-15}$$

$$p_{rev}(\alpha) \approx \frac{1}{2}\frac{P(\alpha,\alpha) - P(\alpha,\alpha-\Delta\beta)}{\Delta\beta} \qquad \text{Eq. 2-16}$$

The other is a polynomial surface fit to the local $P(\alpha,\beta)$[9, 11]. The polynomials reported are $P(\alpha,\beta)=a_1+a_2\alpha+a_3\alpha^2+a_4\beta+a_5\beta^2+a_6\alpha\beta$ and $P(\alpha,\beta)=b_0+b_1\alpha+b_2\beta+b_3\alpha\beta$ for the irreversible FORC distribution and $P(\alpha,\beta)=d_0+d_1\alpha+d_2\beta$ for the reversible FORC distribution where a_i, b_i, and d_i are fitting coefficients. a_6 and b_3 correspond to the irreversible FORC distribution and d_1 or d_2 corresponds to the reversible FORC distribution.

Chapter 3

Experimental Procedure

The subsequent chapters include a brief experimental procedure characteristic of the experiments utilized in that work. This chapter provides details on the experimental procedures employed which are not covered elsewhere.

3.1 Dielectric Measurement

3.1.1 AC Electric Field Dependence of Dielectric Constant and Loss

The ac field dependence of the dielectric constant and loss was measured in two ways. For samples with thinner dielectric thickness, i.e. MLCCs and PZT thin films, it was measured using LCR meters (4284A, Agilent). For bulk ceramic samples, the ac field dependence was measured using a lock-in technique so that higher electric fields could be applied. In this approach, a lock-in amplifier (SR830, Stanford Research), a custom made voltage amplifier, and a charge converter were used. A schematic of the measuring system is shown in Fig. 3.1. The lock-in amplifier generates a sinusoidal voltage $V_o\exp(j\omega t)$, where V_o is the voltage amplitude, $j^2 = -1$, ω is the angular frequency, and t is time. The voltage is amplified by a homemade voltage amplifier to $100V_o\exp(j\omega t-\delta_{amp})$ with a constant, field-independent phase delay δ_{amp}. First, the voltage is applied to a reference capacitor (a linear capacitor) with capacitance C_r. The charge generated by the reference capacitor, Q_r, is expressed as

$$Q_r = C_r \cdot 100V_0 \exp(j\omega t - \delta_{amp}) \quad \text{Eq. 3-1}$$

The current, $i_r (= \frac{dQ_r}{dt})$, flows into the charge converter. An operational amplifier in the charge converter integrates i_r and returns a voltage $V_r = -Q_r/C_o$ to the lock-in amplifier. Here, C_o is the capacitance of a capacitor in the charge converter.

Next, the amplified voltage is applied to a ferroelectric sample with capacitance C_s. The charge generated by the sample, Q_s, is expressed as

$$Q_s = C_s \cdot 100V_0 \exp(j\omega t - \delta_{amp} - \delta) + \sum_k C_{s,k} \cdot 100V_0 \exp(jk\omega t - \delta_{amp} - \delta_k) \quad \text{Eq. 3-2}$$

where δ is the phase delay of the 1st order harmonics and $C_{s,k}$ and δ_k are the amplitude and phase delay of the k^{th} order harmonics, respectively. The current, $i_s (= \frac{dQ_s}{dt})$, flows into the charge converter. The operational amplifier in the charge converter integrates i_s and returns a voltage $V_s = -Q_s/C_o$ to the lock-in amplifier.

In this study, the capacitance of the sample, C_s, at high fields was calculated using the amplitude of the fundamental of the charge, Q_s. Comparison of V_r, V_s, and Eqs. 3-1 and 3-3 leads to the capacitance of the sample as $C_s = C_r \cdot V_s/V_r$ and the dielectric loss, tan δ, can be calculated the difference of the phases of V_r and V_s, δ.

3.1.2 FORC Measurements

First order reversal curves were measured using a homemade polarization measurement system, which could accept a user-defined time dependent applied field, with a custom made voltage amplifier or a commercial voltage amplifier (BOP 1000M, Kepco; TREK 609C-6, Trek;

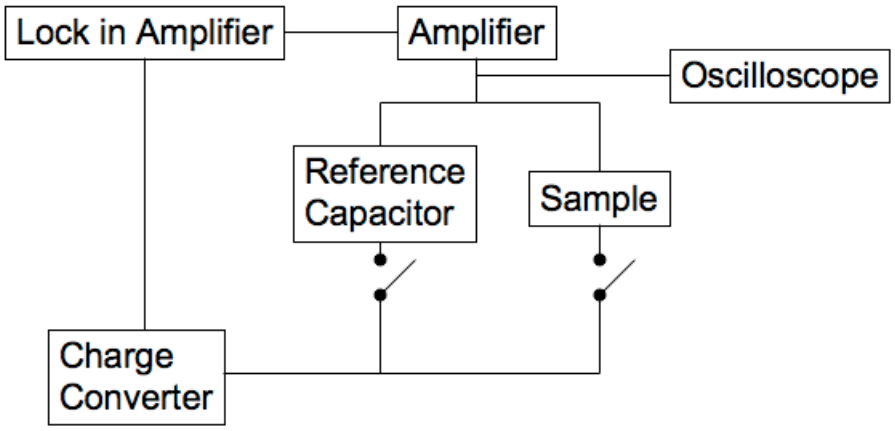

Figure **3-1**: Schematic of the measuring system for the high field dielectric constant and loss.

790 series power amplifier, Piezotronics, Inc.).

Forty FORC were measured using a custom P-E measurement system with the electric field sequence shown in Fig. 3-2. Initially, the field was decreased to a negative electric field, $-E_{min}$, in order to saturate the response of the irreversible hysterons. Then, the field was increased to $-E_{min}+\Delta E$ and decreased to $-E_{min}$ ($\Delta E = E_{min}/20$) in order to assess the polarization change. The waveform of the electric field was sinusoidal with a frequency of 20 Hz. Subsequently, the field increased to $-E_{min}+n\Delta E$ (n = 2 to 40) and decreased to $-E_{min}$ in steps until the maximum electric field was $+E_{min}$. After the measurement, each curve was linearly interpolated at $-E_{min}+k\Delta E$ (k=0, 1, 2, …, n for the n^{th} step) so that the polarization of the FORC $P(\alpha, \beta)$ was an evenly discretized function of the returning fields α and the fields of the descending curves β (which correspond to $-E_{min}+n\Delta E$ and at $-E_{min}+k\Delta E$, respectively). For $\alpha>\beta$, the hysterons are irreversible (See Fig. 3-3) and the irreversible FORC distribution $p(\alpha, \beta)$ was defined as Eq. 2-15, where $\Delta\alpha = \Delta\beta = \Delta E$. Since the distribution is discrete, $p(\alpha,\beta)$ represents the distribution of hysterons with switching fields $\alpha_o-\Delta\alpha \le \alpha \le \alpha_o$ and $\beta_o \le \beta \le \beta_o+\Delta\beta$ for $(\alpha, \beta)=(\alpha_o, \beta_o)$. For $\alpha=\beta$, the hysterons are reversible and the reversible FORC distribution $p_{rev}(\alpha)$ was defined as Eq. 2-16.

A reversible hysteron is shown in Fig. 3-3. At returning fields especially near the coercive field, the polarization may increase as the field decreases, because of the finite time dependence of switching. Here, $P(\alpha,\alpha)$ was defined as the maximum polarization of fields between α and $\alpha-\Delta\beta$.

The polarization and dielectric constant could then be calculated using the obtained discrete distribution. Eq. 1-3 is approximated to calculate the polarization as:

$$P = \sum q(\alpha,\beta)\cdot\ p(\alpha,\beta)\Delta\alpha\Delta\beta + \sum k(\alpha)\cdot\ p_{rev}(\alpha)\Delta\alpha \qquad \text{Eq. 3-3}$$

The dielectric constant, ε, is calculated as:

$$\varepsilon = \frac{\Delta P}{2\varepsilon_0 E_{ac}} \qquad \text{Eq. 3-4}$$

where ΔP (the polarization change induced by an ac field with amplitude E_{ac}) is expressed as

$$\Delta P = 2 \sum_{\substack{E_{dc}-E_{ac}<\alpha\le E_{dc}+E_{ac} \\ E_{dc}-E_{ac}\le\beta<E_{dc}+E_{ac}}} p(\alpha,\beta)\Delta\alpha\Delta\beta + 2 \sum_{E_{dc}-E_{ac}<\alpha\le E_{dc}+E_{ac}} p_{rev}(\alpha)\Delta\alpha \qquad \text{Eq. 3-5}$$

where E_{dc} is a dc bias field.

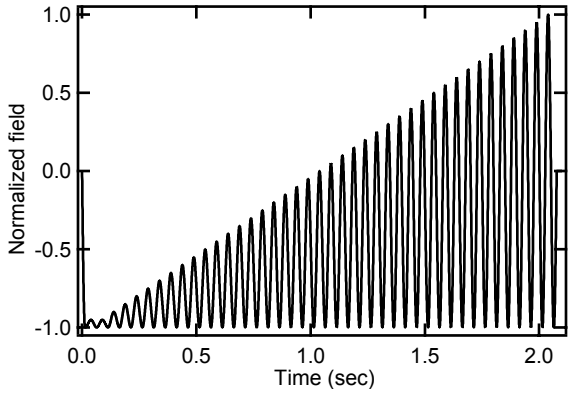

Figure **3-2** The time dependence of the electric field for the first order reversal curves.

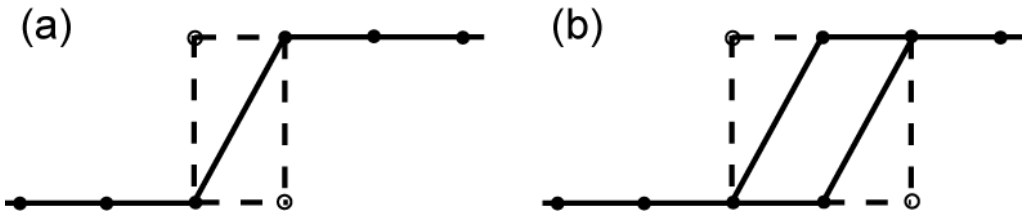

Figure **3-3**: Schematics of (a) a reversible hysteron and (b) an irreversible hysteron.

Chapter 4

Thickness Dependence of the Dielectric Nonlinearity of Lead Zirconate Titanate Films∗

Abstract

The first order reversal curves (FORC) distribution of $PbZr_{0.52}Ti_{0.48}O_3$ thin films was characterized as a function of film thickness. It was found that the thickness dependence of the small field dielectric constant is due primarily to differences in the domain wall contributions to the properties. The irreversible FORC distribution decreased and the switching fields increased as the thickness decreased; this is compatible with reported Rayleigh analyses. The polarization-electric field data and the ac field dependence of the dielectric constant were modeled using the FORC distributions, and were found to give a good fit to the experimental results. Some discrepancies remain in the high field dielectric constant, probably caused by its definition.

∗ The majority of this chapter is reproduced from I. Fujii, E. Hong, and S. Trolier-McKinstry (submitted to IEEE Transactions on Ultrasonic, Ferroelectrics, and Frequency Control).

4.1 Introduction

Lead zirconate titanate (PZT) films have attracted attention for applications such as nonvolatile memory and microelectromechanical systems due to their large switchable polarization and piezoelectric coefficients. For these applications, a wide range of film thicknesses are utilized; for ferroelectric memories, device thicknesses of 70-200 nm were reported recently[13]. On the other hand, much thicker PZT films are useful for actuators, accelerometers, piezoelectric energy harvesting[12] and acoustic sensing devices, among others[14, 50].

The dielectric and piezoelectric responses of PZT films are often reported to be thickness dependent; typically, as the thickness decreases, the small field dielectric constant and piezoelectric coefficients decrease and/or the coercive field increases for PZT capacitors with Pt top and bottom electrodes. Several models have been proposed to explain this, as is summarized elsewhere[51, 52]. Among the models describing the thickness dependence are a low dielectric constant interfacial layer,[50, 53, 54] a Schottky depletion region,[55] or a layer with significant levels of injected charge[56-58]. The observation of a smaller thickness dependence of the dielectric constant[55] and coercive field[56] in PZT films with oxide electrodes suggests the importance of interface chemistry[56].

Another factor that could contribute to the thickness dependence of the properties is the film domain structure along with the domain wall mobility[34, 59]. At subcoercive fields and stresses, the polarization-electric field, strain-stress, and strain – electric field responses of ferroelectrics become nonlinear, primarily due to domain wall or phase boundary motion[1, 3]. In many cases, the domain wall contributions to the dielectric and piezoelectric properties can be described by the Rayleigh Law[6, 60]. It has been reported that the reversible and irreversible Rayleigh constants increase with PZT film thickness up to ~ 1 μm and then are almost constant

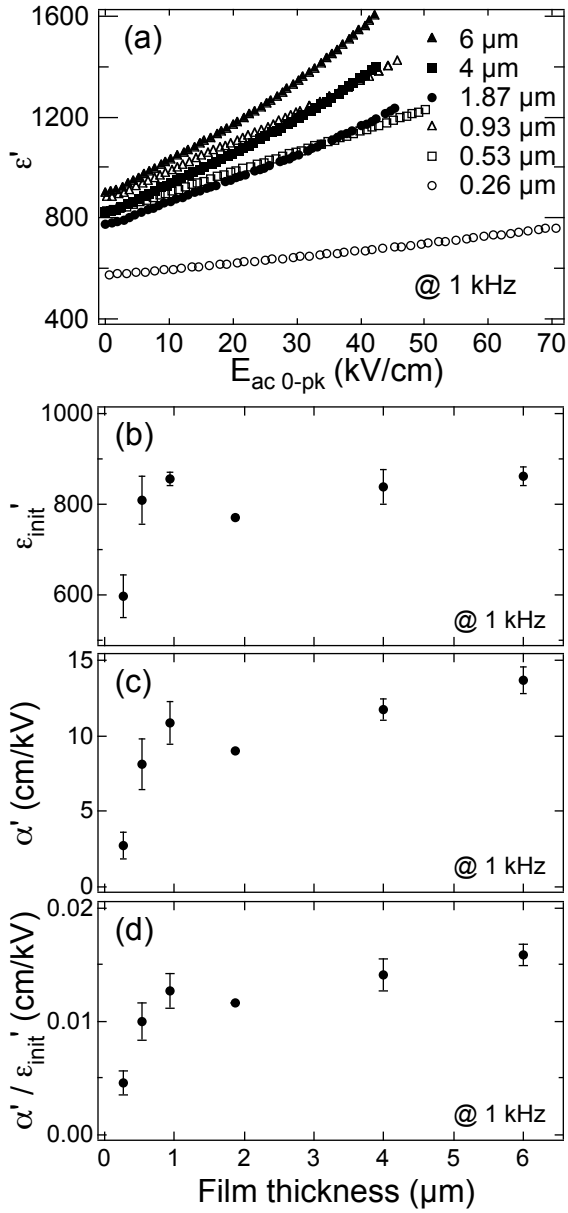

Figure **4-1**: (a) The ac field amplitude (0 to peak value, $E_{ac\ 0\text{-}pk}$) dependence of the dielectric constant of $PbZr_{0.52}Ti_{0.48}O_3$ films with various film thicknesses. (b)-(d) The corresponding reversible and irreversible Rayleigh constants and the ratio.[4]

above that thickness,[4, 61, 62] as shown in Fig. 4-1.[4]

However, the Rayleigh regime is appropriate only for excitation levels that do not significantly alter the domain structure, and so cannot be used for higher ac field amplitudes. In this case, the Preisach model[8-10] and first order reversal curves (FORC)[11, 44] have been employed to understand the switching characteristics for ferroelectrics both within and beyond the Rayleigh regime.

In this work, the FORC approach was employed to characterize the effect of film thickness on the high field dielectric responses of $PbZr_{0.52}Ti_{0.48}O_3$ films. The validity of the model was then assessed via a comparison of the experimental and modeled high field dielectric responses.

4.2 Experimental Procedure

$PbZr_{0.52}Ti_{0.48}O_3$ films with thicknesses of 0.26, 0.53, 0.925, 1.89, 4, and 6 μm were prepared by Dr. Eunki Hong (Penn State) on Pt-coated Si substrates by a chemical solution deposition method. A detailed fabrication method was presented elsewhere (excepting that a 0.4 M solution was used to prepare the 0.26 μm thick film)[33, 63]. Sputter deposited Pt top electrodes were formed by a lift-off process to enable electrical characterization.

Structural characterization was performed by X-ray diffraction (XRD) (Scintag Pad V, Thermo Scientific) with Cu-Kα radiation. XRD patterns showed the perovskite phase with no preferential orientation and no secondary phases, as shown in Fig. 4-2. The low intensities of the 0.26 μm thick PZT film are attributed to small volume of PZT (thin film thickness). The film microstructure was studied using field emission scanning electron microscopy (FE-SEM). Figure 4-3 shows surface FE-SEM images of the PZT films. An average of a short diameter and a long

diameter was calculated for more than 80 grains. The grain size is reported as an average of these averages; the error bar gives the standard deviation. The average grain sizes are summarized in Fig. 4-4; they were 50-150 nm. The grain size was not dependent on the thickness within the error limits, although the grain size distribution of the 0.26 μm-thick film was smaller. All of the films illustrated some features of a columnar microstructure, but decorated with porosity at each of the original interfaces associated with the rapid thermal annealing steps (See Fig. 4-5). No strong differences in microstructure with thickness were apparent.

Forty first order reversal curves were measured using a custom polarization-electric field loop measurement system with the electric field sequence shown in Fig. 3-2. The dielectric constant was measured using an LCR meter at several ac field excitations (4284A, Agilent). The effect of the dc bias on the dielectric constant was also studied.

4.3 Results and Discussion

Figure 4-6 shows the FORC data for the PZT films as a function of film thickness. For the major loops, a larger coercive field as well as an imprint was found for the 0.26 μm-thick film (See Fig. 4-7). The remanent polarization decreased as the film thickness decreased. The increased coercive field and reduced remanent polarization for thinner PZT films have been attributed to the effect of an interfacial layer due to the charge injection near the electrodes or to extra pinning of domain walls in thinner films [51, 57]. The non-monotonic variation of maximum and remanent polarizations and coercive field is likely to arise from film-to-film variations.

The reversible and irreversible distributions were calculated from the FORC. The reversible distribution is shown as a function of α in Fig. 4-8. It was found that although the reversible distributions for the films at zero bias differed, the distributions largely converged under high bias field fields. The reversible distribution is proportional to the ascending curve of a

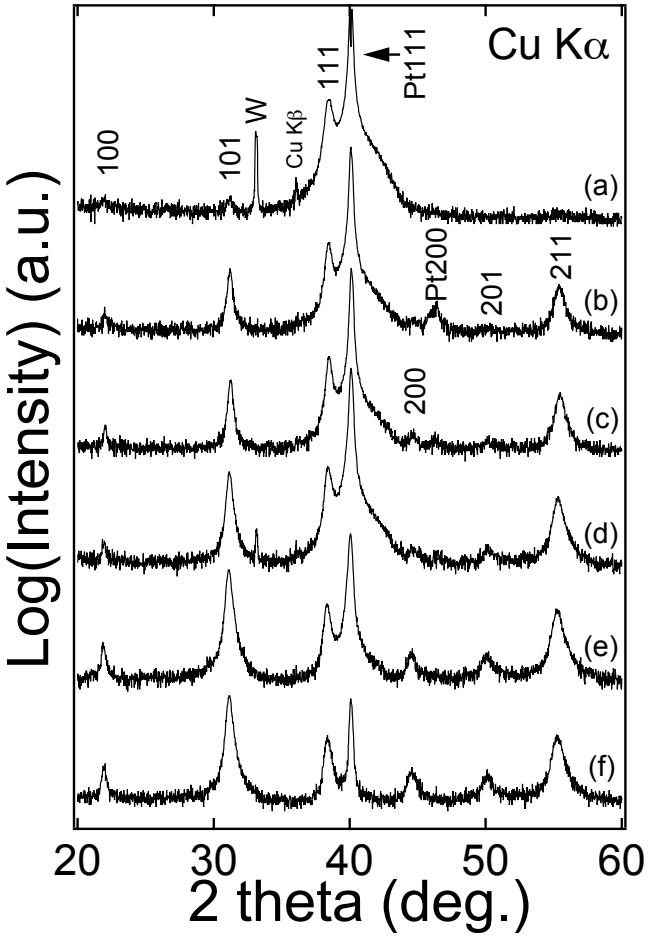

Figure **4-2**: XRD patterns of the PZT films with film thicknesses of (a) 0.26 μm, (b) 0.53 μm, (c) 0.925 μm, (d) 1.87 μm, (e) 4 μm, and (f) 6 μm.

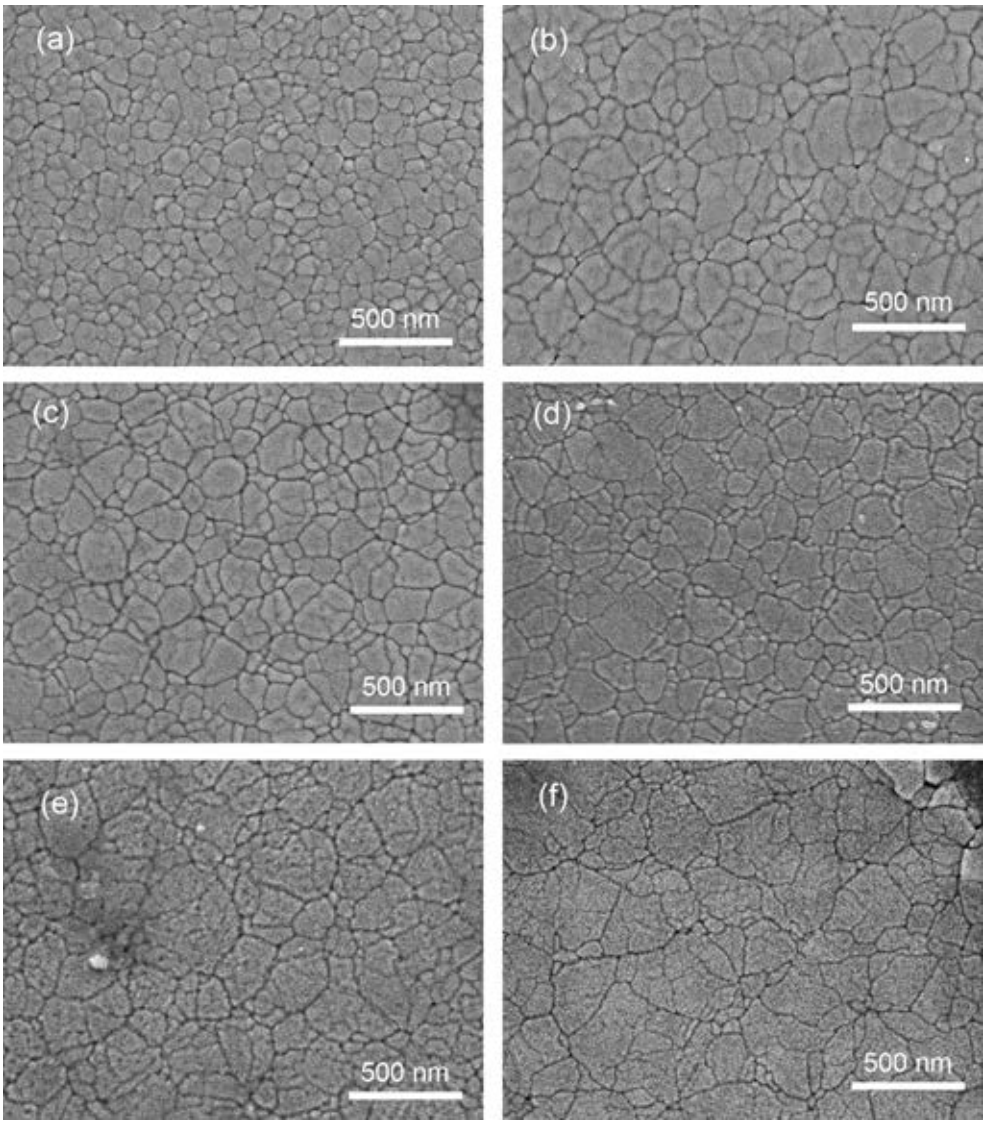

Figure **4-3**: Surface FE-SEM images of the PZT films with varied film thicknesses of (a) 0.26 µm, (b) 0.53 µm, (c) 0.925 µm, (d) 1.87 µm, (e) 4 µm, and (f) 6 µm.

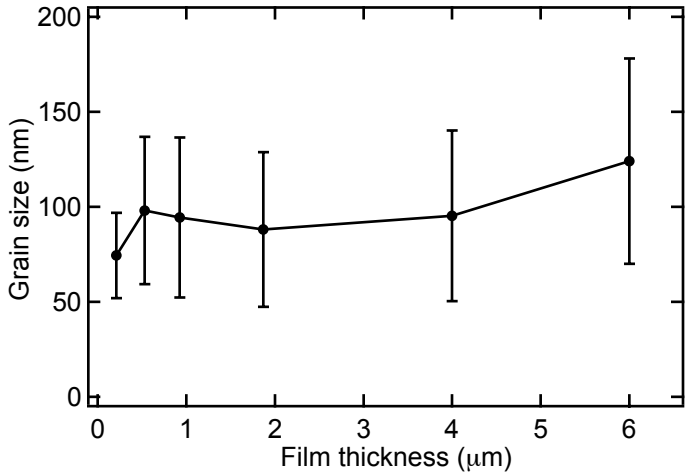

Figure **4-4**: Grain size of the PZT films as a function of the film thickness.

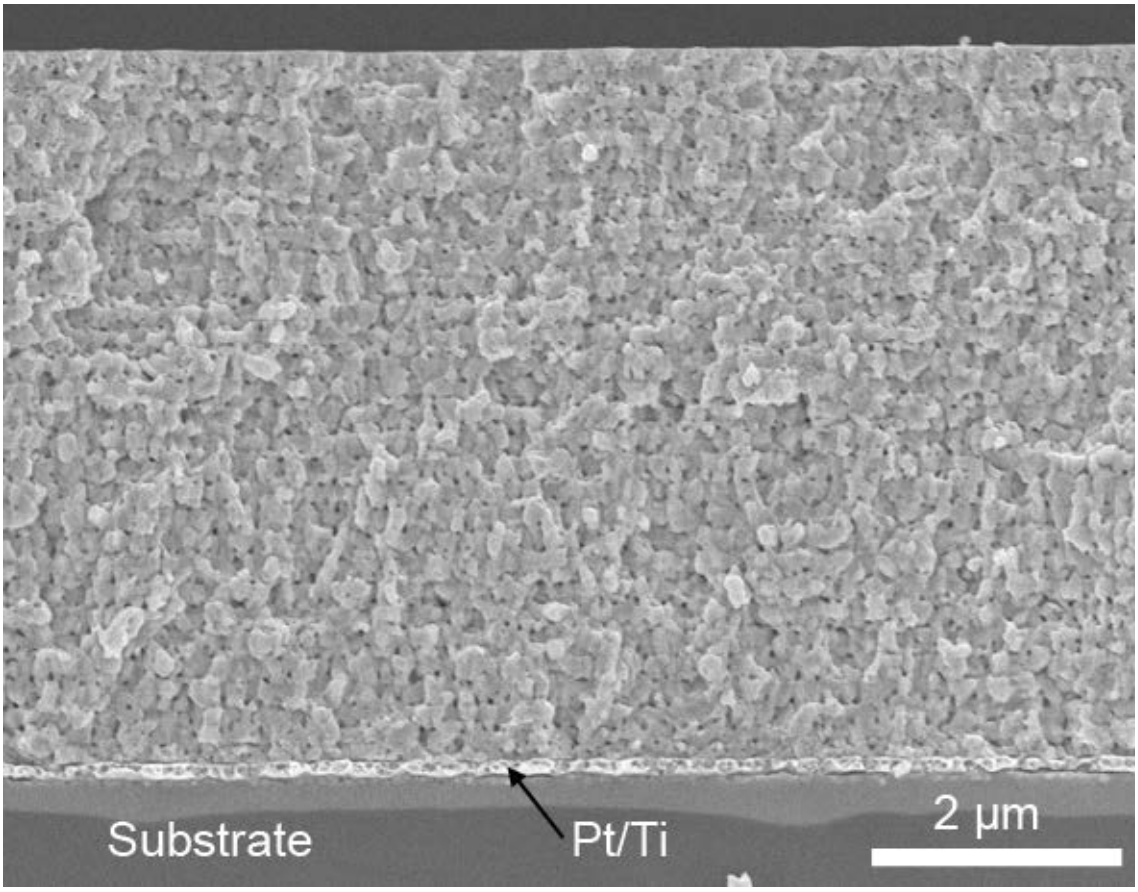

Figure **4-5**: A cross-sectional FE-SEM image of the 6 μm-thick PZT film.

small electric field capacitance vs. voltage plot (See Eqs. 2-16). The convergence of all of the curves at high biases, where extrinsic contributions are expected to be negligible, strongly suggests that all the films show comparable intrinsic dielectric constants. This implies that the difference of the reversible distribution at zero bias can be attributed to domain wall contributions, rather than to the existence of an interfacial layer.

The thickness dependence of the high field dielectric response was analyzed using the irreversible FORC distributions as shown in Fig. 4-9. In all cases, it was found that the FORC distribution showed a central maximum on a comparatively flat background. It is also seen that the major concentration of hysterons decreased as the thickness decreased, while the switching fields increased. That is, the FORC distribution was broadened and flattened in the thinner films. This is consistent both with the observed thickness dependence of the coercive field (since many of the hysterons switch near the coercive field) and with the more pronounced tilting of the hysteresis loop in thinner films.

At small fields (i.e. well below the coercive field), the FORC distribution is relatively flat, as would be expected for films that show Rayleigh-like behavior [8]. The larger peak in the FORC distribution for thicker films is consistent with the larger observed irreversible Rayleigh coefficients. As mentioned earlier, reductions in either domain wall density [34] or mobility by extra pinning [51] would be consistent with the thickness dependence of the dielectric nonlinearity.

Note that the major concentration of the 0.26 μm - thick film is located above $\alpha = -\beta$ line and this is characteristic of imprint. It was found that if the FORC was measured starting from the opposite polarization, the distribution was almost mirrored against the $\alpha = -\beta$ line. This means that the FORC distribution is somewhat path-dependent.

Another systematic feature in these FORC diagrams is a negative distribution in the switching fields where both α and β are positive. Similar negative distributions were also

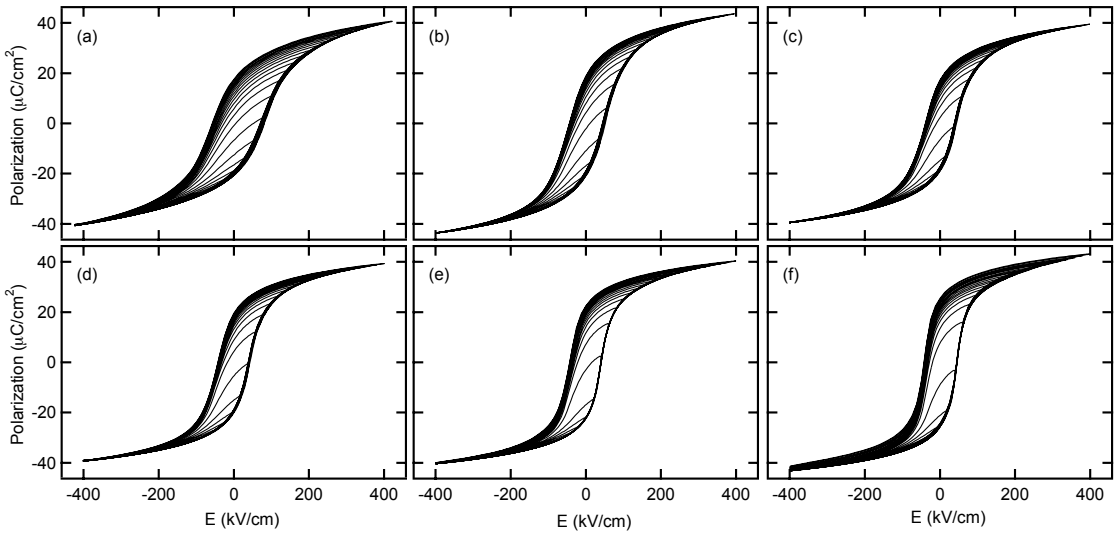

Figure **4-6**: The first order reversal curves of the PZT films with the thickness of (a) 0.26 μm, (b) 0.53 μm, (c) 0.925 μm, (d) 1.87 μm, (e) 4 μm, and (f) 6 μm.

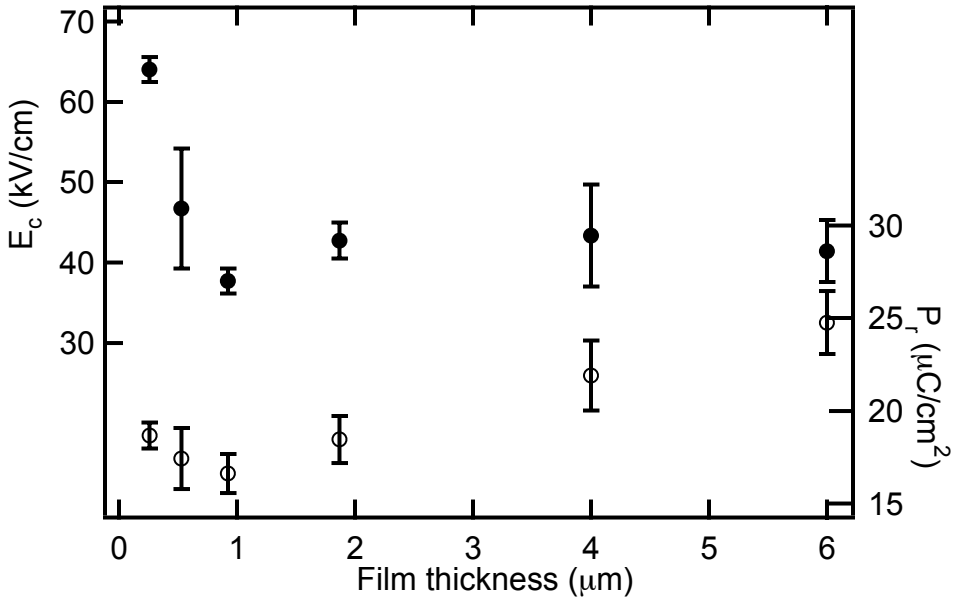

Figure **4-7**: The coercive field, E_c, and remanent polarization, P_r, as a function of the film thickness.

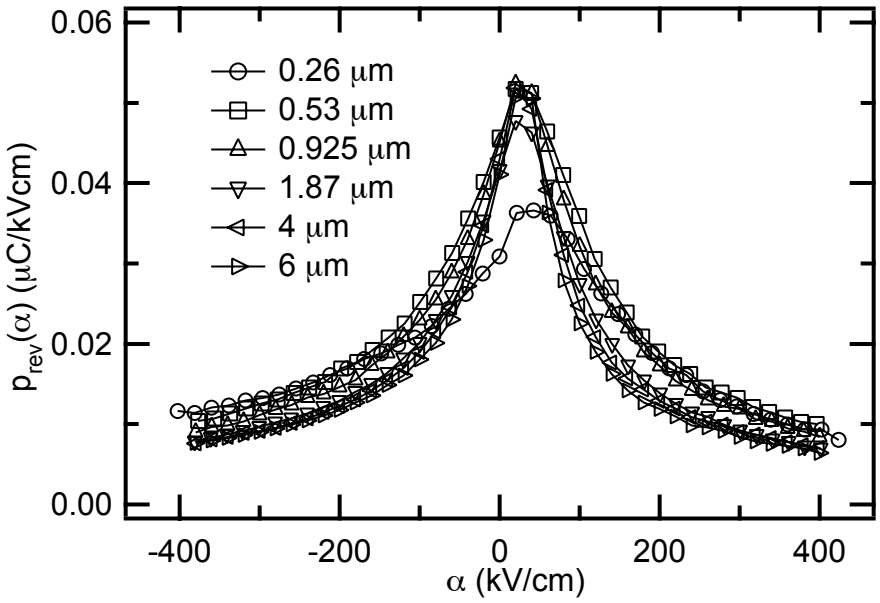

Figure **4-8**: The reversible FORC distributions.

reported for PZT ceramics [46] and some magnetic materials [11, 64, 65]. This implies a finite time-dependence of the switching.

To assess the self-consistency of the FORC distribution, it was used to describe the dielectric properties of the 1.87μm-thick PZT film under other measurement conditions. Here, in order to improve the sensitivity to small field perturbations, a set of FORC curves with E_{max}=250 kV/cm was used to calculate the FORC distribution. Figures 4-10 (b) and (c) show a comparison of measured and calculated polarizations (from equation (6)), obtained using the voltage-time excursion shown in Fig. 4-10(a). It was found that the Preisach model gave an acceptable prediction, although some discrepancies were observed for the polarization at subcoercive fields. Since a somewhat path-dependent polarization was observed for the PZT films, it is expected that these residual discrepancies are a consequence of a violation of the congruency and deletion properties,[9] so that the FORC distribution may be Preisach-like, rather than purely Preisach in character.

Fig. 4-11 shows a comparison of the measured and calculated 20 Hz dielectric constants as a function of the ac field amplitude and the dc bias, along with the measured polarization amplitude over the ac field amplitude (P/E). The ac field dependence can readily be separated into two regions: the Rayleigh-like region, where the dielectric constant increased linearly with the ac field amplitude, and a high field region, where the dielectric constant goes through a shallow maximum. For the Rayleigh region, the calculated dielectric constant gave a reasonable fit to that measured by the LCR meter, with some discrepancies which may be caused by the path-dependence. With increasing dc bias, an extension of the Rayleigh region and a decrease in the irreversible Rayleigh constant (e.g. the slope) were observed. This is physically interpreted as the stabilization of the domain structure under dc bias. Equivalently, in the language of the Preisach model, under dc bias, the switching of the hysterons induced by the ac field is reduced, as the

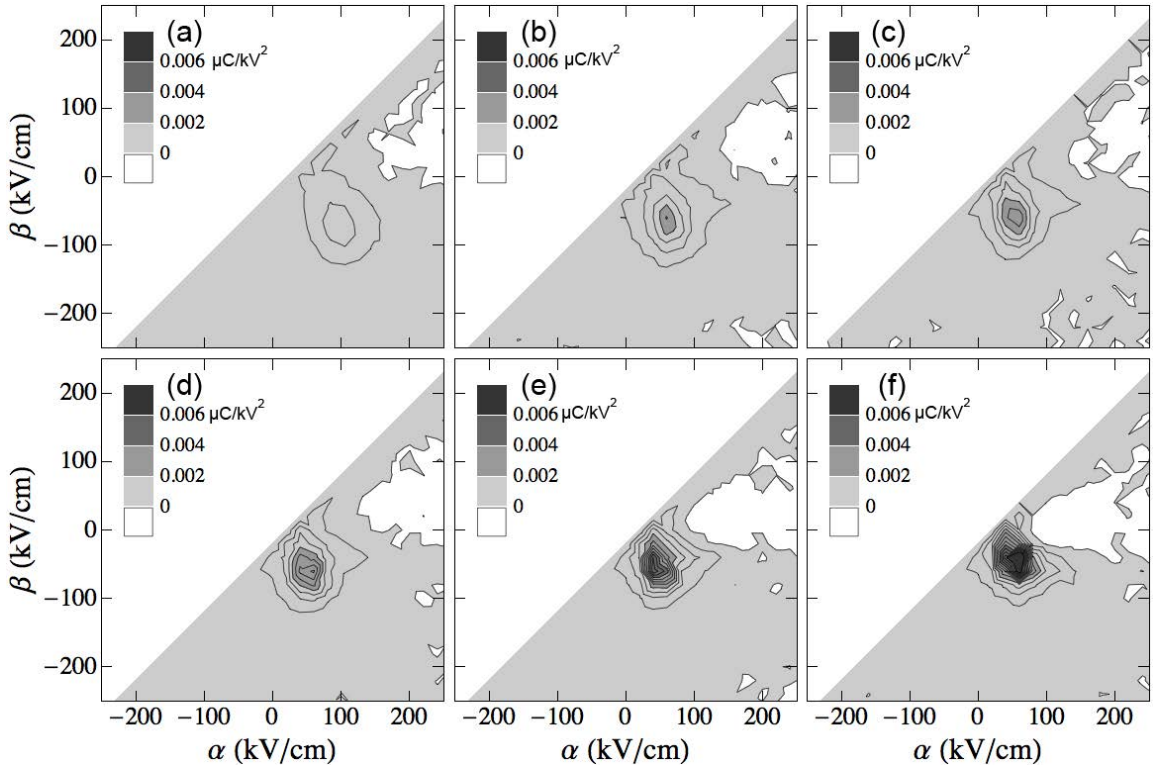

Figure **4-9**: The irreversible FORC distributions of the PZT films with the thickness of (a) 0.26 μm, (b) 0.53 μm, (c) 0.925 μm, (d) 1.87 μm, (e) 4 μm, and (f) 6 μm. The contour line appears each 0.0005 μC/kV^2.

measurement is made under conditions where the FORC distribution is smaller in amplitude and flatter.

For the high field region, the calculations become less accurate when the dielectric constant starts to saturate. One possible reason for this discrepancy is the definition of the dielectric constant used. As the ac field amplitude increases, the PZT films become progressively more nonlinear. As a result, higher harmonic terms of the polarization with respect to the electric field are generated along with a fundamental term. However, the LCR meter assesses only the fundamental term and then calculates the dielectric properties. To determine the importance of this effect, the P-E loops were first measured by applying sinusoidal fields with different ac field amplitudes, and then the first harmonic was calculated by Fourier transforming the time dependence of the polarization. It can be seen that the polarization response calculated in this manner provides a better match to the LCR measurements. The remaining discrepancies are likely to be due to the large dielectric loss at high ac field amplitudes ($\tan \delta \sim 0.4$ at saturation).

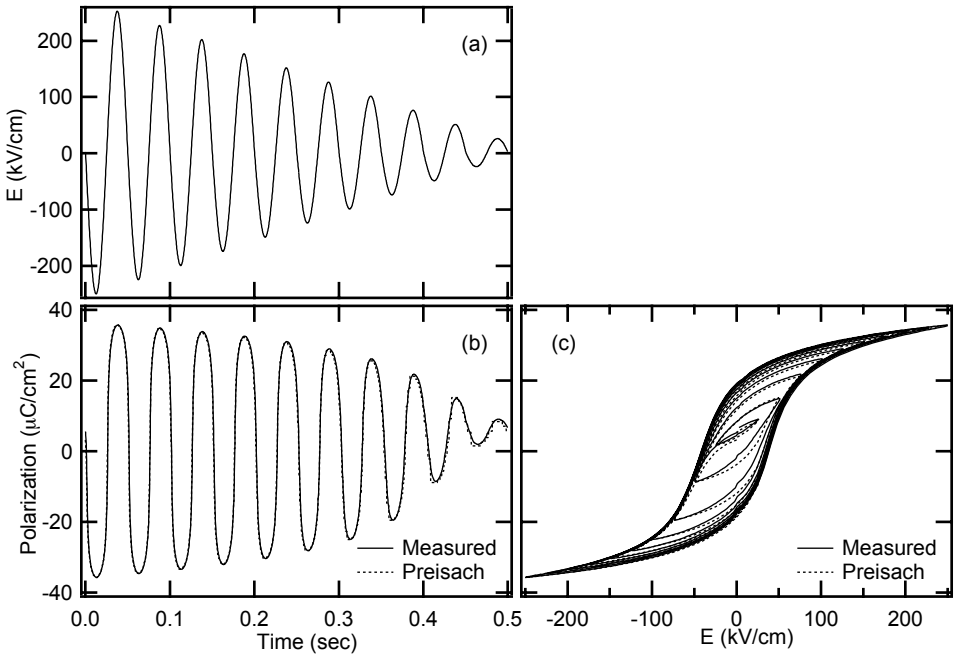

Figure **4-10**: The time dependence of (a) the electric field and (b) measured and calculated polarizations, and (c) the measured and calculated polarization - electric field loops.

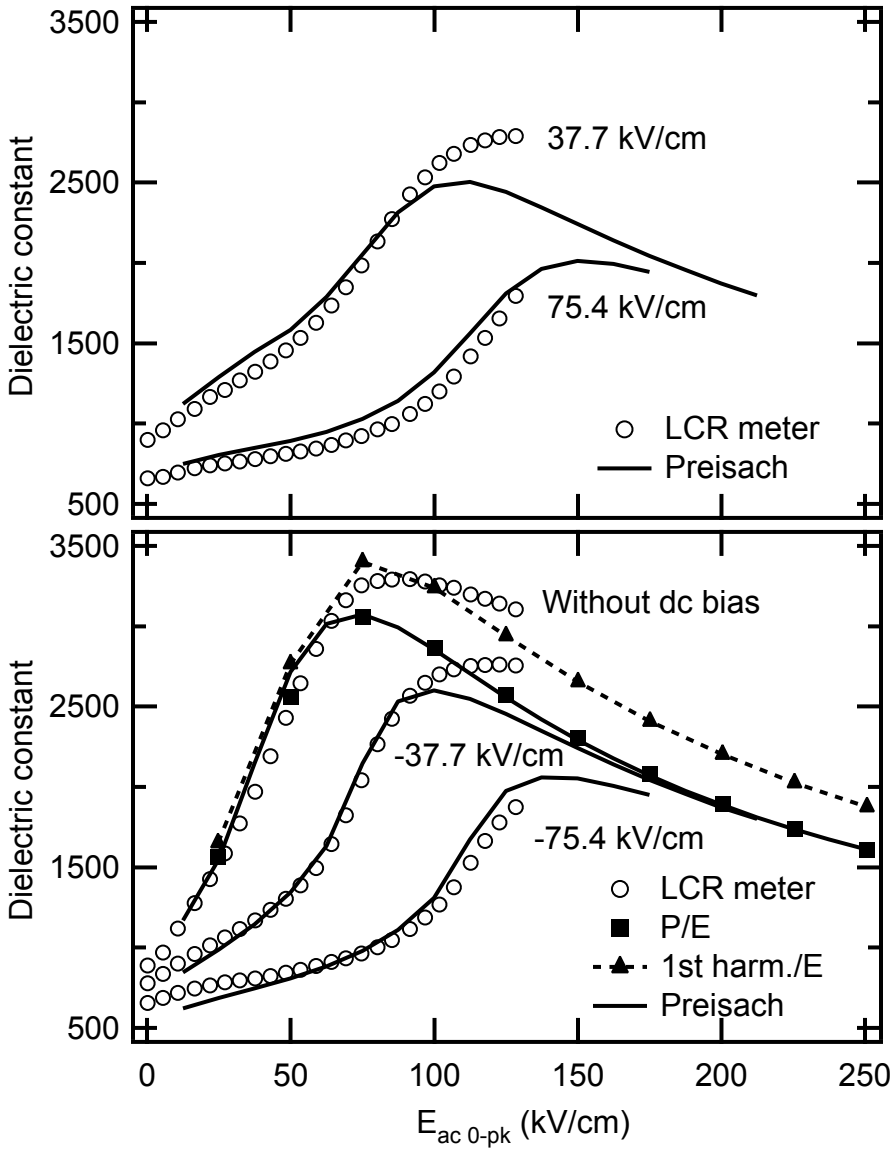

Figure **4-11**: The measured and calculated dielectric constant as a function of the ac and dc fields, along with the polarization amplitude or fundamental of the polarization over the ac field amplitude (P/E and 1st harm./E). The latter was calculated only for zero dc bias.

4.4 Conclusions

The dielectric nonlinearity of PZT films of different thickness was investigated using the FORC distribution obtained by the first order reversal curves method. Over the thickness range from 0.26 to 6 μm, the majority of the thickness dependence in the dielectric properties can be attributed to extrinsic, rather than intrinsic effects. Significant differences were observed in the irreversible FORC distribution; as the film thickness decreased, the concentration was depressed and the switching fields for the concentration increased. This is consistent with the thickness dependence of the irreversible Rayleigh constant. The polarization-electric field and the dielectric constant calculated by the Preisach model gave a reasonable fit to the experimental data, although the high field dielectric constant differed from the experimental data, probably due to a difference in the definition of the dielectric constant.

Chapter 5

Grain Size Effect on Dielectric Nonlinearity of $BaTiO_3$ Ceramics∗

Abstract

The dielectric nonlinearity of $BaTiO_3$ ceramics with grain sizes from 1.2 to 76 μm was investigated using the ac electric field dependence of the dielectric properties and the first order reversal curves (FORC) distribution. Defect dipoles in samples with large grains led to pinching of minor polarization – electric field hysteresis loops as well as a threshold field in the ac field dependence of the dielectric constant and loss. For samples with small grains, a sublinear ac field dependence was observed. The irreversible FORC distributions characterizing the responses showed two strong and narrow peaks for large-grained samples and a weak, broad peak centered near the origin for samples with small grains. As the grain size decreased, the reversible FORC distribution at zero-bias field increased. No grain size dependence of the reversible FORC distributions was observed at high dc electric fields. These results indicate that the grain size dependence of the small field dielectric constant is attributable to a domain wall contribution. Furthermore, the potential profile through which the domain walls travel changes from a landscape with shallow widely-spaced wells with deep local wells to one with deep widely-spaced wells with shallow local wells, as the grain size decreases.

∗ The majority of this chapter appears in I. Fujii, M. Ugorek, and S. Trolier-McKinstry (submitted to J. Appl. Phys.)

5.1 Introduction

$BaTiO_3$ is the major dielectric component of multilayer ceramic capacitors. Progressive miniaturization in the dielectric layer thickness has been reported over the last decade, with dielectric layer thicknesses under 1 μm in commercial production.[66] While the decrease in layer thicknesses has enabled improved volumetric efficiency, the dielectric properties of $BaTiO_3$ ceramics are also a function of size, so that there may ultimately be a limit in capacitor scaling.

There are two key factors that influence the observed thickness dependence of the dielectric response of capacitors. First, the grain size has to be small, with the upper limit governed by the dielectric layer thickness, though typically base metal capacitors use layers that are several grains thick to improve the reliability. It is known that the dielectric constant of $BaTiO_3$ ceramics depends on the grain size,[67] as shown in Fig. 5-1.[68] For undoped $BaTiO_3$, the room temperature, small field dielectric constant is ~ 1500-2000 for grain sizes larger than 10 μm. However, as the grain size decreases, the permittivity rises to 3500-6000 for grain sizes near 1 μm, and then drops. The permittivity maximum has been attributed to changes in domain structure along with internal stresses.[21, 69, 70] Stress may increase the dielectric constant, as calculated for a single-domain crystal from phenomenological theory.[71] In addition, the density of 90˚ domain walls increases as the grain size decreases.[21, 69, 72] Since both reversible and irreversible domain wall motion contributes to the dielectric constant,[1-3] the dielectric constant increases as the grain size decreases (although the magnitude of the increase may be modulated by the grain size dependence of the force constant).[73] Thus, the twinning may increase the dielectric constant both intrinsically and extrinsically. The reduction in permittivity for grain size < 1 μm appears to be due primarily to non-ferroelectric grain boundaries.[25]

The second major contributor to the thickness dependence of the dielectric response of capacitors is that the applied field over the dielectric increases as devices are scaled down in layer

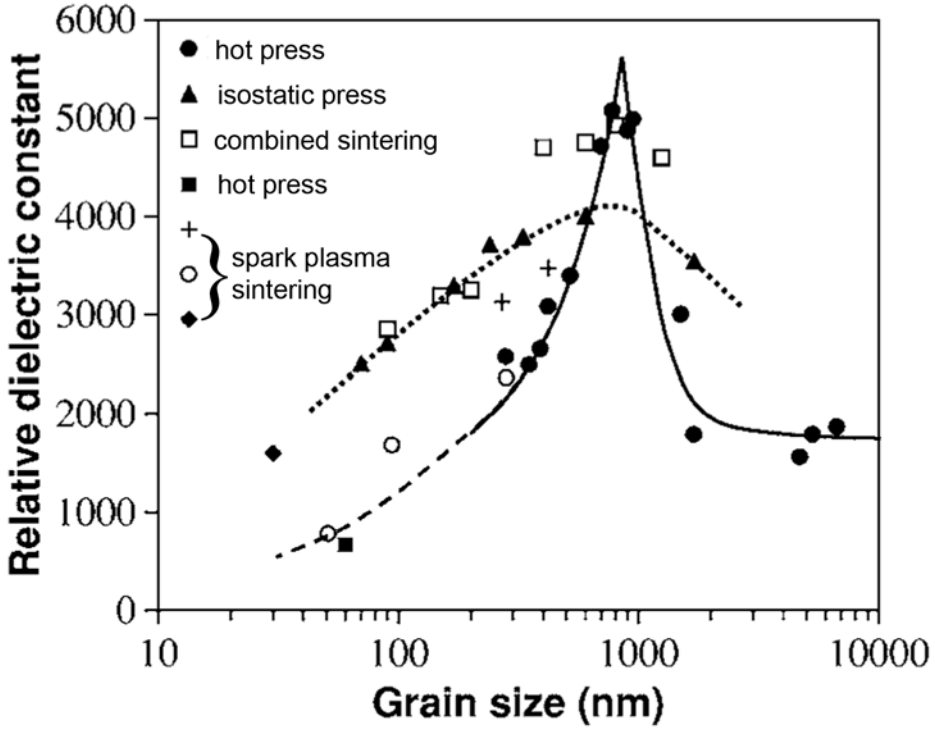

Figure **5-1**: Grain size dependence of the dielectric constant of $BaTiO_3$ ceramics prepared by several methods.[68]

thickness, if the operating voltage does not scale down as rapidly. For ferroelectrics, the polarization-electric field (P-E) trace is almost linear at small ac field amplitudes. However, with increasing driving field, the loop opens up and the response become nonlinear and hysteretic. Since the dielectric constant is roughly expressed as the slope of the P-E loop, it changes as well. Dielectric nonlinearity is primarily attributed to irreversible domain wall motion.[3] Many factors influence the domain wall motion, and hence the dielectric nonlinearity[74]. The ac electric field dependence of the dielectric constant has been fit using polynomial[75], power[76], and linear[6] functions at subcoercive fields to quantify the contributions. However, these approximations do not hold at high electric fields. In such a case, the Preisach and FORC distributions[9, 11, 41, 44, 77, 78] have been utilized. They describe a distribution of hysterons, or bi-stable units, with different switching fields. The macroscopic response is then the sum of the responses from the hysterons for a given field excursion.

The dielectric nonlinearity of doped and undoped $BaTiO_3$ ceramics has been reported for various grain sizes. Some results are shown in Fig. 5-2. When measured at fields below the coercive field, the ac field dependence of the permittivity of Co-doped $BaTiO_3$ ceramics (grain size: 4.1 μm)[79] and Mn-doped ceramics (grain size: 88 μm)[7] was superlinear, while that of $BaZr_{0.15}Ti_{0.85}O_3$ ceramics (grain size: 1-3 μm)[15] and some formulated multilayer ceramic capacitors with submicron grain size was sublinear. By "superlinear" and "sublinear", it is meant that the dielectric properties versus ac field response curves up or down with increasing amplitude, respectively. At ac field amplitudes near the coercive field, the experimental increase in the dielectric constant and loss of undoped $BaTiO_3$ ceramics was suppressed as the grain size was reduced from 60 to 0.6 μm[80]. This was attributed to a severe restriction of large scale domain

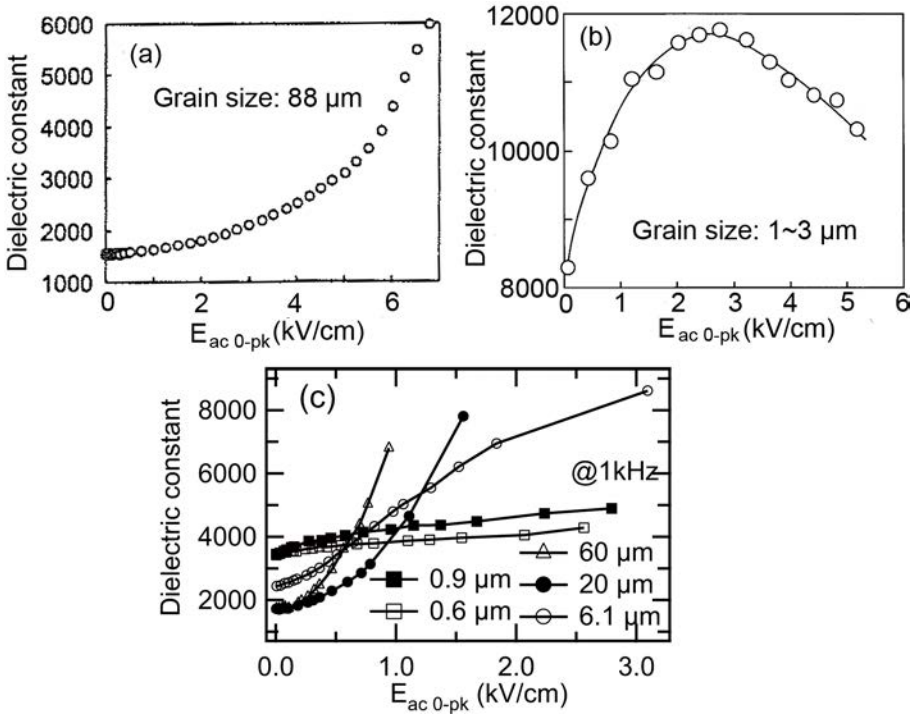

Figure **5-2**: The ac field dependence of the dielectric constant of (a) Mn-doped $BaTiO_3$ ceramics, [7] (b) $BaZr_{0.15}Ti_{0.85}O_3$ ceramics,[15] and (c) Undoped $BaTiO_3$ ceramics with different grain sizes (data were extracted and re-plotted on a linear scale for the ac field amplitude)[80].

wall motion in small grains.[80] However the superlinear and sublinear responses are not well understood.

In contrast to the intensive studies reported for subcoercive fields, data on the size effects for the dielectric properties measured over the coercive field is limited.[49] Thus, the aim of this study is to investigate the grain size effect on the ac field dependence of the dielectric properties and the FORC distributions of undoped $BaTiO_3$ ceramics.

5.2 Experimental Procedure

$BaTiO_3$ powder (BT-02, Sakai Chemical Industry, Inc.) with a Ba/Ti ratio of 0.996 was used. Compacts were prepared via tape-casting by Dr. Michael Ugorek (Penn State).[81] They were sintered at 1250˚C, 1300˚C, 1320˚C, or 1350˚C for 2h in flowing dry air with a heating rate of 2000 ˚C/h; throughout this chapter these will be referred to as Samples A, B, C, and D, respectively. The density was measured by the immersion method. Following sintering, the samples were polished down to ~1/2 mm in thickness using SiC powders. Structural characterization was performed by X-ray diffraction (XRD)(Scintag Pad V, Thermo Scientific) with Cu Kα radiation. The grain size was measured using scanning electron microscopy (SEM)(S-3000H, Hitachi). The samples were polished and thermally etched for the SEM observation. An average of two diameters of a grain was calculated for more than 90 grains (except for the large grains of Sample C and the small grains of Sample D). The grain size is defined as an average of these averages, while the reported error bar is the standard deviation.

For electrical characterization, the samples were electroded with 100 nm of sputtered Au (SCD 050, BAL-TEC). The temperature dependence of the dielectric properties of all the samples was measured in the same run upon cooling from 150˚C to -150˚C at a rate of 2˚C/min using an

LCR meter (4284A, Agilent) and a furnace with temperature control (DELTA 9023, Delta Design). The P-E field loops were measured using a custom made measurement system with voltage amplifiers (BOP 1000M, Kepco and TREK 609C-6, Trek). The room-temperature capacitance and tan δ were measured using a lock-in amplifier (SR830, Stanford Research Systems), a voltage amplifier, and a charge converter[81]. The FORC distribution was calculated by the first order reversal curves (FORC) method.[9, 11, 44, 45]

5.3 Results and Discussion

To assess the role of grain size on the high field behavior of $BaTiO_3$ ceramics, a series of samples was prepared with a range of grain sizes. XRD patterns confirmed that all samples were single-phase perovskite within the detection limits (See Fig. 5-3). The grain size and density of samples A – D are summarized in Table 1. The density of all samples was above 98% of the theoretical density of $BaTiO_3$. Figure 5-4 shows SEM images of the microstructure as a function of the sintering temperature. The grain size of Samples A and B was similar: 1.29±0.56 μm and 1.23±0.49 μm, respectively. A bimodal microstructure was observed for Sample C; the grain size of the matrix was 1.23±0.58 μm, while that of the exaggerated grains was 122±73 μm. In some exaggerated grains, a straight line was observed. This is consistent with twin-plane reentrant

Table **5-1**: The sintering temperature, theoretical density, and grain size.

Name	Sintering temperature (˚C)	Theoretical density (%)	Grain size (μm)
Sample A	1250	98.5	1.29±0.56
Sample B	1300	98.5	1.23±0.49
Sample C	1320	99.9	1.23±0.58, 122±73
Sample D	1350	99.0	75.6±36.6

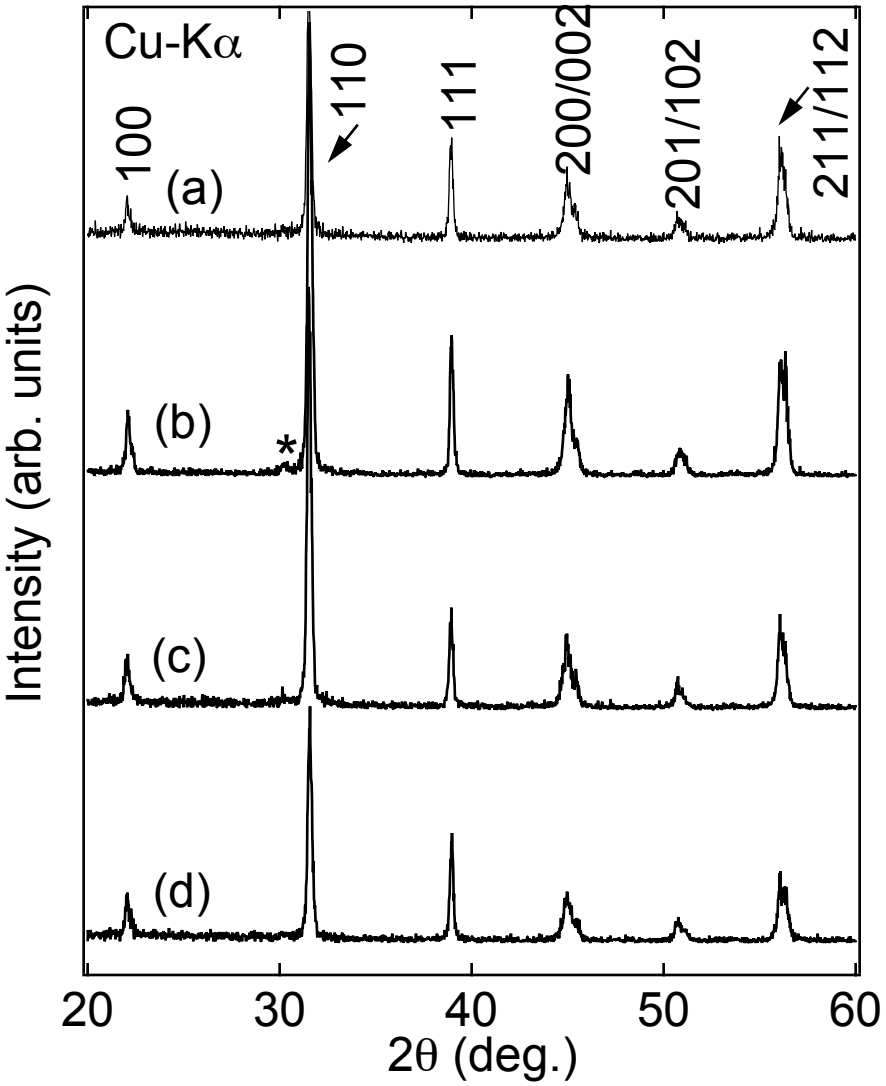

Figure **5-3**: XRD patterns of (a) Sample A, (b) Sample B, (c) Sample C, and (d) Sample D. An asterisk indicates a peak due to W contamination of the X-ray tube.

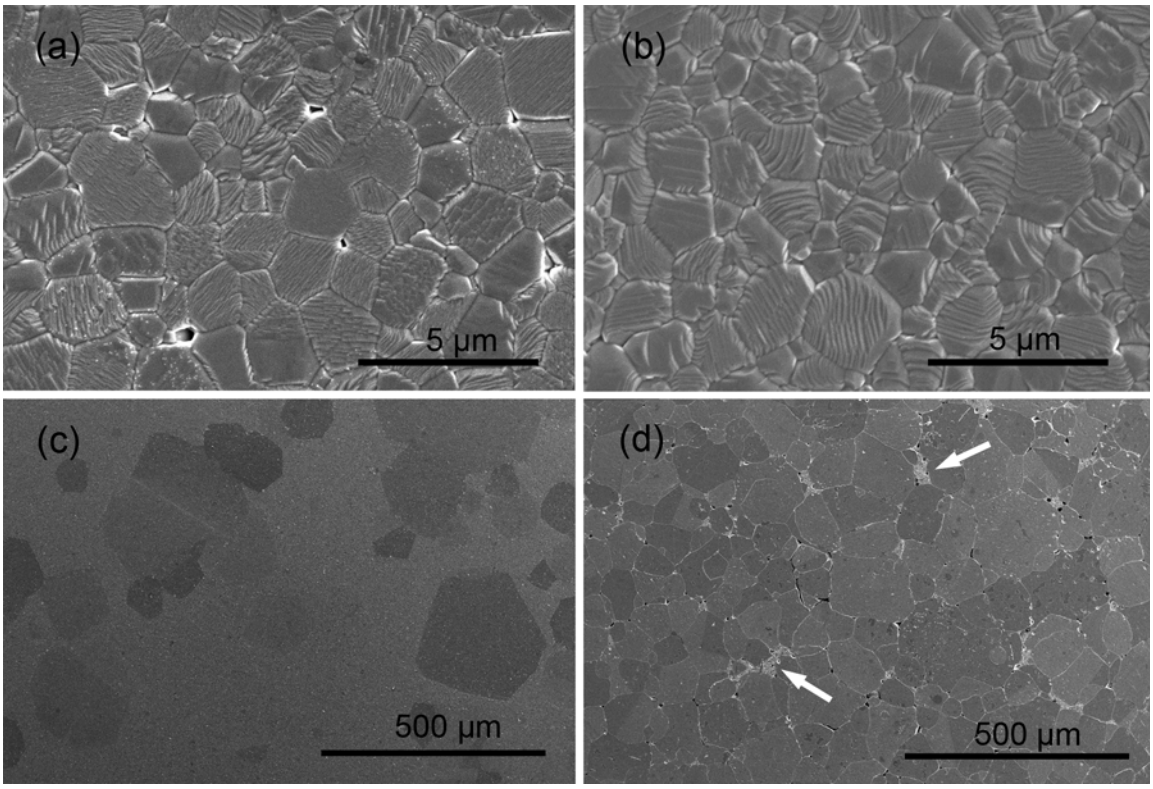

Figure **5-4**: SEM images of (a) Sample A, (b) Sample B, (c) Sample C, and (d) Sample D. White arrows specify pockets of small grains.

grain growth associated with {111} twin planes.[82, 83] Sample D consisted primarily of large grains (75.6±36.6 μm) with pockets of small grains (1.94±0.66 μm) marked with arrows.

The observed microstructural evolution is similar to previous studies of $BaTiO_3$ ceramics with a small excess of TiO_2 (Ba/Ti ratio < 1).[82-86] The small, uniform grain sizes of Samples A and B were attributed to an inhibited grain growth rate.[84] Exaggerated grain growth has been reported to occur both above and below the $BaTiO_3$-$Ba_6Ti_{17}O_{40}$ eutectic temperature ~1320˚C by liquid phase sintering[85] and solid state sintering,[82, 84] respectively. In this work, the mechanism for the exaggerated grain growth was not established definitively. It is possible that the exaggerated grain growth occurred by liquid phase sintering, since these samples were sintered above the eutectic temperature. However, the Ba/Ti ratio of the starting powders is 0.996, which corresponds to ~50.1 mol% TiO_2. This composition is within the single-phase perovskite region on the phase diagram (See Fig. 5-5), suggesting that the grain growth occurred by the solid state sintering, providing the local composition matched the global composition.

Figure 5-6 shows the temperature dependence of the small field dielectric constant. As expected, the dielectric constant of the samples decreased with increasing grain size below the Curie temperature, T_c. Three permittivity peaks associated with the phase transitions were observed. The permittivity peak for the orthorhombic to tetragonal phase transition of Samples A and B was diffuse, possibly due to an inhomogeneous internal stress distribution.[67] Small shifts of the peak temperatures were observed; compared to Sample D, T_c of Samples A and B was lowered, while the peak temperatures of the tetragonal to orthorhombic and the orthorhombic to rhombohedral phase transitions were raised. The increase in the sheer stress stabilized the orthorhombic phase, resulting in an increase in the tetragonal to orthorhombic phase transition temperature[87]. Two peaks were observed for each phase transition of Sample C as shown in the insets, presumably due to the bimodal microstructure. Such shifts were reported in previous studies[72, 87-89].

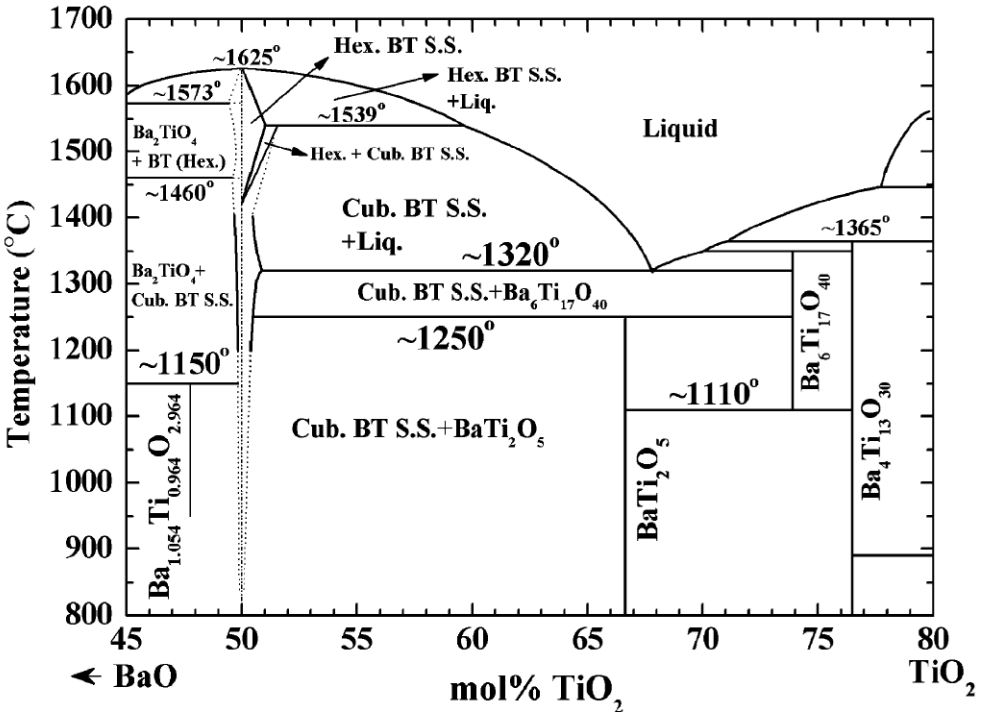

Figure **5-5**: $BaTiO_3$ phase diagram.[90]

It is unlikely that the shifts in T_c are associated with a reduction in tetragonality, as intrinsic size effects are not expected for grain sizes of ~ 1 μm.[72, 87] It is possible that the T_c shifts are due to the partial Schottky defect concentration. It was reported that T_c decreases with increasing partial Schottky defect concentration.[89] Lee et al. explained the observed increase in T_c with increasing annealing temperature as being a function of a relative decrease in partial Schottky defects compared to the full Schottky defect concentration. A comparable effect would explain the data in this study.

Figure 5-7 shows the temperature dependence of the dielectric loss measured at various frequencies. In addition to the phase transition peaks, three peaks were observed; one found above 100˚C (HT relaxation peak, circular symbols), one found at lower temperatures in the tetragonal phase (tetragonal relaxation peak, square symbols), and one found in the rhombohedral phase (rhombohedral relaxation peak, triangular symbols). The peaks were frequency dependent. Similar peaks were reported for $BaTiO_3$ ceramics[81, 91] and other perovskites[92]. It is likely that the relaxation peaks are related to oxygen vacancies. Multiple relaxation peaks indicate a different relaxation mechanism for each peak[91, 92]. In general, dielectric relaxation is caused by either reorientation of dipoles or long-range migration of space charge.

Previously, it was shown that the tetragonal relaxation peak in similar samples can be attributed to reorientation of oxygen vacancy - defect dipoles[81]. Here, it is possible that the defect dipoles are associated either with partial Schottky defects created during sintering or $V_{Ba}'' - V_O^{\bullet\bullet}$ dipoles which arise in response to the Ti-rich composition of the samples (i.e. Ba/Ti = 0.996). Because there was little evidence for strong space charge polarizability at temperatures < 80˚C[81], the HT relaxation peak is attributed to the long range migration of the oxygen vacancies created by disassociating defect dipoles. An increase in tan δ above T_c for lower frequency supports this. The HT relaxation peak was not observed for Sample D, probably because the large domain wall

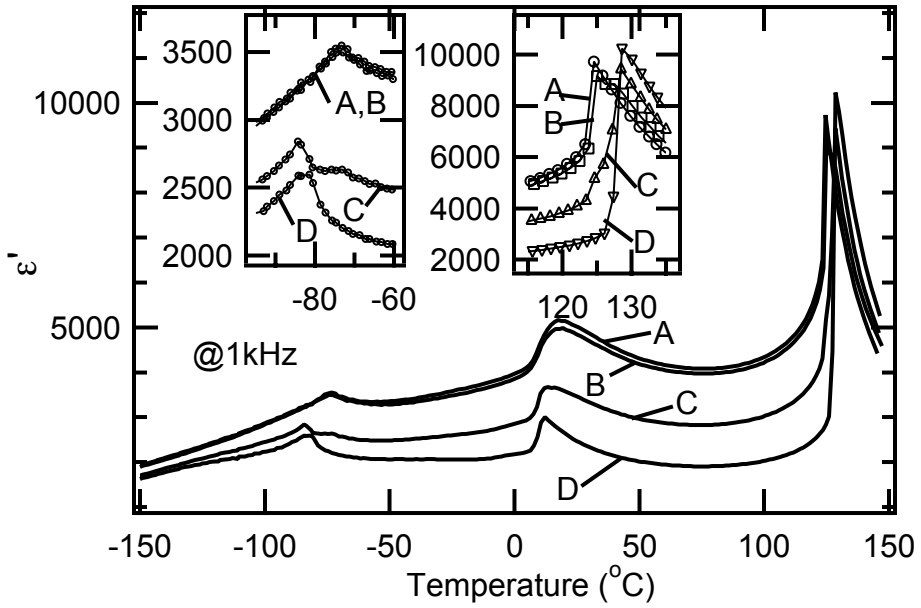

Figure **5-6**: The temperature dependence of the dielectric constant of the samples: the letters denote samples A, B, C, and D.

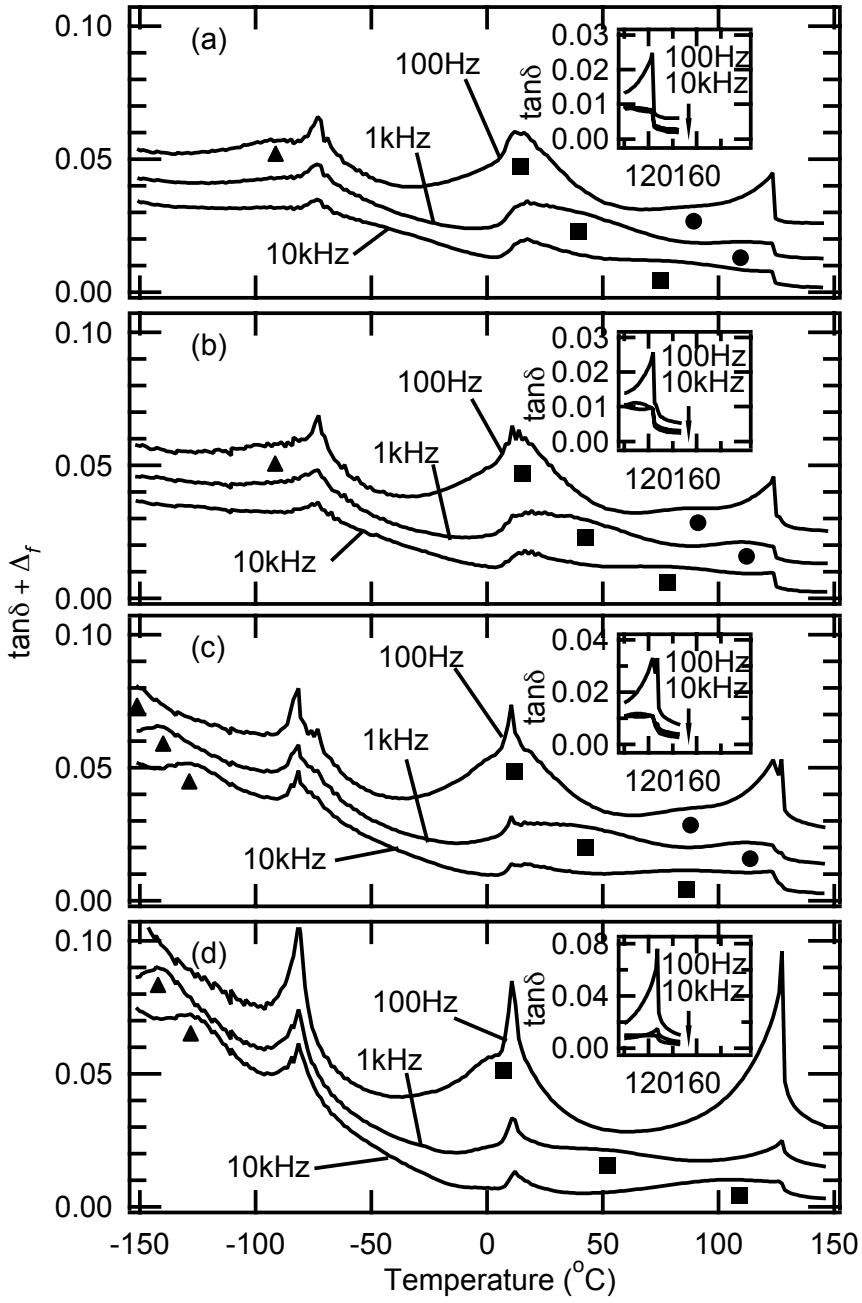

Figure **5-7**: The temperature dependence of the dielectric loss with an offset Δ_f of (a) Sample A, (b) Sample B, (c) Sample C, and (d) Sample D measured at the frequencies of 100Hz, 1kHz, and 10kHz. Δ_f= 0.02, 0.01, and 0 for the frequencies of 100Hz, 1kHz, and 10kHz, respectively, for display purpose. The symbols indicate the approximate peak temperatures of the relaxations. The insets show the dependence above 100˚C without the offset.

contribution hid the peak. It is believed that the rhombohedral relaxation peak is due to the same mechanism responsible for the tetragonal relaxation peak, but with the activation energy modulated by the crystal and domain structures of the phase.[91] Note that the rhombohedral relaxation peak of Samples C and D was stronger that of Samples A and B. Suppression of the relaxation peaks for small grains $BaTiO_3$ ceramics has previously been reported[91]. Presumably, the domain structure changes[21, 69] influence the relaxation of defect dipoles.

Figure 5-8 shows the major and minor polarization-electric field loops. It was found that minor loops of Samples A and B appeared quadratic, while those of Samples C and D were pinched. The major loops were not pinched and appeared similar, except that the polarization of Samples C and D was somewhat more difficult to saturate. In previous work, pinching was reported to disappear after repeated cycling through the hysteresis loop[93, 94]. Hence, the cycling effect for Sample D was investigated to confirm whether the pinching disappeared or not. Following repeated cycling through the major loops, fatigue (a decrease in the remanent polarization with increasing cycle number) was observed. However, even after cycling 1000 times through the full bipolar loop, pinching was still observed in minor loops. Similar pinched loops have been reported for Co-doped $BaTiO_3$ (grain size: 4.1 μm)[79], Mn-doped $BaTiO_3$ (grain size: 88 μm)[95], and acceptor doped $BaTiO_3$ ceramcis[93] as well as for other ferroelectrics[94]. The pinching is attributed to local electric fields created by the defect dipoles. Thus, the observed pinching for Samples C and D is consistent with the relaxation peaks of the dielectric loss.

Figure 5-9 shows the ac field dependence of the dielectric constant and loss measured at subcoercive fields. The ac field dependence of Samples A and B was sublinear, while that of Sample D was superlinear before the saturation and decrease. The dielectric response of Sample C sits between the two cases, possibly due to the bimodal microstructure. The response is similar to the grain size dependence of the dielectric nonlinearity reported for the doped $BaTiO_3$ ceramics[15, 79, 95] and some ceramic capacitors. This confirms that the grain size strongly influences

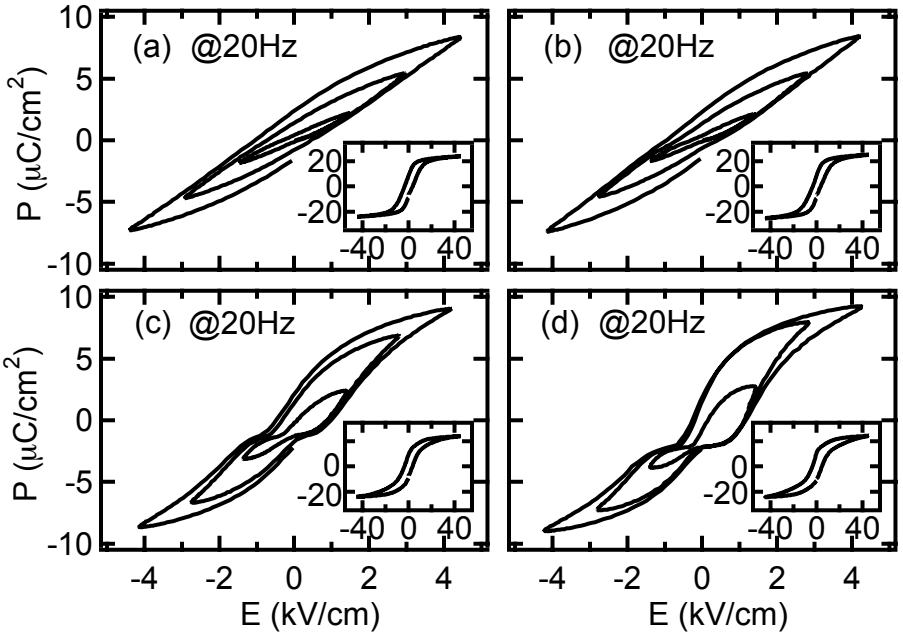

Figure **5-8**: The ac field dependence of the minor polarization-electric field loops of (a) Sample A, (b) Sample B, (c) Sample C, and (d) Sample D. The major loop is shown in the inset.

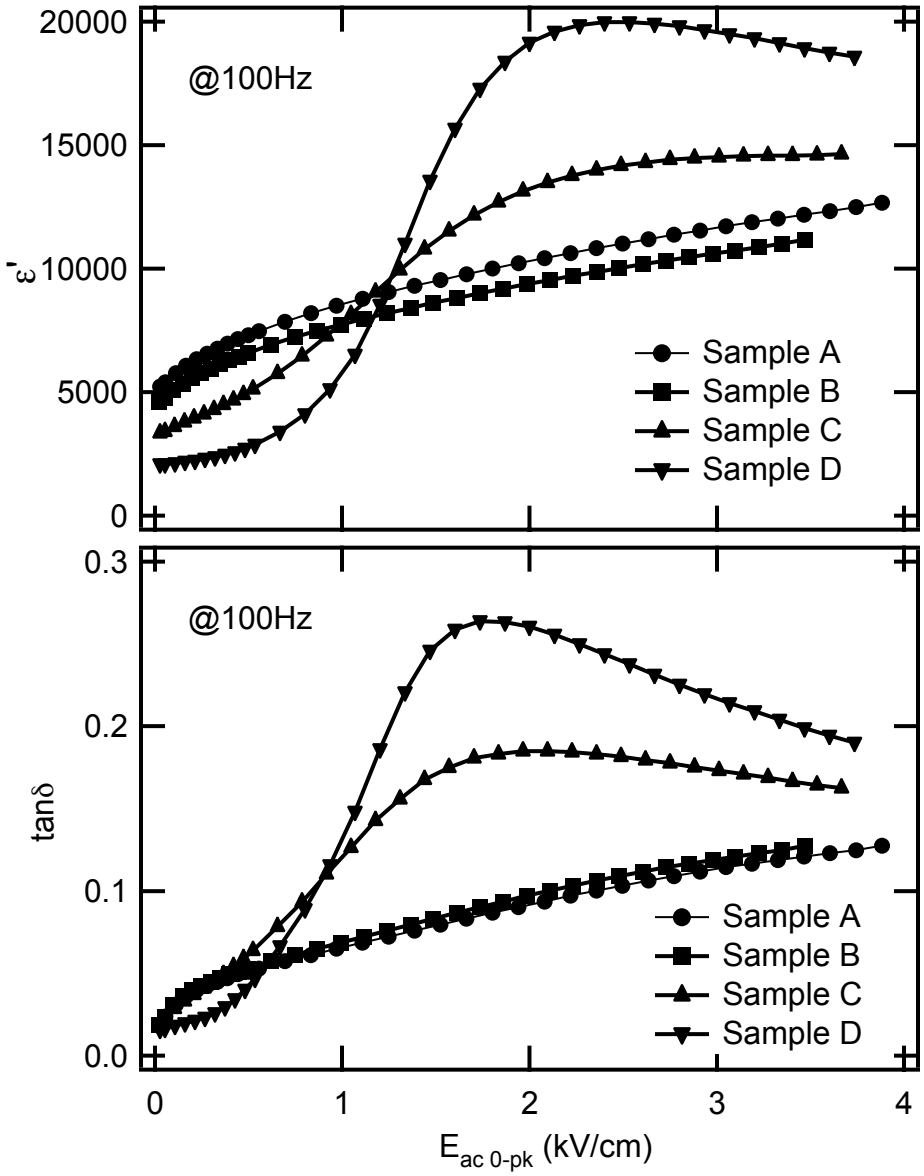

Figure **5-9**: The ac field dependence of the dielectric constant and tanδ.

the ac field dependence. For Sample D, the dielectric properties were nearly independent of the ac field amplitude below the threshold field of 0.5 kV/cm. This is attributable to a stabilization of the domains by the strong local fields surrounding the defect dipoles[93]. When the ac field amplitude exceeded the threshold field, the domain walls could be pried free from their pinning sites, which resulted in the large increase in the dielectric properties. The saturation and decrease of the dielectric properties at higher ac fields were caused by the saturation of the P-E loop.

For Samples A and B, the origin of the sublinear response is not clear. A similar sublinear response was reported for the piezoelectric nonlinearity in undoped $BaTiO_3$ ceramics with grain size of 0.7 μm, suggesting the effect of the internal stress.[96] One possible explanation for the sublinear response is the following: the large dielectric constant at small field is due, at least in part, to a high domain wall density.[72] These domain walls are weakly pinned and can be de-pinned at modest ac electric fields. However, *long-range* domain wall motion is strongly pinned,[80] possibly by the large density of grain boundaries in small grained samples. In other words, the domain walls travel a potential profile with deep widely-spaced wells with shallow local wells (See Fig. 5-10). On the other hand, the potential profile for samples with large grains is one with shallow widely-spaced wells with deep local wells.

To assess how realistic this model is, the FORC distributions were calculated from the first order reversal curves (See Fig. 5-11). Some upward drift in the saturated polarization was observed in the FORC, especially for Samples C and D. This could be due to field-induced reorientation of the defect dipoles, allowing strongly pinned domains to realign after long exposures to high fields.

Figure 5-12 shows the irreversible FORC distributions for all samples. For Samples C and D, two strong, narrow peaks are apparent. Such separated peaks are characteristic of a pinched loop[97]. A valley between the peaks near the origin corresponds to the pinching in minor

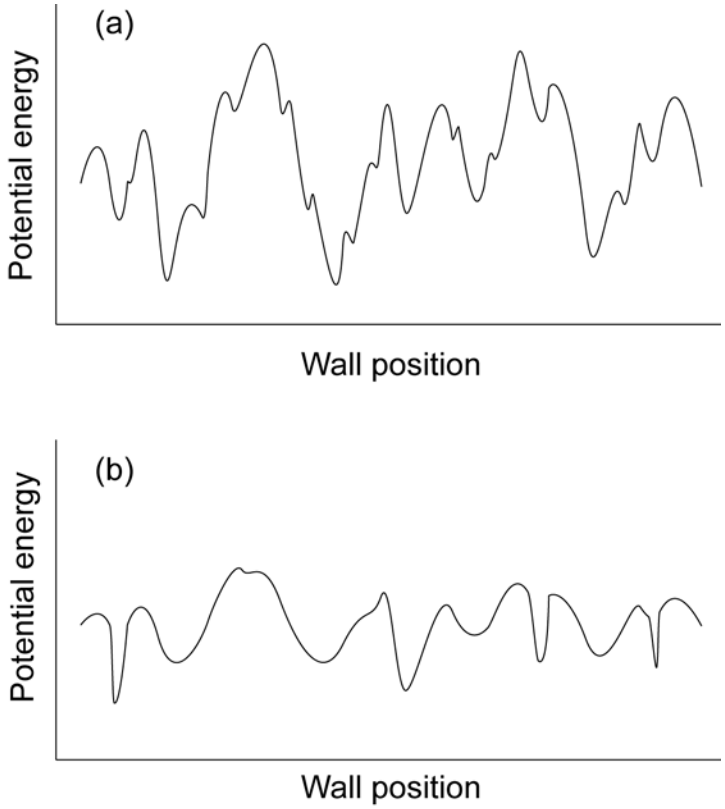

Figure **5-10**: Estimated potential landscape of a domain wall for (a) small grains and (b) large grains.

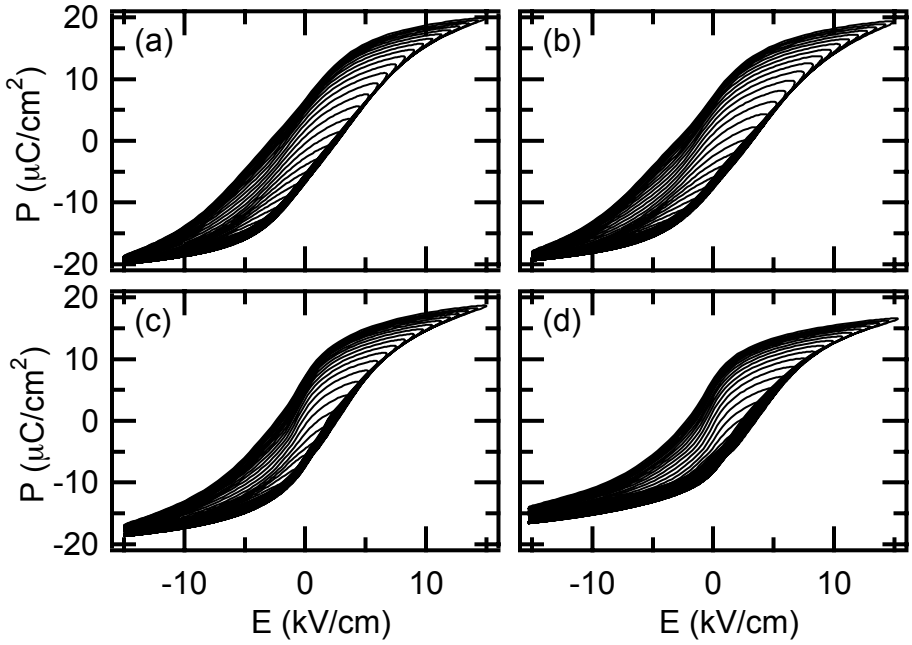

Figure **5-11**: First order reversal curves of (a) Sample A, (b) Sample B, (c) Sample C, and (d) Sample D.

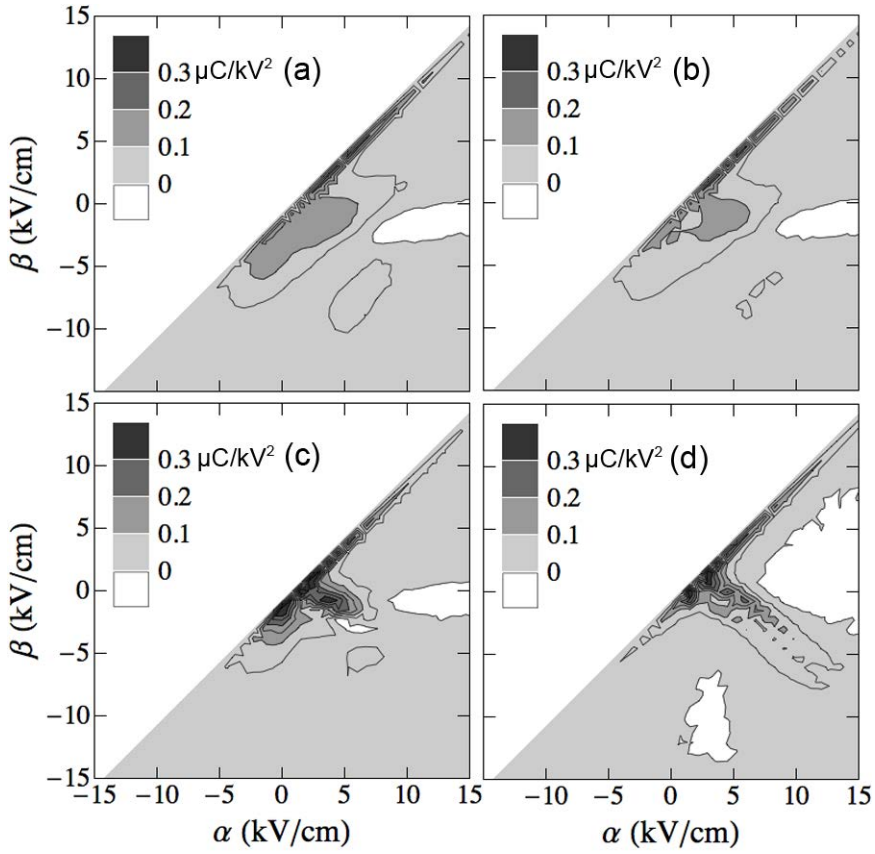

Figure **5-12**: Irreversible FORC distribution of (a) Sample A, (b) Sample B, (c) Sample C, and (d) Sample D.

loops and the weak ac field dependence at sub-threshold fields. The strong narrow peaks are responsible for the large increase in the dielectric properties above the threshold field. In contrast, a weak broad peak centered around the origin was observed for Samples A and B. This corresponds to the sublinear ac field dependence of the dielectric constant and loss. It was reported that the FORC distribution of $Ba(Zr, Ti)O_3$ ceramics became broadened and weakened as the grain size decreased from 3.3 μm to 0.75 μm[49]. This is consistent with our result, except for the peak splitting. Note that the streak along the $\alpha=\beta$ line for positive α and β is due to the finite time-dependence of the switching (that is, the polarization response lags the applied voltage).

Figure 5-13 shows the reversible FORC distribution. A reversible FORC distribution is proportional to an ascending capacitance – voltage curve (See Eqs. 2-16). The zero-bias reversible FORC distribution of Sample D is smaller than that of the other samples. This is consistent with the dielectric constant measured at modest ac field amplitudes. The FORC distribution of all samples largely converged at high fields. This suggests that the reversible responses are similar in the samples, and therefore the difference in the reversible distribution at zero bias is attributed to the domain wall contributions.

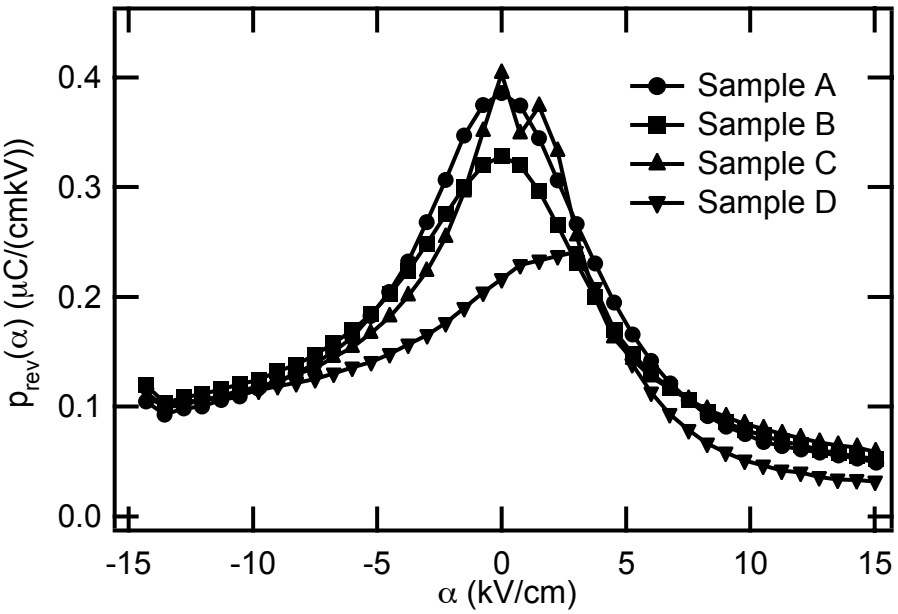

Figure **5-13**: The reversible FORC distribution.

5.4 Conclusions

The increase in the small field dielectric constant with decreasing grain size is influenced by an increase in the reversible domain wall contribution. For $BaTiO_3$ ceramic samples with large grains, defect dipoles are found to stabilize domains, producing pinched minor loops, a threshold field in the ac field dependence of the dielectric constant and loss, and splitting the peak in the irreversible FORC distribution. For samples with small grain sizes, domain walls are de-pinned at modest electric fields and contribute to the dielectric properties, although the long-range motion is restricted.

Chapter 6

Effect of Oxygen Partial Pressure during Firing on Dielectric Nonlinearity of $BaTiO_3$ Dielectrics∗

Abstract

The effect of the oxygen partial pressure during firing on the high field dielectric response of formulated and undoped $BaTiO_3$ ceramics was investigated. For the formulated ceramics, the dielectric constant of both oxygen and air fired samples increased almost linearly with the amplitude of the ac driving field. Formulated $BaTiO_3$ samples sintered in a reducing atmosphere produced a sub-linear increase in the permittivity with the ac field amplitude. For undoped $BaTiO_3$ ceramics, the dielectric constant increased sub-linearly over a wide range of oxygen partial pressures during firing. It is proposed for the formulated ceramics that the dopant – oxygen vacancy defect dipoles in the shell region accounted for the curvature in the field dependence of the permittivity. These defects appear to add a concentration of weak pinning centers to the potential energy profile through which domain walls move.

∗ Large portions of this chapter are published in I. Fujii, M. Ugorek, Y. Han, and S. Trolier-McKinstry (J. Am. Ceram. Soc., in press)

6.1 Introduction

$BaTiO_3$-based dielectrics are widely used for multilayer ceramic capacitors (MLCCs) due to their high and stable dielectric constant over a wide temperature range. Over the last several decades, commercial demand for downsizing MLCCs and increasing the capacitance density has led to a continual reduction in the dielectric layer thickness. As a consequence, the applied fields over the dielectric layers are increasing. As this occurs, the use of a small signal dielectric constant can be misleading due to either dielectric stiffening under dc fields, or domain wall motion.

The dielectric response of ferroelectrics exposed to ac electric fields can be separated into two contributions: intrinsic and extrinsic[3, 98]. The former is characteristic of the response of a single domain single crystal, while the latter is mainly due to motion of domain walls and phase boundaries. The extrinsic contribution to the dielectric response both produces hysteretic phenomena in ferroelectrics and changes the dielectric properties. Moreover, it is strongly dependent on use conditions, composition, and sample preparation (with concomitant changes in grain size, defect populations, density, etc.). Therefore, it is important to understand the extrinsic contribution in designing the response of devices utilizing ferroelectric materials.

Reflecting the above, the high field dielectric response of $BaTiO_3$-based ceramics has been studied. Hagemann studied the effect of donors and acceptors in $BaTiO_3$ ceramics[93]. He demonstrated that acceptor dopants and the associated oxygen vacancies reduced the domain wall contributions. Hall and co-workers studied the effect of aging in Co-doped $BaTiO_3$ ceramics[79]. They observed a reduced ac field dependence of the dielectric response with time due to stabilization of the domain wall positions by defect associates. Wu and Schulze reported that the domain wall contributions of fine-grained samples were severely restricted compared to those of

large-grained $BaTiO_3$ ceramics[80]. Tsurumi and co-workers also reported a reduced dielectric nonlinearity in fine-grained $BaTiO_3$-based ceramics[27]. Demartin and Damjanovic found a similar grain size effect for the direct piezoelectric response in $BaTiO_3$ ceramics[96]. They suggested that the internal stress increased in fine-grained samples, and that this clamped the domain wall motion, resulting in reduced domain wall contributions. Tsurumi and co-workers also reported the effect of the microstructures in $BaTiO_3$-based multilayer ceramic capacitors [27]. They observed different dielectric nonlinearities for core, shell, and core/shell microstructures. For other ferroelectrics: defects, crystallographic orientation, crystal structure, external stresses, temperature, and the frequency of applied electric field also affect the mobility of domain walls[4, 74].

In the case of MLCCs, the following factors would be anticipated to differ from conventionally processed $BaTiO_3$ ceramics. First, most MLCCs utilize Ni for internal electrodes instead of precious metals to reduce production costs. There is also on-going interest in the use of higher conductivity base metals such as Cu[99, 100]. As a result, MLCCs are sintered at a lower oxygen partial pressure, pO_2, to prevent formation of nickel oxide. While they are subsequently re-oxidized, large concentrations of oxygen vacancies remain. As these are charged defects, it is possible that they may act to provide local pinning sites for domain walls. Secondly, MLCCs are typically heavily formulated with dopants in order to both flatten the dielectric response as a function of temperature (often through development of core-shell microstructures) and to control the lifetime under dc fields. One of the consequences of this is formation of potential distributions associated with the core-shell interfaces, the grain boundaries, and the dielectric/electrode interfaces[29, 101, 102]. Thirdly, the grain sizes of MLCCs are often substantially smaller than conventionally processed $BaTiO_3$ ceramics. As pointed out earlier, grain boundaries can also provide pinning points for domain walls[27, 80, 96].

Thus, it is important to assess the relative influence of these factors on domain wall mobility. For this purpose, the dielectric properties of X7R $BaTiO_3$ based ceramics as well as undoped $BaTiO_3$ ceramics with different concentrations of oxygen vacancies were compared. Of particular interest were measurements where the microstructure could be held constant, in order to enable separation of the relative influence of oxygen vacancies and core-shell structures on domain wall motion.

6.2 Experimental Procedure

Formulated $BaTiO_3$-based powder (EV540N, Ferro Electronic Materials Systems), which includes common dopants such as Y_2O_3, MnO_2, CaO, and SiO_2 and fulfills X7R specifications and provides high reliability for base metal electrode dielectrics, was combined with 5 wt% polypropylene carbonate binder (QPAC 40, Empower Materials) and mixed with acetone using a mortar and pestle. The mixture was dried and then crushed. Pellets were loosely pressed under uniaxial pressure in a 6 mm diameter die and cold isostatic pressed at 200 MPa. For binder burnout, the samples were heated at 25˚C/h to 400˚C and held for 1 h.

For undoped samples, the compact was prepared using a tape casting method by Dr. Michael Ugorek (Penn State). $BaTiO_3$ power (Sakai Chemical, BT-02) was initially sieved to 90 μm (170 mesh) to remove large agglomerates. The powder was then mixed with ethanol and xylene in a 50/50 ratio with 3.5 wt% blown menhaden fish oil and ball milled for 24 h. Afterwards, 2.8 wt% polyvinyl butyral, 1.3 wt% of polyethylene glycol and butylbenzyl phthalate each were added to the suspension and ball milled for an additional 24 h. The slurry was then de-aired and a few drops of cyclohexanone were added prior to tape casting to prevent skin formation. Tapes were cast at a 200 μm doctor blade height and a speed of 30 cm/min. The dried tape was cut into 10 cm^2 samples, stacked and uniaxially laminated at 70˚C for 5-10 min and then

isostatically laminated at 70˚C and 20 MPa for up to 30 min. The samples were heated at 650˚C for 2 h in air to remove the organics and isostatically pressed to 175 MPa prior to sintering.

Both types of compacts were then sintered in a reducing furnace with a gas control system. The oxygen partial pressure was controlled using the flow rates of dry N_2, wet N_2, and 0.1%H_2-99.9%N_2 gases, and was measured using a zirconia oxygen sensor. The sintering was done at 1300˚C for 2 h with a heating rate of 2000˚C/h.* At 1300˚C, the pO_2 was maintained at 10^{-2} (air), 10^{-6}, 10^{-9}, and 10^{-11} or 10^{-12} atm. Another compact was also sintered in oxygen (1 atm pO_2) in a tube furnace. The sintering was done at 1300˚C for 2 h with a heating rate of 180˚C/h. Density measurements were made using the immersion method. The densities of all sintered pellets were more than 98% of the theoretical density of $BaTiO_3$. Samples for dielectric characterization were sawed out and then polished to ~1/2 mm in thickness with SiC powders.

Structural characterization was performed by X-ray diffraction (XRD) (Scintag Pad V, Thermo Scientific) with Cu-Kα radiation. XRD patterns showed only $BaTiO_3$ and no secondary phases for all pO_2 conditions (Fig. 6-1). Grain sizes were measured using scanning electron microscopy (SEM). For this, the samples were polished with SiC powders, diamond slurries, and/or colloidal silica and then thermally etched at 1000˚C for 30 min in the same gas flow condition as used for sintering or chemically etched in a 95:4:1mixture of water, HCl, and HF. Microstructures of the samples are shown in Figs. 6-2 and 6-4. The average grain sizes are summarized in Figs. 6-6 and 6-7 and Table 6-1; they were about 0.45 μm for formulated samples and 1.29 μm for undoped samples. No significant difference in the grain size was observed due to the pO_2 during firing. It was reported that the average grain size of $BaTiO_3$ ceramics decreased with lower pO_2[103-105]. The difference between this work and those previous reports may stem from differences in the details of the processing such as Ba:Ti ratio[103], sintering temperature[104],

* The furnace was originally intended to study the effects of a heating rate on the properties of ceramics, so samples could be heated at a high rate.

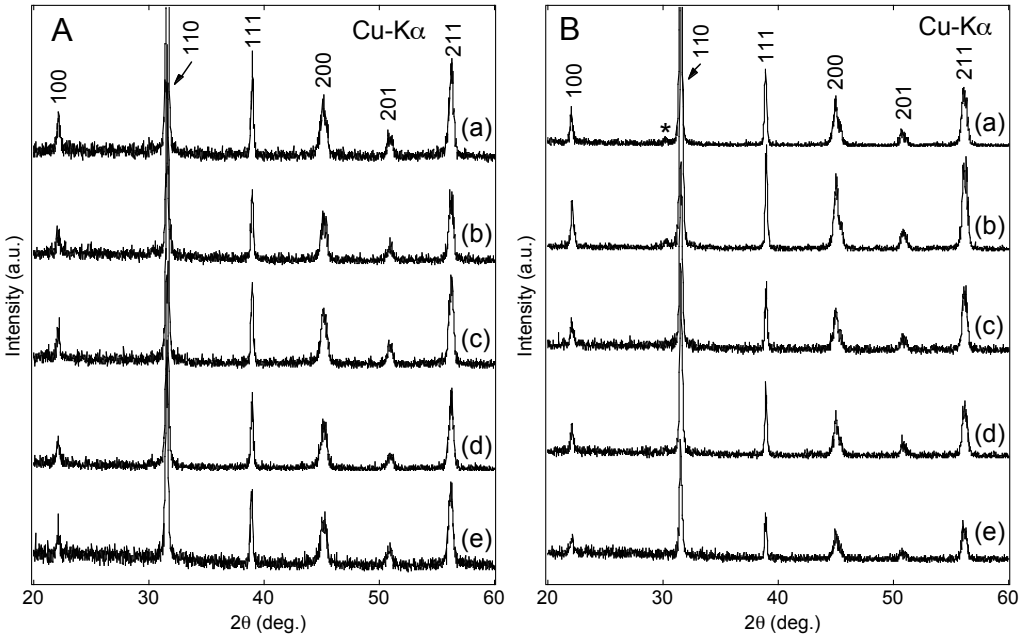

Figure **6-1**: XRD patterns of **A** the formulated and **B** undoped $BaTiO_3$ ceramics sintered at (a) 1 atm pO_2 (b) 10^{-2} atm pO_2 (c) 10^{-6} atm pO_2 (d) 10^{-9} atm pO_2, and (e) 10^{-12} atm pO_2 for the formulated /10^{-11} atm for the undoped. An asterisk indicates W contamination of X-ray tube. The samples are indexed based on a pseudocubic cell.

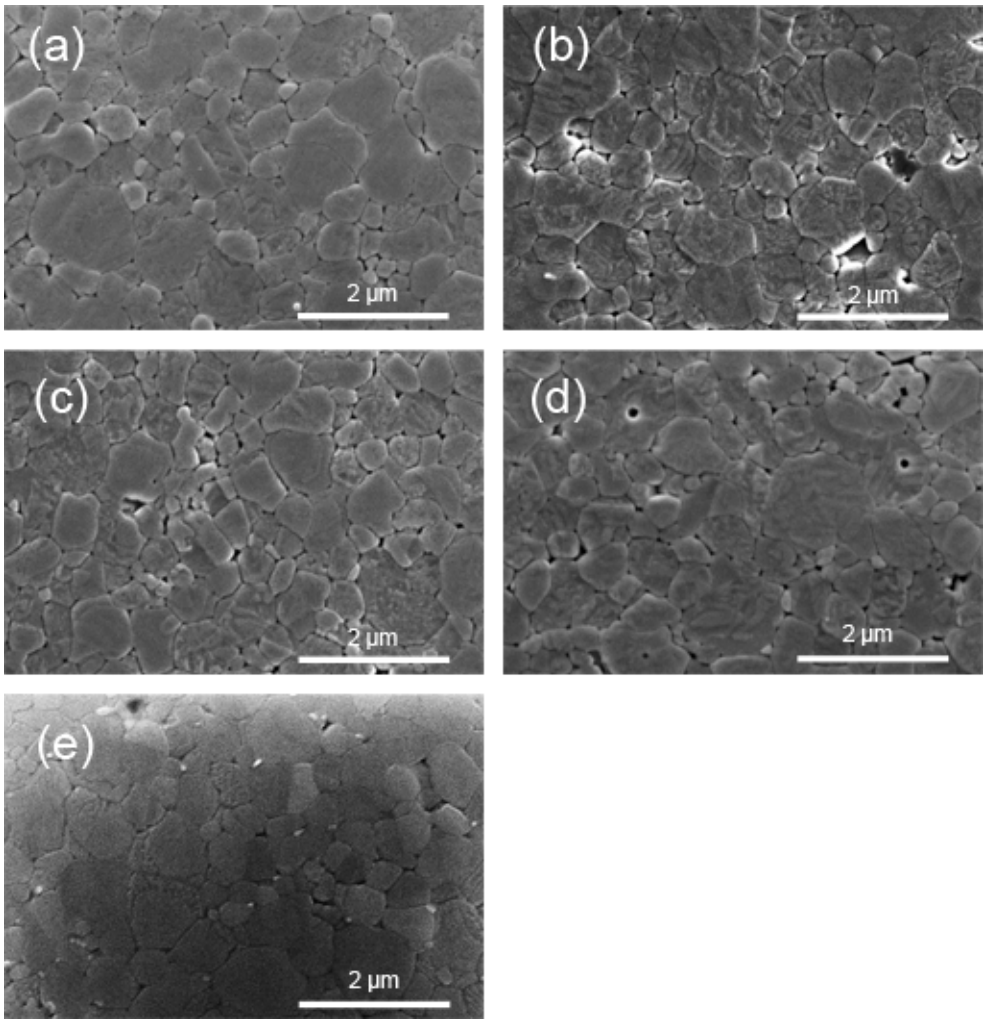

Figure **6-2**: SEM images of the formulated $BaTiO_3$ ceramics sintered at (a) 1 atm pO_2 (b) 10^{-2} atm pO_2 (c) 10^{-6} atm pO_2 (d) 10^{-9} atm pO_2, and (f) 10^{-12} atm pO_2.

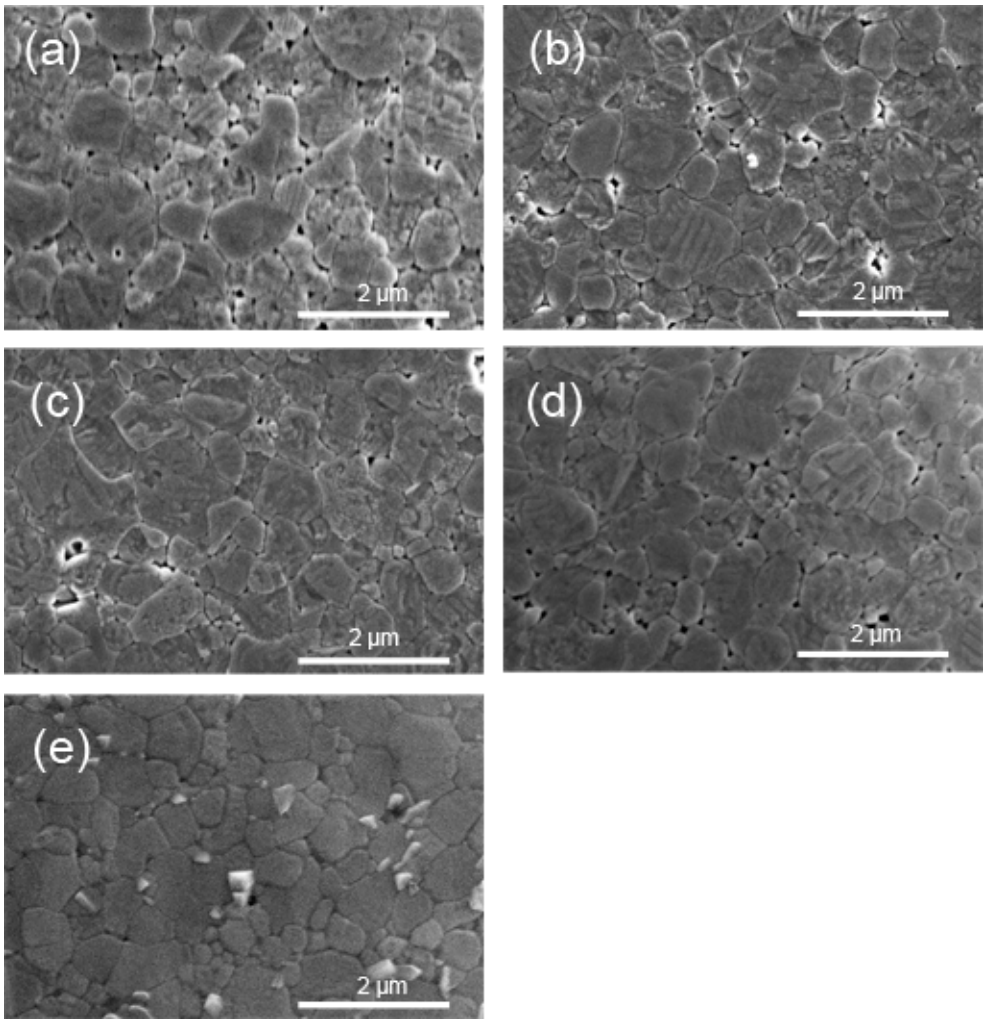

Figure **6-3**: SEM images of the formulated $BaTiO_3$ ceramics initially sintered at (a) 1 atm pO_2 (b) 10^{-2} atm pO_2 (c) 10^{-6} atm pO_2 (d) 10^{-9} atm pO_2, and (f) 10^{-12} atm pO_2, followed by annealing in air.

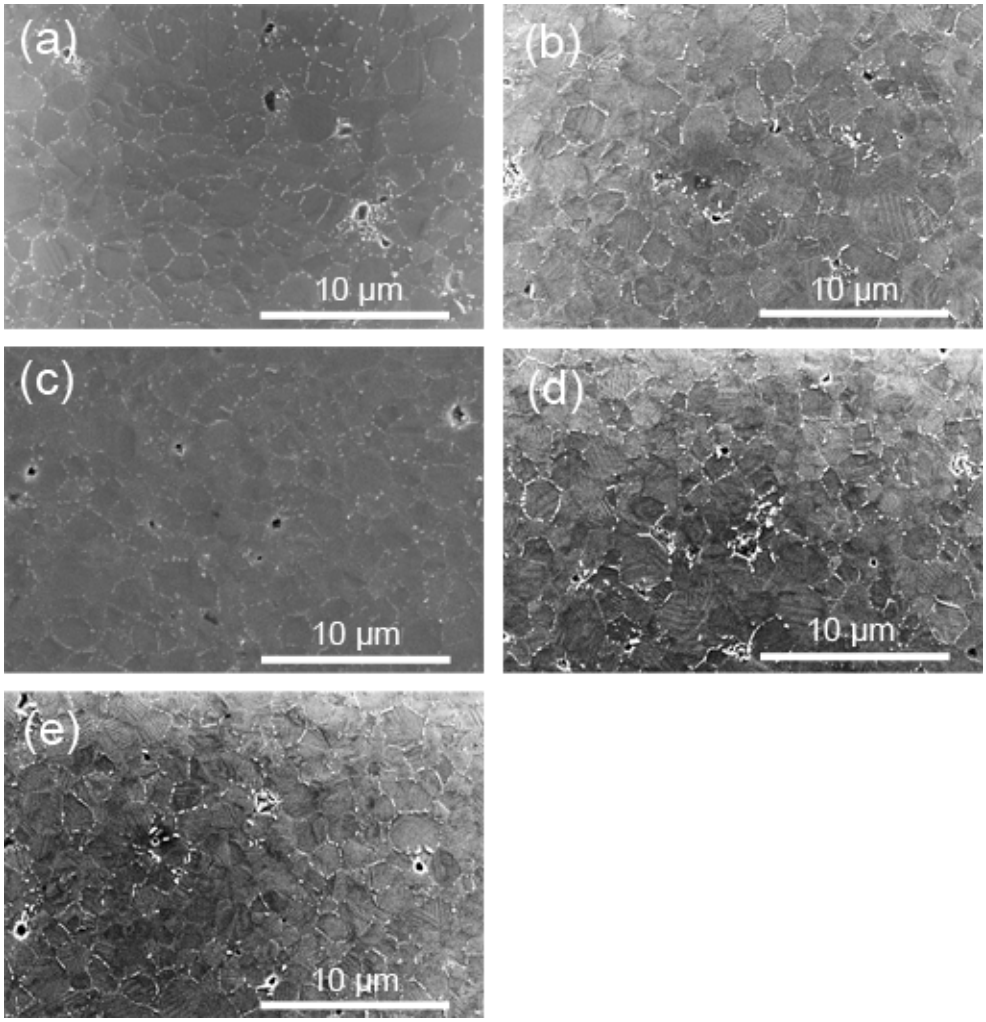

Figure **6-4**: SEM images of the undoped $BaTiO_3$ ceramics initially sintered at (a) 1 atm pO_2 (b) 10^{-2} atm pO_2 (c) 10^{-6} atm pO_2 (d) 10^{-9} atm pO_2, and (f) 10^{-11} atm pO_2. White particles on samples surface are residual colloidal silica.

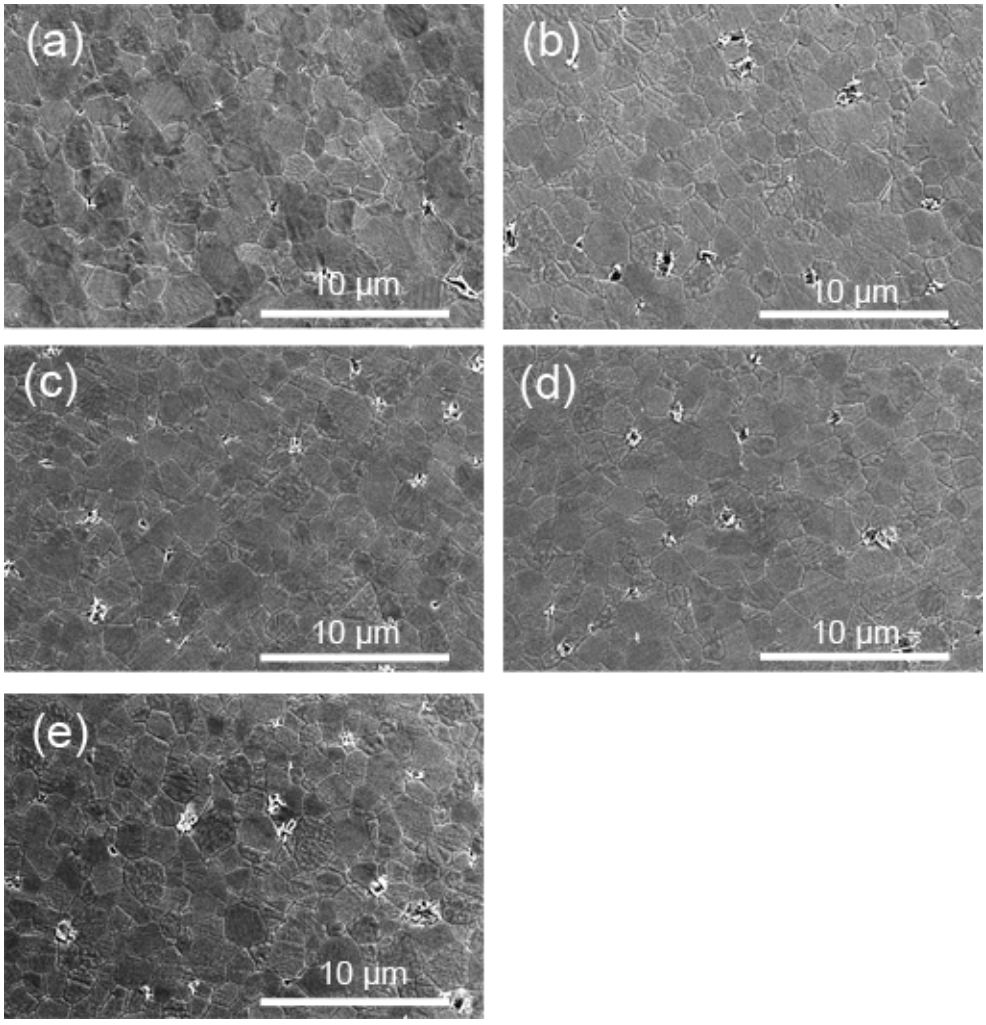

Figure **6-5**: SEM images of the undoped $BaTiO_3$ ceramics initially sintered at (a) 1 atm pO_2 (b) 10^{-2} atm pO_2 (c) 10^{-6} atm pO_2 (d) 10^{-9} atm pO_2, and (f) 10^{-11} atm pO_2, followed by annealing in air. White particles on samples surface are residual colloidal silica.

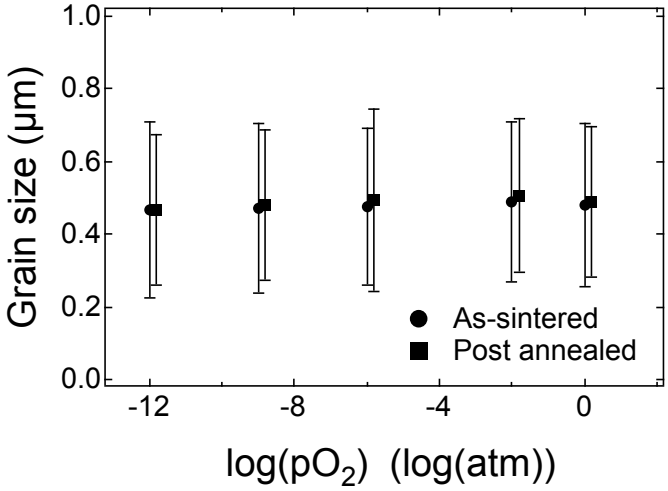

Figure **6-6**: Grain size of the formulated $BaTiO_3$ ceramics.

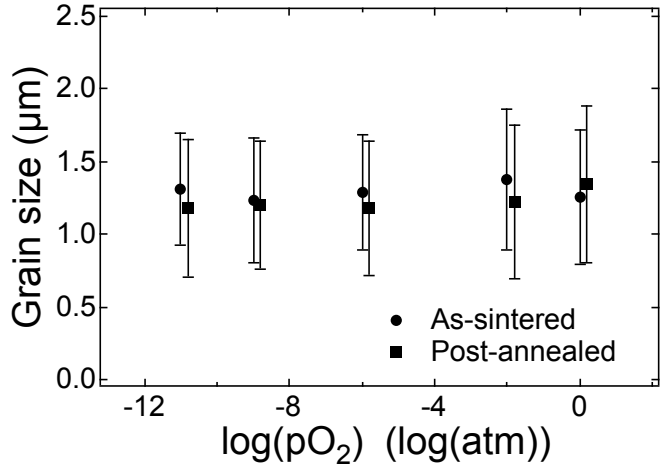

Figure **6-7**: Grain size of the undoped $BaTiO_3$ ceramics.

and grain size distribution[105]. The microstructure of the formulated $BaTiO_3$ ceramics was studied with a transmission electron microscope (TEM) (EM420T, Phillips). For electrical characterization, the samples were electroded with 100 nm of sputtered Au (SCD 050, BAL-TEC).

The capacitance and tanδ were measured using a lock-in amplifier (SR830, Stanford Research), a voltage amplifier (BOP 1000M, KEPCO), and a charge converter. The capacitance was defined as the fundamental of the charge over the ac voltage amplitude and the tanδ was determined from the phase shift of the fundamental of the charge compared to the applied ac voltage. AC voltages up to about the coercive voltage (which was determined in advance by polarization-electric field loops) were utilized. The loops were measured using a homemade polarization measurement system with voltage amplifiers (BOP 1000M, KEPCO and TREK 609C-6, Trek). The frequency and temperature dependence of the weak field dielectric properties was measured using a LCR meter (4284A, Agilent). The temperature was controlled by a furnace (DELTA 9023, Delta Design).

After electrical characterization, the electrodes were polished off. The samples were then annealed in air at 1000˚C for 9.5 h using a furnace to change the oxygen content without significantly changing the grain size. The heating rate was 730˚C/h. No significant grain growth was observed due to the annealing (See Figs. 6-3, 5, 6, and 7, and Table 6-1). Then, the electrical

Table **6-1**: Grain sizes (in microns) of the formulated and undoped $BaTiO_3$ ceramics.

pO_2 (atm)	Formulated $BaTiO_3$		Undoped $BaTiO_3$	
	As-sintered	Post-annealed	As-sintered	Post-annealed
1	0.48±0.22	0.49±0.21	1.25±0.46	1.35±0.54
10^{-2}	0.49±0.22	0.51±0.21	1.37±0.48	1.22±0.52
10^{-6}	0.48±0.22	0.49±0.25	1.29±0.39	1.18±0.46
10^{-9}	0.47±0.24	0.48±0.21	1.24±0.43	1.20±0.44
$10^{-12}/10^{-11}$	0.47±0.24	0.47±0.21	1.31±0.39	1.18±0.47

characterization and grain size measurements were performed in the same way. A selected sample was re-annealed in a reducing atmosphere and re-measured.

6.3 Results and Discussion

6.3.1 Formulated $BaTiO_3$ Ceramics

The temperature dependence of the dielectric properties of the formulated $BaTiO_3$ ceramics is shown in Fig. 6-8(a). Since large dielectric loss was observed for the sample sintered at 10^{-12} atm pO_2 in the as-sintered state, the dielectric data for that sample are not shown. For the other as-sintered parts, it was observed that the temperature profile was pO_2 dependent; in particular, the signature of a phase transition around 30˚C for air- and oxygen-fired samples was smaller than samples sintered at lower pO_2. That peak is associated with the dielectric response from the shell region[27, 106-108] as well as the tetragonal to orthorhombic phase transition of $BaTiO_3$. In addition, at temperatures between the low temperature peak and the cubic – tetragonal phase transition at ~130˚C, the dielectric constant of air- and oxygen-fired samples increased with heating, while that of samples sintered at reducing atmospheres decreased. In particular, a peak around 90˚C for oxygen-fired samples was observed along with a larger dielectric constant at the cubic – tetragonal phase transition.

When samples originally sintered at the various pO_2 (= 1, 10^{-2}, 10^{-6}, 10^{-9}, and 10^{-12} atm) were post-annealed in air at 1000°C, the dielectric peak near room temperature decreased, the dielectric peak at the cubic – tetragonal phase transition increased, and the temperature dependence of the permittivity became comparable to parts originally fired at higher pO_2 values, as shown in Fig. 6-8(b). The exception is samples originally fired in oxygen, for which larger dielectric constants were observed. From these results, it is concluded that the peak associated

with the diffuse phase transition of the shell region shifted to a higher temperature with increasing pO_2 during the heat treatments.

This was further confirmed by re-reducing a sample. The sample initially sintered at 10^{-9} atm pO_2 and then post-annealed in air was annealed at 10^{-8} atm pO_2 at 1000˚C for 10 h. The temperature dependence is shown in Fig. 6-8 (c). It was found that on re-reduction, the temperature dependence returned to that of the as-sintered state, except that a larger dielectric constant at the cubic – tetragonal phase transition was obtained. The principal changes that are anticipated to occur on the oxidation and re-reduction steps are changes in the oxygen content of the samples, since the temperatures are well below sintering temperatures.

Such shifts in the dielectric response of the shell have previously been reported for $BaTiO_3$ based ceramics[107-110]. There are two reported explanations for the shift. One explanation hinges on the fact that the oxidation state of Mn and Cr will change with the oxygen partial pressure during the annealing,[109, 110] which leads to changes in the oxygen vacancy concentration. Since the valence-dependent ionic radius of the dopant and the oxygen vacancy concentration change the tetragonality, the phase transition temperatures also changes (See Fig. 6-9).[110] The other explanation for this behavior is that the relative volume fraction of the core and shell regions may depend on the pO_2 during firing. A careful study revealed secondary phases that have high dopant concentrations at triple-points (and consequently a lowered dopant concentration in the shell region) for dielectrics sintered at a lower pO_2.[107] They deduced that a decrease in the shell regions leads to a change in the dopant distribution and core/shell ratio, and hence the temperature dependence of the permittivity[107].

Figure 6-10 shows TEM images of the samples sintered at 10^{-2} and 10^{-6} atm pO_2. Core/shell grains having lamellar domain patterns (core) surrounded by a region without the pattern (shell), were observed for both samples. In addition, grains which were fully ferroelectric, i.e. which don't have a shell region, were observed. Note that the z-axis of the TEM stage was

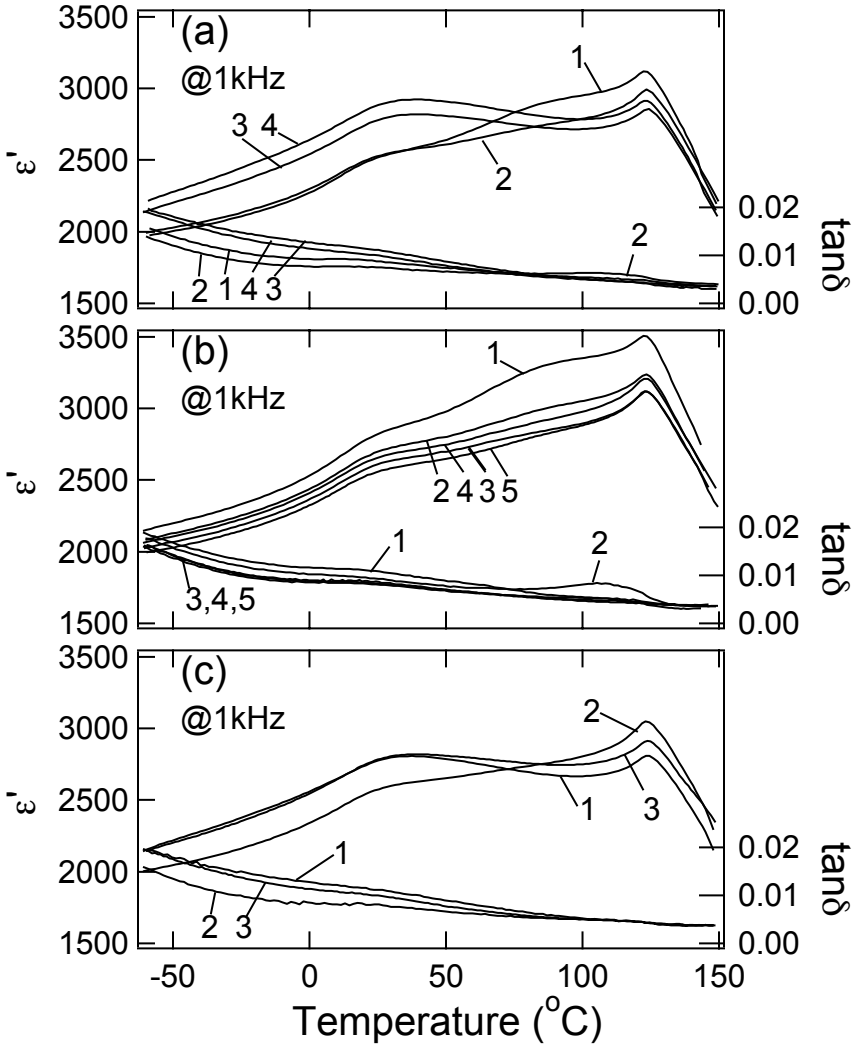

Figure **6-8**: The temperature dependence of the dielectric properties for the formulated ceramics sintered at different pO_2 (a) as-sintered, and then (b) post-annealed in air. The legends indicate the pO_2; 1: 1, 2: 10^{-2}, 3: 10^{-6}, 4: 10^{-9}, and 5: 10^{-12} atm. (c) That of the sample initially sintered at 10^{-9} atm pO_2 (1), re-oxidized in air (2), and re-reduced at 10^{-8} atm pO_2 (3).

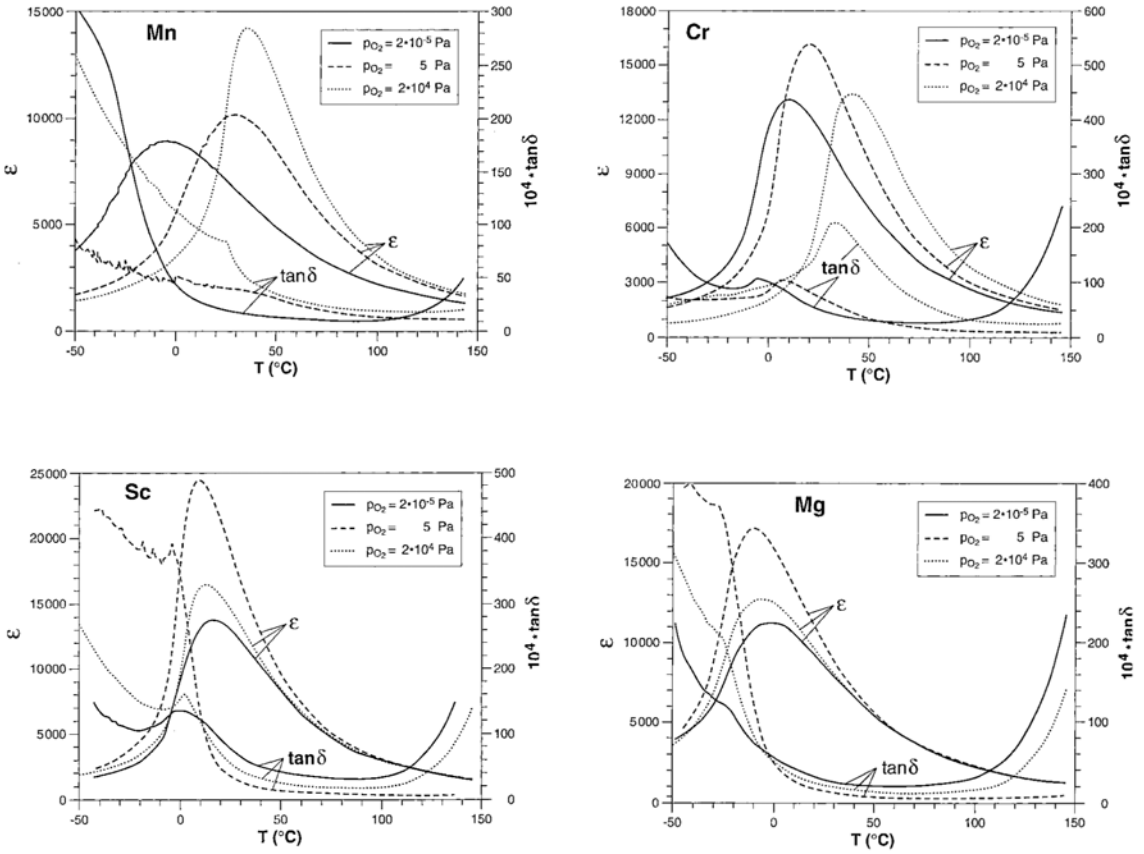

Figure **6-9**: Temperature dependence of the dielectric constant ε and loss tan δ for $(Ba_{0.96}Ca_{0.04})(Ti_{0.815-x}Zr_{0.18}A_x)_{0.995}\ O_{3-\delta}$ (A=Mn, Cr, Sc, or Mg). The samples were sintered at $2x10^{-5}$ Pa, and then annealed at 5 Pa or $2x10^{4}$ Pa.[110]

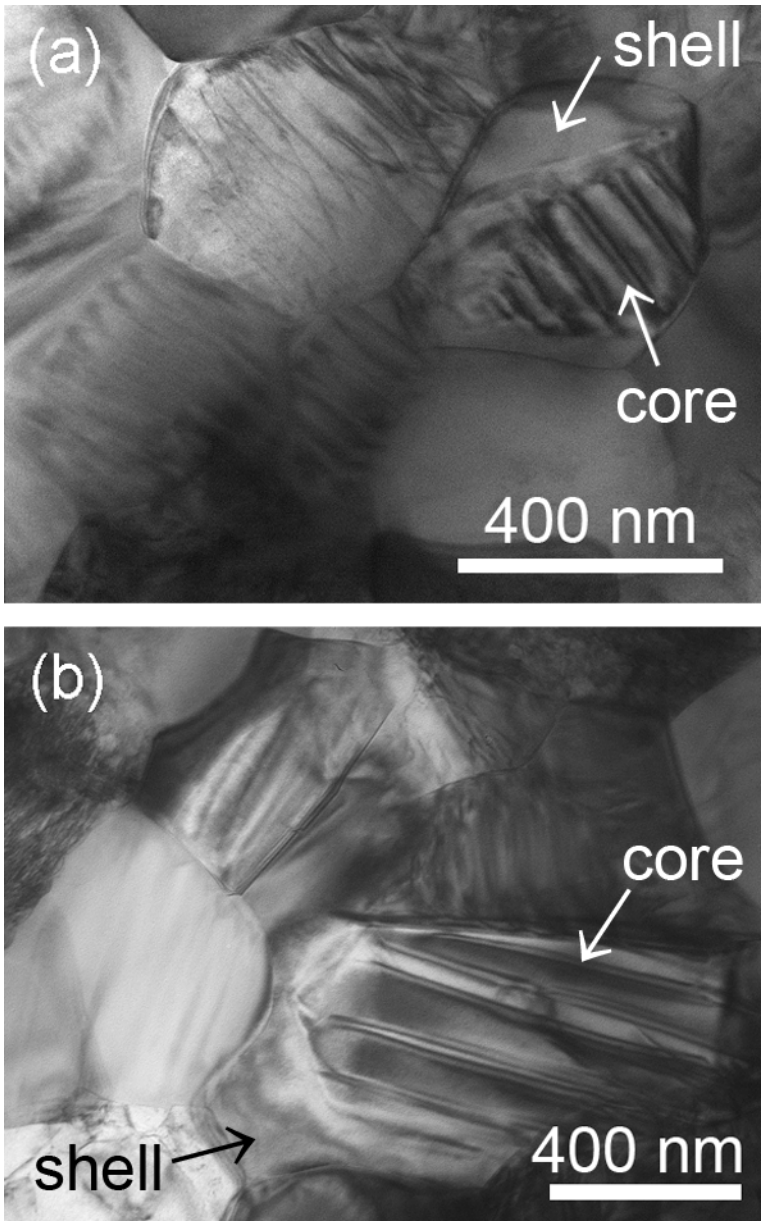

Figure **6-10**: TEM images of the formulated $BaTiO_3$ ceramics sintered at (a) 10^{-2} atm pO_2 and (b) 10^{-6} atm pO_2.

tilted in order to see the domain structures of the randomly oriented grains. Therefore, grains apparently without domain patterns in the figure are not necessarily shell grains. The shell region was confirmed by the absence of a domain pattern during the tilting. Similar microstructures with core/shell and core grains were observed for both samples, although it was difficult to statistically quantify the core/shell ratio. Given the lack of a large difference in core/shell ratio on oxidation, the valence change of the manganese in the shell, along with the associated oxygen vacancy concentration is likely to account for the dielectric peak shift.

It should be noted that there are also likely to be defect dipoles associated with defects such as $Ca_{Ti}'' - V_O^{\bullet\bullet}$, which may influence domain wall mobility. However, the concentration of these defects would not be expected to change substantially at temperatures much below sintering temperatures. The influence of such defect dipoles would be more readily studied via the evolution of the FORC distribution during highly accelerated lifetime testing.

The room temperature ac field dependence of the dielectric properties of the as-sintered samples is shown in Fig. 6-11(a) and (b). The dielectric constant of samples sintered in reducing atmospheres increased sublinearly, while that of the samples sintered in oxygen or air showed a nearly linear increase (Fig. 6-11 (a)). By “sublinear”, it is meant that the permittivity vs. ac field response curves down with increasing field amplitude. The smaller dielectric constant of the samples sintered in oxidizing atmosphere at small ac electric fields is a consequence of the higher temperature for the permittivity peak of the shell. The dielectric loss also increased with the ac field amplitude as shown in Fig. 6-11(b). Again, samples sintered in reducing atmospheres showed a sublinear increase in the dielectric loss, whereas the oxygen- and air-fired samples showed a linear increase. In contrast, the ac field dependence after post-annealing showed an approximately linear dielectric response for all the samples, as shown in Figs. 6-3(c) and (d).

Note that the nonlinearity is also a function of temperature, so the linear ac field dependence of the dielectric constant of the air- and oxygen-fired samples does not hold at other temperatures.

For samples with an approximately linear increase in the permittivity with ac field, Eq. 1-1 (the Rayleigh Law) was used to quantify the response. The resulting Rayleigh coefficients are shown in Fig. 6-12. It was found that both ε_{init}' and α' of the oxygen- and air-fired samples increased after the annealing. It is believed that this may be due to either a decrease in oxygen vacancy concentration or a very limited amount of grain growth. The post-annealing step also increased the ratio of $\alpha'/\varepsilon_{init}'$, largely because of the increase in α'. No clear pO_2 dependence of the reversible contribution was observed. The increase in the irreversible response corresponds to an increase in the concentration or mobility of domain walls as a result of annealing the samples in a higher oxygen partial pressure. It is intriguing that the pO_2 used during the sintering of $BaTiO_3$ - based ceramics influenced the high field dielectric response even after a post-sintering annealing.

The reason for the observed variations in the ac field dependence of the permittivity could be either the different oxygen vacancy concentrations in the core (almost undoped $BaTiO_3$) or shell regions ($BaTiO_3$ plus additives). To clarify which is responsible, model experiments were conducted on undoped $BaTiO_3$ ceramics sintered at various pO_2. After dielectric characterization, samples were post-annealed as described above, and re-measured.

6.3.2 Undoped $BaTiO_3$ Ceramics

Figure 6-13 shows the temperature dependence of the dielectric properties of the undoped $BaTiO_3$ ceramics sintered at various pO_2 for (a) as-sintered and (b) post-annealed ceramics. Since the sample sintered at 10^{-11} atm pO_2 showed high dielectric loss in the as-sintered condition, it is not on the figure. Larger dielectric constants were observed for the undoped samples compared to

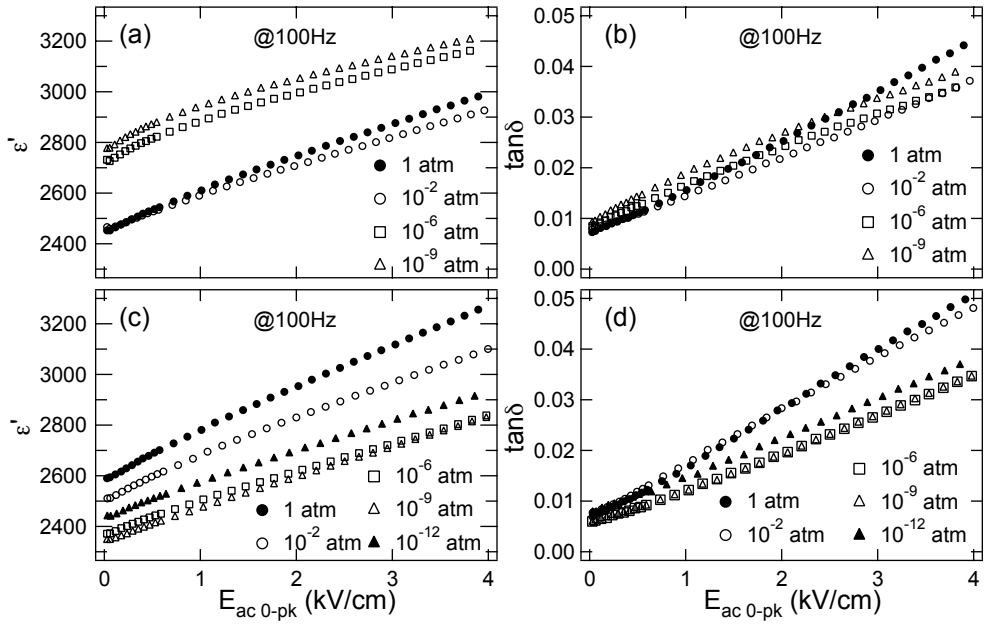

Figure **6-11**: The ac field dependence of the dielectric properties for the formulated ceramics sintered at different pO_2 (a, b) as-sintered, and (c, d) post-annealed in air.

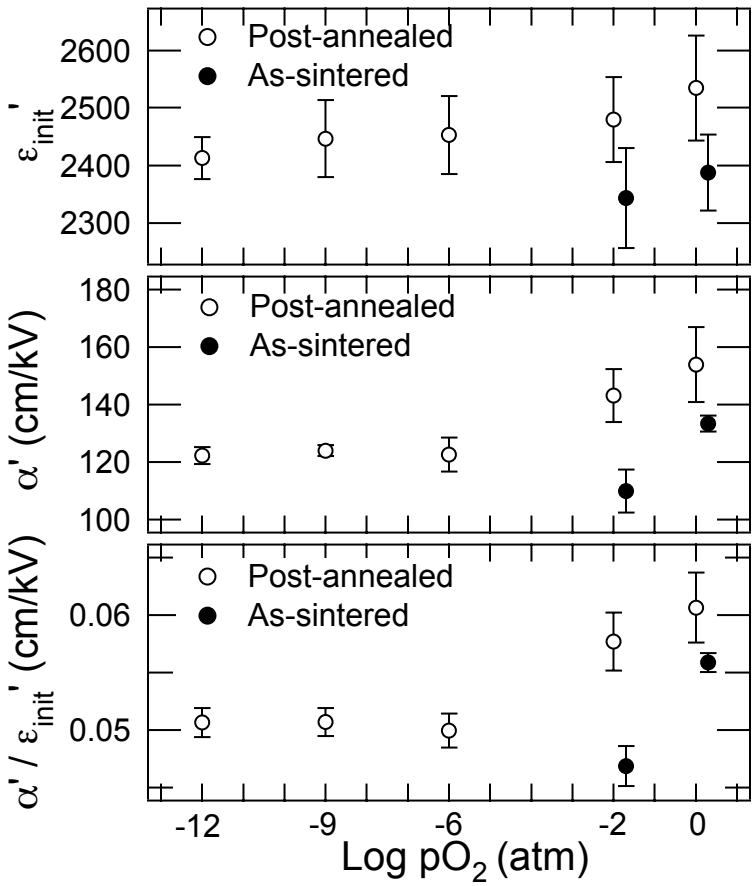

Figure **6-12**: The Rayleigh coefficients of the formulated $BaTiO_3$ ceramics as a function of the oxygen partial pressure used in the original sintering step, before and after post-annealing in air.

the formulated ceramics, which is attributable, at least in part, to the larger grain size (1.29 μm compared to 0.45 μm for formulated ceramics). As expected, no core-shell behavior was observed for any pO_2 conditions. In fact, almost the same profile for the dielectric constant was observed. On the other hand, the dielectric loss was pO_2 dependent. A broad peak in the dielectric loss was observed for non air-fired samples at temperatures between the cubic-tetragonal and tetragonal-orthorhombic phase transition temperatures. The loss peak was suppressed after post-annealing in air.

The unexpected loss peak was studied in detail. The frequency dependence of the dielectric properties of the as-sintered undoped $BaTiO_3$ ceramics is shown in Fig. 6-14(a) and (b). A clear relaxation peak was observed in the dielectric loss tangent profile for the as-sintered samples, which was not observed for the formulated $BaTiO_3$ ceramics (not shown). After post-annealing, the dielectric loss was reduced and the relaxation peak disappeared (Fig. 6-14(d)). This result suggests that the relaxation peak can be attributed to the oxygen vacancies. Note that the relaxation peak was observed even in as-sintered oxygen- and air-fired samples; in this case, the oxygen vacancies might be caused by native Schottky (or partial Schottky) defects formed at the sintering temperature. The temperature evolution of the frequency dependence of the loss tangent peak for the as-sintered samples is shown in Fig. 6-15. It was found that the peak frequency increased with temperature, suggesting that the relaxation was thermally activated. A linear relationship was observed between the peak relaxation frequency and inverse temperature (Fig. 6-15); the activation energy for the relaxation was calculated using an Arrhenius equation:

$$f = f_0 \exp\left(-\frac{E_a}{kT}\right) \qquad \text{Eq. 6-1}$$

Here, f is the peak relaxation frequency, f_0 is the characteristic relaxation frequency, E_a is the activation energy, k is Boltzmann's constant, and T is absolute temperature. The activation

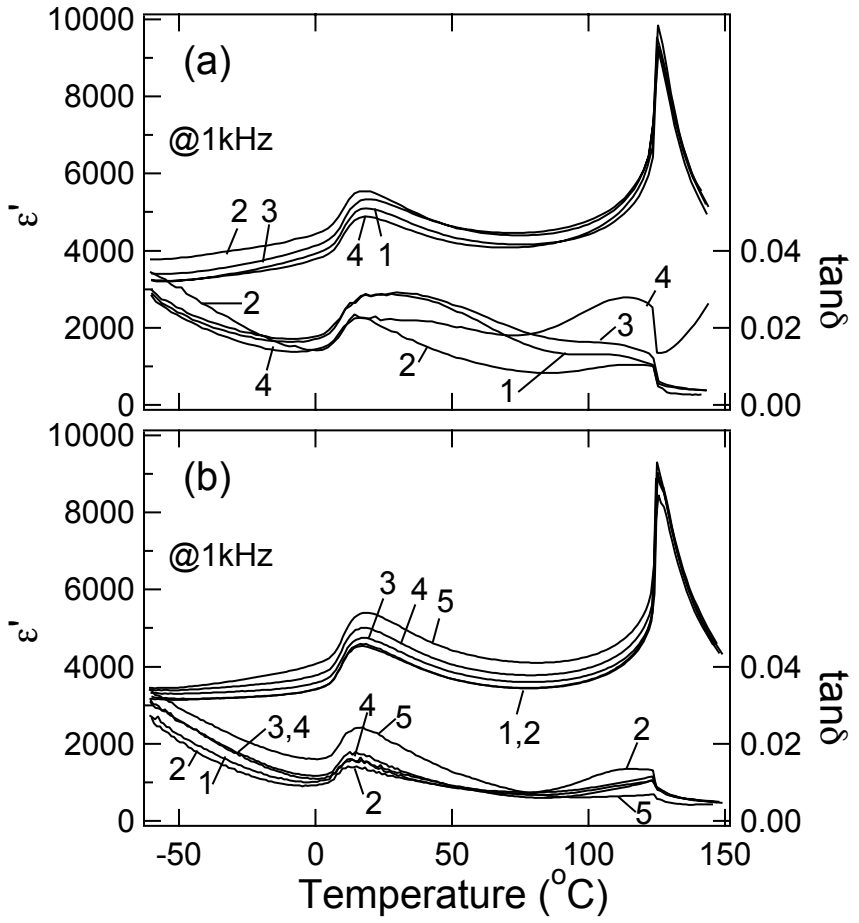

Figure **6-13**: The temperature dependence of the dielectric properties for the undoped $BaTiO_3$ ceramics sintered at different pO_2 (a) as-sintered, and (b) post-annealed in air. The legends indicate the pO_2; 1: 1, 2: 10^{-2}, 3: 10^{-6}, 4: 10^{-9}, and 5: 10^{-11} atm.

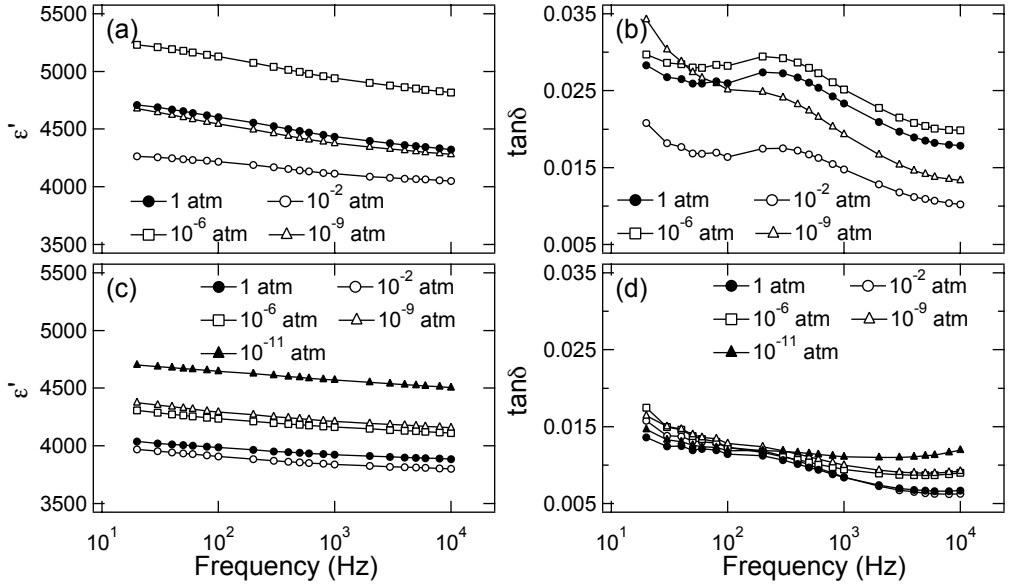

Figure **6-14**: The frequency dependence of the dielectric properties of the undoped $BaTiO_3$ ceramics sintered at different pO_2 (a, b) as-sintered, and (c, d) post-annealed in air.

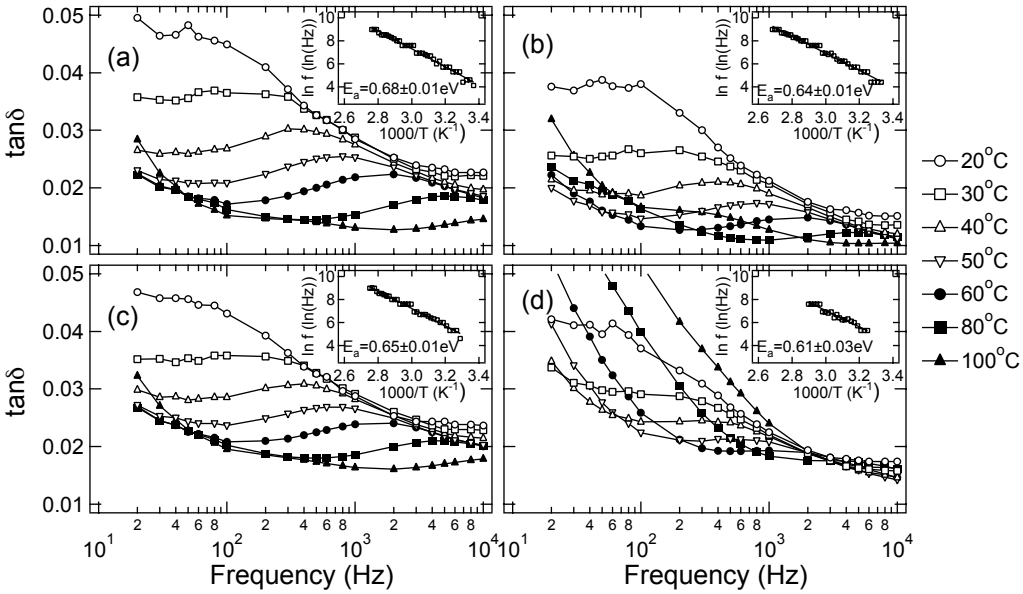

Figure **6-15**: The effect of the temperature on the frequency dependence of the dielectric loss for the undoped $BaTiO_3$ ceramics sintered at (a) 1 atm pO_2, (b) 10^{-2} atm pO_2, (c) 10^{-6} atm pO_2, and (d) 10^{-9} atm pO_2. The inset indicates peak relaxation frequency as a function of inverse absolute temperature. The line is a linear fit.

Table **6-2**: Activation energy, temperature range, proposed mechanism, and experimental method for dielectric relaxation of perovskites.

Sample	Activation energy (eV)	Temperature range (˚C)	Proposed mechanism	Method	Ref
$BaTiO_3$ ceramics (this work)	0.61 ~ 0.68	20 ~ 110	Defect dipole reorientation	Dielectric loss peak	-
$BaTiO_3$ ceramics	1.2	400 ~ 700	-	Debye fit	111
$BaTiO_3$ single crystal	1.0	400 ~ 700	-		
$BaTiO_3$ single crystal	1.56	< 527	Space charge	Debye fit	112
	0.6	> 527	Charge injection		
$BaTiO_3$ ceramics	0.29	-120 ~ -90	Domain wall motion controlled by oxygen vacancies	Dielectric loss peak	91
	0.47	-40 ~ 110			
$BaTiO_3$ ceramics	0.91	24 ~ 110	Defect dipole reorientation	Electron paramagnetic resonance	113
$BaTiO_3$	0.62	-	Defect model	Simulation	114
$BaTi_{1-x}Mg_xO_3$ (x=0.0005-0.01) ceramics	0.46 ~ 0.53	150 ~ 300	Defect dipole reorientation	Dielectric loss peak	115
	1.08 ~ 1.12	350 ~ 450	Oxygen vacancy motion		
$BaTi_{0.995-y}Mg_{0.005}Mn_yO_3$ (y=0.005, 0.01) ceramics	0.69 ± 0.01, 0.62 ± 0.04	150 ~ 300	Defect dipole reorientation	Dielectric loss peak	116
	1.28 ± 0.04, 1.47 ± 0.09	400 ~ 500	Oxygen vacancy migration		
$Pb_{1-x}La_xTiO_3$ (x=0.2-0.40) ceramics (as-sintered in air)	1.17 ~ 1.48	500 ~ 800	Oxygen vacancy migration	Debye fit	112
$Pb_{0.65}La_{0.35}TiO_3$ ceramics (as-sintered in air)	1.48				
$Pb_{0.65}La_{0.35}TiO_3$ ceramics (annealed at reduced ambient)	1.20				
$Sr_{1-1.5x}Bi_xTiO_3$ (x=0.0133-0.08) ceramics	0.31 ~ 0.49	-143 ~ 107	Coupled effect of conduction electrons with motion of off-center Bi and Ti ions	Debye fit	92
$Sr_{1-1.5x}Bi_xTiO_3$ (x=0.0267-0.10) ceramics	0.74 ~ 0.86	77 ~ 377	Motion of defect dipole		
$Sr_{0.9201}Bi_{0.0533}TiO_3$ ceramics (as-sintered in air)	0.82				
$Sr_{0.9201}Bi_{0.0533}TiO_3$ ceramics (annealed in O_2)	0.76				
$Sr_{0.9201}Bi_{0.0533}TiO_3$ ceramics (annealed in N_2)	0.64				
$Sr_{1-1.5x}Bi_xTiO_3$ (x=0.0133-0.133) ceramics	0.99 ~ 1.12	227 ~ 527	Short-range motion of oxygen vacancies		
Fe doped $SrTiO_3$ single crystal	0.76 ± 0.05	90	Defect dipole reorientation	Thermally stimulated depolarization current	117
	0.91 ± 0.05	200	Oxygen vacancy migration		

energies for the samples sintered at 1, 10^{-2}, 10^{-6}, and 10^{-9} atm pO_2 are 0.68±0.01, 0.64±0.01, 0.65±0.01, and 0.61±0.03 eV, respectively.

Such a dielectric relaxation could, in principle, be attributed to either space charge or defect dipoles. In Fig. 6-15, there is little evidence for large increases in the dielectric loss at higher temperatures (which would be characteristic of space charge), except for the sample sintered at 10^{-9} atm pO_2. Therefore a pure space charge origin of the loss peak is unlikely. Dielectric relaxations associated with oxygen vacancies reported in perovskites such as $CaTiO_3$,[112] doped and undoped $BaTiO_3$,[91, 111-113, 115, 116] doped $SrTiO_3$,[92, 117] and doped $PbTiO_3$,[112] are summarized in Table 6-2. The activation energy has been reported to be influenced by the measurement temperature range, grain boundaries[111], dopant concentration[92, 112, 115, 116], and oxygen vacancy concentration[92, 112]. There are largely two types of dielectric relaxation mechanisms proposed: space charge or long-range migration of oxygen vacancies, and reorientation of oxygen vacancies in defect associates. The first mechanism applies at higher temperature and is characterized by an activation energy ranging from 0.91 to 1.56 eV, while the second mechanism applies at lower temperatures with a reported activation energy from 0.46 to 0.91 eV. The activation energies found in this study fall in the range of those characteristic of defect dipole reorientation. Moreover, the theoretical diffusion activation energy of the oxygen vacancies is 0.62 eV.[114] These support the hypothesis that the dielectric relaxation is caused by reorientation of the defect – oxygen vacancy dipoles.

The ac field dependence of the dielectric properties for the undoped $BaTiO_3$ ceramics sintered at various pO_2 is shown in Fig. 6-16. A larger ac field dependence of the dielectric constant was observed for the as-sintered undoped ceramics, compared with the formulated ceramics. This is attributed to the lower dopant concentration and larger grain size. Significant curvature was observed in the ac field dependence of the permittivity for all pO_2 conditions. The

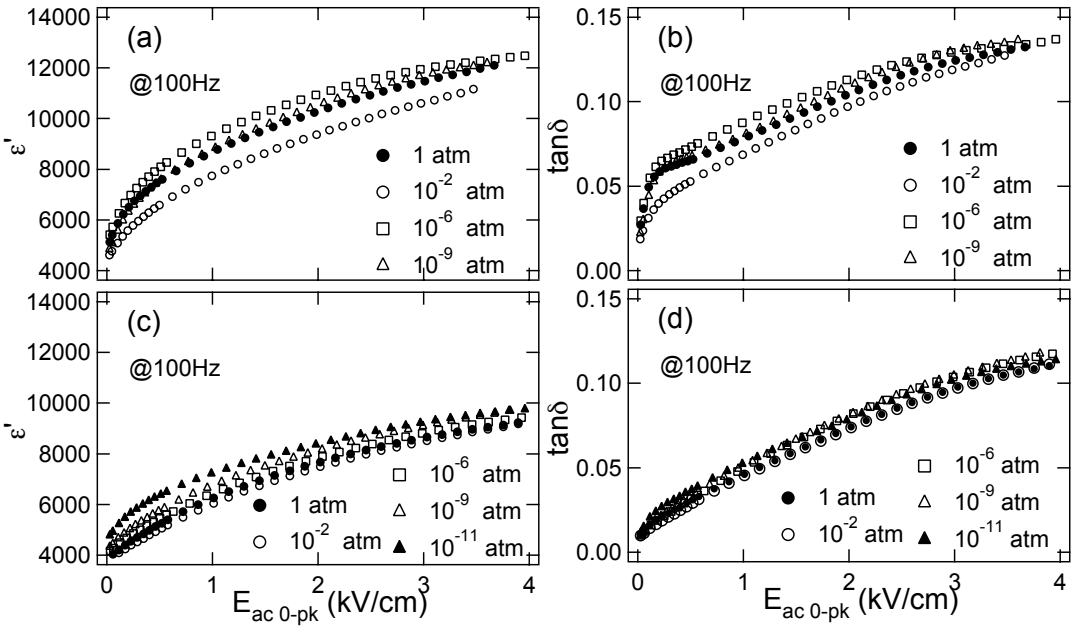

Figure **6-16**: The ac field dependence of the dielectric properties of the undoped $BaTiO_3$ ceramics sintered at different pO_2 (a, b) as-sintered, and (c, d) post-annealed in air.

curvature depends on the pO_2; the dielectric constant increased more slowly for the air-fired sample than for other pO_2 conditions. In particular, at small ac field amplitudes, a faster increase in the dielectric loss with increasing drive levels was observed. After post-annealing, the rapid initial increase in the dielectric properties as a function of the ac excitation field disappeared and the dielectric profiles became similar to those of air-fired samples. From this result, it is believed that the stronger initial field dependence of the dielectric properties for the as-sintered samples may be associated with defect dipoles. When the dielectric properties were measured above the Curie temperature, they were independent of the ac field. This indicates that the origin of the field dependence of the dielectric response is due to domain wall contributions. A possible explanation for the rapid initial increase was that the domain walls were pinned very weakly by the defects dipoles, and that application of the ac field rapidly de-pinned them.

It should be noted that there was significant curvature to the field dependence of the dielectric response for both the as-sintered and post-annealed states of the undoped $BaTiO_3$ ceramics, and therefore the oxygen vacancy concentration in and of itself was not the main factor to determine whether the ac field dependence is linear or not. As discussed in Chap. 5, it strongly depends on the grain size. Also, a strong internal stress could be a reason for the non-Rayleigh response of the undoped $BaTiO_3$ ceramics.[96]

Comparing formulated and undoped $BaTiO_3$ ceramics, it is clear that in all cases, the high field dielectric response is controlled by domain wall motion. For the formulated $BaTiO_3$ ceramics, the oxygen vacancy concentration of the shell region (which was controlled by the oxidation state of the dopants) controlled whether or not Rayleigh-like behavior was observed. The Rayleigh-like response of the oxidized samples is correlated with a reduced defect dipole concentration in the shell. When the samples are reduced, the concentration of defect dipoles is increased in the shell. As was the case for the undoped $BaTiO_3$ ceramics, the defect dipoles pin

the domain walls weakly. Under larger ac electric fields, the domain walls de-pin, producing the nonlinear ac field dependence. Such weak pinning can be regarded as an additional roughness in a force profile, e.g. the spatial distribution of the interaction force between a domain wall and defects. The roughness provides a force density distribution with a smaller force mean on top of the approximately Gaussian force density distribution responsible for the Rayleigh-like response[36]. This makes the overall distribution non-Gaussian, and therefore the dielectric response deviates from the Rayleigh law, particularly at weak ac electric fields.

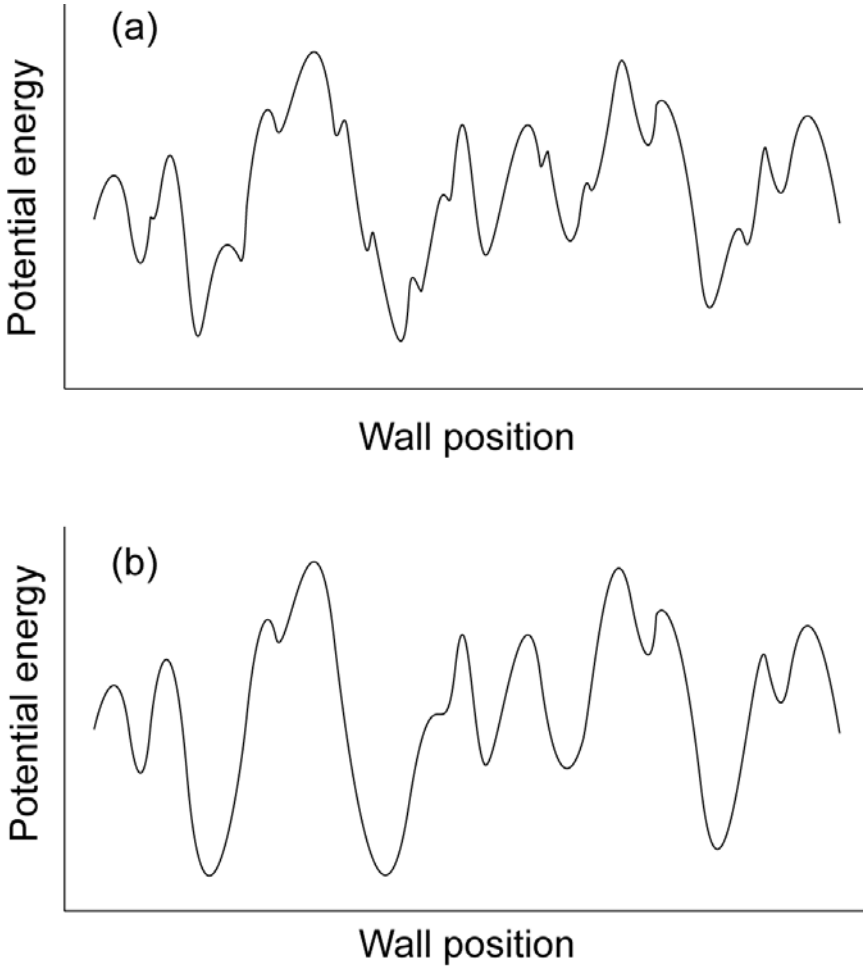

Figure **6-17**: Estimated potential landscape of a domain wall for the formulated $BaTiO_3$ ceramics reduced (a), and then oxidized (b).

6.4 Conclusions

The formulated $BaTiO_3$ ceramics sintered in reducing atmospheres showed sublinear ac field dependence of the dielectric properties, while those sintered in oxidizing atmospheres showed a relatively linear dependence. The difference could be attributed to the oxygen vacancy concentration induced by the change of the oxidation state of the dopants and resultant defect dipoles in the shell region. The ac field dependence of the dielectric properties of the undoped $BaTiO_3$ ceramics was sublinear. For the undoped $BaTiO_3$ ceramics sintered in reducing atmospheres, a rapid increase in the ac field dependence of dielectric properties was observed as a result of defect dipoles including oxygen vacancies. This effect on the observed dielectric nonlinearity was substantially larger than the changes induced by the oxygen vacancy concentration.

Chapter 7

Effect of Dielectric Layer Thickness and Grain Size on Dielectric Nonlinearity in Model $BaTiO_3$-Based Multilayer Ceramics Capacitors

Abstract

FORC distributions as well as the ac field dependence of the dielectric constant were investigated for model $BaTiO_3$ – based multilayer ceramic capacitors with dielectric layer thicknesses from 2.2 μm to 8.6 μm and those in which the grain size of the dielectrics varied from 0.28 μm to 0.39 μm while the layer thickness was held constant. In both cases, core-shell microstructures were observed. It was found that as the dielectric thickness decreased, the small and high electric field dielectric constants decreased, as did the peaks near the origin in the irreversible and reversible parts of the FORC distribution. The reversible FORC distributions of all the parts did not converge at high bias. These results indicate that the thickness dependence is attributable to a low dielectric constant interfacial layer and/or Schottky depletion layer at dielectric – electrode interfaces.

It was also found that the high field dielectric constant, the peak in the irreversible FORC distribution at the origin, and the reversible FORC distribution at zero bias decreased as grain size decreased, as was observed for the undoped ceramics in Chapter 5. The reversible FORC distribution of all the parts converged at high biases, indicating the grain size dependence was influenced by domain wall contributions. Dielectric contributions from the core and shell were estimated based on the temperature dependence of the permittivity. Not unexpectedly, the relative response of the core decreased while that of the shell increased as the grain size decreased.

A Preisach model using the measured FORC distribution gave a good fit to the experimental polarization-electric field loops as a function of grain size and dielectric layer thickness.

7.1 Introduction

Ferroelectric materials like $BaTiO_3$ are widely used in multilayer ceramic capacitors (MLCCs). In order to flatten the temperature dependence of the permittivity, the dielectrics are typically prepared with core-shell microstructures. An early study for undoped $BaTiO_3$ dielectric showed a suppression of the dielectric nonlinearity as the grain size decreased from 60 μm down to 0.6 μm[80]. However, the $BaTiO_3$ grain size in modern MLCCs is much smaller than 0.6 μm. As the dielectric layers are thinned to increase the volumetric efficiency of the capacitor, the volume of the ferroelectric core in each grain is decreasing. As a result, it would be anticipated that the domain structure and the domain wall mobility in the ferroelectric core might be more strongly affected by interactions within the shell or with the nearby electrodes.

An understanding of this might shed light on the observation that at the same electric field amplitude, the permittivity for MLCCs depends on the dielectric layer thickness.[118] Such a thickness dependence has frequently been reported for ferroelectric thin films[51, 52]. Among the sources for the thickness dependence in films is a low dielectric constant interfacial layer at a dielectric – electrode interface[53, 54] or a Schottky depletion region[55]. For MLCCs, Schottky barriers were reported at the Ni internal electrode - $BaTiO_3$ dielectric interface[29, 101]. Electrode/ dielectric interfaces could also influence domain wall motion[34, 59]. This, in turn, will influence the dielectric nonlinearity measured via the ac electric field dependence of the dielectric constant[4, 61, 62] or the first order reversal curves (FORC) distribution[45]. The FORC distribution represents the polarization response by a distribution of bi-stable units, or hysterons, and has the advantage of describing the nonlinearity over a wider range of the electric field compared to Rayleigh-like fitting.

At present, little is known about the volume of material that is affected by motion of domain walls, and how this might change with a core-shell microstructure. For barium titanate and lead zirconate titanate, grain size and domain size are coupled.[21, 119] For small grains, the domains are laminar. It has been hypothesized that the domain walls move collectively, so the mobility decreases with the domain size.[73, 120] For lead zirconate titanate films, spatially inhomogeneous collective motion, or clustering in a switching response, was reported,[121, 122] which is analogous to clustering of Barkhausen jumps in ferromagnetics.[123] The size of the clustering was reported to depend on the film thickness, resulting in thickness dependence of the dielectric properties.[124]

Consequently, in this study, the effect of dielectric layer thickness and grain size on the dielectric nonlinearity was quantified for test MLCCs with X7R specifications (the capacitance at 25˚C changes no more than 15% over a temperature range between -55˚C and 125˚C) via the ac field dependence of the dielectric properties and FORC distribution. To assess the FORC data, dielectric properties were calculated from FORC data using a Preisach model and compared with experimental results.

7.2 Experimental Procedure

Two sets of MLCCs with Ni internal electrodes and X7R specifications were prepared. The first set of MLCCs with various dielectric thicknesses was prepared by Dr. Youichi Mizuno (Taiyo Yuden). The dielectric thickness was varied from 2.2 to 8.6 μm. The size of the MLCCs is 1005, or 1 mm x 0.5 mm x 0.4 mm. The main starting material was hydrothermally derived $BaTiO_3$ powder (BT04, Sakai Chemical). Reagent-grade Ho_2O_3, MgO, MnO, and $BaSiO_3$ powders were added to the $BaTiO_3$ powder. The power was ball-milled with ZrO_2 media and ionized water in a resin pod, dried at 150˚C, and calcined. Organics such as polyvinyl butyral

binder and plasticizer were dissolved with a toluene – ethanol mixed solvent, which were added to the powder and they were ball-milled with ZrO_2 media in a resin pod for 48 h. The slurry was cast into green sheets via a doctor blade method. The thickness of the dielectric layer was controlled by the number of the green sheet stacked. Ni paste was printed on green sheets for internal electrodes. The green sheets were then stacked with top and bottom cover margins, pressed, and cut into pieces. Ni paste was painted on both ends of the chip for termination electrodes and dried. After the chips underwent binder-burnout at 350˚C in air, they were sintered at 10^{-6} Pa (~10^{-10} atm) pO_2, followed by an annealing at 1000˚C at 30 Pa (~$3x10^{-4}$ atm) pO_2. Then, the chips were cooled to near room temperature in a more oxidizing atmosphere (30 Pa pO_2 at 1000˚C).

The second set were MLCCs in which the grain size of the dielectrics was varied from 0.28 to 0.39 μm as described elsewhere[125]. The size of those MLCCs is 3216, or 3.2 mm x 1.6 mm x 0.4 mm. The composition was formulated to meet the X7R specifications for each sample. The samples were prepared using standard nickel electrode MLCC construction procedures. Green MLCCs underwent binder burnout and were fired at peak temperatures from 1170˚C to 1260˚C, followed by a reoxidation process. The specifications for both sets are shown in Table 7-1.

The dielectric layer thickness and the effective area of the internal electrodes were measured by scanning electron microscopy (SEM)(S-3000H, Hitachi) images of polished cross sections of the MLCCs. Grain size was measured from SEM images of a chemically etched, polished surface of the dielectrics between the internal electrodes (See Figs 7-1 to 7-2). The etchant was a mixture of H_2O:HCl:HF=95:4:1. The grain sizes of the samples are shown in Table 1. An average of a short diameter and a long diameter of a grain was calculated for more than 100 grains. The grain size was defined as an average of the averages and the reported error bar is the standard deviation. Although the grain size distributions for MLCCs with various grain sizes

overlap substantially, the dielectric properties depend on the average grain size, as shown below. This suggests that the average grain size is a useful metric. Both small and large electric field dielectric constants and losses were measured using an LCR meter (4284A, Agilent Technologies). The temperature dependence of the small field dielectric properties was measured at 1 V_{rms} and 1 kHz upon cooling from 150˚C or 180˚C to -60˚C at a cooling rate of 2˚C/min. The temperature was controlled by a furnace (DELTA 9023, Delta Design).

Table **7-1**: Dielectric layer thickness, average grain size, and number of the layers

Dielectric layer thickness (μm)	Grain size (μm)	Number of layers
2.2, 4.2, 6.6, 8.6	0.35±0.20, 0.36±0.11, 0.36±0.14, 0.34±0.12	1
7.7	0.28±0.10, 0.36±0.12, 0.39±0.13	10

Forty FORC were measured using a custom-made polarization-electric field (P-E) loop measurement system with a voltage amplifier (790A01, AVL Instrumentation). The FORC distribution was calculated from the first order reversal curves method[9, 44, 45, 49]. As described in Chapter 2, the polarization was calculated for arbitrary electric field excursions using a Preisach model with the FORC distribution.

7.3 Results and Discussion

7.3.1 MLCCs with Various Dielectric Thickness

Figure 7-3 shows the temperature dependence of the dielectric constant and loss of the MLCCs measured at 1 V_{rms}. The rather flat temperature dependence of the samples is attributed to the core/shell microstructure. Two peaks are apparent; one around 120˚C is associated with the cubic – tetragonal phase transition of the core, while the peak near 40˚C is associated with the diffuse phase transition of the shell. The tetragonal to orthorhombic phase transition peak of the

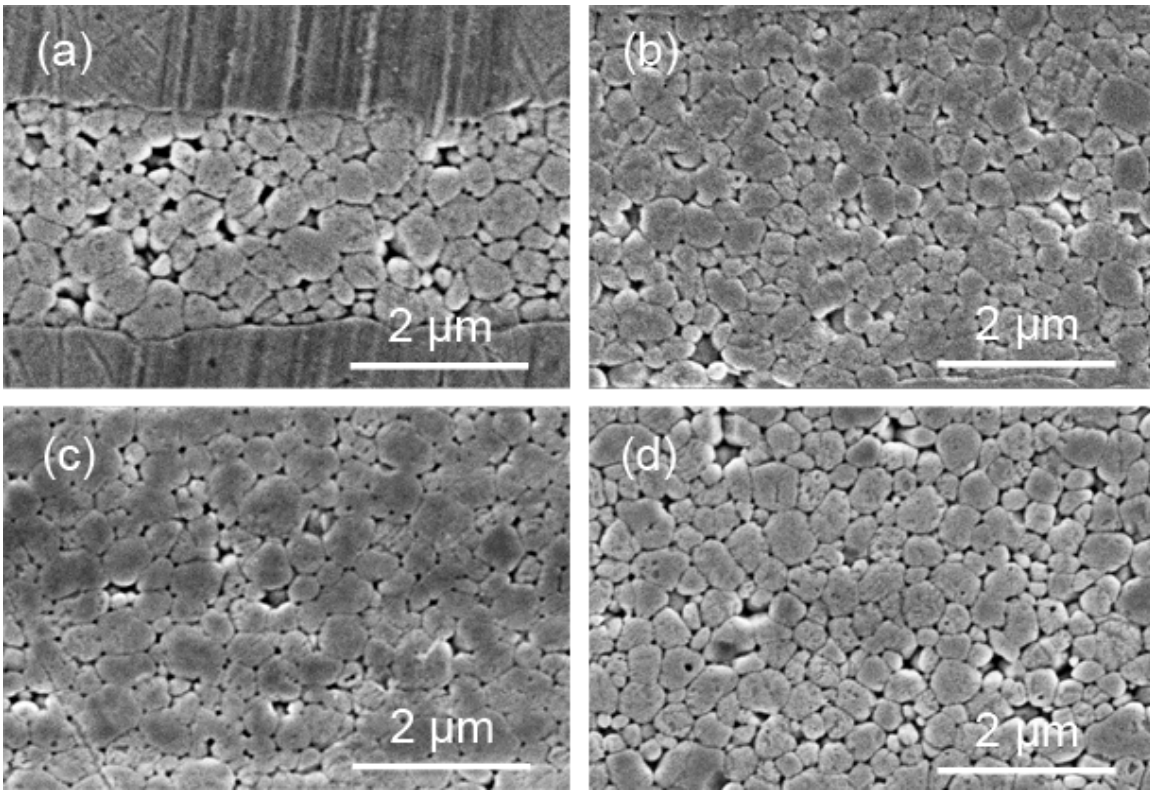

Figure **7-1**: Microstructure of the MLCCs with dielectric thicknesses of (a) 2.2 μm, (b) 4.2 μm, (c) 6.6 μm, and (d) 8.6 μm.

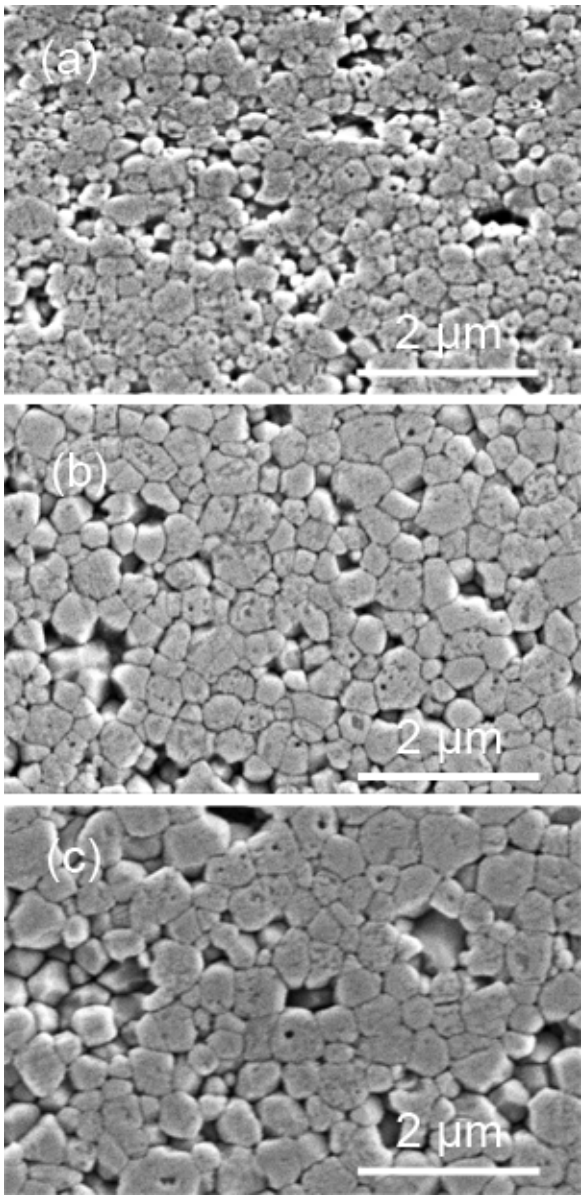

Figure **7-2** Microstructure of the MLCCs with grain sizes of (a) 0.28 μm, (b) 0.36 μm, and (c) 0.39 μm.

core was smeared, possibly due to the small grain size[67]. It was observed that the dielectric constant increased with the dielectric layer thickness. At room temperature, measurements at 1kV/cm and 1kHz gave: 2300±60, 2330±60, 2620±120, and 2950±140 for 2.2, 4.2, 6.6, and 8.6 μm-thick parts, respectively.

There are three possible explanations for this. The first is a low dielectric constant interfacial layer. The formation of a Ni-Ba-(Ti) alloy interfacial layers at the $BaTiO_3$ dielectrics/Ni internal electrode interface were reported both for MLCCs[126, 127] and $BaTiO_3$ thin films on Ni foils.[28] These result from residual carbon that creates a local heavily reducing atmosphere during firing of the MLCC, which can reduce $BaTiO_3$ to Ba and Ti.[126] The alloy generally has more Ba than Ti, which would lead to the $BaTiO_3$ dielectric near the interface being Ti-rich. The lower permittivity of such a layer could cause the thickness dependence due to the series connection. A consequence of the interface layer is that the permittivity did not converge above T_C. The second possibility is a Schottky depletion layer at the dielectric - electrode interfaces. Schottky barriers have been reported for MLCCs[29, 101]; the resulting electric field would be expected to produce a lower permittivity at the interface, and so decrease the net dielectric constant at temperatures above and below T_C. The third possibility for the decreased permittivity would be dilution associated with (partial) pinning of domain wall motion near the electrodes. As the dielectric thickness decreases, the proportion of the low domain wall mobility increases, and the dielectric constant decreases. The last mechanism might produce the larger peak in the dielectric constant at T_c with dielectric layer thickness, but it would be expected that if this was the dominant mechanism, the permittivity would collapse onto a master curve above T_C, where domain walls were eliminated. The fact that it does not suggests that the layer thickness dependence of the permittivity results primarily from either nonstoichiometry or an electric field at the dielectric/electrode interface.

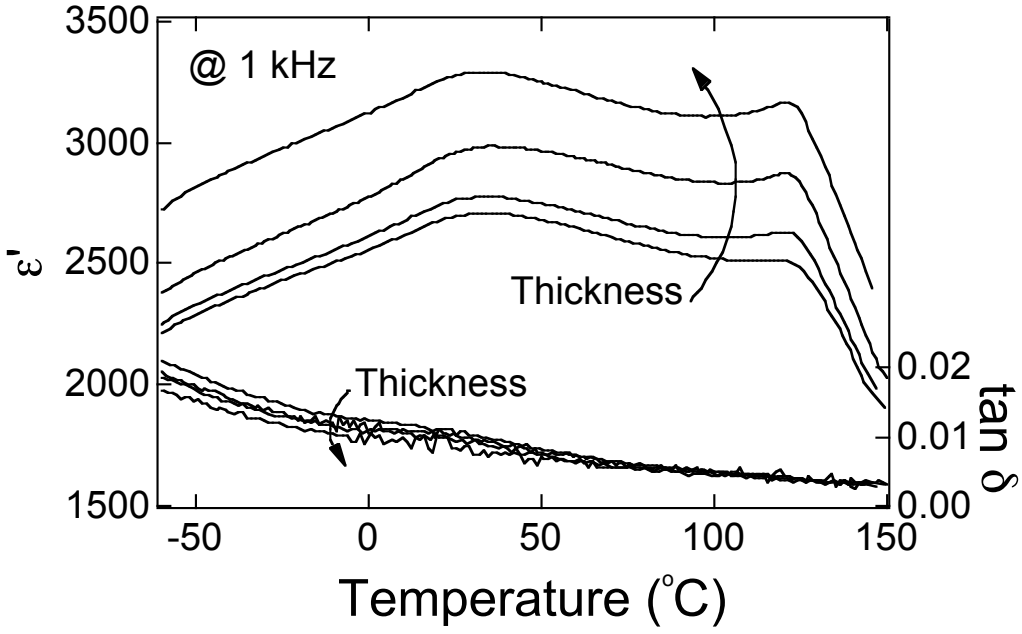

Figure **7-3**: The temperature dependence of the dielectric constant and loss of the MLCCs with varied dielectric thicknesses. The thicknesses are 2.2, 4.2, 6.6, and 8.6 μm.

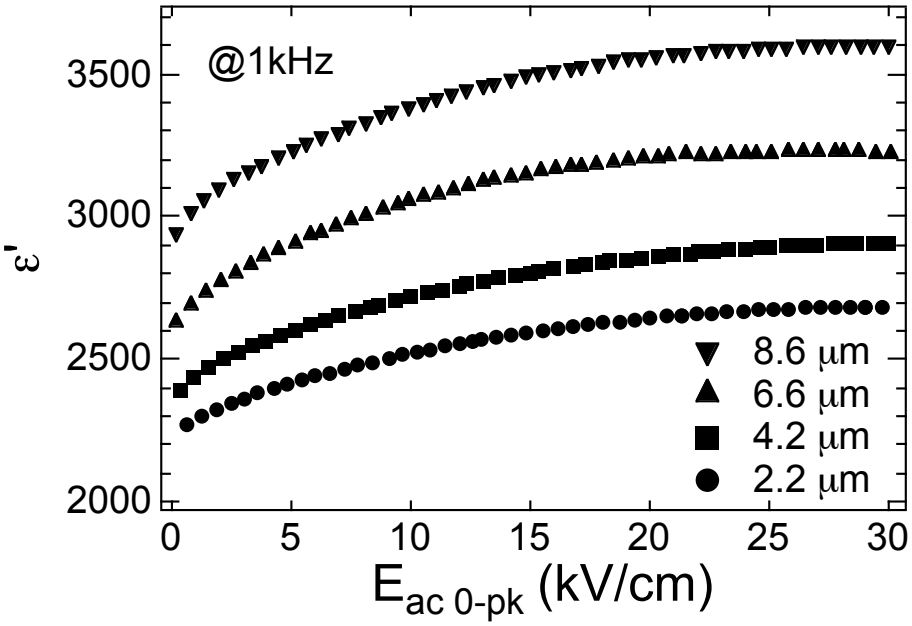

Figure **7-4**: The ac field dependence of the dielectric constant for MLCCs with different dielectric thicknesses.

Figure 7-4 shows the ac field dependence of the dielectric constant. The ac field dependence was sublinear, that is, the dielectric constant curved down with increasing ac field amplitude. This response is often observed for X7R MLCCs and small grained $BaTiO_3$ ceramics, yet the mechanism is not understood. It was suggested that a strong internal stress caused the response.[96] The ac field dependence was suppressed as the dielectric layer thickness decreased. This is consistent with the thickness dependence of the small field dielectric constant. A low dielectric constant interfacial layer or Schottky layer would lead to a lower electric field across the dielectric for a given applied electric field. Likewise, pinning of the domain walls at the dielectric – electrode interface would decrease the domain wall contribution to the properties for smaller layer thicknesses.

The FORC distributions were calculated from the first order reversal curves shown in Fig. 7-5. Only 4 FORC are shown in the figure for clarity; otherwise the overlap between curves makes the field dependence difficult to see. It was observed that the maximum polarization increased as the dielectric layer thickness increased, consistent with a low permittivity layer. Figure 7-6 shows the reversible FORC distributions as a function of α. The reversible FORC distribution is proportional to an ascending capacitance – voltage curve. The reversible FORC distributions for various dielectric layer thicknesses did not converge at high fields. This suggests that the reversible dielectric response of the samples is different, since domains are stabilized due to high bias. It is expected that the difference in the reversible FORC distributions is strongly influenced by the effect of the interfacial layer and/or Schottky depletion layer.

Figure 7-7 shows the irreversible FORC distributions. A peak irreversible FORC distribution is located at the origin, as has been reported for $BaTiO_3$ dielectrics[49, 128]. The peak intensity decreased as the dielectric thickness decreased. This indicates that the dielectric

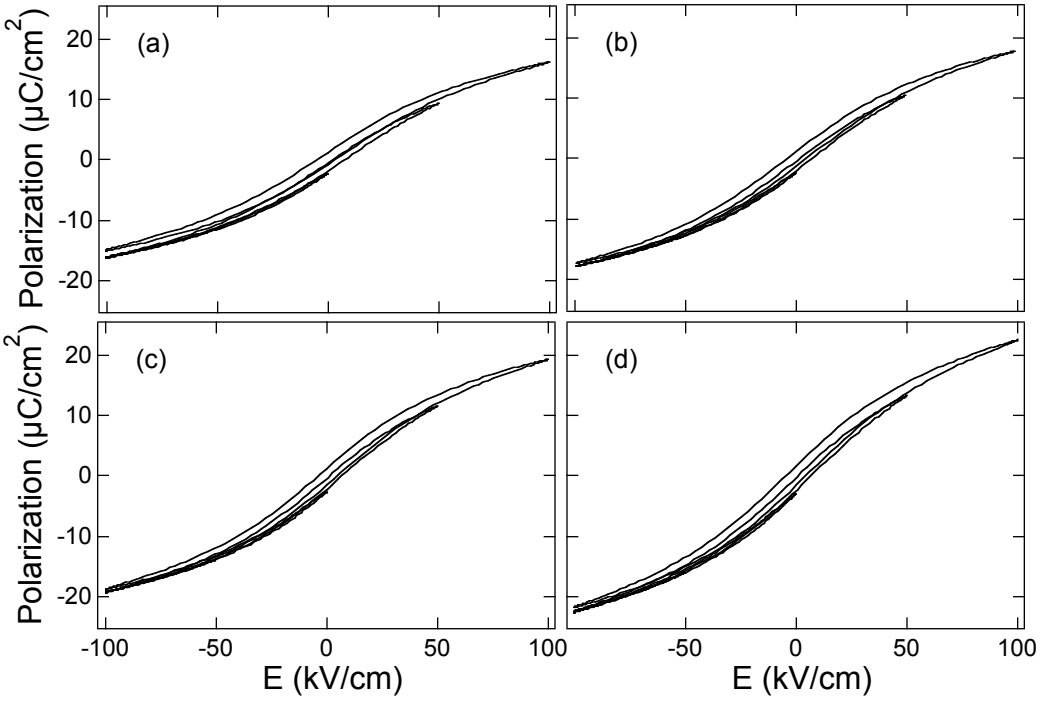

Figure **7-5**: The FORC of the MLCCs with dielectric thicknesses of (a) 2.2 μm, (b) 4.2 μm, (c) 6.6 μm, and (d) 8.6 μm. Only 4 minor loops were shown for clarity.

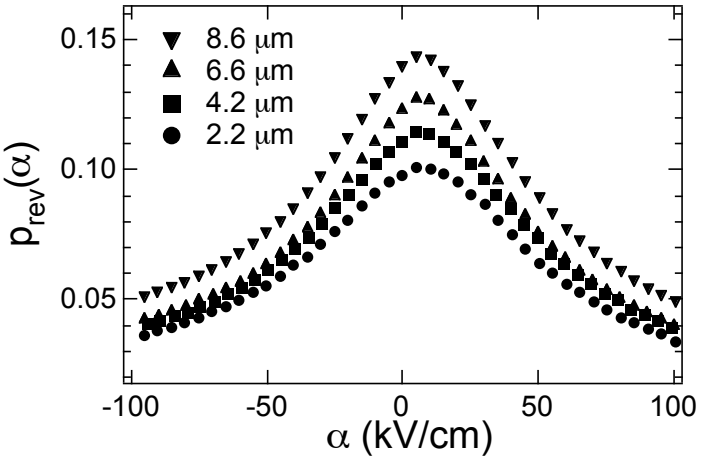

Figure **7-6**: The reversible FORC distributions as a function of α of the MLCCs with various dielectric thicknesses.

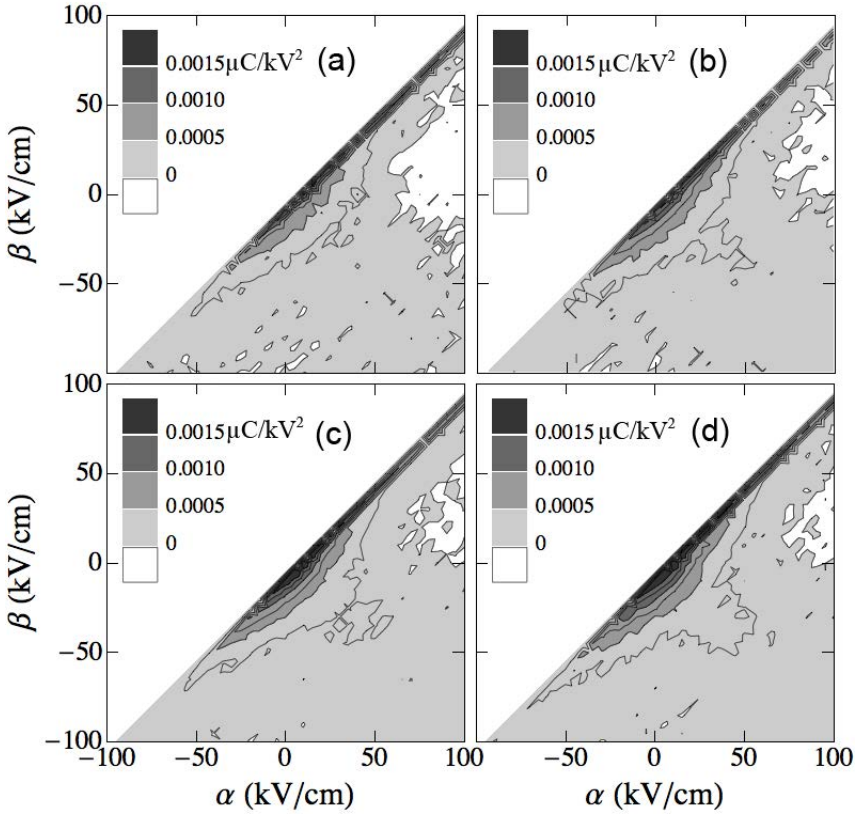

Figure **7-7**: The irreversible FORC distributions of the MLCCs with dielectric thicknesses of (a) 2.2 μm, (b) 4.2 μm, (c) 6.6 μm, and (d) 8.6 μm.

nonlinearity decreased with the dielectric thickness; this is consistent with the observed ac field dependence of the dielectric constant.

7.3.2 MLCCs with Various Grain Sizes

Figure 7-8 (a) shows the temperature dependence of the small field dielectric constant and loss. As expected, the dielectric constant decreased as grain size decreased over this size range. As the grain size decreased, the peak temperature associated with the shell increased. This is presumably due to a change in either the dopant concentrations and/or distribution. The peak temperature associated with the cubic-tetragonal phase transition stayed around 120˚C for all grain sizes. The difference in the dielectric constant of the samples *above* the cubic-tetragonal phase transition could be due, in principle to compositional heterogeneity (core/shell structure) as well as the increased density of grain boundaries [25].

Figure 7-8 (b) shows the temperature dependence of the inverse dielectric constant. Above T_C, Curie-Weiss behavior was observed:

$$\frac{1}{\varepsilon'} = a + bT = \frac{T - \theta}{C} \qquad \text{Eq. 7-1}$$

where a and b are fitting coefficients, C is Curie constant, and θ is the Curie-Weiss temperature. The fitting parameters are summarized in Table 7-2. It was observed that as the grain size decreased, b increased while C and θ decreased. It was reported that the Curie constant of undoped $BaTiO_3$ ceramics is not a strong function of grain size[87, 129]. On the other hand, the Curie constant does depend on doping; the Curie constant of the shell is smaller than that of the core[29, 66]. Thus, the observed decrease in the Curie constant with decreasing grain size is believed to be a consequence of the an increase in the volume fraction of shell material.

Table **7-2**: Curie-Weiss fitting parameters.

Grain size (μm)	a x10^4	b x10^6 ($^\circ C^{-1}$)	C x10^{-5} (K)	θ ($^\circ$C)
0.28	-6.49 ± 0.07	9.44 ± 0.04	1.06 ± 0.00	68.8 ± 1.0
0.36	-6.80 ± 0.07	9.04 ± 0.04	1.11 ± 0.00	75.3 ± 1.1
0.39	-6.89 ± 0.06	8.50 ± 0.04	1.18 ± 0.00	81.0 ± 1.1

As explained earlier, the differences in the inverse dielectric constant at temperatures and the Curie-Weiss temperature is likely due to a combination of the microstructural heterogeneity and a dielectric contribution from grain boundaries. For example, the progressive decrease in the Curie-Weiss temperature with grain size is likely to be linked to a lower permittivity layer in the dielectric. Frey *et al.* estimated a grain boundary thickness by assuming $BaTiO_3$ ceramics to consist of cubic $BaTiO_3$ grains (with side length d_G) separated by grain boundaries with thickness d_{GB}. In this case, an inverse dielectric constant of $BaTiO_3$ ceramics $1/\varepsilon'$ could be expressed as:[25]

$$\frac{1}{\varepsilon'} = \frac{v_G}{\varepsilon_G'} + \frac{g v_{BG}}{\varepsilon_{GB}'} \qquad \text{Eq. 7-2}$$

where ε_G' is a dielectric constant of the grain, ε_{GB}' is a dielectric constant of the grain boundaries. g is a geometric factor. ε_{GB}' and g were reported to be 100 and 0.8, respectively.[25] v_G and v_{GB} are the volume fraction of the grain and grain boundaries: [25]

$$v_G = \left(\frac{d_G}{d_G + d_{GB}}\right)^3 = \left(1 + \frac{d_{GB}}{d_G}\right)^{-3} \qquad \text{Eq. 7-3}$$

$$v_{GB} = 1 - v_G = 1 - \left(1 + \frac{d_{GB}}{d_G}\right)^{-3} \qquad \text{Eq. 7-4}$$

Substituting Eqs. 7-3 and 7-4 into Eq. 7-2 and the fact that ε_G' follows the Curie-Weiss law yields: [25]

$$\frac{1}{\varepsilon'} = \left(\frac{T-\theta}{C}\right)\left(1 + \frac{d_{GB}}{d_G}\right)^{-3} + \frac{g}{\varepsilon_{GB}'}\left[1 - \left(1 + \frac{d_{GB}}{d_G}\right)^{-3}\right] \qquad \text{Eq. 7-5}$$

The inverse dielectric constant of fine-grained BaTiO3 ceramics, evaluated at the Curie-Weiss temperature of a large grained $BaTiO_3$ ceramic is expressed as: [25]

$$\left.\frac{1}{\varepsilon'}\right|_{T=\theta} = \frac{g}{\varepsilon_{GB}'}\left[1-\left(1+\frac{d_{GB}}{d_G}\right)^{-3}\right] \qquad \text{Eq. 7-6}$$

With Eq. 7-6, the grain boundary thickness can be calculated. Following Frey *et al.*, a grain boundary thicknesses for the 0.28 and 0.36 μm grain size parts were estimated at the Curie-Weiss temperature of the 0.39 μm grain size parts using d_G was grain size. The grain boundary thickness was estimated to be 1.4 nm and 0.8 nm, respectively, These values are reasonable and hence support the grain boundary dilution model for the reduction in the dielectric constant with the grain size.

In an attempt to minimize the effect of the grain boundaries on the grain size dependence, all of the data were normalized to that of the 0.39 μm grain size parts at 150˚C. The 0.39 μm parts is assumed to consist of only core/shell grains (without grain boundaries). The inverse dielectric constant for the 0.28 μm parts or 0.36 μm parts measured at 150˚C is expressed as:

$$\frac{1}{\varepsilon'_{150^\circ C}} = \frac{v_{CS}}{\varepsilon'_{0.39\mu m,150^\circ C}} + \frac{g v_{GB}}{\varepsilon'_{GB}} \qquad \text{Eq. 7-7}$$

where $\varepsilon_{0.39\mu m,150^\circ C}$' is the dielectric constant of the 0.39μm parts at 150˚C and v_{CS} is the volume fraction of the core/shell grains of the parts in question. As calculated above, the grain boundary thickness may be small enough to be neglected compared to the core/shell grain size, so that v_{CS} ~1. As a result, the grain boundary contribution is calculated to

$$\frac{g v_{GB}}{\varepsilon'_{GB}} = \frac{1}{\varepsilon'_{150^\circ C}} - \frac{1}{\varepsilon'_{0.39\mu m,150^\circ C}} \qquad \text{Eq. 7-8}$$

Thus, the dielectric constant of core/shell grains ε_{CS}' for the 0.28 μm parts or 0.36 μm parts is expressed as:

$$\frac{1}{\varepsilon_{CS}'} = \frac{1}{\varepsilon'} - \frac{g v_{GB}}{\varepsilon_{GB}'} \qquad \text{Eq. 7-9}$$

Figure 7-8 (c) shows the result. It was found that the contribution of the shell to the measured dielectric constant increased with decreasing grain size.

Figure 7-9 (a) shows the measured ac field dependence of the dielectric constant. It was found that the ac field dependence was sublinear for all parts. Moreover, the ac field dependence was suppressed as the grain size decreased. This is attributable to a combination of the pinning of domain wall motion by the grain boundaries and dilution from the low permittivity grain boundaries.

In an attempt to extract the influence of the grain boundary dilution, the same correction as in Eqs. 7-8 and 7-9 was used on the field dependence. Figure 7-9 (b) shows the ac field dependence of the dielectric constant for the core and shell. A larger high field dielectric constant was observed for the parts with 0.28 μm grain size, in which the dielectric contribution from the shell is strong. This is consistent with a previous study showing a larger high field dielectric constant of shell dielectrics over that core dielectrics, as shown in Fig. 7-10.[27] The large polarizability and domain wall contributions could be associated with the diffuse phase transition of the shell near room temperature. The smaller high field dielectric constant for the parts with 0.36 and 0.39 μm grain sizes is attributable to the lower domain wall mobility of the core dielectrics.

The FORC of the parts are shown in Fig. 7-11. Again, only 4 FORC are shown in the figure for clarity. It was found that as the grain size decreased, the maximum polarization decreased and the polarization-electric field trace become less hysteretic, possibly due to the pinning of the domain wall motion by the grain boundaries and the dilution from the grain boundaries. Figures 7-12 and 7-13 shows the reversible and irreversible FORC distributions,

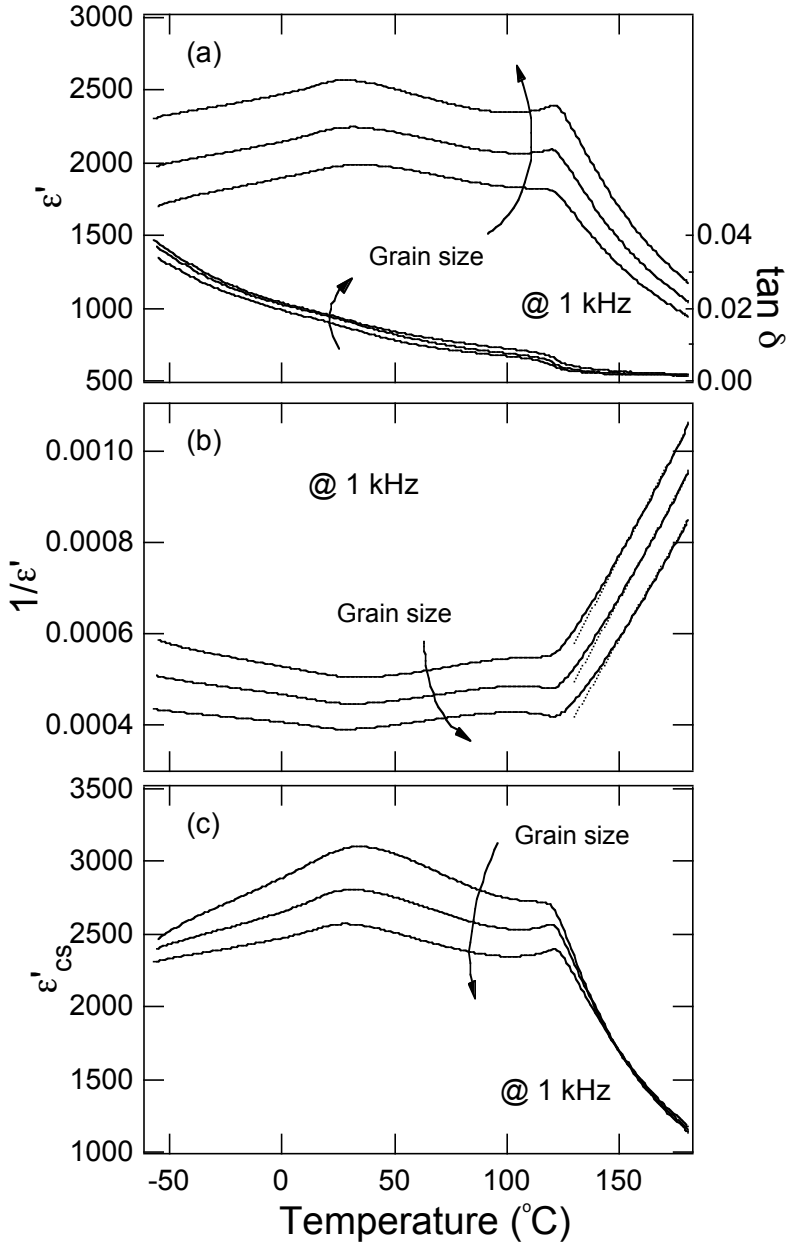

Figure **7-8**: The temperature dependence of (a) the small field dielectric constant and loss, (b) inverse dielectric constant with dotted lines showing the linear fit, and (c) dielectric constant of core/shell component for MLCCs with different grain sizes. The grain sizes are 0.28, 0.36, and 0.39 μm.

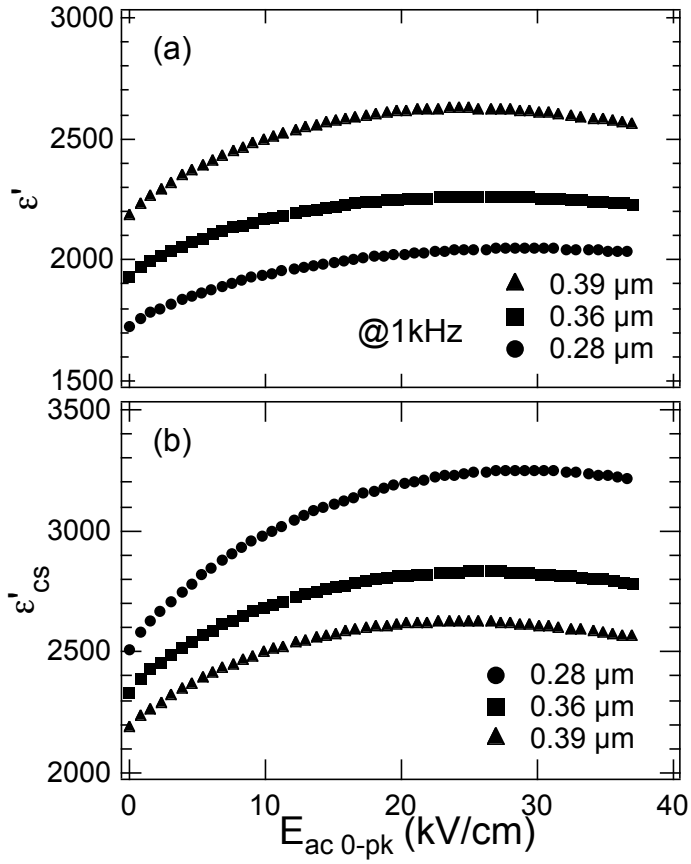

Figure **7-9**: The ac field dependence of (a) the dielectric constant and (b) the dielectric constant of core/shell component for the MLCCs with various grain sizes.

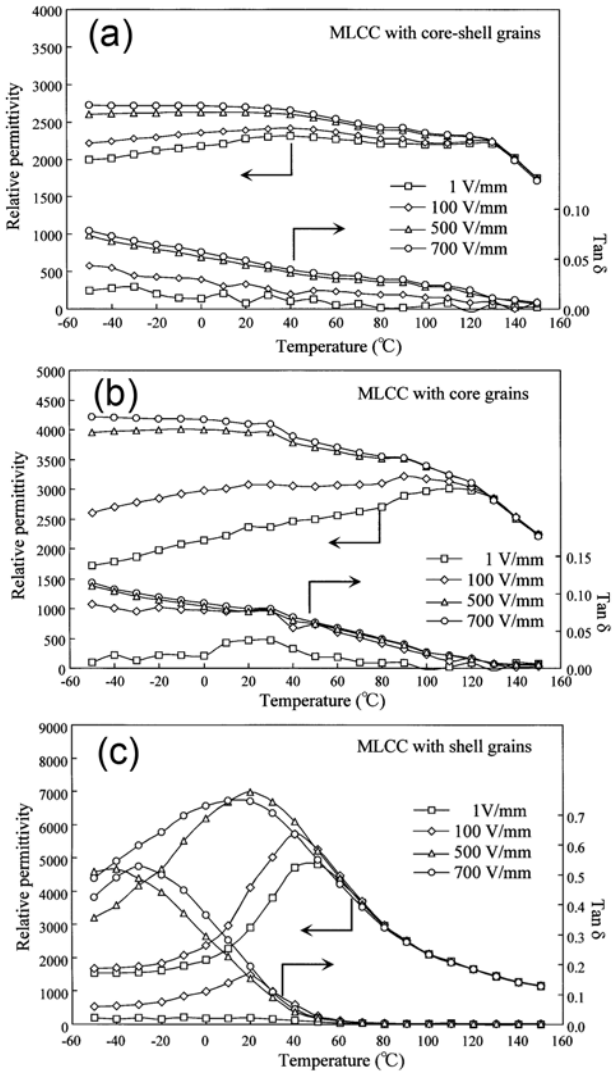

Figure **7-10**: Temperature dependence of the dielectric properties measured at various ac field amplitudes for MLCC with (a) core-shell grains, (b) core grains, or (c) shell grains.[27] The average grain size of the dielectrics for the MLCCs was 0.4 μm.

respectively. The reversible FORC distribution largely converged at high fields. This suggests that grain boundary dilution is less critical at high biases, presumably because the permittivity of the ferroelectric material has decreased substantially due to dielectric tunability. For the irreversible FORC distributions, a peak centered at the origin was observed. The peak was suppressed with the grain size, consistent with previous studies[49, 128]. This indicates that the domain wall contributions decreased with the grain size. Note that the streak along the $\alpha=\beta$ line for positive α and β is due to the finite time-dependence of the switching, which was also observed in Chapters 4 and 5.

In order to assess the self-consistency of the FORC distribution, the polarization – electric field loops were calculated for the 0.28 μm parts using the Preisach model to compare with the experimental loops. For this purpose, the FORC distribution was re-calculated from FORC measured with E_{max}~52kV/cm to increase the resolution. Figures 7-14 (b) and (c) show the comparison of the calculated and measured polarizations as a function of the time and electric field, respectively, for the electric field excursion shown in Fig. 7-14 (a). It was found that the Preisach model gave a good prediction to the experimental data.

Figure 7-15 shows the ac field dependence of the dielectric constant measured and calculated at various dc bias fields, along with the polarization amplitude or fundamental of the polarization over the ac field amplitude (P/E and 1st harm./E). Here, the dielectric properties were measured at 20Hz. The ac field dependence of the dielectric constant was measured by the LCR meter first under -15.6 kV/cm dc bias. Then, the measurements were repeated with increasing the dc bias field up to +15.6 kV/cm. To calculate the first order harmonics, the P-E loops were measured by applying sinusoidal fields with different ac field amplitudes, and then the first order harmonics were calculated by Fourier transforming the time dependence of the polarization. The small and high field dielectric constants decreased with increasing dc bias field. This is because of a combination of tunability in the intrinsic dielectric constant and the fact that the domains

were stabilized with the dc bias field. It was found that the calculation gave a reasonable fit to the experimental data for ac field amplitudes <15 kV/cm under negative dc bias field. Otherwise, some discrepancies were observed. At high ac fields, the discrepancies stem from the difference in the definition of the dielectric constant[45]. The dielectric constant calculated by the Preisach model was defined as polarization over the ac field amplitude. This fits the measured P/E data well. On the other hand, the LCR meter calculates the dielectric constant as the first order harmonics of the polarization over the ac field amplitude. The LCR dielectric constant fits to the calculation for the 1st harmonic/E. When the parts were exposed to positive dc bias field, the dielectric constant calculated by Preisach model is larger than the LCR dielectric constant for the ac field amplitudes smaller than some 15 kV/cm. This is attributable to the contribution from the streak along the $\alpha=\beta$ line for the irreversible FORC distribution and the finite time-dependence of the switching. That is, all of the FORC data were acquired starting from a negatively saturated state. The resulting imprint leads to FORC distributions that are not centered on the $\alpha = -\beta$ line. Instead, for many of the samples measured in this thesis, the center of the FORC distribution lies under this line. Thus, the resulting FORC distribution is expected to be most accurate for measurements made under negative biases. Under positive bias, the net polarization state of the sample would be expected to change. This produces the larger discrepancies between measured and calculated data at high positive biases.

The data set for Fig. 7-15 was re-plotted to yield the dc bias dependence of the dielectric constant. Figure 7-16 shows the dc bias dependence of the dielectric constant of the 0.28 μm parts measured and calculated at various ac field amplitudes. The experimental dielectric constant was obtained by interpolating for specific field values from the data set in Fig. 7-15. Therefore, the dc bias dependence shown corresponds to the ascending branch of a butterfly loop for the permittivity. Data for the dielectric constant at ac field amplitudes higher than ~20 kV/cm was not shown due to the difference in the definition of the dielectric constant. The dc bias field range

was reduced for higher ac field data because the FORC data were collected over the field range of $E_{ac} + E_{dc} \leq E_{max} \sim 52$ kV/cm. Overall, the agreement was reasonable. Some discrepancies were found in data for positive dc bias. As discussed earlier, this is attributed to the finite time-dependence of the switching.

With this Preisach model, it is not possible to describe the butterfly response of the dc bias dependence. In order to describe it, it is necessary to incorporate a hysteretic response for the FORC distribution itself into the Preisach model. Use of a more sophisticated Preisach model (i.e. a moving Preisach model) would enable this description.[10]

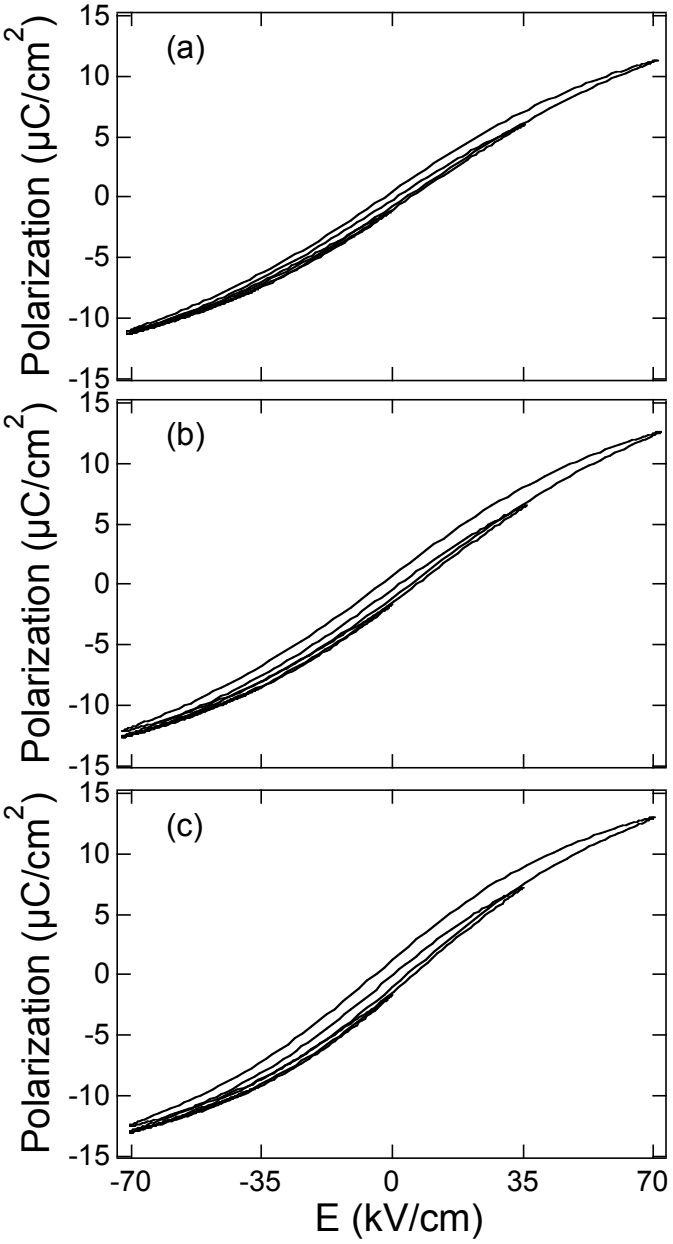

Figure **7-11**: The FORC of the MLCCs with varied grain sizes: (a) 0.28 μm, (b) 0.36 μm, and (c) 0.39 μm. Only 4 minor loops were shown for clarity.

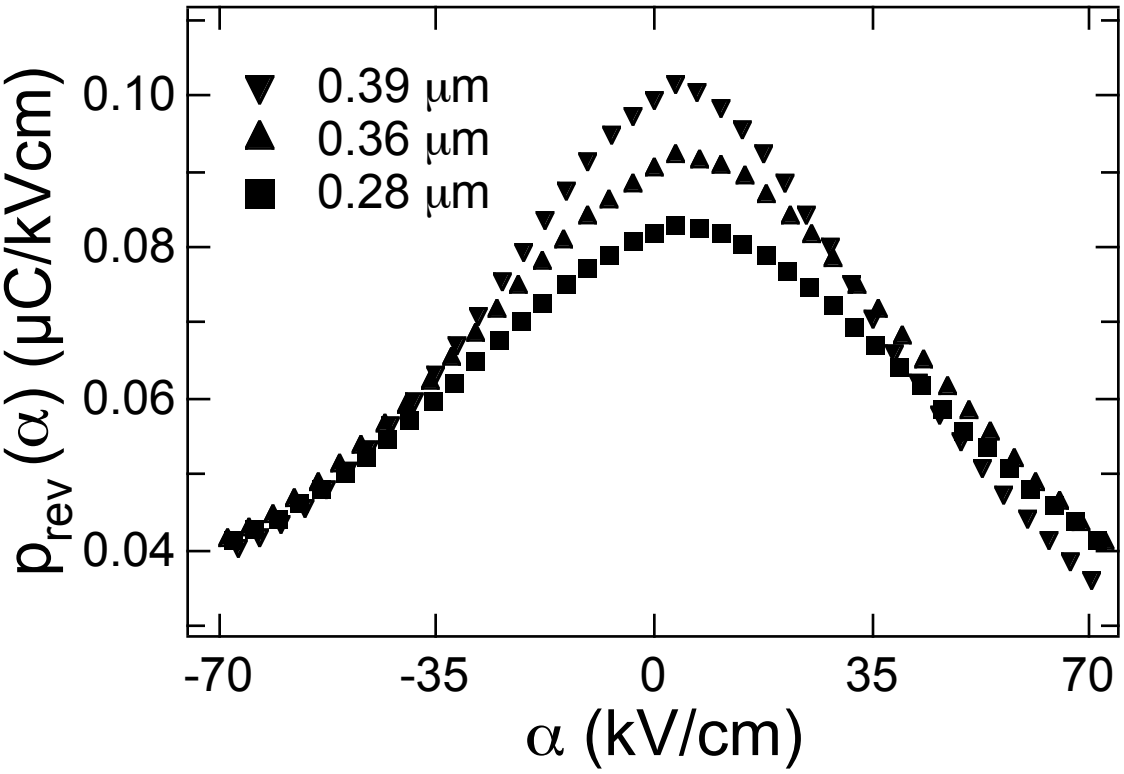

Figure **7-12**: The reversible FORC distributions of the MLCCs with various grain sizes.

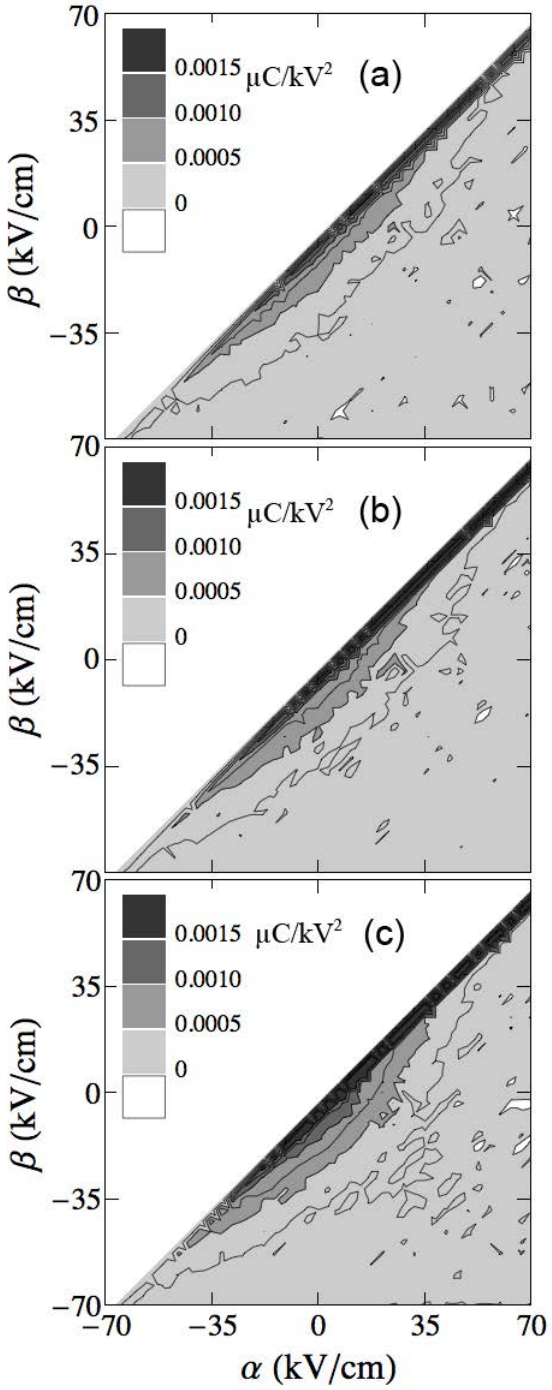

Figure **7-13**: The irreversible FORC distributions of MLCCs with different grain sizes: (a) 0.28 μm, (b) 0.36 μm, and (c) 0.39 μm.

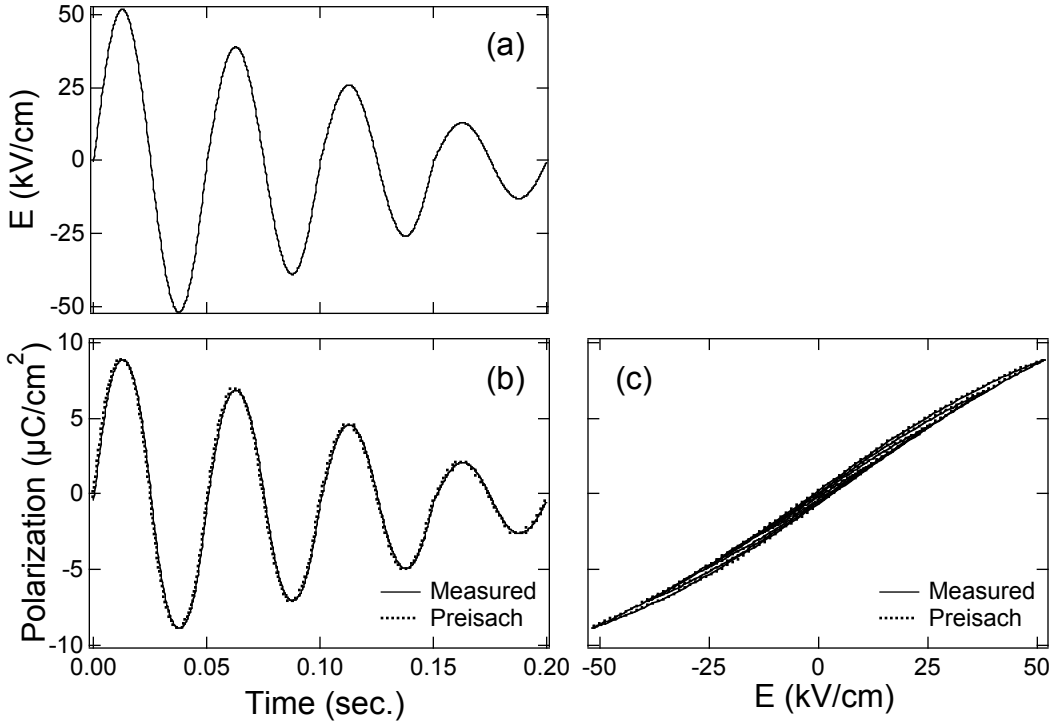

Figure **7-14**: (a) Applied electric field as a function of time. Comparison of calculated and measured polarizations of 0.28 μm grain size parts as a function of the (b) time and (c) electric field for the electric field excursion shown in (a).

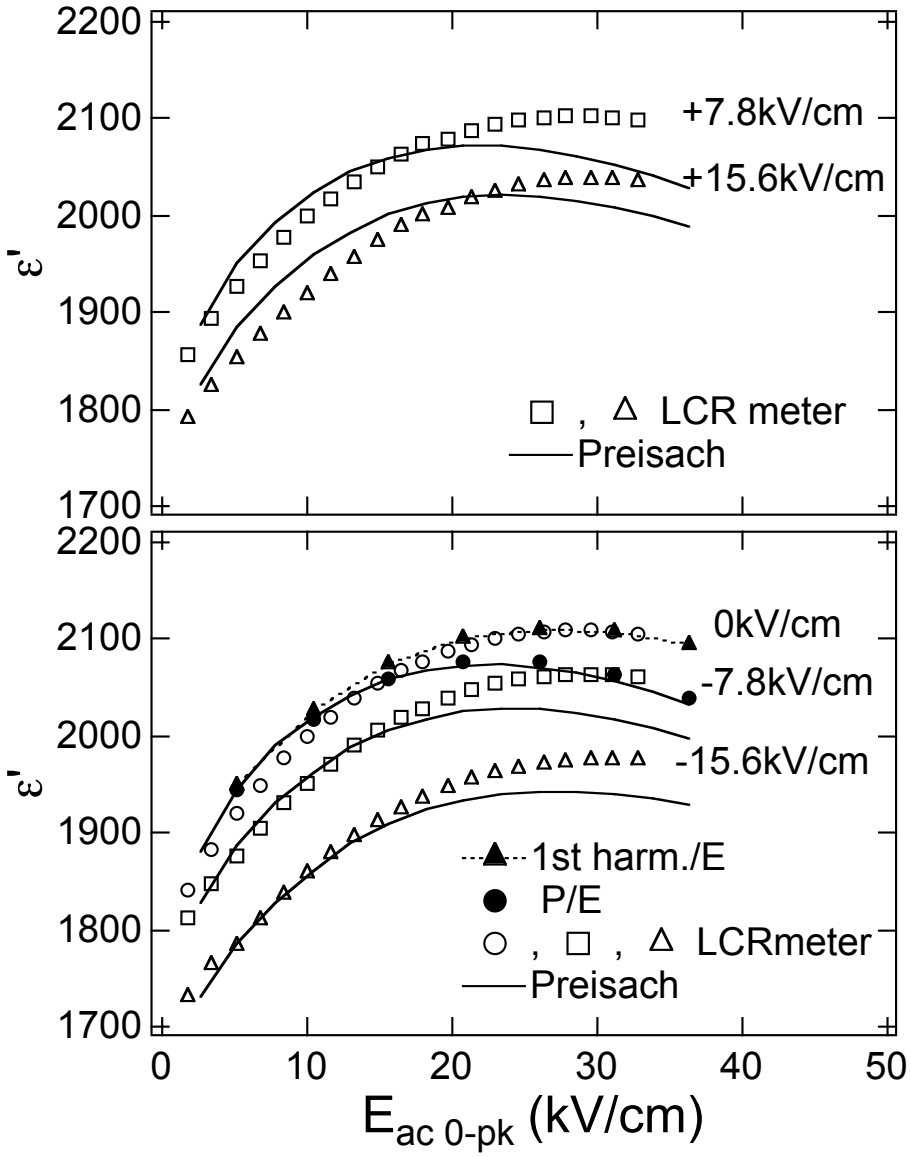

Figure **7-15**: The measured and calculated dielectric constant of the 0.28 μm parts as a function of ac and dc fields, along with the polarization amplitude or fundamental of the polarization over the ac field amplitude (P/E and 1st harm./E). The latter was calculated only for zero dc bias.

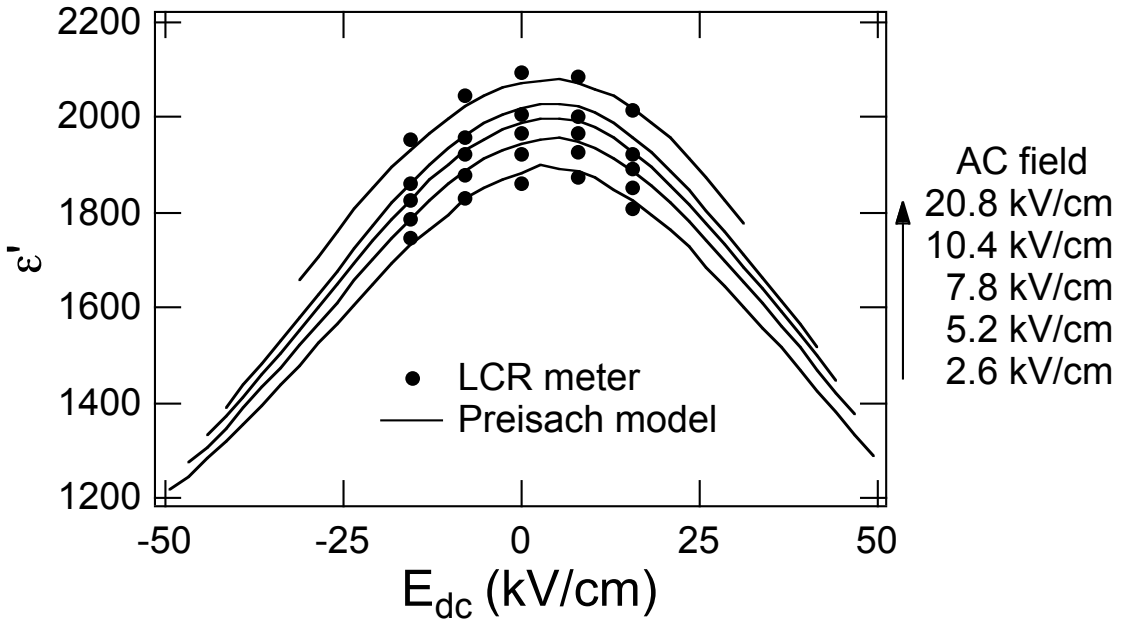

Figure **7-16**: The dc bias dependence of the dielectric constant of the 0.28 μm parts measured and calculated at various ac field amplitudes. The measured dielectric constant was obtained from interpolating date set in Fig. 7-15. The FORC distributions used for Fig. 7-15 was used to calculate the dc bias dependence of dielectric constant.

7.5 Conclusions

The dielectric nonlinearity of X7R MLCCs was studied as functions of the dielectric layer thickness and the dielectric grain size. It was found that the small field dielectric constant and dielectric nonlinearity decreased as the dielectric layer thickness decreased from 8.6 μm to 2.2 μm. The thickness dependence was attributed to a low dielectric constant interface and/or a Schottky depletion layer. The small field dielectric constant and dielectric nonlinearity decreased with grain size. This reflected an increase in the area of grain boundaries. As the grain size decreased, the relative importance of the shell in controlling the measured dielectric response increased. In contrast, the dielectric nonlinearity of the larger grained sample was dominated by the core; since the nonlinearity of the core was somewhat smaller than that of the shell, the nonlinearity of the dielectric itself (once corrected for grain boundaries) was smaller for the large-grained sample.

Preisach model using FORC distribution give a good fit to the experimental polarization-electric field loops. However, some discrepancies were observed between the measured and calculated dielectric constants, which was attributed to the difference in the definition as well as the path-dependence of the FORC distributions.

Chapter 8

Conclusions and Future Work

8.1 Conclusions

8.1.1 Thickness Dependence of Dielectric Nonlinearity of Lead Zirconate Titanate Films

The dielectric nonlinearity of PZT films of different thickness was investigated using the FORC distribution obtained by the first order reversal curves method. Over the thickness range from 0.26 to 6 μm, the majority of the thickness dependence in the dielectric properties can be attributed to extrinsic, rather than intrinsic effects. Significant differences were observed in the irreversible FORC distribution; as the film thickness decreased, the concentration was depressed and the switching fields for the concentration increased. This is consistent with the thickness dependence of the irreversible Rayleigh constant. The polarization-electric field and the dielectric constant calculated by the Preisach model gave a reasonable fit to the experimental data, although the high field dielectric constant differed from the experimental data, probably due to a difference in the definition of the dielectric constant.

8.1.2 Grain Size Effect on the Dielectric Nonlinearity of $BaTiO_3$ Ceramics

The increase in the small field dielectric constant with decreasing grain size is influenced by an increase in the reversible domain wall contribution. For samples with large

grains, defect dipoles are found to stabilize domains, producing pinched minor loops, a threshold field in the ac field dependence of the dielectric constant and loss, and splitting the peak in the irreversible FORC distribution. For samples with small grain sizes, domain walls are de-pinned at modest electric fields and contribute to the dielectric properties, although the long-range motion is restricted.

8.1.3 Effect of Oxygen Partial Pressure during Firing on Dielectric Nonlinearity of $BaTiO_3$ Dielectric

The formulated $BaTiO_3$ ceramics sintered in reducing atmospheres showed sublinear ac field dependence of the dielectric properties, while those sintered in oxidizing atmospheres showed a relatively linear dependence. The difference could be attributed to the oxygen vacancy concentration induced by the change of the oxidation state of the dopants and resultant defect dipoles in the shell region. The ac field dependence of the dielectric properties of the undoped $BaTiO_3$ ceramics was sublinear. For the undoped $BaTiO_3$ ceramics sintered in reducing atmospheres, a rapid increase in the ac field dependence of dielectric properties was observed as a result of defect dipoles including oxygen vacancies.

8.1.4 Effect of Dielectric Layer Thickness and Grain Size on Dielectric Nonlinearity in Model $BaTiO_3$-Based Multilayer Ceramic Capacitors

The dielectric nonlinearity of X7R MLCCs was studied as functions of the dielectric layer thickness and the dielectric grain size. It was found that the small field dielectric constant and dielectric nonlinearity decreased as the dielectric layer thickness decreased from 8.6 μm to

2.2 μm. The thickness dependence was attributed to a low dielectric constant interface and/or a Schottky depletion layer. The small field dielectric constant and dielectric nonlinearity decreased with grain size. This reflected an increase in the area of grain boundaries. As the grain size decreased, the relative importance of the shell in controlling the measured dielectric response increased. In contrast, the dielectric nonlinearity of the larger grained sample was dominated by the core; since the nonlinearity of the core was somewhat smaller than that of the shell, the nonlinearity of the dielectric itself (once corrected for grain boundaries) was smaller for the large-grained sample.

Preisach model using FORC distribution could give a good fit to the experimental polarization-electric field loops. However, some discrepancies were observed between the measured and calculated dielectric constants, which was attributed to the difference in the definition as well as the path-dependence of the FORC distributions.

8.2 Future Work

$BaTiO_3$ Platelet

The dielectric layer thickness of $BaTiO_3$ based multilayer ceramic capacitor has decreased to increase the volumetric efficiency. However, as is investigated in this study and other works, the dielectric constant of $BaTiO_3$ ceramics decreases with grain size below 1μm. Thus, it is difficult to obtain large capacitance in a small capacitor.

While the grain size *perpendicular* to the layer is limited by the layer thickness, there is room for increasing grain size *parallel* to the layer. If the dielectric constant can be increased by extending the grain along the layers while keeping it small perpendicular to the layers, it would

be possible to increase the volumetric efficiency. Thus, it is interesting to study the aspect ratio dependence of the dielectric properties of $BaTiO_3$ ceramics. Platelet grains with a high aspect ratio can be prepared by molten salt synthesis with a topochemical reaction.[130] Platelets with 0.5 μm in thickness and 4~10 μm in length were reported.[130]

Methods to prepare smaller $BaTiO_3$ platelets and to change the aspect ratio should be investigated. This could be approached using Bi layer structured ferroelectrics such as $Ba_2BiTi_5O_{18}$ and $BaBi_4Ti_4O_{15}$ prepared by a molten salt method. From these, $BaTiO_3$ platelets with various aspect ratios could be prepared by topochemical reaction. Disc samples and MLCC samples made from these parts could then be prepared; reasonable alignment of the platelets should be facilitated by tape casting. Then, the microstructure and the dielectric properties could be studied as a function of the aspect ratio.

Analytical Function of Ferroelectrics for Preisach Model

Acceptable fits to P-E loops of the PZT film and the MLCC were given by the Preisach model using the FORC distributions. To improve the modeling accuracy, an analytical function is necessary in order to perform comparable Preisach-type modeling as is currently implemented for magnetics[10]. To this end, an appropriate function should be developed for fitting the FORC distribution. For PZT ceramics, a Gaussian function is reported.[131] The appropriate function is not known for $BaTiO_3$ dielectrics. Early studies conducted as part of this thesis research showed a stretched exponential function yielded a better fit over polynomials at small switching fields (See Figs. 8-1 to 8-3). This would form a starting point for the study.

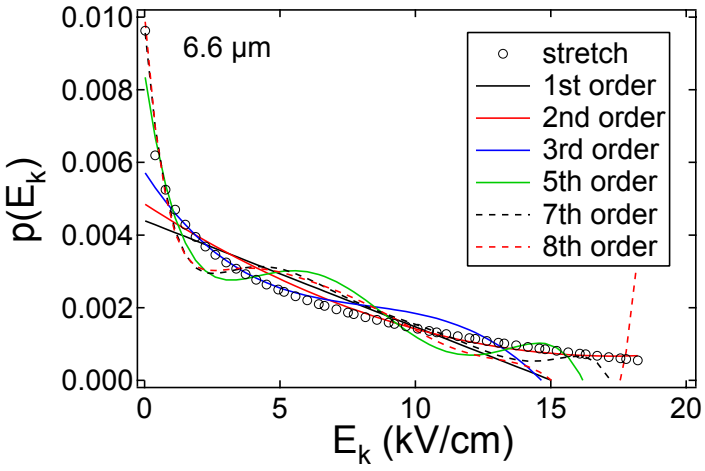

Figure **8-1**: Polynomials and stretched exponential fits for the Preisach distributions of an MLCC with the dielectric thickness of 6.6 μm. As can be seen, the polynomials converged to the stretched exponential function for higher order polynomials. Note that the Preisach distributions were described in critical field E_k and interaction field E_i coordinates ($E_k=(\alpha-\beta)/2$, $E_i=(\alpha+\beta)/2$) and the distributions were assumed to depend only on E_k.

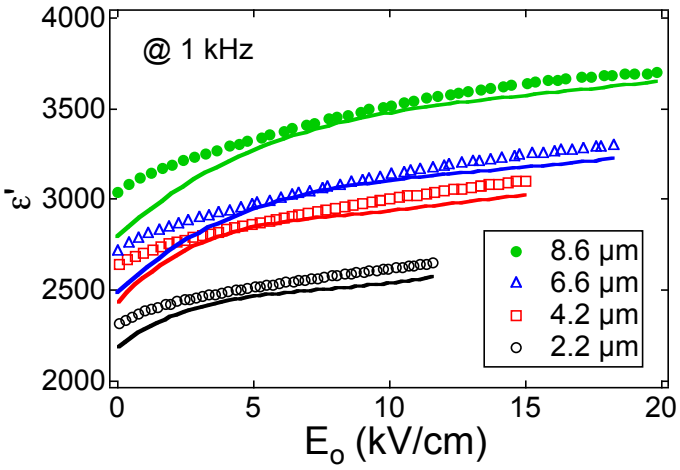

Figure **8-2**: The calculated and measured dielectric constants as a function of the ac field amplitude. Markers indicate the measured dielectric constant and lines denote the dielectric constant calculated with a 3rd order polynomial Preisach distribution. Colors specify the dielectric thickness of the MLCCs. The Preisach distribution was determined by fitting the P-E loop measured at the same ac field amplitude. Relatively poor agreement is apparent at low fields.

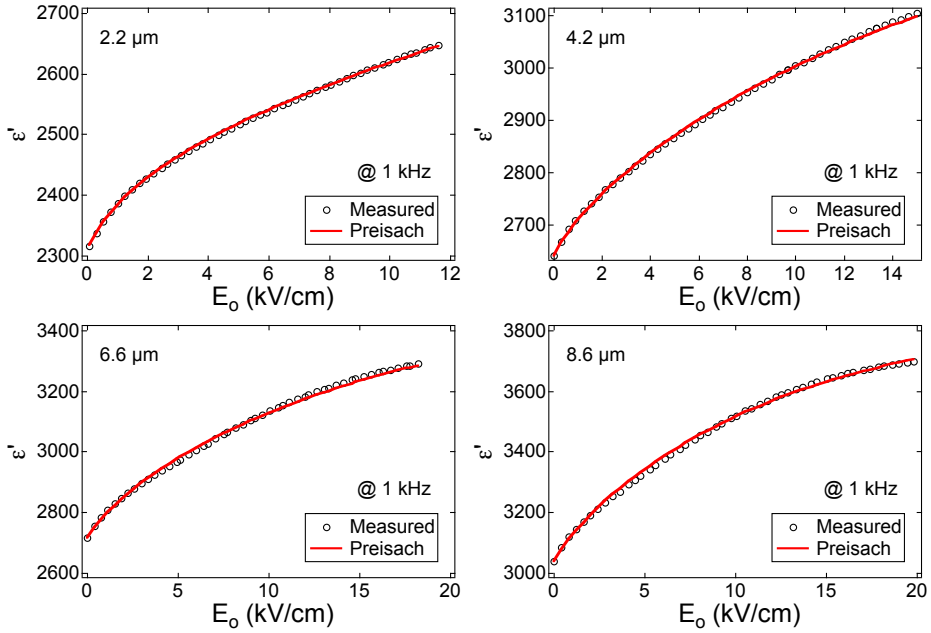

Figure **8-3**: The measured and calculated dielectric constants as a function of the ac field amplitude. The dielectric constant was calculated with a stretched exponential Preisach distribution. The distribution was determined by fitting the P-E loop measured at the same ac field amplitude. The stretched exponential Preisach distribution is only valid for a small field range, because a Preisach distribution depends on both E_k and E_i at high fields.

Effect of oxygen vacancy distribution on the dielectric nonlinearity

In Chapter 6, the effect of the oxygen partial pressure during sintering of the formulated $BaTiO_3$ ceramics on the high field dielectric response was investigated. It was found that the ac field dependence of the dielectric constant of the oxygen- and air-fired samples was almost linear and that of the samples prepared at reducing ambient was sublinear. A disparity in the concentration of defect – oxygen vacancy associates accounted for the difference, as shown in Figs. 8-4 (a) and (b).

It is widely reported that the oxygen vacancies in MLCCs migrate to a cathode at elevated temperatures on exposure to a high voltage (See Fig. 8-4 (c)), which results in failure[29]. Thus, it is interesting to access the importance of the oxygen vacancy distribution on the high field dielectric response.

Initial work was conducted by investigating FORC distributions for aged MLCC in order to see how it changes with the oxygen vacancy distribution. To this end, a Preisach analyzer was designed and constructed, which enabled the FORC distributions and leakage current to be measured as function of time with well-defined temperature and voltage set points. A picture of the Preisach analyzer is shown in Fig. 8-5. It consists of three parts: a P-E measuring unit, a furnace and a computer. The unit applies voltage to samples and measures charge. It also set the temperature of the furnace for the leakage measurement. The furnace is equipped with 4 heaters and a fan. The heaters are on and the fan is off when heating, and vice versa when cooling. Samples are mounted on a DIP with a solder, and the DIP holder is mounted to the furnace door. Up to 15 samples can be measured for a run. The computer controls the measurements. Initial measurements were conducted to assess the system viability.

A commercial X7R Ni-MLCC (C0603C274K9RACTU, KEMET) with the following specifications was investigated in this study; the capacitance is 270nF, unit size 0603, rated

voltage = 6.3V, dielectric thickness = 3.1μm, 77 dielectric layers, total effective area of internal electrode = 0.43cm^2, and average grain size = 0.34±0.13μm. The dielectric thickness, area, and grain size were measured using SEM images of etched, polished surfaces of cross sections of the MLCC.

Initially, first order polarization reversal curves were measured at room temperature by applying triangular voltages with a progressively increasing voltage amplitude. A voltage was applied for 0.01 second. The maximum and minimum voltages were ±50V. The voltage sequence is shown in Fig. 8-6. Then, 50V was applied, the heater was turned on, the fan was turned off, and sample was heated to 150˚C. It took about 55 minutes to reach temperature. The leakage current was measured for 1 second and it was re-measured every 15 minutes 10 times. Then, the sample was cooled to 30˚C (this took 60 minutes). After this, the applied voltage was removed. This process was repeated until the charge exceeded 10^{-4}C (see Fig. 8-7).

A method was developed with the help of Paul Moses (Penn State) to facilitate calculation of the FORC distributions for the large amount of FORC data produced in the aging experiment. The FORC distribution H was calculated with the applied voltages V and the charges Q, where Q are the charges measured for a series of voltages V applied for the sample. Here, the initial voltage should be either the maximum or minimum of the voltages in order to set all of the hysterons to either the up-state (-1) or down-state (+1). Then, a switching matrix S, which describes the state of hysterons, was calculated for V. Here, H, Q, and S satisfy the following relation:[132]

$$S \cdot H = Q$$
$$\Leftrightarrow$$
$$\begin{pmatrix} s_{11} & s_{12} & \cdots & s_{1n} \\ s_{21} & s_{22} & \cdots & s_{2n} \\ s_{31} & s_{32} & \cdots & s_{3n} \\ \vdots & \vdots & \ddots & \vdots \\ s_{m1} & s_{m2} & \cdots & s_{mn} \end{pmatrix} \cdot \begin{pmatrix} h_1 \\ h_2 \\ \vdots \\ h_n \end{pmatrix} = \begin{pmatrix} q_1 + c \\ q_2 + c \\ q_3 + c \\ \vdots \\ q_m + c \end{pmatrix} \qquad \text{Eq. 8-1}$$

where c is a constant. V must be chosen to solve Eq. 8-1, and the number of V steps, which is the same as Q, is no less than the number of hysterons (thus, m≥n). Therefore, S become a square or overdetermined matrix. Eq. 8-1 can be solved with a singular value decomposition method, in which S is decomposed to:[132]

$$S = U \cdot w \cdot V^T \qquad \text{Eq. 8-2}$$

where U is a m x n orthogonal matrix (m≥n), w is a n x n diagonal matrix, and V^T is a transpose of the n x n orthogonal matrix. Substituting Eq. 8-2 to Eq. 8-1 gives:[132]

$$H = V \cdot w^{-1} \cdot U^T \cdot Q \qquad \text{Eq. 8-3}$$

Figure 8-8 shows the leakage current as a function of the time. Note that the timing was started when the experiment started, so it is not identical to the time that the sample was heated at 150˚C. The leakage current was almost constant ($2x10^{-8}$ A/mm^2) up to $1.5x10^5$ seconds, and then it started increasing, as would be expected for the onset of dielectric degradation.

For the FORC measurement, the charges were measured continuously with a reference state when the voltages were applied. Figure 8-9 shows selected FORC measured at time = $1x10^4$, $1x10^5$, $2x10^5$, and $3x10^5$ sec. The leakage current was constant at time = $1x10^4$ and $1x10^5$ sec., while it was increasing at the time = $2x10^5$, and $3x10^5$ sec. The loops appeared similar, except that the saturation polarization dropped as the time elapsed.

Figures 8-10 and 8-11 show the reversible and irreversible FORC distribution measured at the time = $1x10^4$, $1x10^5$, $2x10^5$, and $3x10^5$ sec. No significant difference was observed for the samples measured over this time scale in this initial study. Since MLCC has small, flat irreversible FORC distribution, it may be difficult to see the difference at this field range. Work should continue on optimizing the field amplitude and the system, and assessing its use in characterizing degradation processes.

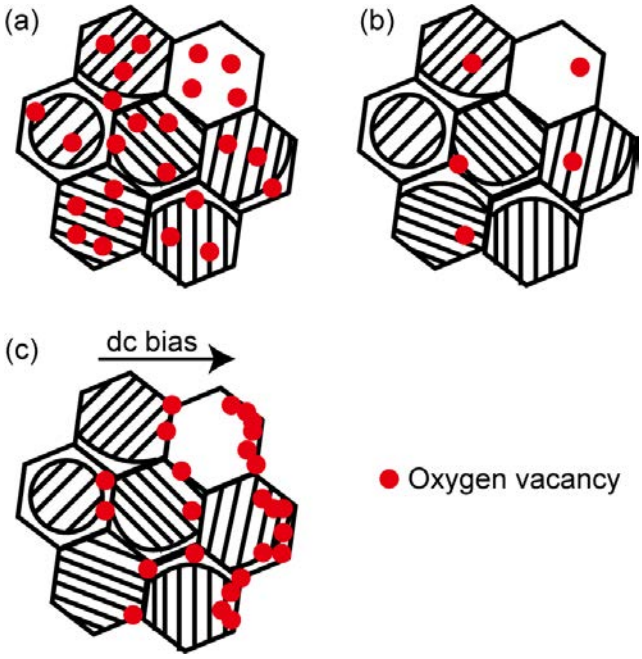

Figure **8-4**: Schematics of oxygen vacancy distribution in $BaTiO_3$ based dielectric. (a) reduced state, (b) oxidized state, and (c) reduced state with oxygen vacancy migration in dc bias.

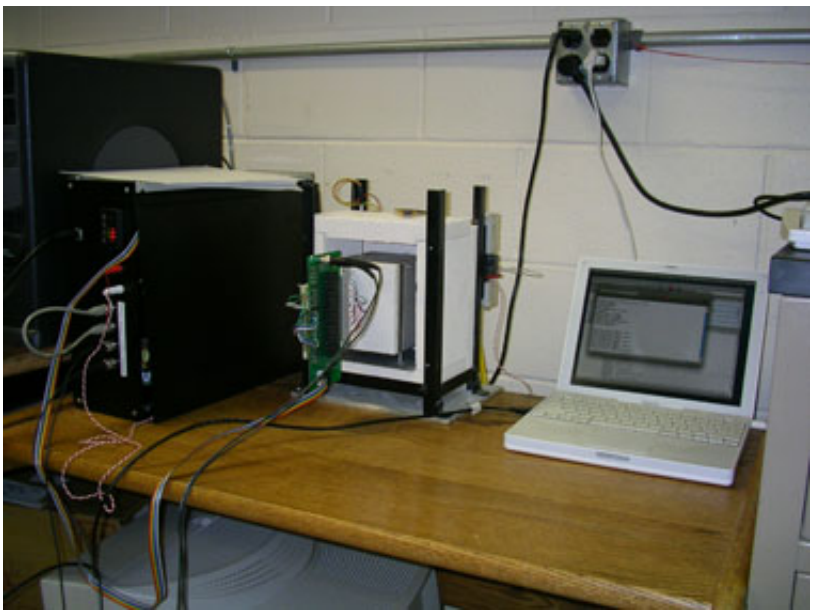

Figure **8-5**: A picture of the Preisach analyzer.

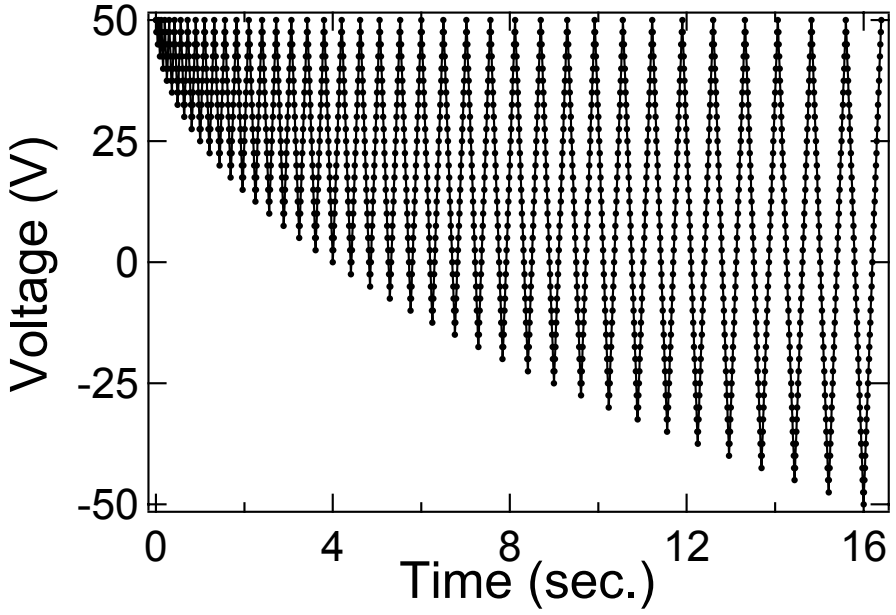

Figure **8-6**: Time dependence of the applied voltage for FORC measurement.

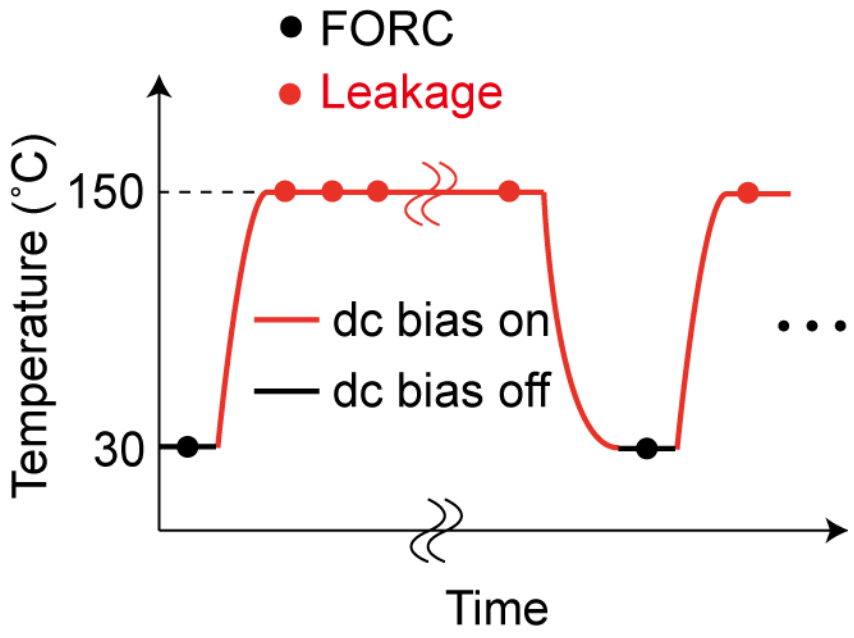

Figure **8-7**: Schedule for the FORC – leakage measurement.

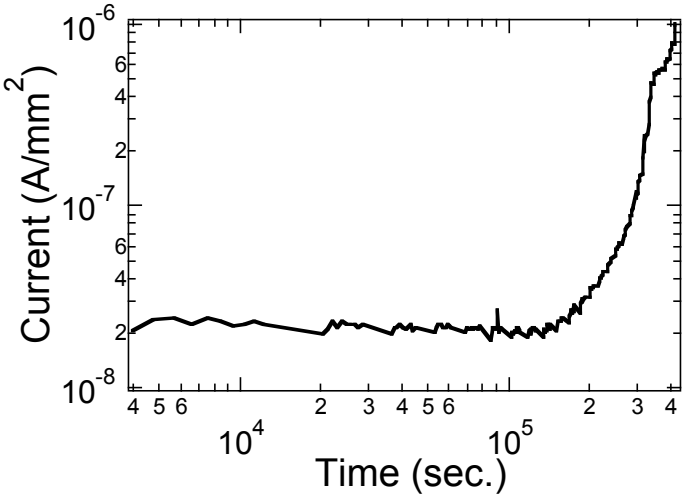

Figure **8-8**: The leakage current measured at 150˚C and 50V (~16V/μm).

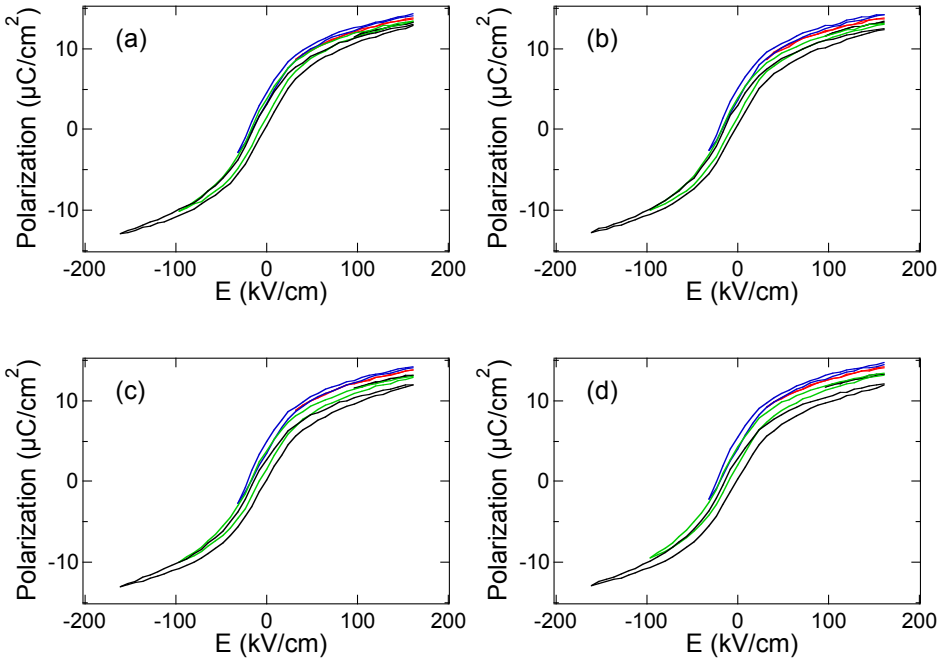

Figure **8-9**: Selected FORC measured at the time = (a) 1x10^4, (b) 1x10^5,(c) 2x10^5, and (d) 3x10^5 sec. The color specifies different field amplitudes.

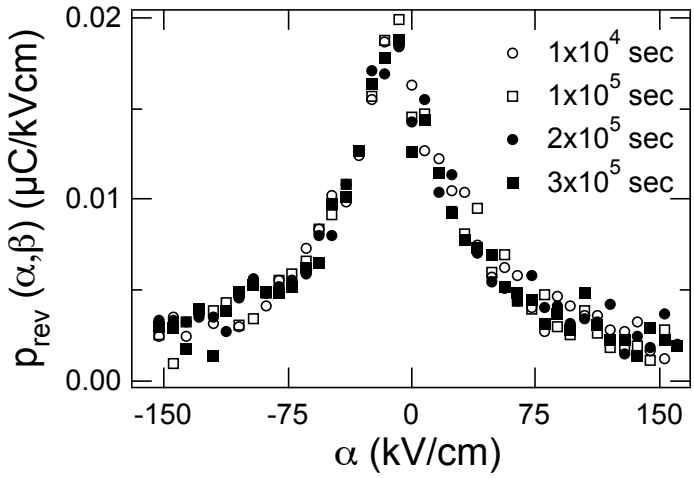

Figure **8-10**: The reversible FORC distributions measured at various elapsed time.

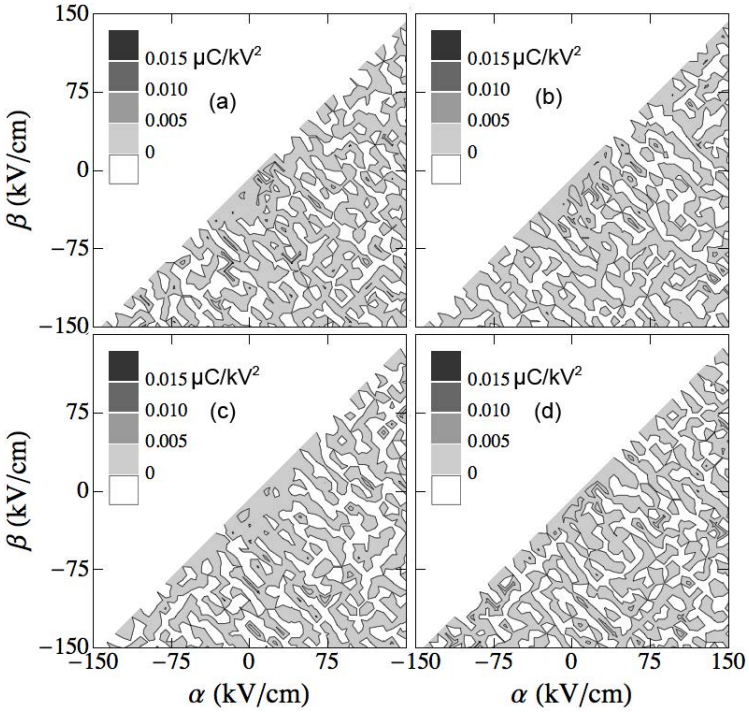

Figure **8-11**: The irreversible FORC distributions measured at the time = (a) 1x10^4 sec, (b) 1x10^5 sec, (c) 2x10^5 sec, and (d) 3x10^5 sec.

Appendix

Temperature Dependence of Dielectric Nonlinearity of Ferroelectrics

The ac field dependence of the dielectric properties changes with temperature, as shown in Fig. A-1. This appendix provides data for the temperature dependence of the dielectric nonlinearity of samples studied in this thesis. The temperature dependence of the domain wall contributions was quantified with (pseudo-) Rayleigh analyses and FORC distributions.

Figure A-1 shows the ac field dependence of the dielectric constant of the PZT films with film thicknesses of 0.26, 0.53, and 0.93 μm measured at various temperatures between 200˚C and -150˚C. The maximum applied ac field amplitude was set to half the coercive field. With increasing temperature, the coercive field decreased, decreasing the field range over which Rayleigh behavior was observed. Rayleigh-like responses was observed at temperatures below 200˚C, where a strong space charge contribution contaminated the measurement. The Rayleigh parameters are shown in Fig. A-2. Both ε_{init}' and α' increased with temperature. This suggests that the potential energy profile through which domain walls move became smoother with increasing the temperature. The Rayleigh parameters increased with the dielectric thickness, as discussed in chapter 4. It was found that the temperature dependence of ε_{init}' and α' depended on the dielectric thickness; thicker dielectric showed a stronger temperature dependence. This is consistent with the result of chapter 4 that the domain wall contributions increased with the dielectric thickness.

Figure A-3 shows the ac field dependence of the dielectric properties of the undoped $BaTiO_3$ ceramics with a grain size of 76 μm (studied in chapter 5) measured at various temperatures. Above T_c, the dielectric properties were essentially independent of the ac field amplitude due to loss of ferroelectricity. Below T_c, they depend on the amplitude. At

temperatures between 80˚C and 125˚C, the peak dielectric constant decreased with increasing temperature. It is believed that this is attributable to a reduction in maximum polarization with temperature. At temperatures below 80˚C, the ac field dependence of the dielectric constant was suppressed with decreasing temperature, except at temperatures near one of the phase transitions, where the domain wall contributions increase. Similar responses were observed for the dielectric loss over most of the temperature range. However, at lower temperatures (-50˚C to -150˚C), the loss increased with decreasing temperature, suggesting a strong irreversible domain wall contribution. The increase in small field dielectric loss at -150˚C is associated with the dielectric relaxation, as discussed in chapter 5.

Figure A-4 shows the ac field dependence of the dielectric properties of the undoped $BaTiO_3$ ceramics with a grain size of 1.2 μm (see chapter 6: the ceramics were sintered at an oxygen partial pressure of 10^{-2} atm and post-annealed in air) measured at temperatures between 150˚C and -150˚C. It was observed that the ac field dependence was suppressed compared to the large grained sample. This is attributable to strong pinning of domain walls from grain boundaries.

These responses were quantified by a pseudo-Rayleigh analysis that replaced ε_{init}' with a dielectric constant measured at a small field amplitude j, ε'_j and replaced α' with a slope for the dielectric constants measured at the field amplitudes j and i (i > j), α'_i. Figure A-5 shows the temperature dependence of the pseudo-Rayleigh parameters of the $BaTiO_3$ ceramics with grain size of 76 μm or 1.2 μm. The field i was chosen to be ~0.5 kV/cm and ~2kV/cm in order to quantify domain wall contributions at subcoercive fields and at fields for the peak dielectric constant. The $\varepsilon'_{0.03kV/cm}$ traced the temperature dependence of the dielectric constant (See chapter 5). For the 76 μm grain size sample, the temperature dependence of $\alpha'_{2kV/cm}$. is consistent with that of the peak dielectric constant. Above -70˚C, $\alpha'_{2kV/cm}$ is larger than $\alpha'_{0.5kV/cm}$, indicating a superlinear ac field dependence. This, in turn, suggests a sublinear response below this temperature, which would be consistent with a restriction in long-range domain wall motion. A

clear peak associated with the orthorhombic to rhombohedral phase transition was observed for $\alpha'_{0.5kV/cm}$. For the 1.2 μm grain size sample, $\alpha'_{2kV/cm}$ and $\alpha'_{0.5kV/cm}$ were suppressed relative to the large grained sample. The $\alpha'_{2kV/cm}$ was smaller than $\alpha'_{0.5kV/cm}$, which is a consequence of a sublinear ac field dependence of the dielectric constant. A peak associated with the tetragonal to orthorhombic phase transition and one associated with the orthorhombic to rhombohedral phase transition were observed.

The temperature dependence of the high field dielectric response of the sample was characterized using FORC distributions. Figure A-6 shows the FORC of the sample measured at temperatures between 135˚C and -70˚C. Above T_c, the response was nonhysteretic. With decreasing temperature, the response became hysteretic and the maximum polarization increased. Below 20˚C, upward drift of minor loops became stronger and the sample became more difficult to polarize. In addition, a small pinching was observed. As discussed in chapters 5 and 6, oxygen vacancy-related defect dipoles exist in the sample, which could account for the pinching. With decreasing temperature, the mobility of domain walls decreases and therefore the effectiveness of the pinning field increased.

The irreversible FORC distributions are shown in Fig. A-7. Above T_c, the irreversible FORC distribution is essentially zero due to loss of ferroelectricity. With decreasing temperature, a peak centered at the origin appeared, its intensity and breadth increased. This is consistent with the temperature evolution of the FORCs; both the switchable polarization and the coercive field increased with decreasing temperature. Moreover, a streak appeared along $\alpha=\beta$ line at positive α and β. This is attributable to the finite time-dependence of the switching. Below 20˚C, an additional peak appeared along α axis. This is due to the pinning. The intensity of the streak increased due to the rounding of the edges of FORC. Note that the peak intensity was smaller than those calculated in chapter 5 due to an increase in the maximum applied field; the larger maximum applied field is, the more the distribution function is smoothed.

The reversible FORC distributions are shown in Fig. A-8. Above T_c, the field dependence of the reversible FORC distribution was reduced due to loss of the domain wall contributions. Below T_c, the distributions at zero bias decreased with temperature due to reductions in both the intrinsic dielectric response and reversible domain wall contribution with temperature. Taken together, the reversible and irreversible FORC distributions indicate that, as expected, domain walls moved more irreversibly with decreasing temperature. At high negative biases, the reversible distribution converged into two values; one for temperatures between 120˚C and 50˚C and the other for temperatures between 20˚C and -70˚C. The latter has a lower value. This could be caused by the pinching, which created weak pinning centers that reduce the reversible and irreversible domain wall motion. At positive high biases, the reversible FORC distribution did not converged because of the rounding of the FORCs.

Figure A-9 shows the ac field dependence of the dielectric properties of $BaTiO_3$ ceramics sintered at 10^{-9} atm pO_2 with a 1.2 μm grain size (studied in chapter 6) measured at various temperatures. It was found that the response was similar to that of the sample sintered at 10^{-2} atm pO_2, except that the rapid increase in the dielectric properties at moderate ac fields at 20˚C and larger loss above T_c, as discussed in chapter 6. The effect of the pO_2 on the dielectric nonlinearity was quantified at various temperatures, as shown in Fig. A-10. It was found that the temperature dependence of the pseudo-Rayleigh parameters were similar, except that the α'_i of 10^{-9} atm pO_2 sample were larger than those of 10^{-2} atm pO_2 sample, which is attributable to the de-pinning of domain walls from weak pinning centered associated with the defect dipoles, as was discussed in chapter 6.

Figures A-11 and A-12 show the ac field dependence of the dielectric properties of the formulated $BaTiO_3$ ceramics sintered at 10^{-2} and 10^{-9} atm pO_2, respectively (studied in chapter 6). Above T_c, the dielectric constant of both samples was independent of temperature. At 20˚C, the ac field dependence of the 10^{-2} atm pO_2 sample was almost linear, while that of the 10^{-9} atm pO_2

sample was sublinear, which is consistent with the results in chapter 6. The dielectric responses were quantified using pseudo-Rayleigh analysis, as shown in Fig. A-13. As expected, the temperature dependence of the small field dielectric constant was consistent with the data in chapter 7. Below T_c, the dielectric constant of the 10^{-2} atm pO_2 sample monotonically decreased with temperature, while that of the 10^{-9} atm pO_2 sample showed a core/shell response. With decreasing temperature, α'_i increased up to the orthorhombic to rhombohedral phase transition, and then decreased, which is consistent with the α'_i for the small grained $BaTiO_3$ ceramics (although an increase at the tetragonal to orthorhombic phase transition was smeared). It was found that the difference of the α'_i between the samples was small above the T_c of the shell region. This suggests that the domain wall contributions are strongly influenced by the shell region. Note that near room temperature, $\alpha'_{2kV/cm}$ and $\alpha'_{0.5kV/cm}$ of the 10^{-2} atm pO_2 sample was similar, which corresponds to the Rayleigh behavior.

Figure A-14 shows the ac field dependence of the dielectric constant for MLCCs with various grain sizes (studied in chapter 7) measured at various temperatures. Above T_c, the dielectric constant was independent of the ac field amplitude. Below T_c, the dielectric constant depends on the ac field and the ac field dependence increased with decreasing temperature. The ac field dependence was quantified using pseudo-Rayleigh analysis, as shown in Fig. A-15. The ε'_j follow a core/shell response of the dielectric constant. With decreasing grain size, the dielectric constant decreased, as discussed in chapter 7. The temperature dependence of the α'_i was similar to the formulated $BaTiO_3$ ceramics sintered in 10^{-9} atm pO_2. The peak at the orthorhombic to rhombohedral phase transition decreased with grain size. This is consistent with the grain size dependence of the undoped $BaTiO_3$ ceramics. It was observed that the grain size dependence of α'_i was relatively weak above the T_c of the shell. This result is consistent with the

pO_2 dependence of α'_i for the formulated $BaTiO_3$ ceramics, suggesting the influence of the shell region on irreversible domain wall contributions.

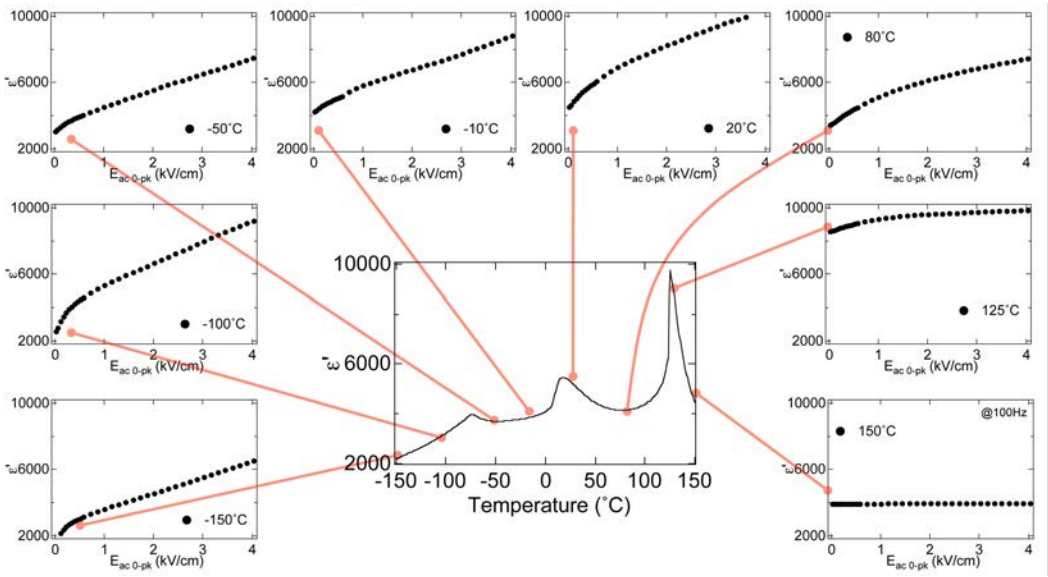

Figure **A-1**: Temperature dependence of the ac field dependence of the dielectric constant of a $BaTiO_3$ ceramic.

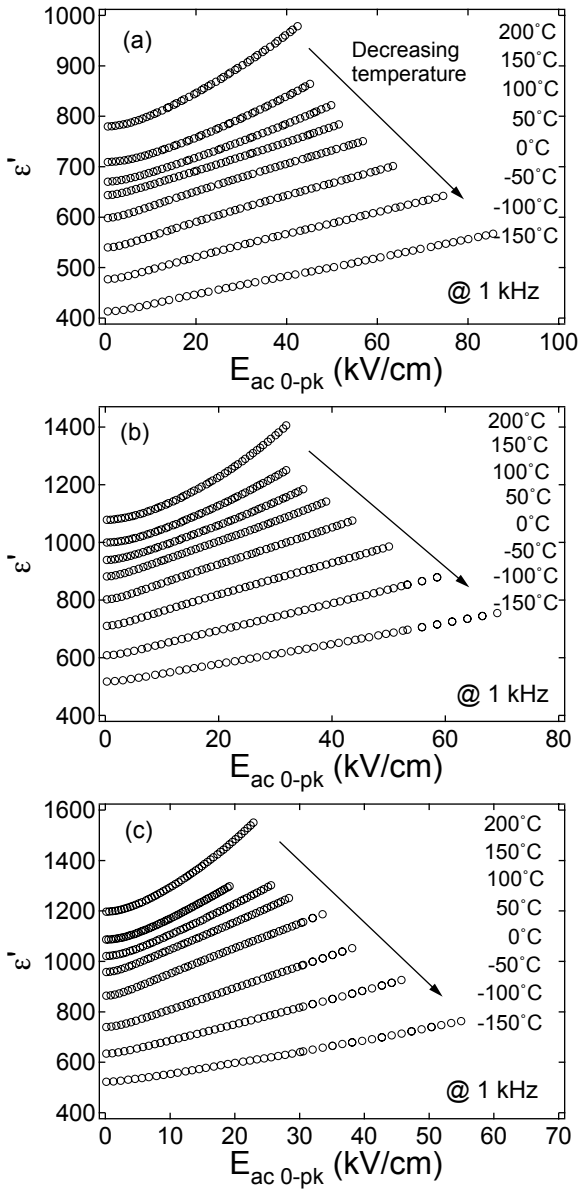

Figure **A-2**: The ac field dependence of the dielectric constant of PZT films with thicknesses of (a) 0.26 μm, (b) 0.53 μm, and (c) 0.925 μm (studied in chapter 4) measured at various temperatures.

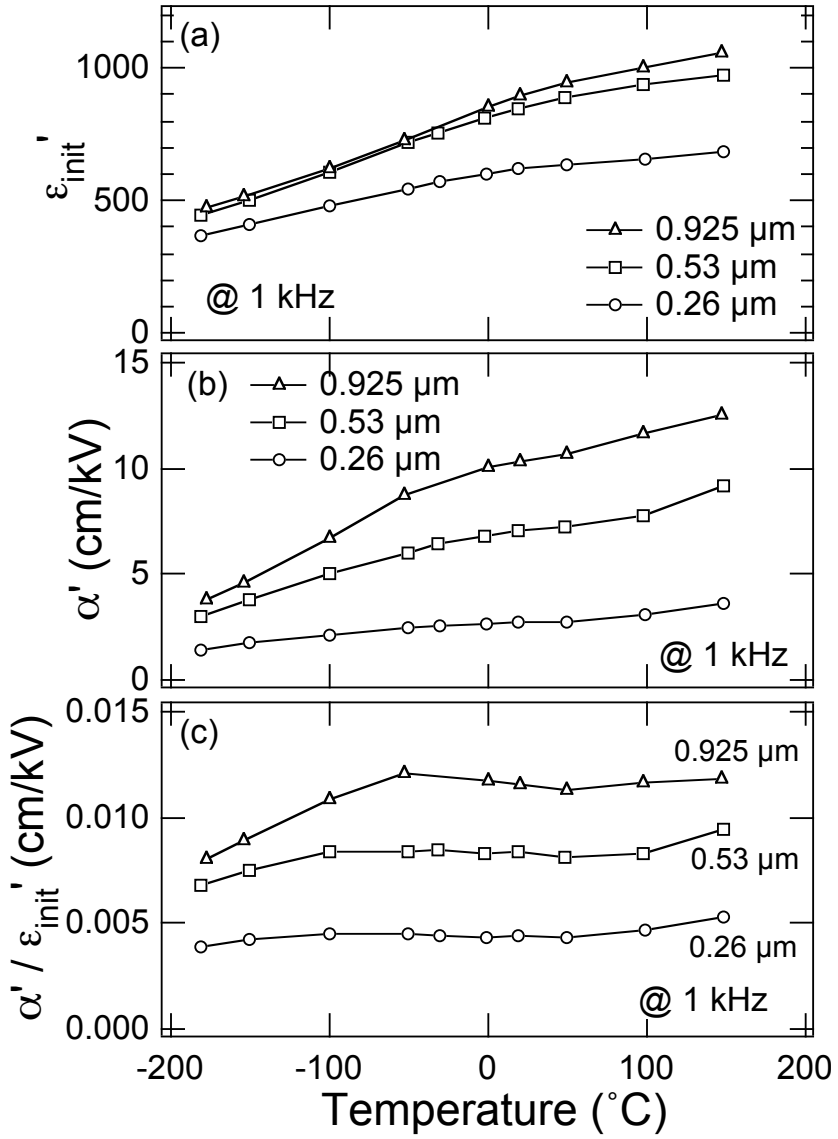

Figure **A-3**: The Rayleigh parameters (a) ε_{init}', (b) α', and (c) $\alpha'/\varepsilon_{init}$' for PZT films with various dielectric thicknesses (studied in chapter 4).

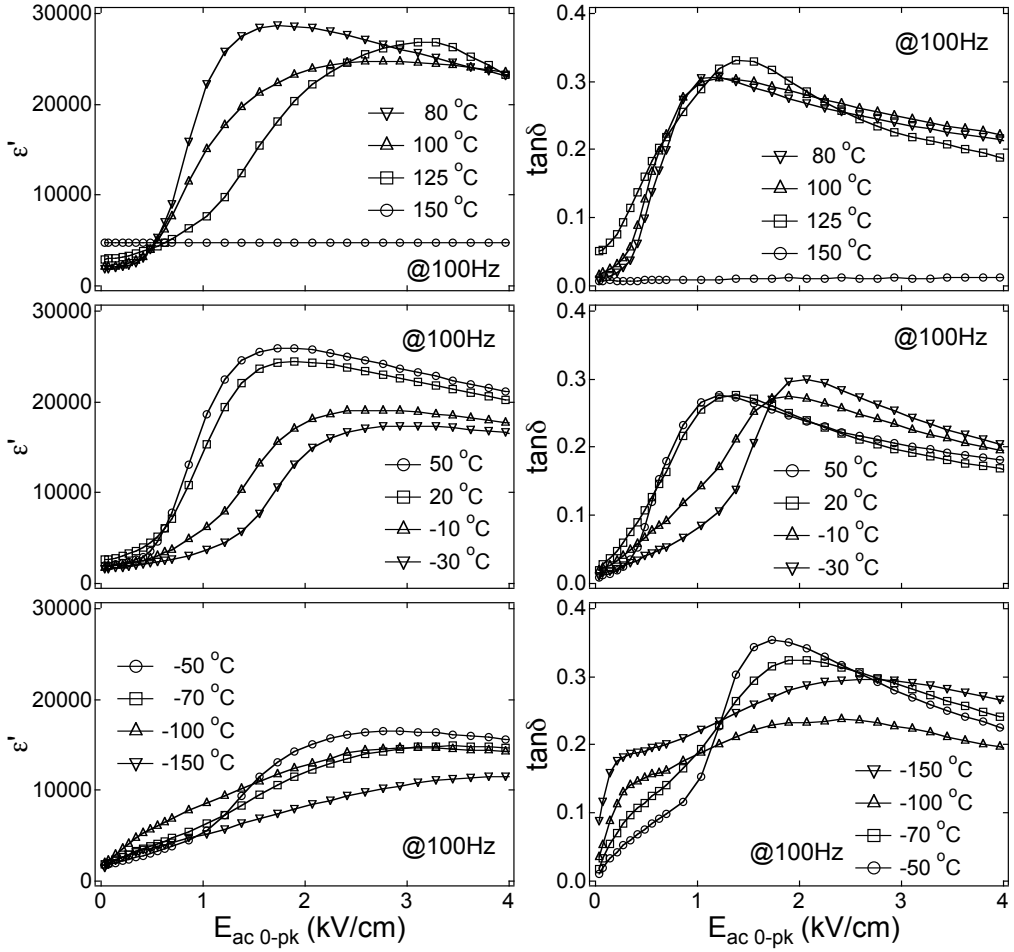

Figure **A-4**: The ac field dependence of the dielectric properties of an undoped $BaTiO_3$ ceramic with a grain size of 76 μm (Sample D in chapter 5) measured at various temperatures.

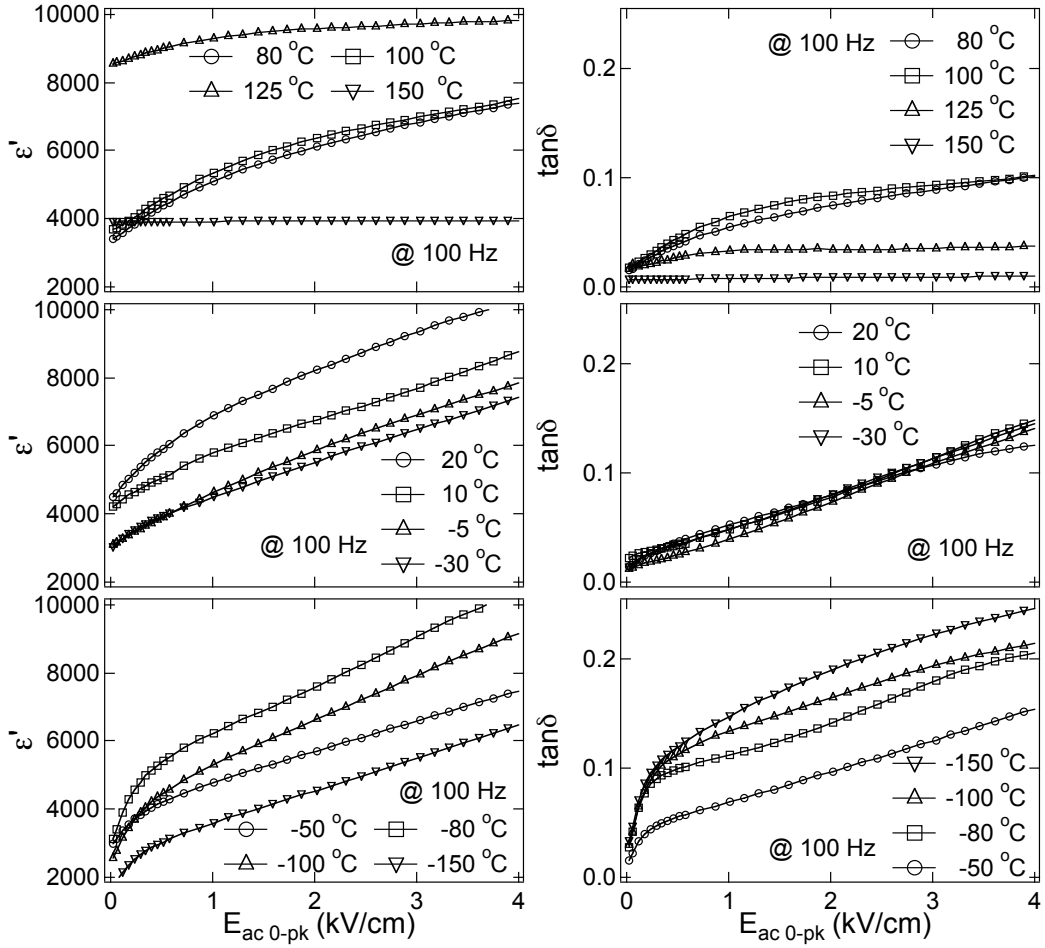

Figure **A-5**: The ac field dependence of the dielectric properties of undoped $BaTiO_3$ ceramics with a grain size of 1.2 μm (the ceramic was sintered at 1300˚C at 10^{-2} atm pO_2 and then post-annealed, as described in chapter 6) measured at various temperatures.

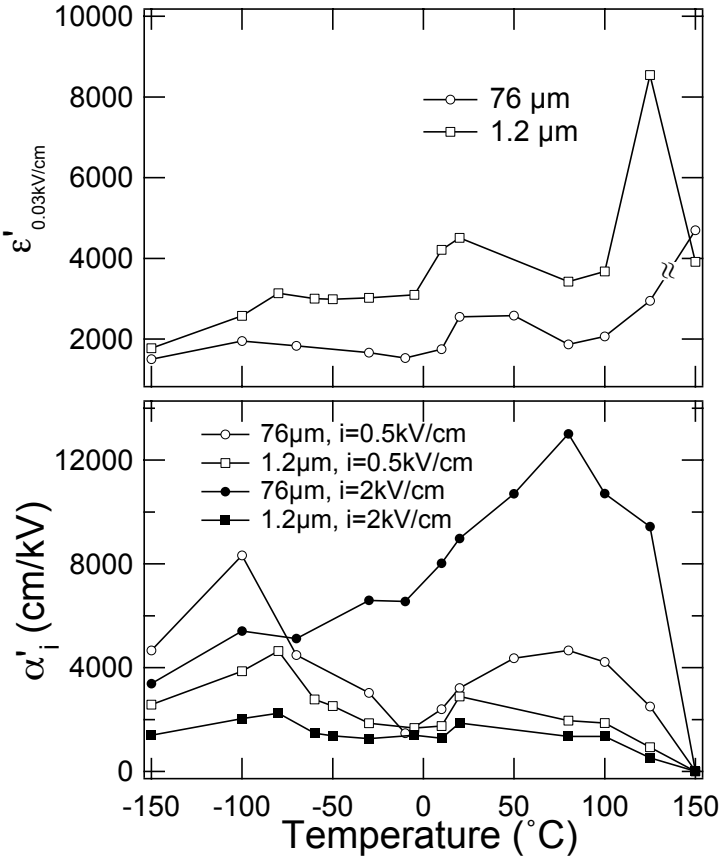

Figure **A-6**: The temperature dependence of the pseudo-Rayleigh parameters of the $BaTiO_3$ ceramics with grain sizes of 76 μm or 1.2 μm.

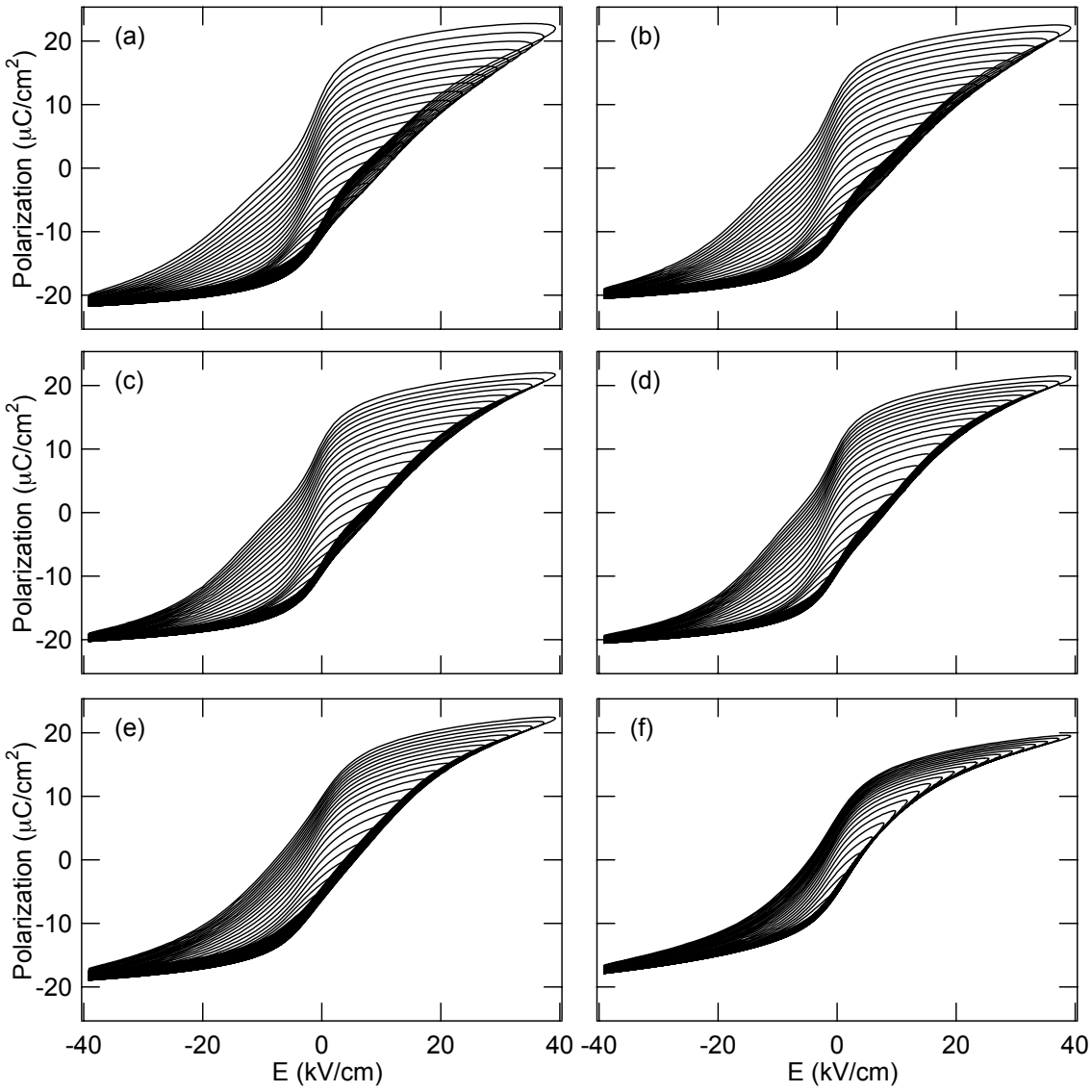

Figure **A-7**: The FORC of the undoped $BaTiO_3$ ceramics with grain size of 1.2 μm (sintered at 1300˚C at 10^{-2} atm pO_2 and then post-annealed, as detailed in chapter 6) measured at (a) -70˚C, (b) -50˚C, (c) -30˚C, (d) -10˚C, (e) 20˚C, (f) 50˚C, (g) 80˚C, (h) 100˚C, (i) 120˚C, and (j) 135˚C.

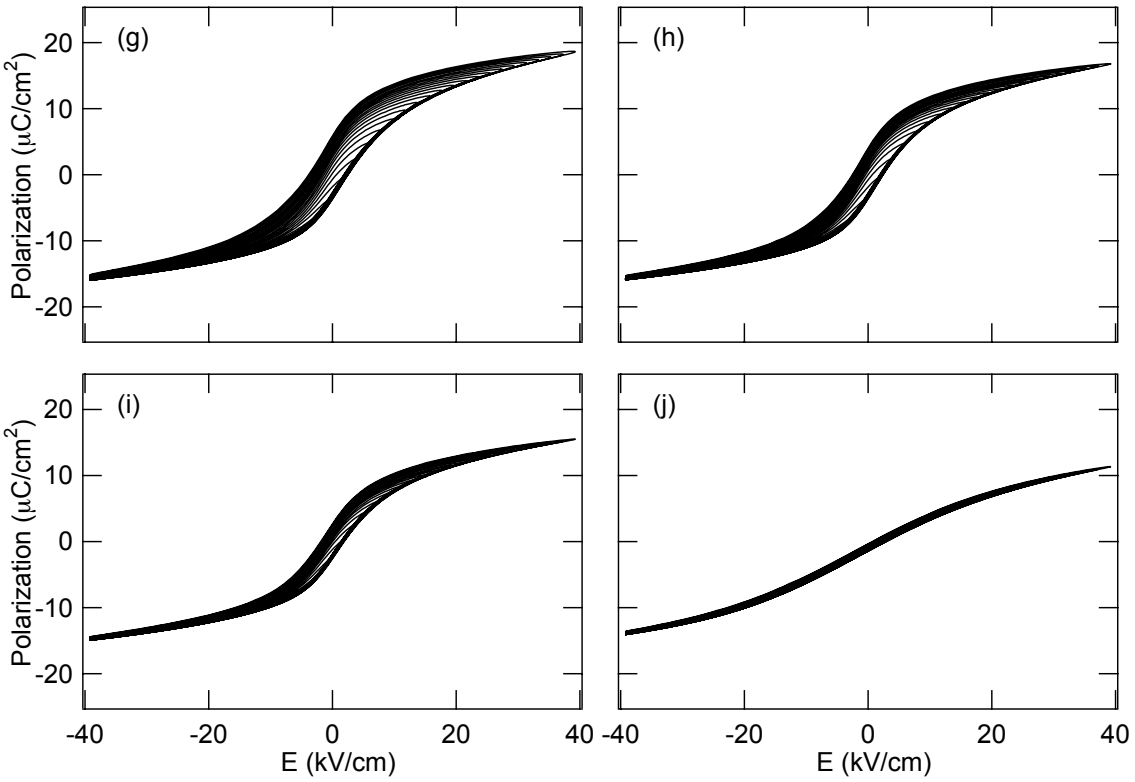

Figure **A-7 continued**: The FORC of the undoped $BaTiO_3$ ceramics with grain size of 1.2 μm (sintered at 1300˚C at 10^{-2} atm pO_2 and then post-annealed, as detailed in chapter 6) measured at (a) -70˚C, (b) -50˚C, (c) -30˚C, (d) -10˚C, (e) 20˚C, (f) 50˚C, (g) 80˚C, (h) 100˚C, (i) 120˚C, and (j) 135˚C.

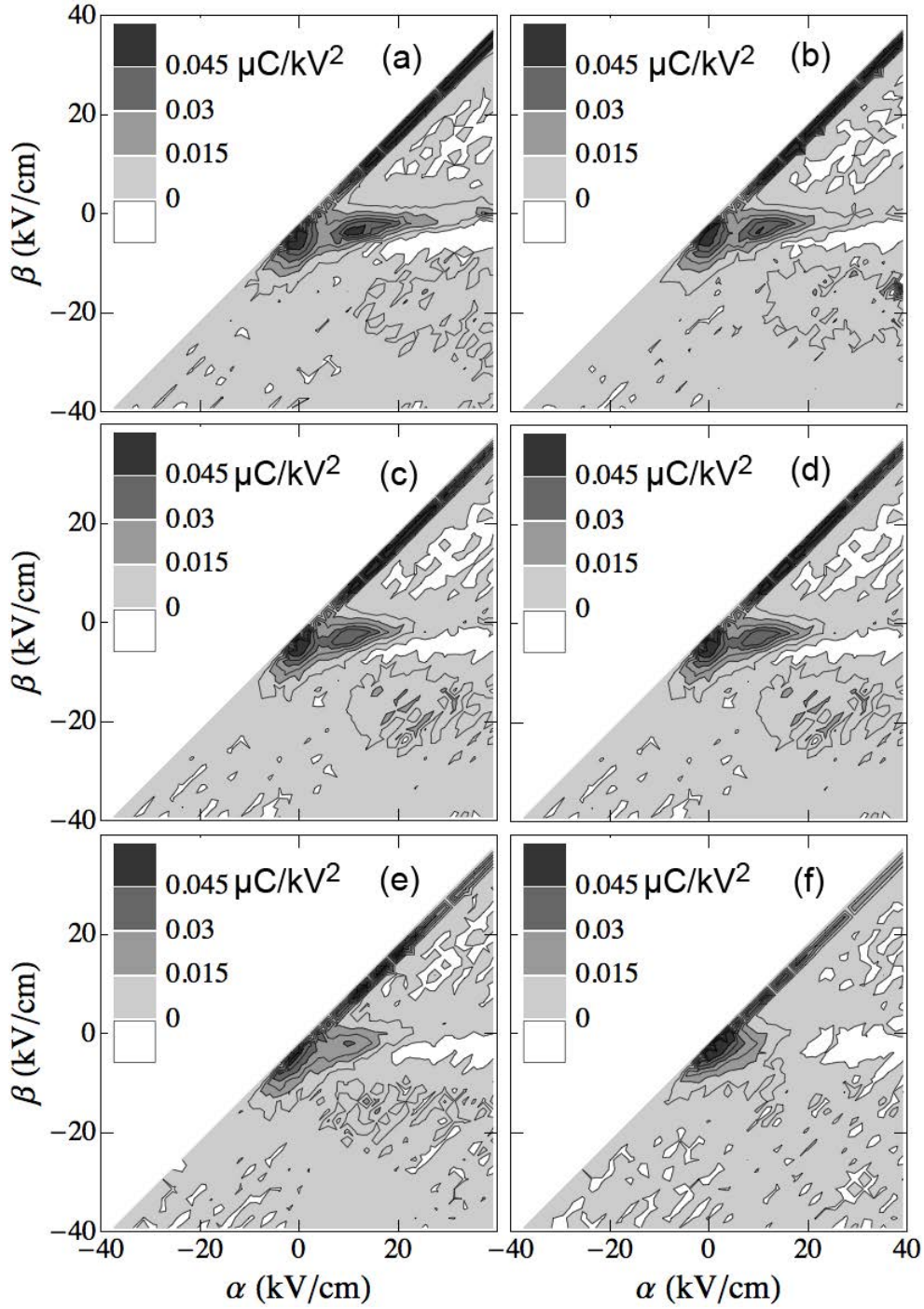

Figure **A-8**: The irreversible FORC distributions for undoped $BaTiO_3$ ceramics with a grain size of 1.2 μm (sintered at 1300˚C at 10^{-2} atm pO_2 and post-annealed, as described in chapter 6) measured at (a) -70˚C, (b) -50˚C, (c) -30˚C, (d) -10˚C, (e) 20˚C, (f) 50˚C, (g) 80˚C, (h) 100˚C, (i) 120˚C, and (j) 135˚C.

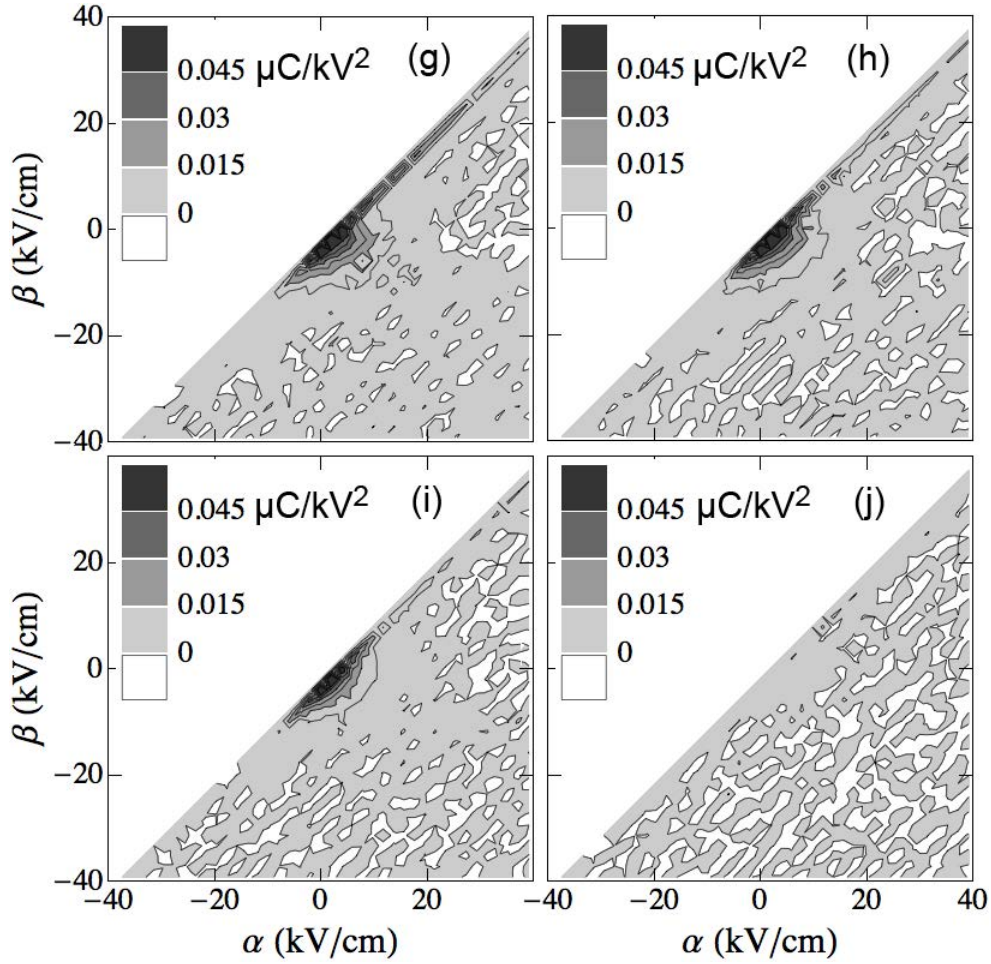

Figure **A-8 continued**: The irreversible FORC distributions for undoped $BaTiO_3$ ceramics with a grain size of 1.2 μm (sintered at 1300˚C at 10^{-2} atm pO_2 and post-annealed, as described in chapter 6) measured at (a) -70˚C, (b) -50˚C, (c) -30˚C, (d) -10˚C, (e) 20˚C, (f) 50˚C, (g) 80˚C, (h) 100˚C, (i) 120˚C, and (j) 135˚C.

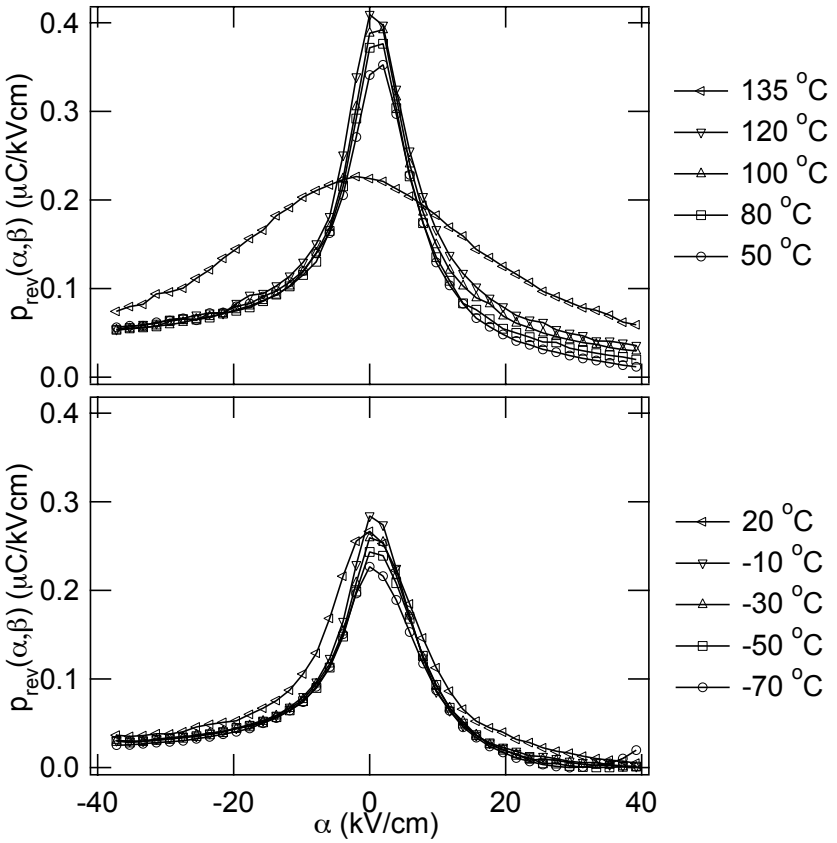

Figure **A-9**: The reversible FORC distributions for undoped $BaTiO_3$ ceramics with a grain size of 1.2 μm (sintered at 1300˚C at 10^{-2} atm pO_2 and then post-annealed, as described in chapter 6) measured at various temperatures.

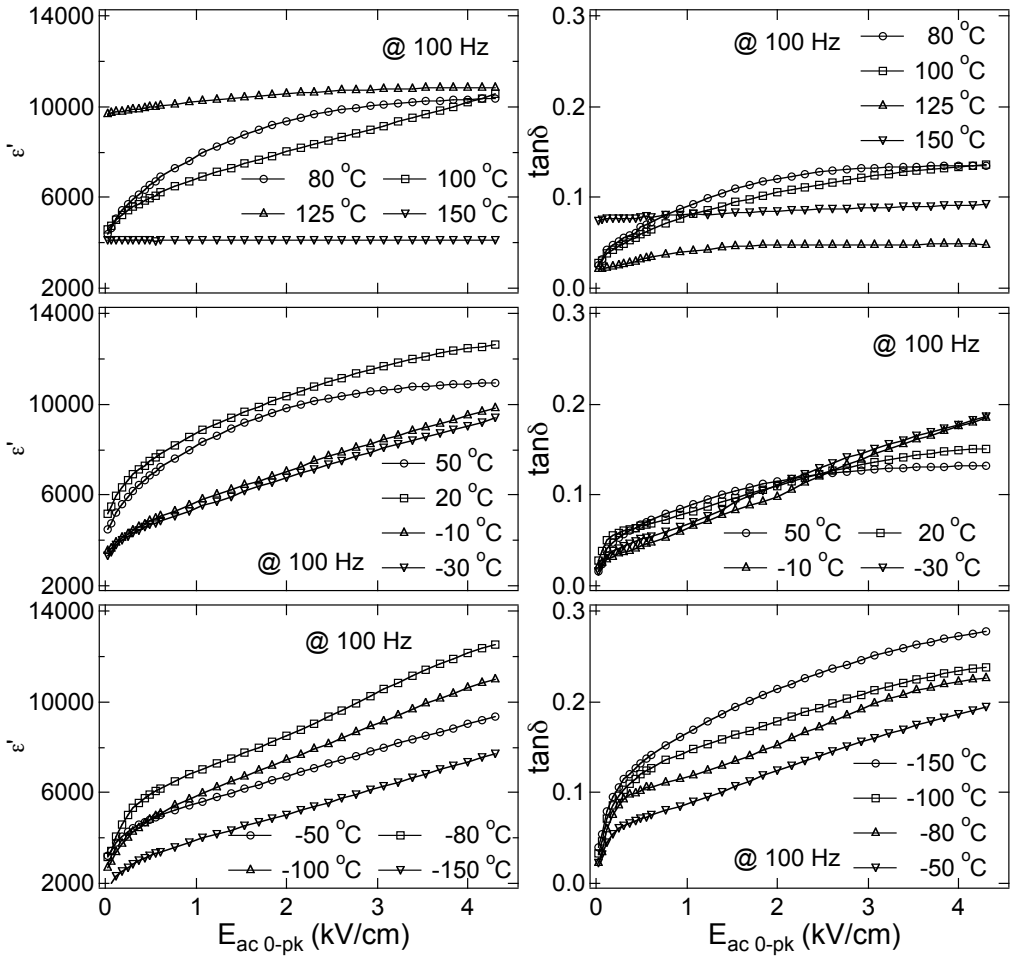

Figure **A-10**: The ac field dependence of the dielectric properties of an undoped $BaTiO_3$ ceramic sintered at 10^{-9} atm pO_2 with a 1.2 μm grain size (studied in chapter 6) measured at various temperatures.

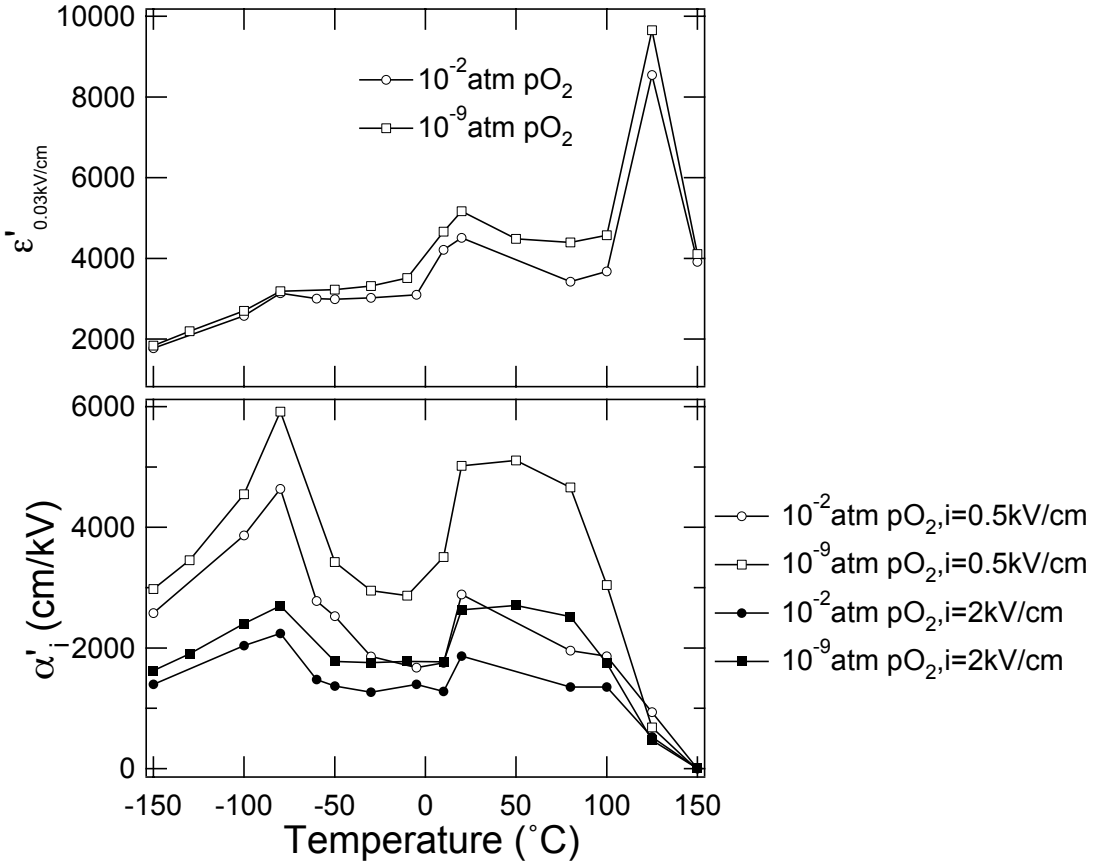

Figure **A-11**: The temperature dependence of the pseudo-Rayleigh parameters of the $BaTiO_3$ ceramics sintered at 10^{-9} atm pO_2 and the $BaTiO_3$ ceramics sintered at 10^{-2} atm pO_2 and post-annealed.

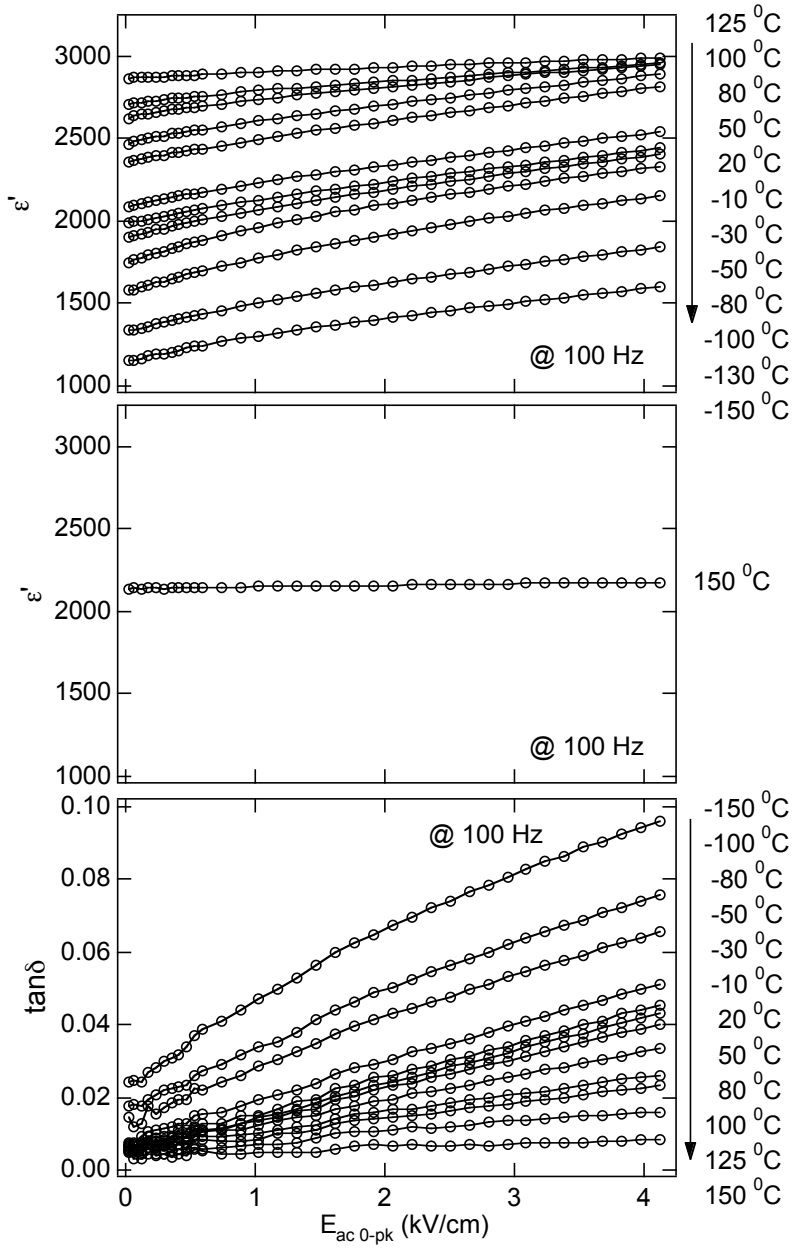

Figure **A-12**: The ac field dependence of the dielectric properties of the formulated $BaTiO_3$ ceramics sintered at 10^{-2} atm pO_2 (studied in chapter 6) measured at various temperatures.

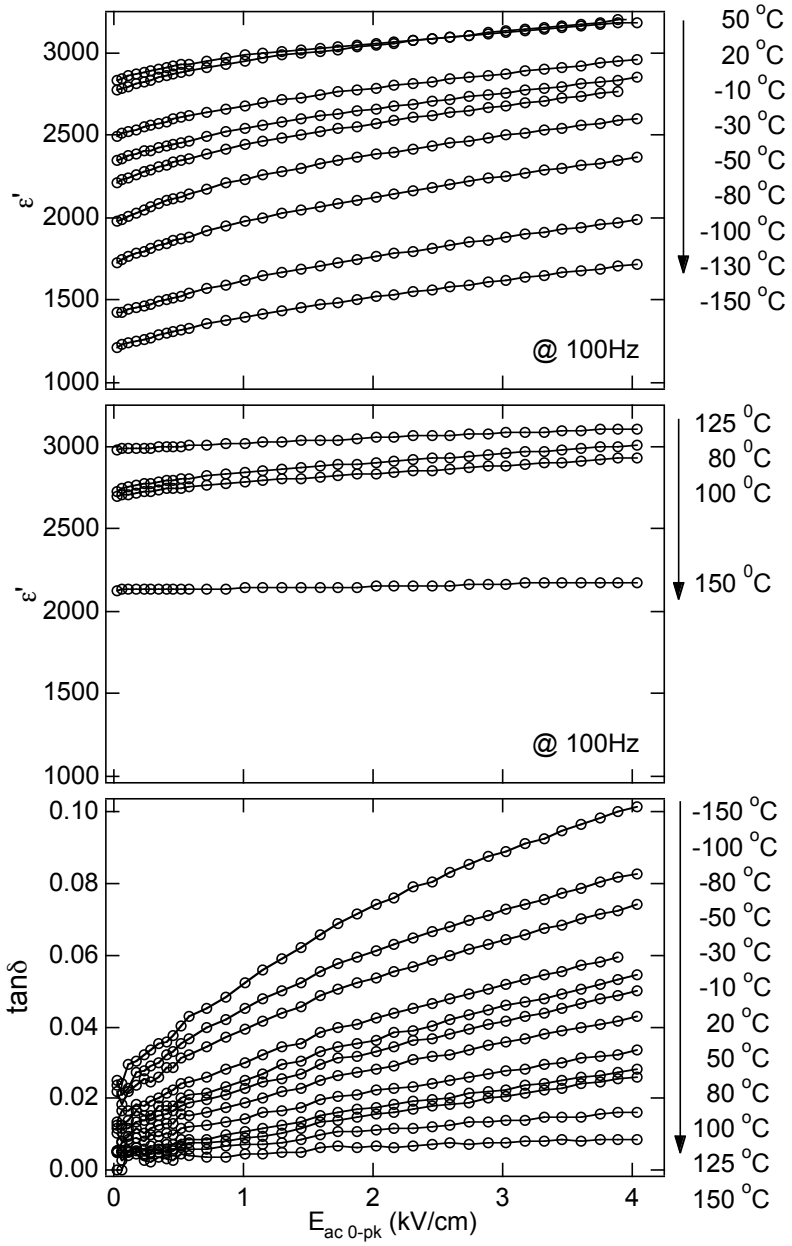

Figure **A-13**: The ac field dependence of the dielectric properties of the formulated $BaTiO_3$ ceramics sintered at 10^{-9} atm pO_2 (studied in chapter 6) measured at various temperatures.

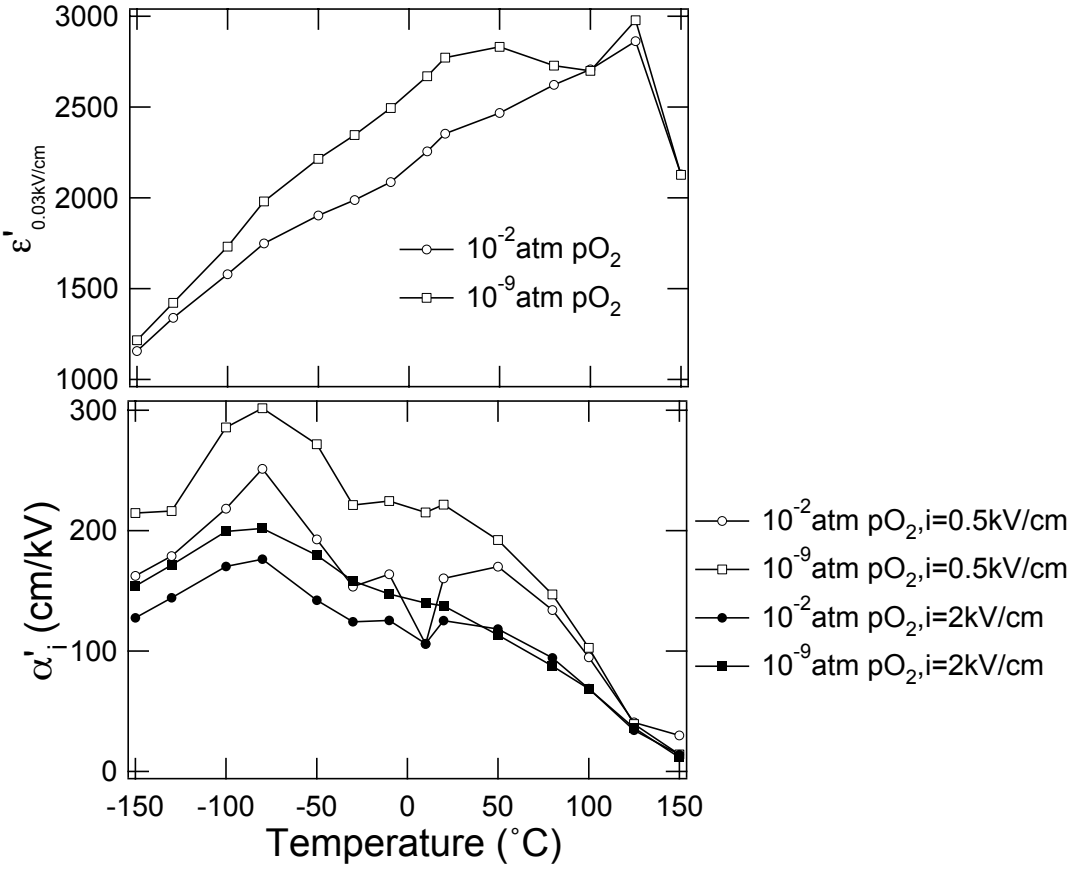

Figure **A-14**: The temperature dependence of the pseudo-Rayleigh parameters of formulated $BaTiO_3$ ceramics sintered at 10^{-9} atm pO_2 or 10^{-2} atm pO_2.

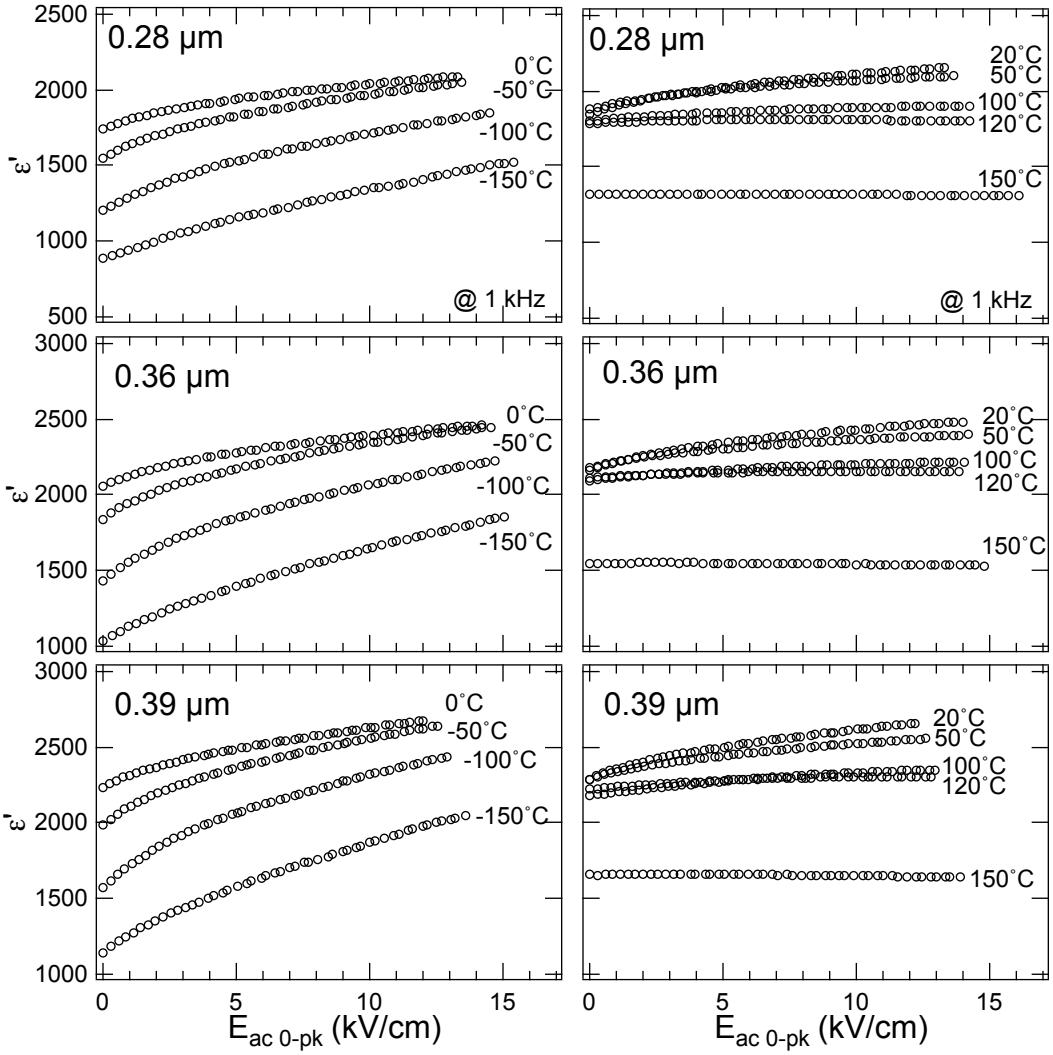

Figure **A-15**: The ac field dependence of the dielectric properties of MLCCs with different grain sizes (studied in chapter 7) measured at various temperatures.

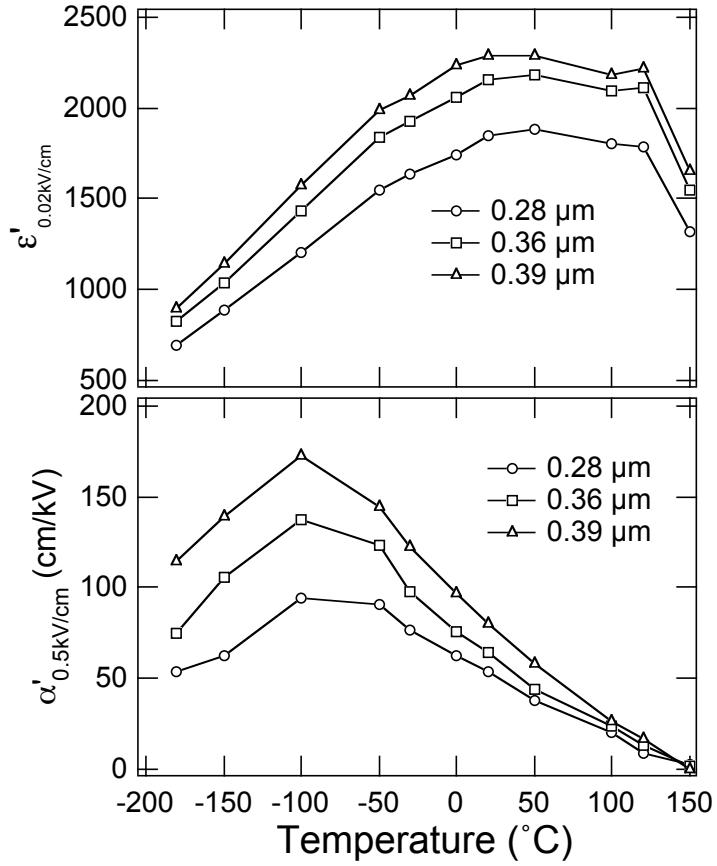

Figure **A-16**: The temperature dependence of the pseudo-Rayleigh parameters of the MLCCs with various grain sizes.

References

[1]G. Arlt and H. Dederichs, "Complex Elastic, Dielectric and Piezoelectric Constants by Domain-Wall Damping in Ferroelectric Ceramics," *Ferroelectrics,* **29**[1-2] 47-50 (1980).

[2]G. Arlt, H. Dederichs, and R. Herbiet, "90-Degrees-Domain Wall Relaxation in Tetragonally Distorted Ferroelectric Ceramics," *Ferroelectrics,* **74**[1-2] 37-53 (1987).

[3]S. P. Li, W. W. Cao, and L. E. Cross, "The Extrinsic Nature of Nonlinear Behavior Observed in Lead Zirconate Titanate Ferroelectric Ceramic," *J. Appl. Phys.,* **69**[10] 7219-24 (1991).

[4]N. Bassiri-Gharb, I. Fujii, E. Hong, S. Trolier-McKinstry, D. V. Taylor, and D. Damjanovic, "Domain wall contributions to the properties of piezoelectric thin films," *J. Electroceram.,* **19**[1] 47-65 (2007).

[5]L. Rayleigh, "Notes on electricity and magnetism: on the behavior of iron and steel under the operation of magnetic forces," *Philos. Mag.,* **23** 225-45 (1887).

[6]D. V. Taylor and D. Damjanovic, "Evidence of Domain Wall Contribution to the Dielectric Permittivity in PZT Thin Films at Sub-Switching Fields," *J. Appl. Phys.,* **82**[4] 1973-75 (1997).

[7]D. A. Hall, "Rayleigh behaviour and the threshold field in ferroelectric ceramics," *Ferroelectrics,* **223** 319-28 (1999).

[8]F. Preisach, "Über die magnetische Nachwirkung," *Zeitschrift fur Physik,* **94**[5-6] 277-302 (1935).

[9]I. D. Mayergoyz, "Mathematical models of hysteresis and their applications", (Elsevier Academic Press, Amsterdam, 2003).

[10]E. Della Torre, "Magnetic hysteresis", (IEEE Press, New York, 1999).

[11]C. R. Pike, A. P. Roberts, and K. L. Verosub, "Characterizing Interactions in Fine Magnetic Particle Systems Using First Order Reversal Curves," *J. Appl. Phys.,* **85**[9] 6660-67 (1999).

[12]S. Trolier-McKinstry and P. Muralt, "Thin film piezoelectrics for MEMS," *J. Electroceram.,* **12**[1-2] 7-17 (2004).

[13]N. Setter, D. Damjanovic, L. Eng, G. Fox, S. Gevorgian, S. Hong, A. Kingon, H. Kohlstedt, N. Y. Park, G. B. Stephenson, I. Stolitchnov, A. K. Taganstev, D. V. Taylor, T. Yamada, and S. Streiffer, "Ferroelectric thin films: Review of materials, properties, and applications," *J. Appl. Phys.,* **100**[5] art. no. 051606 (2006).

[14]H. D. Chen, K. R. Udayakumar, C. J. Gaskey, L. E. Cross, J. J. Bernstein, and L. C. Niles, "Fabrication and electrical properties of lead zirconate titanate thick films," *J. Am. Ceram. Soc.,* **79**[8] 2189-92 (1996).

[15]T. Tsurumi, Y. Yamamoto, H. Kakemoto, S. Wada, H. Chazono, and H. Kishi, "Dielectric Properties of $BaTiO_3$-$BaZrO_3$ Ceramics under a High Electric Field," *J. Mater. Res.,* **17**[4] 755-59 (2002).

[16]A. J. Moulson and J. M. Herbert, "Electroceramics : materials, properties, applications", (Wiley, Chichester, 2003).

[17]B. Jaffe, W. R. Cook, and H. L. Jaffe, "Piezoelectric ceramics", (R.A.N. Publishers, Marietta, Ohio, 1971).

[18]U. Böttger, "Dielectric Properties of Polar Oxides." in Polar oxides : properties, characterization, and imaging**.** Edited by R. Waser, U. Böttger, and S. Tiedke. Wiley-VCH, Weinheim, 2005.

[19]F. Jona and G. Shirane, "Ferroelectric crystals", (Macmillan, New York, 1962).

[20]M. E. Lines and A. M. Glass, "Principles and applications of ferroelectrics and related materials", (Clarendon Press, Oxford, U.K., 1977).

[21]G. Arlt, "Twinning in Ferroelectric and Ferroelastic Ceramics - Stress Relief," *J. Mater. Sci.,* **25**[6] 2655-66 (1990).

[22]N. B. Gharb, "Dielectric and Piezoelectric Nonlinearities in Oriented $Pb(Yb_{1/2}Nb_{1/2})O_3$-$PbTiO_3$ Thin Films," PhD thesis in Materials Science and Engineering, the Pennsylvania State University (2005).

[23]D. Damjanovic, "Nonlinear piezoelectric response in ferroelectric ceramics,″ pp. 125-35 in *Piezoelectric materials: Advances in Science, Technology, and Applications*. *NATO science series. Series 3, High technology* Edited by C. Galassi, M. Dinescu, K. Uchino, and M. Sayer. (Kluwer Academic Publishers, Dordrecht, 2000).

[24]P. Mokry, Y. L. Wang, A. K. Tagantsev, D. Damjanovic, I. Stolichnov, and N. Setter, "Evidence for dielectric aging due to progressive 180 degrees domain wall pinning in polydomain $Pb(Zr_{0.45}Ti_{0.55})O_3$ thin films," *Phys. Rev. B,* **79**[5] art. no. 054104 (2009).

[25]M. H. Frey, Z. Xu, P. Han, and D. A. Payne, "The Role of Interfaces on an Apparent Grain Size Effect on the Dielectric Properties for Ferroelectric Barium Titanate Ceramics," *Ferroelectrics,* **206**[1-4] 337-53 (1998).

[26]H. Kishi, Y. Mizuno, and H. Chazono, "Base-metal electrode-multilayer ceramic capacitors: Past, present and future perspectives," *Jpn. J. Appl. Phys.,* **42**[1] 1-15 (2003).

[27]T. Tsurumi, H. Adachi, H. Kakemoto, S. Wada, Y. Mizuno, H. Chazono, and H. Kishi, "Dielectric Properties of $BaTiO_3$-Based Ceramics under High Electric Field," *Jpn. J. Appl. Phys.,* **41**[11B] 6929-33 (2002).

[28]T. Dechakupt, G. Yang, C. A. Randall, S. Trolier-McKinstry, and I. M. Reaney, "Chemical solution-deposited $BaTiO_3$ thin films on Ni foils: Microstructure and interfaces," *J. Am. Ceram. Soc.,* **91**[6] 1845-50 (2008).

[29]H. Chazono and H. Kishi, "dc-Electrical Degradation of the BT-Based Material for Multilayer Ceramic Capacitor with Ni internal Electrode: Impedance Analysis and Microstructure," *Jpn. J. Appl. Phys.,* **40**[9B] 5624-29 (2001).

[30]Y. Sakabe and H. Takagi, "Nonreducible Mechanism of $\{(Ba_{1-x}Ca_x)O\}_{(m)}TiO_2$ (m > 1) ceramics," *Jpn. J. Appl. Phys.,* **41**[11A] 6461-65 (2002).

[31]D. I. Woodward, J. Knudsen, and I. M. Reaney, "Review of crystal and domain structures in the $PbZr_xTi_{1-x}O_3$ solid solution," *Phys. Rev. B,* **72**[10] art. no. 104110 (2005).

[32]H. D. Chen, K. R. Udayakumar, C. J. Gaskey, and L. E. Cross, "Electrical properties' maxima in thin films of the lead zirconate-lead titanate solid solution system," *Appl. Phys. Lett.,* **67**[23] 3411-13 (1995).

[33]R. A. Wolf and S. Trolier-McKinstry, "Temperature dependence of the piezoelectric response in lead zirconate titanate films," *J. Appl. Phys.,* **95**[3] 1397-406 (2004).

[34]F. Xu, S. Trolier-McKinstry, W. Ren, B. M. Xu, Z. L. Xie, and K. J. Hemker, "Domain wall motion and its contribution to the dielectric and piezoelectric properties of lead zirconate titanate films," *J. Appl. Phys.,* **89**[2] 1336-48 (2001).

[35]H. Kronmüller, "Statistical Theory of Rayleigh's Law," *Z Angew Physik,* **30**[1] 9-13 (1970).

[36]O. Boser, "Statistical theory of hysteresis in ferroelectric materials," *J. Appl. Phys.,* **62**[4] 1344-48 (1987).

[37]D. Damjanovic, "Stress and frequency dependence of the direct piezoelectric effect in ferroelectric ceramics," *J. Appl. Phys.,* **82**[4] 1788-97 (1997).

[38]P. Ge and M. Jouaneh, "Modeling Hysteresis in Piezoceramic Actuators," *Precis Eng,* **17**[3] 211-21 (1995).

[39]G. Robert, D. Damjanovic, N. Setter, and A. V. Turik, "Preisach modeling of piezoelectric nonlinearity in ferroelectric ceramics," *J. Appl. Phys.,* **89**[9] 5067-74 (2001).

[40]C. K. Wong, C. H. Tsang, and F. G. Shin, "Modeling of bias-field-dependent dielectric properties in ferroelectric thin films," *J. Appl. Phys.,* **98**[7] art. no. 074101 (2005).

[41]G. Robert, D. Damjanovic, and N. Setter, "Preisach Distribution Function Approach to Piezoelectric Nonlinearity and Hysteresis," *J. Appl. Phys.,* **90**[5] 2459-64 (2001).

[42]L. Néel, "Theorie des Lois D'aimantation de Lord Rayleigh I - Les Déplacements d'une Paroi Isolée," *Cahiers de Physique,* **12** 1-20 (1942).

[43]L. Néel, "Some Theoretical Aspects of Rock-Magnetism," *Adv Phys,* **4**[14] 191-243 (1955).

[44]A. Stancu, D. Ricinschi, L. Mitoseriu, P. Postolache, and M. Okuyama, "First-Order Reversal Curves Diagrams for the Characterization of Ferroelectric Switching," *Appl. Phys. Lett.,* **83**[18] 3767-69 (2003).

[45]I. Fujii, E. Hong, and S. Trolier-McKinstry, "Thickness Dependence of Dielectric Nonlinearity of Lead Zirconate Titanate Films," *submitted to IEEE Trans. Ultrason. Ferroelectr. Freq. Control* (2009).

[46]L. Stoleriu, A. Stancu, L. Mitoseriu, D. Piazza, and C. Galassi, "Analysis of switching properties of porous ferroelectric ceramics by means of first-order reversal curve diagrams," *Phys. Rev. B,* **74**[17] art. no. 174107 (2006).

[47]J. E. Davies, O. Hellwig, E. E. Fullerton, J. S. Jiang, S. D. Bader, G. T. Zimanyi, and K. Liu, "Anisotropy dependence of irreversible switching in Fe/SmCo and FeNi/FePt exchange spring magnet films," *Appl. Phys. Lett.,* **86**[26] art. no. 262503 (2005).

[48]D. Ricinschi, L. Mitoseriu, A. Stancu, P. Postolache, and M. Okuyama, "Analysis of the switching characteristics of PZT films by first order reversal curve diagrams," *Integr. Ferroelectr.,* **67** 103-15 (2004).

[49]L. Mitoseriu, C. E. Ciomaga, V. Buseaglia, L. Stoleriu, D. Piazza, C. Galassi, A. Stancu, and P. Nanni, "Hysteresis and Tunability Characteristics of $Ba(Zr,Ti)O_3$ Ceramics Described by First Order Reversal Curves Diagrams," *J. Eur. Ceram. Soc.,* **27**[13-15] 3723-26 (2007).

[50]R. Kurchania and S. J. Milne, "Characterization of sol-gel $Pb(Zr_{0.53}Ti_{0.47})O_3$ films in the thickness range 0.25-10 μm," *J. Mater. Res.,* **14**[5] 1852-59 (1999).

[51]A. K. Taganstev, "Mechanisms of polarization switching in ferroelectric thin films," *Ferroelectrics,* **184** 79-88 (1996).

[52]T. M. Shaw, S. Trolier-McKinstry, and P. C. McIntyre, "The properties of ferroelectric films at small dimensions," *Annu. Rev. Mater. Sci.,* **30** 263-98 (2000).

[53]P. K. Larsen, G. J. M. Dormans, D. J. Taylor, and P. J. Vanveldhoven, "Ferroelectric properties and fatigue of $PbZr_{0.51}Ti_{0.49}O_3$ thin films of varying thickness: Blocking layer model," *J. Appl. Phys.,* **76**[4] 2405-13 (1994).

[54]C. D. E. Lakeman and D. A. Payne, "Apparent thickness effect on properties of ferroelectric PZT thin layers," *Ferroelectrics,* **152** 145-50 (1994).

[55]J. J. Lee, C. L. Thio, and S. B. Desu, "Electrode contacts on ferroelectric $Pb(Zr_xTi_{1-x})O_3$ and $SrBi_2Ta_2O_9$ thin films and their influence on fatigue properties," *J. Appl. Phys.,* **78**[8] 5073-78 (1995).

[56]J. F. M. Cillessen, M. W. J. Prins, and R. M. Wolf, "Thickness dependence of the switching voltage in all-oxide ferroelectric thin-film capacitors prepared by pulsed laser deposition," *J. Appl. Phys.,* **81**[6] 2777-83 (1997).

[57]A. K. Tagantsev and I. A. Stolichnov, "Injection-controlled size effect on switching of ferroelectric thin films," *Appl. Phys. Lett.,* **74**[9] 1326-28 (1999).

[58]R. Bouregba, G. Le Rhun, G. Poullain, and G. Leclerc, "Investigation of thickness dependence of the ferroelectric properties of $Pb(Zr_{0.6}Ti_{0.4})O_3$ thin-film capacitors," *J. Appl. Phys.,* **99**[3] art. no. 034102 (2006).

[59]V. Nagarajan, I. G. Jenkins, S. P. Alpay, H. Li, S. Aggarwal, L. Salamanca-Riba, A. L. Roytburd, and R. Ramesh, "Thickness dependence of structural and electrical properties in epitaxial lead zirconate titanate films," *J. Appl. Phys.,* **86**[1] 595-602 (1999).

[60]D. Damjanovic and M. Demartin, "The Rayleigh law in piezoelectric ceramics," *J. Phys. D Appl. Phys.,* **29**[7] 2057-60 (1996).

[61]C. R. Cho, W. J. Lee, B. G. Yu, and B. W. Kim, "Dielectric and ferroelectric response as a function of annealing temperature and film thickness of sol-gel deposited $Pb(Zr_{0.52}Ti_{0.48})O_3$ thin film," *J. Appl. Phys.,* **86**[5] 2700-11 (1999).

[62]D. J. Kim, J. H. Park, D. Shen, J. W. Lee, A. I. Kingon, Y. S. Yoon, and S. H. Kim, "Thickness dependence of submicron thick $Pb(Zr_{0.3}Ti_{0.7})O_3$ films on piezoelectric properties," *Ceram. Int.,* **34**[8] 1909-15 (2008).

[63]E. Hong, "Surface micromachined peristaltic pumps using lead zirconate titanate film," PhD thesis in Materials Science and Engineering, the Pennsylvania State University (2004).

[64]A. Stancu, C. Pike, L. Stoleriu, P. Postolache, and D. Cimpoesu, "Micromagnetic and Preisach analysis of the First Order Reversal Curves (FORC) diagram," *J. Appl. Phys.,* **93**[10] 6620-22 (2003).

[65]P. Postolache, M. Cerchez, L. Stoleriu, and A. Stancu, "Experimental evaluation of the Preisach distribution for magnetic recording media," *IEEE Trans. Magn.,* **39**[5] 2531-33 (2003).

[66]K. Morita, Y. Mizuno, H. Chazono, H. Kishi, G. Y. Yang, W. E. Liu, E. C. Dickey, and C. A. Randall, "Electric conduction of thin-layer Ni-multilayer ceramic capacitors with core-shell structure $BaTiO_3$," *Jpn. J. Appl. Phys. Part 1 - Regul. Pap. Brief Commun. Rev. Pap.,* **46**[5A] 2984-90 (2007).

[67]A. J. Bell, "Grain Size Effects in Barium Titanate - Revisited," pp. 14-17 in *Proceedings of the Ninth IEEE International Symposium on Applications of Ferroelectrics*. Edited by R. K. Pandey, M. Liu, and A. Safari. (IEEE, Piscataway, NJ, 1994).

[68]M. T. Buscaglia, M. Viviani, V. Buscaglia, L. Mitoseriu, A. Testino, P. Nanni, Z. Zhao, M. Nygren, C. Harnagea, D. Piazza, and C. Galassi, "High Dielectric Constant and Frozen

Macroscopic Polarization in Dense Nanocrystalline $BaTiO_3$ Ceramics," *Phys. Rev. B,* **73**[6] art. no. 064114 (2006).

[69]G. Arlt, "The Influence of Microstructure on the Properties of Ferroelectric Ceramics," *Ferroelectrics,* **104** 217-27 (1990).

[70]R. C. Pohanka, R. W. Rice, and B. E. Walker, "Effect of Internal Stress on Strength of $BaTiO_3$," *J. Am. Ceram. Soc.,* **59**[1-2] 71-74 (1976).

[71]W. R. Buessem, L. E. Cross, and A. K. Goswami, "Phenomenological Theory of High Permittivity in Fine-Grained Barium Titanate," *J. Am. Ceram. Soc.,* **49**[1] 33-36 (1966).

[72]G. Arlt, D. Hennings, and G. Dewith, "Dielectric-Properties of Fine-Grained Barium-Titanate Ceramics," *J. Appl. Phys.,* **58**[4] 1619-25 (1985).

[73]G. Arlt and N. A. Pertsev, "Force-Constant and Effective Mass of 90-Degrees Domain-Walls in Ferroelectric Ceramics," *J. Appl. Phys.,* **70**[4] 2283-89 (1991).

[74]D. Damjanovic, "Ferroelectric, Dielectric and Piezoelectric Properties of Ferroelectric Thin Films and Ceramics," *Rep. Prog. Phys.,* **61**[9] 1267-324 (1998).

[75]U. Robels, C. Zadon, and G. Arlt, "Linearization of Dielectric Nonlinearity by Internal Bias Fields," *Ferroelectrics,* **133**[1-4] 163-68 (1992).

[76]V. Mueller and Q. M. Zhang, "Nonlinearity and Scaling Behavior in Donor-Doped Lead Zirconate Titanate Piezoceramic," *Appl. Phys. Lett.,* **72**[21] 2692-94 (1998).

[77]A. V. Turik, "Theory of Polarization and Hysteresis of Ferroelectrics," *Sov. Phys. Solid State,* **5**[4] 885-86 (1963).

[78]A. V. Turik, "Experimental Investigation of the Statistical Distribution of Domains in a Ferroelectric Ceramic," *Sov. Phys. Solid State,* **5**[10] 2141-43 (1964).

[79]D. A. Hall, M. M. Ben-Omran, and P. J. Stevenson, "Field and Temperature Dependence of Dielectric Properties in $BaTiO_3$-Based Piezoceramics," *J. Phys.: Condens. Mat.,* **10**[2] 461-76 (1998).

[80]K. W. Wu and W. A. Schulze, "Effect of the ac Field Level on the Aging of the Dielectric Response in Polycrystalline $BaTiO_3$," *J. Am. Ceram. Soc.,* **75**[12] 3385-89 (1992).

[81]I. Fujii, M. Ugorek, Y. Han, and S. Trolier-McKinstry, "Effect of Oxygen Partial Pressure during Firing on the High ac Field Response of $BaTiO_3$ Dielectrics," *accepted J. Am. Ceram. Soc.* (2009).

[82]H. Schmelz and A. Meyer, "The Evidence for Anomalous Grain Growth below the Eutectic Temperature in $BaTiO_3$ Ceramics," *Ber. Dtsch. Keram. Ges.,* **59**[8/9] 436-40 (1982).

[83]Y. K. Cho, S. J. L. Kang, and D. Y. Yoon, "Dependence of Grain Growth and Grain-Boundary Structure on the Ba/Ti Ratio in $BaTiO_3$," *J. Am. Ceram. Soc.,* **87**[1] 119-24 (2004).

[84]T. Yamamoto, "Influence of Small Ba/Ti Nonstoichiometry on Grain-Growth Behavior in Barium-Titanate," *Br. Ceram. Trans.,* **94**[5] 196-200 (1995).

[85]D. F. K. Hennings, R. Janssen, and P. J. L. Reynen, "Control of Liquid-Phase-Enhanced Discontinuous Grain-Growth in Barium-Titanate," *J. Am. Ceram. Soc.,* **70**[1] 23-27 (1987).

[86]M. Demartin, C. Herard, C. Carry, and J. Lemaitre, "Dedensification and Anomalous Grain Growth during Sintering of Undoped Barium Titanate," *J. Am. Ceram. Soc.,* **80**[5] 1079-84 (1997).

[87]M. H. Frey and D. A. Payne, "Grain-size effect on structure and phase transformations for barium titanate," *Phys. Rev. B,* **54**[5] 3158-68 (1996).

[88]K. Kinoshita and A. Yamaji, "Grain-Size Effects on Dielectric Properties in Barium-Titanate Ceramics," *J. Appl. Phys.,* **47**[1] 371-73 (1976).

[89]S. Lee, Z. K. Liu, M. H. Kim, and C. A. Randall, "Influence of nonstoichiometry on ferroelectric phase transition in $BaTiO_3$," *J. Appl. Phys.,* **101**[5] art. no. 054119 (2007).

[90]S. Lee, C. A. Randall, and Z. K. Liu, "Modified phase diagram for the barium oxide-titanium dioxide system for the ferroelectric barium titanate," *J. Am. Ceram. Soc.,* **90**[8] 2589-94 (2007).

[91]B. L. Cheng, M. Gabbay, M. Maglione, and G. Fantozzi, "Relaxation Motion and Possible Memory of Domain Structures in Barium Titanate Ceramics Studied by Mechanical and Dielectric Losses," *J. Electroceram.,* **10**[1] 5-18 (2003).

[92]C. Ang, Z. Yu, and L. E. Cross, "Oxygen-vacancy-related low-frequency dielectric relaxation and electrical conduction in Bi : $SrTiO_3$," *Phys. Rev. B,* **62**[1] 228-36 (2000).

[93]H. J. Hagemann, "Loss Mechanisms and Domain Stabilization in Doped $BaTiO_3$," *J. Phys. C: Solid State Phys.,* **11**[15] 3333-44 (1978).

[94]K. Carl and K. H. Hardtl, "Electrical After-Effects in $Pb(Ti,Zr)O_3$ Ceramics," *Ferroelectrics,* **17**[3-4] 473-86 (1978).

[95]D. A. Hall and P. J. Stevenson, "High Field Dielectric Behaviour of Ferroelectric Ceramics," *Ferroelectrics,* **228**[1-4] 139-58 (1999).

[96]M. Demartin and D. Damjanovic, "Dependence of the Direct Piezoelectric Effect in Coarse and Fine Grain Barium Titanate Ceramics on Dynamic and Static Pressure," *Appl. Phys. Lett.,* **68**[21] 3046-48 (1996).

[97]G. Robert, D. Damjanovic, and N. Setter, "Preisach Modeling of Ferroelectric Pinched Loops," *Appl. Phys. Lett.,* **77**[26] 4413-15 (2000).

[98]R. Herbiet, U. Robels, H. Dederichs, and G. Arlt, "Domain Wall and Volume Contributions to Material Properties of PZT Ceramics," *Ferroelectrics,* **98** 107-21 (1989).

[99]J. Ihlefeld, B. Laughlin, A. Hunt-Lowery, W. Borland, A. Kingon, and J. P. Maria, "Copper Compatible Barium Titanate Thin Films for Embedded Passives," *J. Electroceram.,* **14**[2] 95-102 (2005).

[100]T. Yonezawa, S. Takeoka, H. Kishi, K. Ida, and M. Tomonari, "The preparation of copper fine particle paste and its application as the inner electrode material of a multilayered ceramic capacitor," *Nanotechnology,* **19**[14] art. no. 145706 (2008).

[101]G. Y. Yang, E. C. Dickey, C. A. Randall, D. E. Barber, P. Pinceloup, M. A. Henderson, R. A. Hill, J. J. Beeson, and D. J. Skamser, "Oxygen nonstoichiometry and dielectric evolution of $BaTiO_3$. Part I - improvement of insulation resistance with reoxidation," *J. Appl. Phys.,* **96**[12] 7492-99 (2004).

[102]G. Y. Yang, G. D. Lian, E. C. Dickey, C. A. Randall, D. E. Barber, P. Pinceloup, M. A. Henderson, R. A. Hill, J. J. Beeson, and D. J. Skamser, "Oxygen nonstoichiometry and dielectric evolution of $BaTiO_3$. Part II - insulation resistance degradation under applied dc bias," *J. Appl. Phys.,* **96**[12] 7500-08 (2004).

[103]Y. I. Jung, S. Y. Choi, and S. J. L. Kang, "Grain-Growth Behavior during Stepwise Sintering of Barium Titanate in Hydrogen Gas and Air," *J. Am. Ceram. Soc.,* **86**[12] 2228-30 (2003).

[104]J. K. Lee, K. S. Hong, and J. H. Chung, "Revisit to the Origin of Grain Growth Anomaly in Yttria-Doped Barium Titanate," *J. Am. Ceram. Soc.,* **84**[8] 1745-49 (2001).

[105]A. Polotai, K. Breece, E. Dickey, C. Randall, and A. Ragulya, "A Novel Approach to Sintering Nanocrystalline Barium Titanate Ceramics," *J. Am. Ceram. Soc.,* **88**[11] 3008-12 (2005).

[106]D. Hennings and G. Rosenstein, "Temperature-Stable Dielectrics Based on Chemically Inhomogeneous $BaTiO_3$," *J. Am. Ceram. Soc.,* **67**[4] 249-54 (1984).

[107]Q. Q. Feng, C. J. McConville, D. D. Edwards, D. E. McCauley, and M. Chu, "Effect of Oxygen Partial Pressure on the Dielectric Properties and Microstructures of Cofired Base-Metal-Electrode Multilayer Ceramic Capacitors," *J. Am. Ceram. Soc.,* **89**[3] 894-901 (2006).

[108]D. E. McCauley, M. S. H. Chu, and M. H. Megherhi, "PO_2 Dependence of the Diffuse-Phase Transition in Base Metal Capacitor Dielectrics," *J. Am. Ceram. Soc.,* **89**[1] 193-201 (2006).

[109]H. J. Hagemann and H. Ihrig, "Valence Change and Phase Stability of 3d-Doped $BaTiO_3$ Annealed in Oxygen and Hydrogen," *Phys. Rev. B,* **20**[9] 3871-78 (1979).

[110]P. Hansen, D. Hennings, and H. Schreinemacher, "Dielectric properties of acceptor-doped (Ba,Ca)(Ti,Zr)O_3 ceramics," *J. Electroceram.,* **2**[2] 85-94 (1998).

[111]B. S. Kang and S. K. Choi, "Diffuse dielectric anomaly of $BaTiO_3$ in the temperature range of 400-700 ˚C," *Solid State Commun,* **121**[8] 441-46 (2002).

[112]O. Bidault, P. Goux, M. Kchikech, M. Belkaoumi, and M. Maglione, "Space-Charge Relaxation in Perovskites," *Phys. Rev. B,* **49**[12] 7868-73 (1994).

[113]W. L. Warren, K. Vanheusden, D. Dimos, G. E. Pike, and B. A. Tuttle, "Oxygen vacancy motion in perovskite oxides," *J. Am. Ceram. Soc.,* **79**[2] 536-38 (1996).

[114]G. V. Lewis and C. R. A. Catlow, "Computer Modeling of Barium Titanate," *Radiat. Eff. Defects Solids,* **73**[1-4] 307-14 (1983).

[115]S. H. Cha and Y. H. Han, "Effects of oxygen vacancies on relaxation behavior of Mg-doped $BaTiO_3$," *Jpn. J. Appl. Phys. Part 1 - Regul. Pap. Brief Commun. Rev. Pap.,* **45**[10A] 7797-800 (2006).

[116]S. H. Cha and Y. H. Han, "Effects of Mn doping on dielectric properties of Mg-doped $BaTiO_3$," *J. Appl. Phys.,* **100**[10] art. no. 104102 (2006).

[117]W. Liu and C. A. Randall, "Thermally Stimulated Relaxation in Fe-Doped $SrTiO_3$ Systems: I. Single Crystals," *J. Am. Ceram. Soc.,* **91**[10] 3245-50 (2008).

[118]H. Chazono, Y. Inomata, N. Kohzu, and H. Kishi, "Relationship between the Microstructure and Electrical Properties for a Multilayer Ceramic Capacitor with a Ni Internal Electrode," *Key Engineering Materials,* **169-170** 31-36 (1999).

[119]W. W. Cao and C. A. Randall, "Grain Size and Domain Size Relations in Bulk Ceramic Ferroelectric Materials," *Journal of Physics and Chemistry of Solids,* **57**[10] 1499-505 (1996).

[120]N. A. Pertsev and G. Arlt, "Forced translational vibrations of 90˚ domain walls and the dielectric dispersion in ferroelectric ceramics," *J. Appl. Phys.,* **74**[6] 4105-12 (1993).

[121]I. Stolichnov, L. Malin, E. Colla, A. K. Tagantsev, and N. Setter, "Microscopic aspects of the region-by-region polarization reversal kinetics of polycrystalline ferroelectric Pb(Zr,Ti)O_3 films," *Appl. Phys. Lett.,* **86**[1] art. no. 012902 (2005).

[122]P. Bintachitt, S. Trolier-McKinstry, K. Seal, S. Jesse, and S. V. Kalinin, "Switching spectroscopy piezoresponse force microscopy of polycrystalline capacitor structures," *Appl. Phys. Lett.,* **94**[4] art. no. 042906 (2009).

[123]H. Bittel, "Noise of ferromagnetic materials," *IEEE Trans. Magn.,* **MAG5**[3] 359-65 (1969).

[124]P. Bintachitt, "Local Origin of Macroscopic Properties and Patterning in $PbZr_{1-x}Ti_xO_3$ Films," PhD thesis in Materials Science and Engineering, the Pennsylvania State University (2009).

[125]C. Nies and M. Berolini, "Factors in Improved DC Bias Performance in X7R Capacitors," *The 12th US-Japan Seminar on Dielectric Piezoelectric Ceramics, Extended Abstract* 357-60 (2005).

[126]G. Y. Yang, S. I. Lee, Z. J. Liu, C. J. Anthony, E. C. Dickey, Z. K. Liu, and C. A. Randall, "Effect of local oxygen activity on Ni-$BaTiO_3$ interfacial reactions," *Acta Mater,* **54**[13] 3513-23 (2006).

[127]A. V. Polotai, G. Y. Yang, E. C. Dickey, and C. A. Randall, "Utilization of Multiple-Stage Sintering to Control Ni Electrode Continuity in Ultrathin Ni-$BaTiO_3$ Multilayer Capacitors," *J. Am. Ceram. Soc.,* **90**[12] 3811-17 (2007).

[128]I. Fujii, M. Ugorek, and S. Trolier-McKinstry, "Grain Size Effect on the Dielectric Nonlinearity of $BaTiO_3$ Ceramics," *Submitted to J. Appl. Phys.* (2010).

[129]T. T. Fang, H. L. Hsieh, and F. S. Shiau, "Effects of Pore Morphology and Grain Size on the Dielectric Properties and Tetragonal—Cubic Phase Transition of High-Purity Barium Titanate," *J. Am. Ceram. Soc.,* **76**[5] 1205-11 (1993).

[130]D. Liu, Y. K. Yan, and H. P. Zhou, "Synthesis of micron-scale platelet $BaTiO_3$," *J. Am. Ceram. Soc.,* **90**[4] 1323-26 (2007).

[131]L. Cima and E. Laboure, "A model of ferroelectric behavior based on a complete switching density," *J. Appl. Phys.,* **95**[5] 2654-59 (2004).

[132]W. H. Press, B. P. Flannery, S. A. Teukolsky, and W. T. Vetterling, "Numerical recipes in C : the art of scientific computing", 2nd **Vol.** (Cambridge University Press, Cambridge ; New York, 1992).

VITA

Ichiro Fujii

Ichiro Fujii was born in Yamaguchi, Japan on May 28th, 1979. He received his Bachelor's and Master's degrees in Materials Science from Tohoku University, Miyagi, Japan in 2003 and 2005, respectively. During his Master course, he studied at the Pennsylvania State University for 9 months as an exchange student. In 2005, he came back to the Pennsylvania State University and began studies toward his doctorate degree in Materials Science and Engineering.